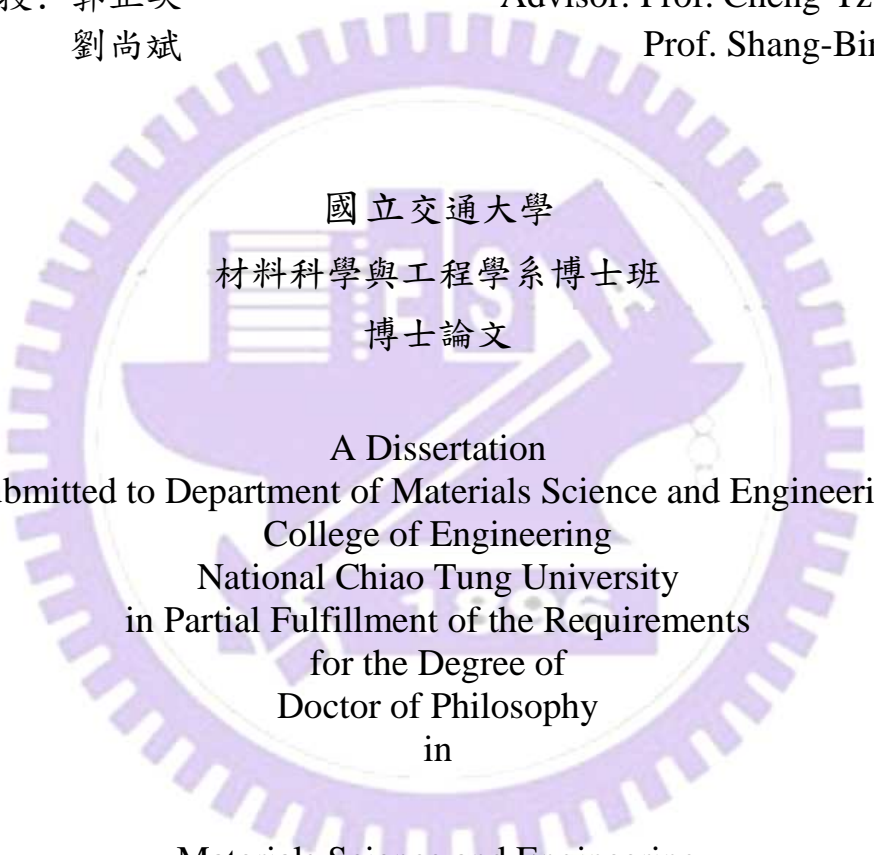


奈米結構碳材之製備、成長機制
及其甲醇氧化反應觸媒之電觸媒效能

Fabrication and Growth Mechanism of Carbon
Nanostructured Materials and Their Electrocatalytic
Performances during Methanol Oxidation Reaction

研究生：駱安亞
指導教授：郭正次
劉尚斌

Student: An-Ya Lo
Advisor: Prof. Cheng-Tzu Kuo
Prof. Shang-Bin Liu



國立交通大學
材料科學與工程學系博士班
博士論文

A Dissertation
Submitted to Department of Materials Science and Engineering
College of Engineering
National Chiao Tung University
in Partial Fulfillment of the Requirements
for the Degree of
Doctor of Philosophy
in
Materials Science and Engineering

July 2010

Hsinchu, Taiwan, Republic of China

中華民國九十九年七月

奈米結構碳材之製備、成長機制及其甲醇氧化反應觸媒之電觸媒效能

研究生：駱安亞

指導教授：郭正次 教授
劉尚斌 教授

國立交通大學

材料科學與工程學系博士班

中文摘要

本研究主要是開發奈米製程以合成具有可調控孔洞結構之碳奈米結構、探索它們對甲醇氧化反應之催化效能，以及討論碳奈米管(CNTs)之成長機制。孔洞性碳材料(CPMs)以及碳奈米管(CNTs)乃利用沸石或二氧化矽為模板，以 C_2H_2 和 H_2 為反應氣體，分別在無或有鐵觸媒的情況下藉模板輔助化學氣相沉積(CVD)法合成之。這些二氧化矽模板材料，包括了 Y 型沸石、MCM-41、MCM-48、SBA-15 和二氧化矽光子晶體(PC)等等，它均由傳統方法製備之。至於直接甲醇燃料電池陽極之製備，乃是先將孔洞性碳材料或碳奈米管與 H_2PtCl_6 混合，以 CVD 製程在 H_2 和 523 K 溫度環境下以將 Pt 前趨物還原，使 Pt 分散在具有孔洞的 CPMs 或 CNTs 陽極擔體上，反應時間為 30 分鐘。採用下列方法來分析在每一研究階段之奈米材料之結構與性質：穿透式電子顯微技術、X-光繞射技術、循環伏安法、化學吸附、熱重、拉曼以及氮氣吸脫附等分析。從實驗結果，可得出以下結論：

關於 CPM 之製備，模板輔助化學氣相沉積製程可以成功製備 CPM，所得之 CPM 孔徑介於 1 到 400 nm 之間，本製程使用之氣態反應於 1073 K 下可以大幅縮短製程時間至 1 小時內，而須經反覆乾燥及除水步驟的傳統液態反應法，則需費時一天。本製程的另一個優點，在於可以複製各種尺度的微孔洞、中孔洞以及大孔洞碳材料，相對的微孔碳材微孔洞碳材料則難以藉由傳統方法製備，達到複製各種尺度的。在移除二氧化矽或沸石模板後之 CPMs 的 I_G/I_D 比值大約介於 0.7-0.8 之間，此比值與 CPMs 之孔徑無關。

關於碳奈米管之製備，中孔洞矽模板成功的被用來製備 CNTs。其製程是在 CVD 沉積之前將鐵觸媒顆粒填入模板之孔洞中。藉由穿透式電子顯微技術之分析發現這裡的 CNTs 主要是多壁碳奈米管(MWCNTs)，且它們的尺寸可以成功的被合成和控制，直徑為 3 到 17 nm 的 CNTs 分別是使用孔洞直徑為 3 到 18 nm 的二氧化矽模板。在移除二氧化矽模板後的 MWCNTs 之 I_G/I_D 比值與商業化單壁碳奈米管、商業化 XC-72 之 I_G/I_D 之比值大約相同。

關於分散有 Pt 觸媒的 CPMs 所製之 DMFC 陽極之甲醇氧化效能而言，循環伏安曲線中之結果顯示正向電流密度峰值， I_f (122 到 655 A/g Pt)，隨著 CPMs 之孔徑增加而增加(從 1 到 400 nm)，其中 I_f 是代表陽極甲醇氧化反應(MOR)活性之指標。其原因可能是在反應時甲醇之質量傳輸受到 CPMs 之孔洞的侷限。正向與逆向電流密度峰值之比值代表陽極的 CO-容忍度之指標；相對於孔洞尺寸為 1 到 400 nm 之 CPMs，其值分別為 4.9 到 1.0。其中 CO-容忍度是代表 Pt 顆粒表面對抗 CO 毒化之能力，其中佔據 Pt 表面的 CO 是 MOR 操作過程中的中間產物，它使得陽極失活。因此一般來講，CO-容忍度是與 Pt 顆粒大小無關的。然而此研究結果顯示，小於 1 nm 的 Pt 顆粒數量增加將使得 CO 容忍力上升，這指出小於 1 nm 之 Pt 顆粒的表面性質由於奈米效應而有明顯改變。然而其背後的原因有待進一步的研究。

關於分散有 Pt 處媒的 CNTs 所製陽極之甲醇氧化效能而言。結果顯示其陽極反應活性(354-414 A/g Pt)隨者管徑增加而增加(3 到 17 nm)。穿透式電子顯微技術分析亦指出具有較大之管徑使得它較不易於聚集成束，Pt 顆粒被包埋在管束中的或然率就比較小，也就有較好的 Pt 分散。這可能是 MOR 活性隨者管徑增加而增加的原因。結果也指出再這些情形下 CO-容忍度約介在 1.2 到 1.3 之間，且 CNTs 尺寸以及 CNTs 中之 Fe 觸媒對於容忍度沒有明顯的效應。此外，在這裡 Fe-Pt 合金對 CO-容忍度並沒有顯著的影響，這是由於碳管的隔離效應使 Fe 免於和 Pt 變成合金。此外，藉由比較 CPM-與 CNT-輔助陽極之效能，結果指出較大的孔徑

或管徑可提升 MOR 活性。而 CO-容忍度與碳奈米結構材料之型態無關，且大量 $< 1 \text{ nm}$ 的 Pt 顆粒會導致較高的 CO-容忍度。換句話說，在本研究中，孔徑 400-nm 或管徑 17-nm 之 CPMs 或 CNTs 輔助陽極具有可導致較好的 MOR 活性。此外，小尺寸 Pt 的數量在孔徑為 1 nm 的 CPMs 輔助陽極上之數量多於其它的碳材料輔助陽極，因此具有最佳之 CO-容忍度。

關於跨越觸媒顆粒之溫度差對於碳奈米管成長機制影響之研究，碳奈米管乃藉由熱以及電漿化學輔助化學氣相沉積法沉積於不同基材，例如中孔洞 SBA-15 以及矽晶圓等，以 C_2H_2 及 H_2 為反應氣體，Co 為觸媒。結果顯示， ΔT 其定義為觸媒顆粒頂端(接近氣氛處)以及底端(接近基材處)之局部溫度差，是決定 CNT 頂端或底端成長機制的重要製程參數。也顯示成長模式在 $\Delta T > 0, \sim 0, < 0$ 時，分別傾向於頂端-、洋蔥狀的-、底端-成長模式。利用 ΔT 可以成功的用來解釋為何底端-和頂端-成長模式的碳奈米管通常分別有較大的趨勢發生在熱-以及電漿輔助-化學氣相沉積製程中，還可進一步地藉由改變 ΔT 的設計成功的改變在熱-以及電漿輔助-化學氣相沉積製程中的成長模式。

Fabrication and Growth Mechanism of Carbon Nanostructured Materials and Their Electrocatalytic Performances during Methanol Oxidation Reaction

Student: An-Ya Lo

Advisor: Prof. Cheng-Tzu Kuo
Prof. Shang-Bin Liu

Department of Materials Science and Engineering
National Chiao Tung University

Abstract in English

In this work, nanofabrication processes to synthesize various carbon nanostructures with tunable pore structure, to explore their DMFC (direct methanol fuel cell) anode applications and to examine growth mechanisms of CNTs (carbon nanotubes) were developed. The CPMs (carbon porous materials) and CNTs were synthesized without and with Fe as catalyst, respectively, using template-assisted CVD process with C_2H_2 and H_2 as the reaction gases. The templates are made of zeolite or silica, and consist of commercial Zeolite-Y, MCM-41, MCM-48, SBA-15, and PC (photonic crystal) porous silicas. The templates were prepared by conventional methods. For DMFC anode preparation, anodes were fabricated by mixing CPMs or CNTs with H_2PtCl_6 , followed by a CVD process to reduce Pt-precursor and to disperse Pt element on porous CPMs or CNTs anode in H_2 atmosphere at 523 K for 30 min. The structure and properties of the nanostructured materials after each step were characterized by transmission electron microscopy (TEM), X-ray diffractometry (XRD), cyclic-voltammetry (C-V), chemisorption, thermogravimetric (TG), Raman, and N_2 adsorption/desorption analyses. From the experimental results, the following conclusions can be drawn.

For CPMs fabrication, the developed silica template-assisted CVD process could be successfully used to control CPMs with pore diameters ranging from 1 nm – 400 nm, using gas reactants at 1073 K to reduce the process time to less than 1 h, in contrast to about 1 day by the conventional processes using liquid reactants and requiring multiple dehydration and drying steps. The additional advantage of the new process is that all range of microporous, mesoporous and macroporous carbons can be replicated. In contrast, microporous carbons are difficult to be fabricated by conventional methods. The I_G/I_D ratios of CPMs after silica or zeolite removal are about 0.7 - 0.8, independent of pore size.

For CNTs fabrication, mesoporous silica templates were also successfully used to fabricate CNTs, by filling Fe catalyst particles into the pores of template before CNTs deposition. From TEM examination, it is found that the CNTs are mainly MWCNTs (multiwalled CNTs), and their sizes can be successfully synthesized and controlled, ranging from 3 nm to 17 nm in diameter by using the pore diameters of silica templates ranging from 3 nm to 18 nm, respectively. The I_G/I_D ratios of MWCNTs after silica removal are about the same as CPMs, commercial SWCNTs and XC-72 activated carbon material.

Regarding methanol oxidation reaction (MOR) performance of DMFC anode made of CPMs with dispersed Pt, the results show that peak forward mass activity I_f (from 122 to 655 A/g of Pt) in the C-V curves, which is an index representing the MOR activity of the anode, increases with increasing pore size (from 1 to 400 nm in diameter) of CPMs. The reason may be due to limitation of pore of CPMs on mass transfer of methanol during reaction. From the C-V curves of the anode, the peak forward to reverse mass activity ratio, I_f/I_r , is an index representing CO-tolerance of the anode; the results indicate that the values ranging from 4.9 to 1.0 are

corresponding to the pore sizes of CPMs ranging from 1 to 400 nm, respectively. The CO-tolerance represents the ability of surface condition of Pt-particles to stand poisoning by the occupied CO, where CO is an intermediate product of MOR during operation, making the anode inactive. Therefore CO-tolerance, in general, is not sensitive to Pt-particle size. However, the results indicate that a higher tolerance value is closely related to a greater amount of smaller Pt particles with sizes less than 1 nm in diameter, signifying surface conditions may change significantly for particle size less than 1 nm due to nano effect. Further study is required to find the reasons behind that.

Regarding MOR performance of DMFC anode made of CNTs with dispersed Pt on outside of the tubes, the results show that the MOR activity (from 354 to 414 A/g of Pt) of the anode increases with increasing tube diameter (from 3 to 17 nm). The TEM examination also indicates that a larger tube size give rise to a less tube bundling, less probability for Pt particles to be embedded within the bundles and so more uniform Pt particle distribution. This may be the reasons for a greater MOR activity for a greater tube size. The results also indicate that the CO-tolerances in these cases are around 1.2 – 1.3, where effects of tube size of CNTs and amount of Fe catalyst in CNTs on tolerance are not significant. It signifies there are no significant differences in surface conditions for Pt-particles on different tube sizes. In addition, there is no significant amount of Pt-particles with sizes less than 1 nm, as discussed in the previous paragraph. Furthermore, the reported effect of Fe-Pt alloys on CO-tolerance is not obvious in these cases due to isolation effect of the tubes to the Fe-particles from alloying with Pt. Furthermore, by comparing the performance between the CPMs- and CNT-assisted anodes, the results indicate that a greater pore size or tube diameter gives rise to a greater MOR activity, and a greater amount of Pt

particles of < 1 nm results in a higher CO-tolerance, independent of the type of carbon nanostructured materials. In other words, the CPMs- or CNT-assisted anodes with 400-nm pore size or 17-nm tube diameter can result in a better MOR activity among the present working cases. In addition, the amount of smaller Pt particles (< 1 nm) in the CPM-assisted anode with 1-nm pore size is much greater than other carbon-assisted anode cases, therefore it results in the best CO-tolerance.

About effect of temperature difference across a catalyst particle on growth mechanism of CNTs, growth of CNTs by thermal and plasma-enhanced CVD on various substrates, such as mesoporous SBA-15 and Si wafer, with C_2H_2 and H_2 as reaction gases and Co as catalyst were conducted. The results show that ΔT , defined as local temperature difference between the top (close to gas atmosphere) and bottom (in contact with the substrate) sides of a catalyst particle, is an important parameter to determine whether growth mode being tip- or base-growth mechanisms. When $\Delta T > 0$, ~ 0 and < 0 , the results show that growth mode of CNTs is more favor to be tip-, onion-like- and base-growth modes, respectively. The ΔT parameter proposed to determine growth modes can be successfully adopted to explain why the base- and tip-growth CNTs are common in thermal CVD and plasma-enhanced CVD processes, respectively. Furthermore, few experiments designed to change ΔT to vary the growth modes in both thermal and plasma-enhanced CVD processes were successfully conducted.

Acknowledgement (誌謝)

隨著論文的付梓，博士班的生涯即將劃上休止符，這段時間以來的點點滴滴，酸甜苦辣都將使我的人生更加成長茁壯。論文能夠順利完成，幸蒙指導教授郭老師、中央研究院劉老師；口試委員潘扶民教授、林景崎所長、林啟瑞院長以及武東星校長對於研究方向的諄諄教誨與提攜，對於研究的方向、觀念的啟迪、架構的匡正、文字的潤飾與求學的態度，恩師們總是字斟句酌、逐一斧正與細心關懷，此外在為人處事與生活態度方面，更是讓學生有許多足堪效法的地方，學生願藉卷首表以謝意，並誠心的祝福恩師身體健康，順心如意。

在此，也要感謝多年來許多學長姐對我的提攜，以及學弟妹們對我的支持和包容。首先，我要感謝的是信靈學長、文華學姊、曼倩學姊、柏林、貞君及必愷，從他們身上讓我學習到對生活認真和研究的執著；感謝孟良、立群、文綬、傳恕、修誠、伊茹和泰瑞，在學術上不斷的相互砥礪；感謝這些年來的好夥伴們—雷志斌教授、鄭安民教授、喻寧亞教授、吳鵬博士、培豪、季諭、芷宜、佳婷、錦德、守恆、建章、旻聰、佳樺等，在實驗室事務上的指點、包容與協助；感謝處世圓滑、胸襟寬大，總是能包容任何事物的登發、昱文、禹宸，每每為我排遣生活以及研究中遇到的挫折和無力感，你們的幽默總是讓我憂鬱一掃而空的良藥；感謝多年的老朋友佳敏、中益、玲君等的支持和鼓勵；此外也感謝黃華宗教授、黃傳道、石傳道在心靈層面上給我不一樣的力量；以及這一年來給我最大支持和動力的佩鈴。謝謝你們在我博士生涯裡曾經的陪伴，有你們時時的關心和慰問，讓我一點都不孤單。

這一路走來，接受太多朋友的關心與鼓勵，這些朋友是一輩子的資產，我會好好的珍惜，也感謝老天爺！賜給我這麼多的善緣，讓我能夠度過心裡的挫折和心酸。感謝生命中所有的曾經，讓我更加成長，並珍惜當下的領悟。

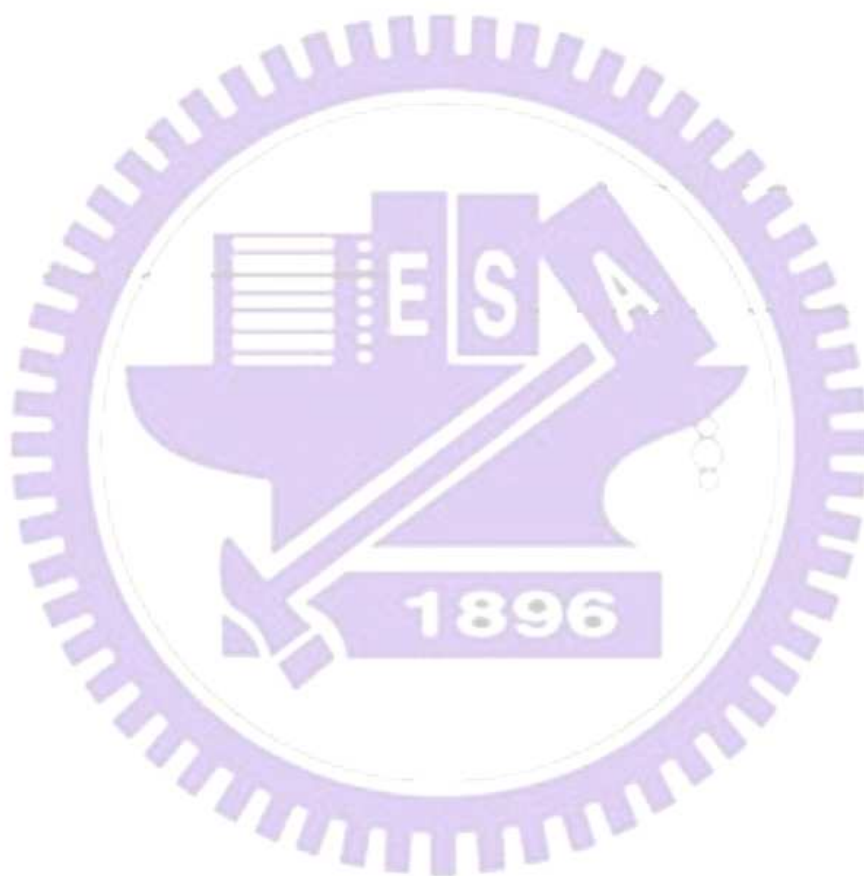
最後，要感謝的是我的父母，父母對我的期許與肯定，是我能夠持續努力的最大動力，謝謝爸媽含辛茹苦的養育之恩，提供最舒適的環境以及全力的支持，使我專心無慮的完成學業，才能成就今日的我。今後，我會更加努力，期能夠學以致用，為社會盡自己一份心力。祝福所有愛我和我愛的人，平安喜樂。

Contents

Abstract in Chinese.....	I
Abstract in English.....	IV
Acknowledgement.....	VIII
Contents.....	IX
List of Symbols.....	XII
Table Captions.....	XV
Figure Captions.....	XVI
Chapter 1 Introduction	1
Chapter 2 Literature reviews.....	4
2.1 Porous silica materials	4
2.1.1 Structure, properties, and synthesis methods.....	4
2.1.2 Applications	10
2.2 Carbon mesoporous materials (CMMs)	13
2.2.1 Structures, properties, and synthesis methods	13
2.2.2 Applications in fuel cells.....	16
2.3 Carbon nanotubes (CNTs).....	19
2.3.1. Structure, property, and classification	19
2.3.2. Synthesis methods	22
2.3.3. Tip- and base-growth mechanisms	26
2.3.4. Other growth mechanisms	30
2.3.5. Applications in fuel cells.....	33
2.4 Characterization of porous and nano carbon materials.....	35
2.5 Electrode performance testing.....	42
Chapter 3 Experimental details.....	45
3.1 Experimental flow chart.....	45
3.2 Row materials.....	47

3.3	Features of CVD systems.....	48
3.4	Preparation of porous silica	52
3.5	Preparation of carbon nanostructures	55
3.6	Preparation of carbon nanostructure-assisted DMFC electrocatalysts	60
3.7	Structure and property characterization	61
3.8	Electrode performance testings	62
Chapter 4 Process, structures and properties of CPMs and their applications in DMFC anodes.....64		
4.1	Effect of processing parameters on structures and properties of various carbon porous nanostructures	64
4.1.1	Conditions of fabrication porous carbon with tubular branches..	64
4.1.2	Effect of deposition temperature on morphology of porous carbons	70
4.1.3	Structure and properties of carbon porous materials.....	72
4.2	Electrocatalyst performance of DMFC anode with Pt-Fe dispersed capsule-like porous carbon.....	81
4.3	Effect of carbon pore size on Pt dispersion in DMFC anodes and their electrocatalytic performance.....	88
Chapter 5 Process, structures and properties of CNTs and their applications in DMFC anodes.....97		
5.1	Effect of Fe catalyst pretreatment procedures on CNTs diameter	97
5.2	Effects of tube diameter on performance of CNT-assisted DMFC anodes.....	106
5.3	Comparison of CPMs- and CNT-assisted DMFC anodes.....	112
Chapter 6 Effects of temperature difference across catalyst particle on CNTs growth mode..... 114		
6.1.	Inherent differences between thermal CVD and plasma-enhanced CVD processes.....	114
6.2.	Effect of substrate and deposition conditions on CNTs growth by thermal CVD	117
6.3.	Effect of deposition conditions on CNT growth by plasma-enhanced CVD	127
6.4.	My proposed CNTs growth mechanism based on temperature difference	130
Chapter 7 Conclusions		
		131

Chapter 8 Future outlooks.....133
References.....134
Vita148



List of Symbols

A_M :	Metallic surface area of Pt particles calculated by H_2 chemisorption at 305 K
A_{N_2} :	Surface area of the N_2 molecular ($16.210^{-20} m^2/\text{molecular}$)
APS:	Active particle size
BJH:	Barrett-Joyner-Halenda
C:	Electrical conductivity
C_h :	chiral vector
CMM:	Carbon mesoporous material
CMK-1:	Carbon mesoporous material (Carbon material from Korea -1)
CMK-3:	Carbon mesoporous material (Carbon material from Korea -3)
CMK-5:	Carbon mesoporous material (Carbon material from Korea -4)
CNT:	Carbon nano-tube
CO-t:	the CO-tolerance estimated by competitive adsorption of H_2 after pretreatment of CO.
CPM:	Carbon porous material
C-V:	Cyclic-Voltammetry
CVD:	Chemical vapor deposition
d:	Interplane distance (d space)
D:	Pt dispersion measured by H_2 chemisorption at 305 K
ΔP	Pressure decument after N_2 adsorption/desorption attend equilibrium station
ΔT :	temperature of catalyst at the top minus at the bottom, an index of the direction of temperature difference
Den.	Calculated metal density (g/ml)
d_{100} :	Interplane distance (d space) between (100) planes
D_{BJH} :	pore diameter estimated by BJH method
D_p :	Pt particle diameter calculated by H_2 chemisorption at 305 K
ECR:	Electron cyclotron resonance
E_B :	electron binding energy
E_k :	kinetic energy
GMW:	Gram molecular weight (g/g-mole)
h_ν :	incident photo energy
I_f :	Maximum mass activity of forward scan peak in C-V analysis
I_G/I_D :	the G-band and D-band ratio of parent CNTs measured by Ramsn spectrum

I_r : Maximum mass activity of reversed scan peak in C-V analysis
 IUPAC: International Union of Pure and Applied Chemistry
 λ : Wavelength of X-ray source, 0.15418 nm
 MCM-41: Mesoporous silica (Mobil Composition of Matter-41)
 MCM-48: Mesoporous silica (Mobil Composition of Matter-48)
 MOR: methanol oxidation reaction
 MP: Microwave plasma
 MWCNT: multi-walled carbon nanotube
 P: Equilibrium pressure (N_2 adsorption/desorption experiments)
 P_0 : Saturation pressure of N_2 , mmHg
 PD: Metal (Pt) particle dispersion
 PSDs: Pore size distributions
 $SA_{Metallic}$: Metal surface area (m^2/g Pt)
 SBA-15: Mesoporous silica (Santa Barbara Amorphous type material -15)
 S_{BET} : Specific pore surface area
 R: Universal gas constant
 r: Radius of pore channel
 γ : Surface tension of the liquid N_2
 R_c : Critical gas (C_2H_2) flow ratio
 R_g : Gas(C_2H_2) folw ratio
 SEM: scanning electron microscope
 SW: Sample weight
 SWCNT: single walled carbon nanotube
 T: Temperature (K)
 θ : Diffraction angle obtained from XRD analysis
 T_a : Ambient temperature
 t_p : thickness of nitrogen sorpted at 77 K
 T_{Cb} : the temperature at the bottom side of the catalyst
 T_{Ct} : the temperature on the top side of catalyst
 TEM: trasmission electron microscope
 T_{sf} : final substrate temperature of the deposition step
 T_{si} : initial substrate temperature of the deposition step
 T_G : the preheated temperature of the reaction gas
 TGA: thermogravimetric analysis
 T_S : the substrate temperature at heating zone
 T_{sf} : final substrate temperature
 T_{si} : initial substrate temperature

V:	Molecular volume of condensed liquid N ₂
V _{ad}	Volume of N ₂ adsorbed under 77 K
V _{dep} :	bais voltage of the deposition step
V _i :	Volume per injection (ml) during chemisorption analysis
V _{na} :	Total volume not sorbed
V _{pre} :	bias voltage during the H-plasma pretreatment step
V _p :	Specific pore volume
V _{STP} :	Specific sorption volume under standard temperature and pressure
W _c :	weight loss attributed to the carbon products
W _d :	Wall thickness estimated from $2d_{100}\sqrt{3}-D_{BJH}$
W _{dep} :	microwave power of the deposition step
W _{pre} :	microwave power during the H-plasma pretreatment step
W _w :	weight of H ₂ O absorbed in the hydrophilic SBA-15 substrate
XC-72	Commercial activated carbon
XRD:	X-Ray diffraction

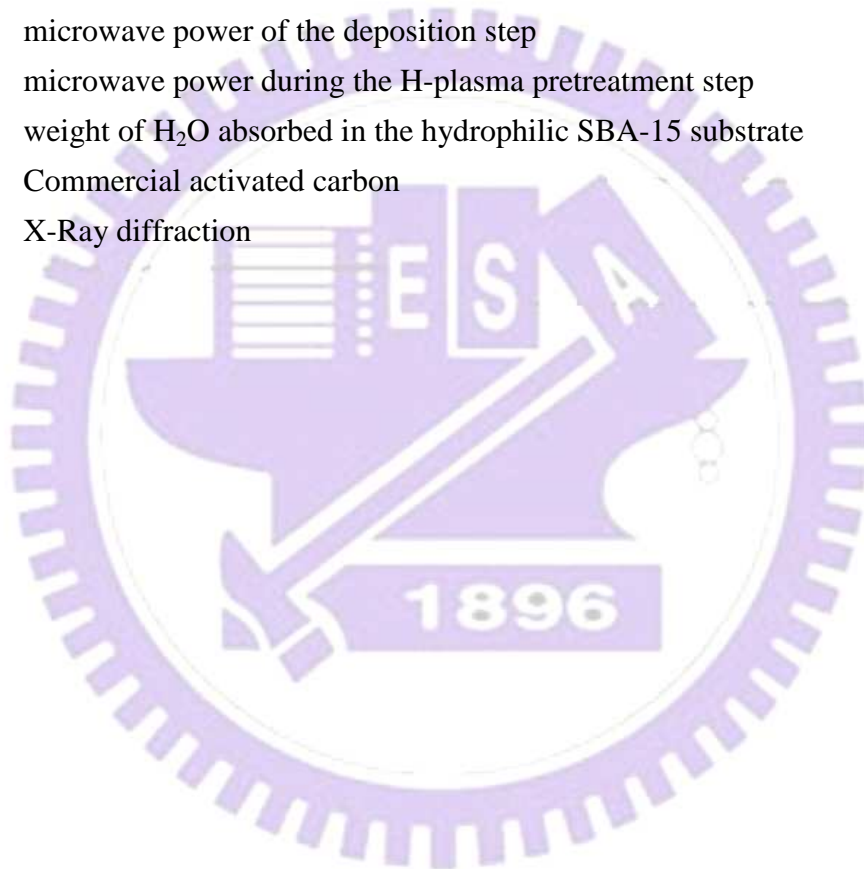


Table Captions

Chapter 2

Table 2- 1 IUPAC classification of porous silica materials. ^[Lowell-2004-p3]	5
-----------------------------------------------------------------------------------------------	---

Chapter 3

Table 3- 1 Chemicals and other raw materials used.	47
Table 3- 2 Sample designations, processing conditions and diameters of CPMs and CNTs prepared by thermal CVD without gas preheating.	57
Table 3- 3 Sample designations and their deposition conditions of CNTs by thermal CVD with gas preheating.	58
Table 3- 4 Sample designations and their deposition conditions by plasma-enhanced CVD.	59

Chapter 4

Table 4- 1 Textural properties of various mesoporous materials.	67
Table 4- 2 List of specific surface area distribution for various CPM samples.	80
Table 4- 3 Sample designations and physicochemical properties of Samples Pt/CPM and Pt/XC-72.	89

Chapter 5

Table 5- 1 Structure features of various porous silica substrates with and without Fe in the pores.	100
Table 5- 2 Sample designations, and their physicochemical properties of Pt- and/or Fe-incorporated samples with the Samples in Table 3 as the substrates.	111

Figure Captions

Chapter 2

Fig. 2- 1 Schematic drawing of (a) Faujasite-type structure zeolite, and (b) primary building unit: cations coordinated tetrahedrally by oxygen. [Baerlocher-2001-p140]	6
Fig. 2- 2 The M41S family mesoporous silica materials. [Selvam-2001-3237]	7
Fig. 2- 3 XRD patterns of (a) MCM-41 and (b) MCM-48 mesoporous silica materials. [Selvam-2001-3237]	8
Fig. 2- 4 TEM images of MCM-41: (a) parallel view and (b) perpendicular view. [Xu-1998-3690]	8
Fig. 2- 5 TEM image of MCM-48, viewing along the [110] plane. [Schumacher-2000-4648]	8
Fig. 2- 6 Possible mechanistic pathways for the formation of MCM-41: (1) liquid-crystal-phase-initiated and (2) silicate-anion-initiated. [Vartuli-1998-97]	9
Fig. 2- 7 (a) SEM image of SiO ₂ photonic crystal. (b) a close-up view. [Mihi-2005-125]	10
Fig. 2- 8 TEM images of (a) SBA-15 template, [Huang-2000-1063] (b) Ag nanowire in SBA-15 template, [Huang-2000-1063] and (c) Pt nanowires replicated from SBA-15 template. [Han-2000-2068]	12
Fig. 2- 9 Schematic representation of the templated synthesis using mesoporous silicas as the hard templates. [Ryoo-2001-677]	13
Fig. 2- 10 XRD pattern and TEM image of CMK-1 carbon after the complete removal of template. [Joo-2001-153]	14
Fig. 2- 11 XRD pattern and TEM image of the CMK-3 carbon obtained after removal of the silica template. [Jun-2000-10712]	15
Fig. 2- 12 XRD pattern and TEM image of the CMK-5 carbon obtained after removal of the silica template. [Darmstadt-2003-3300]	15
Fig. 2- 13 Schematic representation of a MEA structure for a fuel cell. CMM (shown in SEM image) supported catalysts (shown in TEM image) are embedded within the catalyst layer in a MEA. [Chang-2007-3078]	17
Fig. 2- 14 Syntheses of CMM Supported with PtRu Nanocatalysts. [Lin-2008-867]	17
Fig. 2- 15 Schematic drawings of synthesis routes for (a) to (e) Pt-CMMs compared to that of (a) to (f) CMK-5. [Liu-2006a-3435]	17
Fig. 2- 16 TEM images of sample prepared by (a) conventional impregnation, and (b) one-step impregnation methods. [Liu-2006-3435]	18
Fig. 2- 17 Schematics drawings of (a) Chiral-type, (b) Armchair, and (c) Zigzag CNTs. [Lau-2002-263]	19
Fig. 2- 18 (a) The unrolled honeycomb lattice of a nanotube and (b) (4, 2) SWCNT,	

showing the translation vector T. [Dresselhaus-2005-p47]	20
Fig. 2- 19 Schematic of arc-discharge system. [Saito-1996-3062]	22
Fig. 2- 20 Schematic of the laser ablation system. [Guo-1995-49]	23
Fig. 2- 21 Schematic illustration of the thermal CVD system. [Lee -2001-245]	25
Fig. 2- 22 A dc-PE-CVD reactor for the fabrications of CNTs and nanofibers. [Chen-2005-p12]	25
Fig. 2- 23 MWCNT growth scenario from large catalyst particles (typically $\gg 5$ nm). [Gohier-2008-1331]	27
Fig. 2- 24 SWCNT and FWCNT growth scenario from small catalyst particles (typically < 5 nm). [Gohier-2008-1331]	27
Fig. 2- 25 Three-phase model for the CNF growth mechanism. [Melechko-2002-527]	29
Fig. 2- 26 Schematics of the four-step growth model for CNTs growth. [Bower-2000-2767]	30
Fig. 2- 27 Various growth stages of carbon filaments based on the Baker's model. [Baker-1972-51]	32
Fig. 2- 28 (a) Schematics of the poisoning/diffusion model of carbon nanotube growth termination, and (b) plot of the measured nanotube array height as a function of the growth time. [Stadermann-2009-738]	33
Fig. 2- 29 (a) TEM image of Pt/CNTs, (b) distribution of Pt particle size, and (c) C-V voltammograms of Pt/CNTs and a commercial sample, E-TEK Pt/C. [Mu-2005-22212]	34
Fig. 2- 30 IUPAC classification of sorption isotherms.	39
Fig. 2- 31 IUPAC classifications of hysteresis loops.	40

Chapter 3

Fig. 3- 1 Flow chart of the experiments.	46
Fig. 3- 2 Schematic thermal CVD systems (a) without, (b) with gas preheating heater.	49
Fig. 3- 3 Schematic MP-CVD system.....	50
Fig. 3- 4 Schematic ECR-CVD system.....	51

Chapter 4

Fig. 4- 1 XRD patterns of (a) MCM-48, (b) CMK-1, and (c) CMT-1 mesoporous materials.....	65
Fig. 4- 2 N ₂ adsorption/desorption isotherms (77 K) of mesoporous MCM-48 silica, CMK-1, and CMT-1 mesoporous materials, where the isotherms for the CMK-1 and CMT-1 carbons are shifted vertically by 200 and 400 cm ³ STP/g, respectively.	66

Fig. 4- 3 BJH pore size distribution of CMT-1, CMK-1, and MCM-48 (inset) mesoporous materials.....	66
Fig. 4- 4 Raman spectra of (a) CMK-1 and (b) CMT-1 mesoporous carbons.	68
Fig. 4- 5 TEM images of a powder from (a) MCM-48 template and (b) CMT-1 mesoporous materials, respectively. The (c) is higher magnification image of (b).	69
Fig. 4- 6 Schematic pore size and wall thickness of MCM-48 and CMT-1 mesoporous materials.	70
Fig. 4- 7 TEM images of (a) collapsed MCM-48 obtained after thermal CVD process at 1093 K, and (b) HCC mesoporous carbon.	71
Fig. 4- 8 TEM image with an inset at higher magnification for Zeolite-Y.	73
Fig. 4- 9 TEM and the corresponding HRTEM images of the ZRC microporous carbon.	74
Fig. 4- 10 XRD patterns of (a) Zeolite-Y, and (b) ZRC microporous materials.....	75
Fig. 4- 11 N ₂ adsorption/desorption isotherms (77K) of (a) ZRC, (b) CMT-1, (c) CMT-2, (d) HCC, (e) PCC, and (f) XC-72, where (a) to (e) are shifted vertically by 1000, 800, 600, 400, and 200 cm ³ STP/g, respectively.	77
Fig. 4- 12 BJH pore size distributions of (a) ZRC, (b) CMT-1, and (c) CMT-2 porous carbon, where (a) and (b) are shifted vertically by 4 and 2 cm ³ STP/g, respectively.	77
Fig. 4- 13 TEM images of (a) SBA-15, and (b) CMT-2 mesoporous materials.	78
Fig. 4- 14 XRD patterns of (a) SBA-15, and (b) CMT-2 mesoporous materials.....	78
Fig. 4- 15 TEM images of (a) PC, and (b) PCC macroporous materials.	79
Fig. 4- 16 BJH pore size distributions of (a) XC-72, (b) PCC, and (c) HCC, where (a) and (b) are shifted vertically by 0.5 and 0.25 cm ³ /g, respectively.	79
Fig. 4- 17 TEM images of Sample Pt–Fe/HCC (a) with and (b) without silica template.	83
Fig. 4- 18 (a) TEM and (b) HRTEM images of Sample Pt–Fe/HCC.....	84
Fig. 4- 19 (a) TEM and (b) HRTEM images of Sample Pt–Fe/SCC.	85
Fig. 4- 20 Small-angle XRD patterns of Samples (a) MCM-48 template treated at 1073 K, (b) CMT-1, (c) Pt–Fe/SCC, (d) MCM-48 treated at 1093 K, and (e) Pt–Fe/HCC.	86
Fig. 4- 21 Cyclic voltammograms of Samples Pt-Fe/HCC, Pt-Fe/SCC, and Pt-Ru/XC-72 in solution of 0.5 M H ₂ SO ₄ + 1 M MeOH.....	87
Fig. 4- 22 TEM images of Samples (a) Pt/ZRC, (b) Pt/CMT-1, (c) Pt/CMT-2, (d) Pt/HCC, (e) Pt/PCC, and (f) Pt/XC-72, respectively.	90
Fig. 4- 23 (a) Curve of Pt particle size distribution in various Pt/CPM Samples, and (b) the corresponding histogram of the distributions of Pt particle size < 1 nm.	91

Fig. 4- 24 Cyclic voltammograms of various Samples of Pt/CPMs and Pt/XC-72 electrocatalysts in solution of 0.5 M H ₂ SO ₄ + 1 M MeOH.	94
Fig. 4- 25 (a) forward, and (b) reverse C-Vs scans of various Samples of Pt/CPM and Pt/XC-72.	95
Fig. 4- 26 Pulsed H ₂ chemisorption profiles without (square symbol) and with (circular symbol) pre-adsorption of 500 ppm CO for Samples, (a) Pt/ZRC, (b) Pt/CMT-1, (c) Pt/CMT-2, (d) Pt/HCC, (e) Pt/PCC, and (f) Pt/XC-72, respectively.....	96

Chapter 5

Fig. 5- 1 Small-angle XRD patterns with and without Fe in Templates of (a) MCM-41 and (b) SBA-15, respectively.	100
Fig. 5- 2 TEM images of Templates of (a) MCM-41 and (d) SBA-15 with inset showing different viewing directions and Samples of (b) Fe(co)/MCM-41, (c) Fe(im)/MCM-41, (e) Fe(co)/SBA-15, and (f) Fe(im)/SBA-15, respectively. ...	101
Fig. 5- 3 Nitrogen adsorption/desorption isotherms of Template with and without Fe catalyst of (a) MCM-41 and (c) SBA-15, and (b, d) their corresponding pore size distribution curves, where the isotherms of Substrates Fe(co)/MCM-41, Fe(im)/MCM-41, Fe(co)/SBA-15, and Fe(im)/SBA-15 were shifted vertically by 300, 600, 300, and 600, respectively, whereas the corresponding pore size distribution curves were shifted vertically by 1.5, 3.0, 0.3, and 0.6, respectively.	102
Fig. 5- 4 TEM images of Samples in Table 3-2 of CNTs deposited on Substrates of (a) Fe(co)/MCM-41, (b) Fe(im)/MCM-41, (c) Fe(co)/SBA-15, and (d) Fe(im)/SBA-15, respectively.	104
Fig. 5- 5 (a) BJH pore size distribution of Substrate Fe(im)/PE-SBA-15 and (b) the corresponding TEM image of CNTs for Sample CNT-d17.	105
Fig. 5- 6 (Left) TEM images and (Right) the corresponding Pt particle size distribution of Samples, (a) Pt/CNT-d3, (b) Pt/CNT-d8, (c) Pt/CNT-d17, (d) Pt/SWCNT, and (e) Pt/XC-72, respectively.	109
Fig. 5- 7 (a) forward and (b) reverse C-V scans of various Samples Pt/CNT and Pt/XC-72.	110

Chapter 6

Fig. 6- 1 Schematics of temperature profiles across a catalyst particle for different deposition systems: (a) thermal and (b) plasma-enhanced CVD systems.	116
Fig. 6- 2 TEM images of the as-deposited CNTs on SBA-15 substrate by thermal CVD without gas preheating, with insets showing local images at higher magnifications: (a) bright field and (b) the corresponding dark field images, respectively (Sample	

A1-20).	119
Fig. 6- 3 TEM image of the as-deposited CNTs on Si substrate by thermal CVD without gas preheating, with inset at higher magnification (Sample A2-20).....	120
Fig. 6- 4 TEM images of the as-deposited CNTs on SBA-15 substrate by thermal CVD with gas preheating ($T_G > T_S$).	121
Fig. 6- 5 (a) TEM image of the as-deposited CNTs on Si substrate by thermal CVD with gas preheating ($T_G > T_S$), (b) the corresponding image at higher magnification (Sample A4-20).	122
Fig. 6- 6 TEM image of the as-deposited CNTs on Si substrate by thermal CVD with gas preheating, with inset at higher magnification ($T_G = T_S$) (Sample A6-5)....	123
Fig. 6- 7 TGA curve of the as-deposited CNTs on SBA-15 substrate by thermal CVD without gas preheating (Sample A1-20).	125
Fig. 6- 8 Carbon yield (wt %) versus reaction time curves of the as-deposited CNTs deposited by thermal CVD for A1, A6, A7, and A8 series Samples.....	126
Fig. 6- 9 Schematic diagram showing substrate temperature variations during growth stage for (a) temperature-rising and (b) temperature-declining processes.....	128
Fig. 6- 10 TEM images of the as-deposited CNTs on Si substrate by MP-CVD with schemes of (a) B1 and (b) B2 Samples in Table 3-4, respectively.....	128
Fig. 6- 11 TEM images of the as-deposited CNTs on Si substrate by ECR-CVD with schemes of (a) C1 and (b) C2 Samples in Table 3-4, respectively, where the insets are showing images at different locations.....	129
Fig. 6- 12 My proposed CNTs growth models, (a) base-growth and (b) tip-growth mechanisms.....	129

Chapter 1

Introduction

Nanostructured carbon materials have attracted considerable research attentions in the past few decades due to their unique physical properties, such as high specific surface area, good corrosion resistance, tailorable pore size, and excellent electronic conductivity. These properties make nanostructured carbon materials suitable for applications as electrodes or as supports for electrodecatalysts. For example, carbon porous materials (CPMs) and carbon nanotubes (CNTs) have been extensively studied and applied as supports for noble metal (Pt, Ru) catalysts at both anode and cathode in direct methanol fuel cells (DMFCs).

As the past investigations on CPM-assisted DMFC electrodes were mostly focusing on using carbon mesoporous materials (CMM) with pore size ranging from 2 to 50 nm as catalyst supporter, while overlooking the potential applications of microporous (< 2 nm) and macroporous (> 50 nm) carbons^[Joo-2001-169; Joo-2006-1618; Liu-2006-3435; Liu-2008-1622] As for CNT-assisted DMFC anode, numerous efforts have been devoted into optimizing methodology of Pt loading for better dispersion of Pt nanoparticles^[Choi-2002-9058; Li-2003-6292; Mu-2005-22212], however, there are few reports focusing on the effect of tube diameter on CNT-assisted anode. Thus, the effects of pore and/or channel diameter size of CPMs and CNTs on the electrochemical performance of DMFC anode remain as subjects of special research interests.

In order to understand the effect of pore size of CPMs on the performance of DMFC anode, a CVD process was developed and adopted to facilitate easy fabrication of CPMs. Accordingly, a series of CPMs with pore size ranging from

micro-, meso-, to macroporous carbons, such as the ZRC, CMT-1, CMT-2, HCC, and PCC materials respectively prepared by using zeolite-Y, MCM-48, SBA-15, melted MCM-48, and photonic crystal as templates, have been fabricated. These materials were applied as the catalyst supports for DMFC anode and their electrocatalytic performances during methanol oxidation reaction were evaluated and compared.

On the other hand, in order to understand the effect of tube diameter of CNTs on DMFC anode, the diameter control methods of CNTs have also attracted considerable attention. In general, methodologies invoked in controlling the diameter of CNTs during chemical vapor deposition (CVD) process may be classified into two main categories, namely by tuning the processing parameters and by employing auxiliary templates. For the former, it has been reported that carrier gas/carbon source flow rate, plasma intensity, morphology of catalyst, precursor compositions, and treatment duration *etc.*, have effects on diameter of CNTs to some extent.^[Kuo-2005-2760; Lee-2001-245; Li-2001-141; Wei-2001-1394] In comparison with rather complex control of processing parameters, the use of an auxiliary template appears to be an easier route to fabricate CNTs with tailorable diameters. For examples, zeolites^[Wang-2000-50] and anodic metal oxides^[Eswaramoorthi-2007-1571; Hoa-2007-447; Im-2004-1214; Jeong-2004-2073; Kyotani-1996-2109; Yao-2001-11395] have been used as templates during CVD process to fabricate CNTs with uniform diameters, which is largely dictated by the pore size of template used. Nevertheless, it is rather difficult to prepare anodic metal oxides or zeolites with uniform pore size in the range of 1-25 nm^[Yao-2001-11395]. Therefore, mesoporous silica (MCM-41, SBA-15) with tunable pore sizes in the range of 1-50 nm were adopted here to develop a facile synthesis route to CNTs with high yield and tunable diameters by using Fe-containing mesoporous silica as catalyst-template. The resultant CNTs were applied as the catalyst supports for DMFC anode and their electrocatalytic performances during

methanol oxidation reaction were evaluated and compared.

Clearly, the CPMs and CNTs present herein represent two important classes of carbon materials for energy applications, hence, it is necessary for us to understand not only their preparation processes but also their formation mechanisms. Nevertheless, while the replication processes of CPMs were better understood, conflicting mechanisms have been proposed for the growth or the morphology control of CNTs since their first discovery in 1991. For example, even though many factors have been reported concerning the tip- or the base-growth mode of CNTs, [Bower-2000-2767; Lin-2005-778; Hsu-2004-1461; Segura-2006-1945; Song-2004-S590] none of them succeeded in explaining why CNTs grown by thermal CVD method normally follow the base-growth mechanism [Choi-2002-3847; Choi-2001-2095; Fan-1999-512; Gulino-2005-89; Lee-1999-461; Lee-2001-245; Lee-2000-3397; Zhao-2006-159] while those grown by plasma CVD were mostly categorized as tip-growth mechanism. [Abdi-2006-1219; Chen-2004-1949; Chen-2000-2469; Hart-2006-1397; Hsu-2002-225; Kuo-2003-799; Lin-2003-1851; Murakami-2000-1776; Ren-1998-1105; Yap-2006-1622] Clearly, some crucial parameters must have been overlooked. To unravel the factors involved during CNT growth mode, we have conducted a series of experiments by using both thermal and plasma CVD modes. Our results clearly indicate that the direction of temperature difference (ΔT) is the crucial factor dictating the CNTs growth mode. Accordingly, the concept was successfully used to interpret various mechanisms proposed in the literatures. [Choi-2002-3847; Choi-2001-2095; Fan-1999-512; Gulino-2005-89; Lee-1999-461; Lee-2001-245; Lee-2000-3397; Zhao-2006-159]

Chapter 2

Literature reviews

2.1 Porous silica materials

2.1.1 Structure, properties, and synthesis methods

Zeolites are crystalline microporous minerals developed after the pioneering discovery by a Swedish mineralogist Axel Fredrick Cronstedt in 1756. Since it was observed that a large amount of steam would be released when heating these minerals, hence the name “zeolite”, which means “boiling stone” in Greek; ζέω (*zeō*) meaning "boil" and λίθος (*lithos*) meaning "stone". The structure of zeolite is consist of silicon (Si^{+4}) and aluminium (Al^{+3}) cations, which are tetrahedrally coordinated by four oxygen anions (O^{-2}), thus forming a macromolecular three-dimensional framework in such a way that uniform voids and channels are created in the crystals, with pore sizes ranging between 4-12 Å.^[Nagy-1998-192]

The first application of microporous zeolites were used as molecular sieves by McBi at 1932, based on their variation in pore sizes with molecular dimensions. Subsequently, artificial aluminosilicate zeolites with microporosities were widely applied in petrochemical industry as solid acid catalysts for various heterogeneous catalytic reactions, such as isomerisation, alkylation, dehydrogenation, cracking etc. since 1960. However, the applications were limited due to their angstrom scale pore size. It is till the discoveries of M41S^[Kresge-1992-710] and SBA-15^[Zhao-1998-548] series mesoporous silica

materials in early 1900's, the pore size of porous materials open up a new era of research and applications.^[Lu-2004-p6] Over the past decade, extensive studies have been focusing on synthesis and development of mesoporous materials and their applications in a variety of different areas, such as catalysis, separation, adsorption, and electronic/optical devices.

It should be noted that even through the prefix “micro-” always means the dimension of 10^{-6} meter in the field of material science, the prefix have totally different meanings in the field of porous materials, where micropore means the diameter with pore size smaller than 2 nm. Table 2- 1 shows the IUPAC (International Union of Pure and Applied Chemistry) classification and examples of porous silica materials based on their pore sizes.^[Rouquerol-1994-1739] For practical reason, only Zeolite-Y, MCM-41, MCM-48, SBA-15, and photonic crystal will be introduced as representative examples in the following sections.

Table 2- 1 IUPAC classification of porous silica materials.^[Lowell-2004-p3]

Type	Pore Diameter (d)	Examples
Microporous	$d < 2 \text{ nm}$	Zeolite A, Faujasite (Zeolite X, Y), Mordenite, ZSM-5, Beta etc.
Mesoporous	$2 \text{ nm} < d < 50 \text{ nm}$	MCM-41, MCM-48, SBA-15, HMS etc.
Macroporous	$d > 50 \text{ nm}$	Photonic crystal

(a) Zeolites

Zeolites are often classified according to their framework structures by which more than 64 frameworks have been discovered. Each framework type can be described by its secondary building units, framework density, channel system, and unit cell information. For example, Zeolite-Y, one of the most popular zeolites that commonly used as catalyst or catalyst support (see Fig. 2- 1), exhibits the FAU

(Faujasite) structure, It has a 3-dimensional pore structure with a pore aperture of ca. 7.4 Å, defined by the so called “12 member oxygen ring”. Thus, Faujasite (X or Y) zeolites are also known as 12-membered-ring (12MR) zeolites. In addition, Faujasite zeolites also possess larger cavities (supercages) of diameter 12Å. The cavity is surrounded by ten sodalite cages (shown in Fig. 1b; truncated octahedra) connected on their hexagonal faces. The unit cell is cubic ($a = 24.7\text{\AA}$) with $Fd\bar{3}m$ symmetry. Zeolite-Y has a void volume fraction of 0.48, with a Si/Al ratio of 2.43.^[Nagy-1998-192]

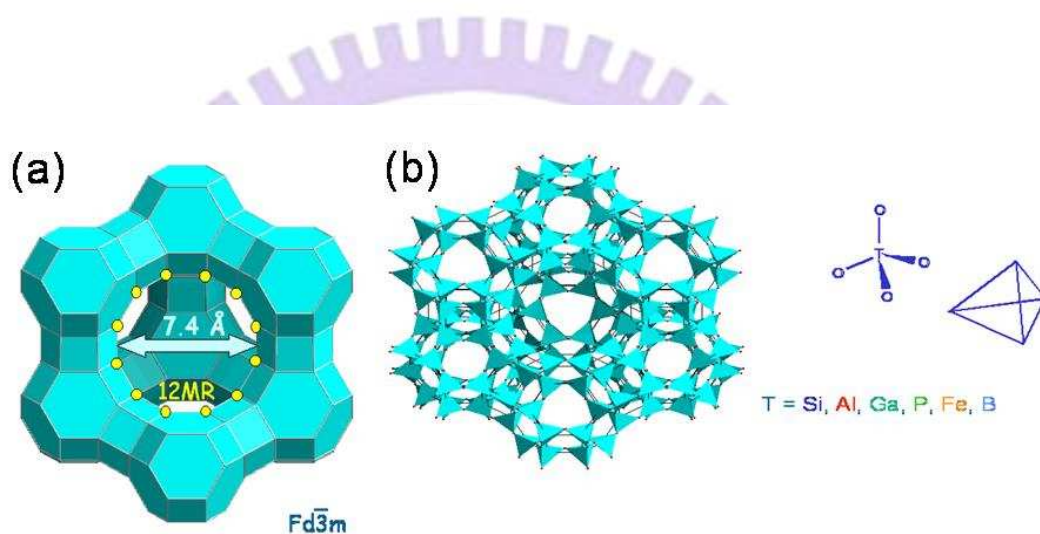


Fig. 2- 1 Schematic drawing of (a) Faujasite-type structure zeolite, and (b) primary building unit: cations coordinated tetrahedrally by oxygen.^[Baerlocher-2001-p140]

(b) MCM-41 and MCM-48^[Selvam-2001-3237; Vartuli-1998-97; Xu -1998-3690]

Mobil Composition of Matter (MCM) is the initial name given for a series of mesoporous materials that were first synthesized by the Mobil researchers in 1992. They proposed a self-assembly synthesis route, by which surfactant micelles such as cetyltrimethylammonium (CTMA) cation was used as the soft-template to facilitate condensation of the silicate anions, leading to the discovery of the so-called M41S family of mesoporous materials. Typically, the structures of these mesoporous materials depend on their synthesis conditions, such as pH value, compositions of

surfactant, and hydrothermal temperature etc. The M41S materials can be divided into four main categories, as depicted in Fig. 2- 2. Among them, MCM-41 and MCM-48 have been widely investigated and applied due to their high thermal stabilities and large specific surface areas (typically, ca. $1000 \text{ m}^2\text{g}^{-1}$). The other two phases, lamellar MCM-50 and molecular organic octomer (a surfactant-silica composite species) are structurally unstable and hence less useful.

MCM-41 and MCM-48 are mesoporous materials with 2D hexagonal ($P6mm$) and cubic ($Ia3hd$) structure, respectively, as revealed by their XRD patterns in Fig. 2- 3. The nanostructure of MCM-41 and MCM-48 can be observed by TEM as shown in Fig. 2- 4 and Fig. 2- 5. To understand the formation mechanism, MCM-41 is given as a typical example, as illustrated in Fig. 2- 6. First, micelles formed in surfactant (CTABr) solution prefer to stack by self-assembly to form hexagonal array. Then, the silicate anions would precipitate on the micelle template. Finally, the surfactant template was removed by calcinations, leading to mesoporous silica with hexagonal structure.^[Selvam-2001-3237]

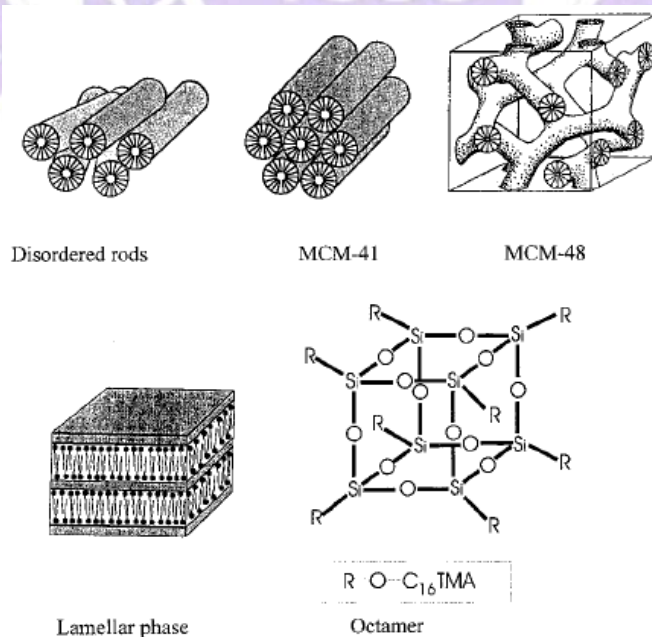


Fig. 2- 2 The M41S family mesoporous silica materials.^[Selvam-2001-3237]

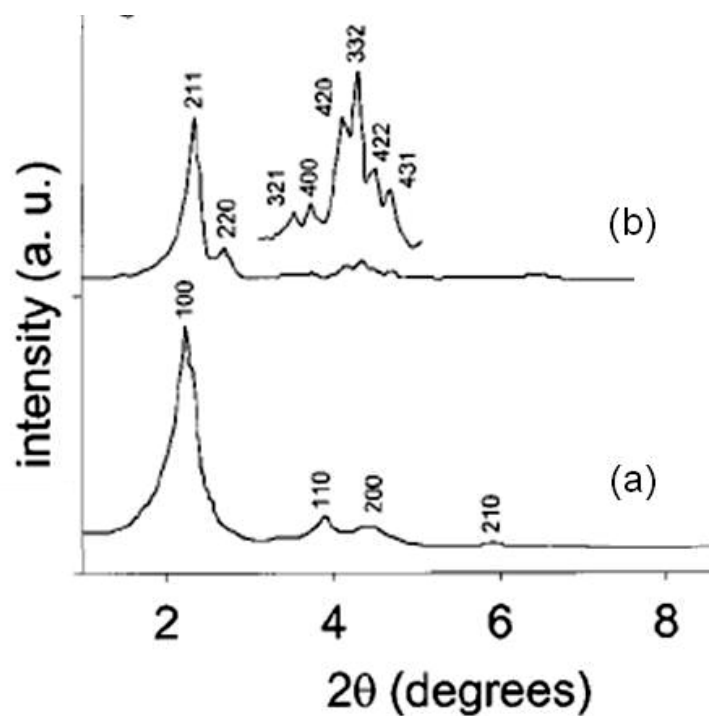


Fig. 2- 3 XRD patterns of (a) MCM-41 and (b) MCM-48 mesoporous silica materials. [Selvam-2001-3237]

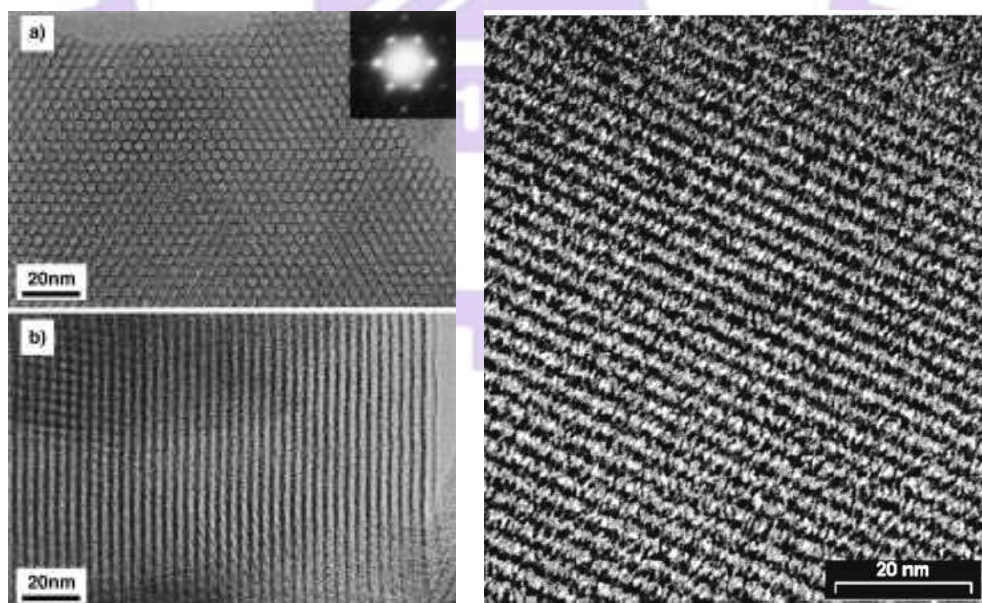


Fig. 2- 4 TEM images of MCM-41: (a) parallel view and (b) perpendicular view. [Xu-1998-3690]

Fig. 2- 5 TEM image of MCM-48, viewing along the [110] plane. [Schumacher-2000-4648]

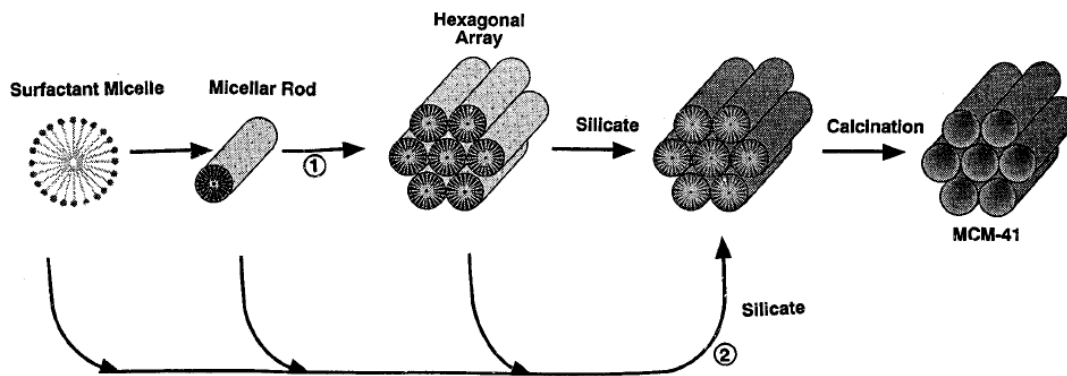


Fig. 2- 6 Possible mechanistic pathways for the formation of MCM-41: (1) liquid-crystal-phase-initiated and (2) silicate-anion-initiated. [Vartuli-1998-97]

(c) **SBA-15**^[Zhao-1998-548]

SBA-15, Santa Barbara Amorphous type material, was first reported by Stucky and his co-workers in 1992. It was synthesized under an acidic medium with poly triblock copolymers, such as poly(ethylene oxide)–poly(propylene oxide)–poly(ethylene oxide) (PEO–PPO–PEO), whose role is analogous to that of CTABr during the synthesis of MCM-41. Despite of the similarity in their 2-D hexagonal structures, SBA-15 and MCM-41 mesoporous silicas are known to have markedly different pore connectivity and pore diameter. Unlike MCM-41 silica, which possesses 1-D non-interconnected channels with typical pore diameter of ca. 2-3 nm, SBA-15 normally possesses much larger 1-D mesoporous channels (typically, 9 nm in diameter) that are interconnected through randomly distributed micropores oriented perpendicular to the 1-D channels. SBA-15 has attracted much R&D attractions due to its much higher hydrothermal stability compared to MCM-41. Moreover, the pore size of SBA-15 may also be accessible in a much wider range (2-30 nm) than MCM-41 (typically < 3 nm).

(d) **Photonic crystal**^[Mihi-2005-125]

Photonic crystals (PC) are macroporous materials composed of periodic pore structures typically with pore size greater than 200 nm, as such, it tends to affect the propagation of electromagnetic (EM) waves with half-wavelength > 200 nm (blue light). In other word, photons (behaving as waves) with a suitable wavelength may propagate through photonic crystals with a given pore diameter; as anticipated for the diffraction of visible lights. Nowadays, for the sake of cost-down effectiveness, the preparaion of such ordered macropores normally invokes lithography using latex particle as template.^[Campbell-2000-53; Holland-1998-538; Mihi-2005-125] The SEM images of the photonic crystal so fabricated are shown in Fig. 2- 7. Further studies on structure and defect control of photonic crystals are crucial for their future applications in optoelectronics and telecommunications.^[Mihi-2005-125]

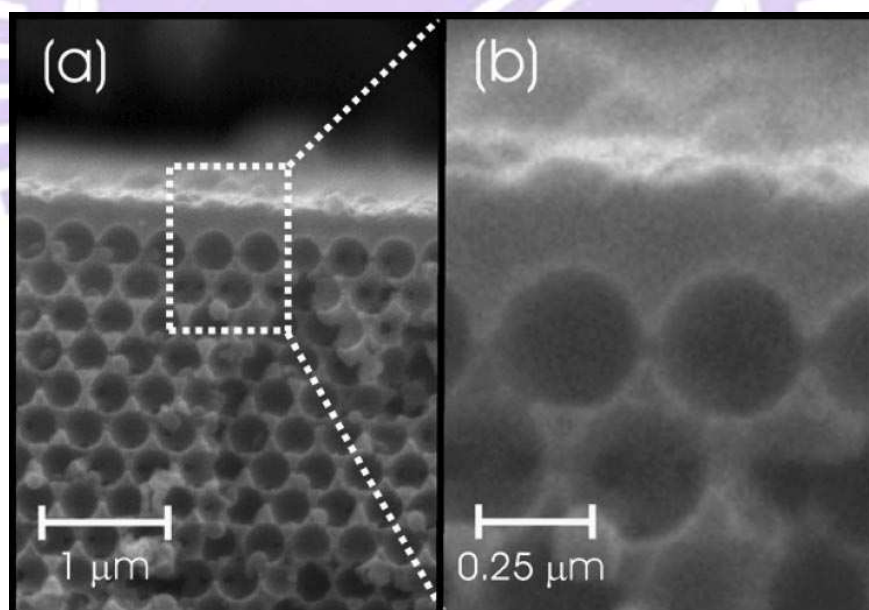


Fig. 2- 7 (a) SEM image of SiO₂ photonic crystal. (b) a close-up view.^[Mihi-2005-125]

2.1.2 Applications

Traditional microporous zeolite materials have been widely used in gas

separation, ion-exchanging agents, and petroleum industries. However, the relatively smaller pore size restricts their future use in separation and catalytic processes in which large molecules are involved. Since mesoporous silicas were developed in early 1990's, a much wider range of applications were made possible, as briefly summarized below:

(a) Catalysis:^[Calleja-2002-215; James -2002-9975]

A great amount of mesoporous silicas were reported with various catalytic applications depending on their pore structures, pore sizes, and surface functionalizations. For example, a propanesulfonic acid-derivatized mesoporous SBA-15 catalyst was found to exhibit high selectivity for alcohol couplings to form ethers, e.g., coupling of methanol and isobutanol to form methyl isobutyl ether. On the other hand, SBA-15 is also commonly used as support for metal catalysts, for examples, Al-, Ti-, V-, and Co-SBA-15. Moreover, a Ti-containing SBA-15 was found to be catalytically active during epoxidation reaction of styrene with tert-butylhydroperoxide exhibiting a superior selectivity of epoxide under negligible leaching of the Ti species.

(b) Adsorption^[Liu-2000-1145]:

Mesoporous materials functionalized with organic functional groups are known to be good adsorbents for heavy metal ions. For examples, thiol- and amino-functionalized SBA-15 silicas were employed for removing heavy metal ions from waste water. The thiolated SBA-15 exhibited a higher complexation affinity for Hg^{2+} , while other metal ions (Cu^{2+} , Zn^{2+} , Cr^{3+} , and Ni^{2+}) showed exceptional binding ability with its amine-functionalized analogues. In addition, they have been widely utilized for adsorption of biomolecules.

(c) Separation^[Han-1999-9897; Zhao-2002-752].

It is reported that SBA-15 functionalized by propylthiol groups showed strong and size selective adsorption of proteins. A C18 modified SBA-15 is reported as a satisfactory substrate in high performance liquid chromatography to separate peptides and various kinds of proteins.

(d) Templates: ^[Gao-2001-743; Gao -2002-585; Han-2000-2068; Huang-2000-1063]

Mesoporous silicas are normally considered to be ideal template or host materials because their ordered channels provide excellent confined spaces for controlling the size and shape of guest materials in nanoscale. For example, SBA-15 was utilized as template to synthesize Ag and Pt nanowires with diameter analogous to the pore size of the SBA-15 template, as shown in Fig. 2- 8. Furthermore, binary sulfides such as CdS and PbS nanoparticles and nanowires have also be prepared using SBA-15 as the template. An alternative approach of using the mesoporous silica materials as templates is for the fabrication of carbon mesoporous materials (CMMs) by replication method; as will be described in the following section.

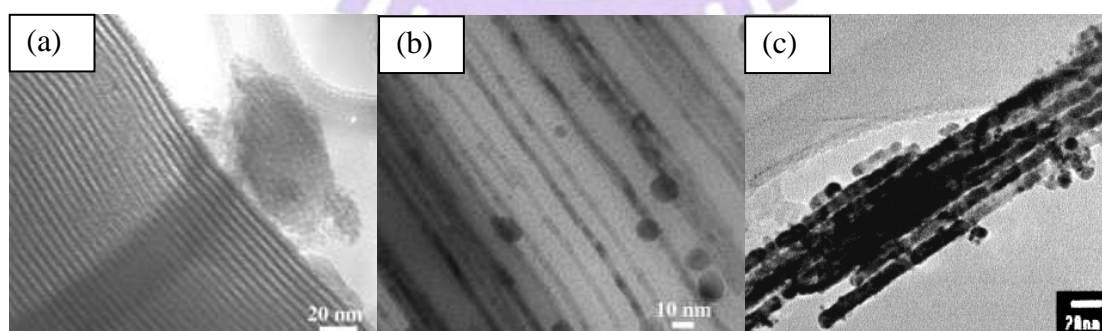


Fig. 2- 8 TEM images of (a) SBA-15 template,^[Huang-2000-1063] (b) Ag nanowire in SBA-15 template,^[Huang-2000-1063] and (c) Pt nanowires replicated from SBA-15 template.^[Han-2000-2068]

2.2 Carbon mesoporous materials (CMMs)

2.2.1 Structures, properties, and synthesis methods

The principle of the templated synthesis is shown in Fig. 2- 9. Various carbon sources such as sucrose solution, furfuryl alcohol, or phenol-resin monomers are polymerized inside the pore channels of the mesoporous silicas at elevated temperatures and were subsequently converted into carbon by pyrolysis. Finally, the silica template was normally removed at room temperature using a 10 % HF or hot 1 M NaOH solution in ethanol-water.

As shown in Fig. 2- 9, either rod- or tube-like carbon mesoporous materials may be obtained depending on the synthesis conditions applied. The rod-like carbons are normally achieved if carbon precursors were completely graphitized in the pore channels of the template. On the other hand, the tube-like carbons are obtained when the carbon precursors were carbonized on the silica pore walls, such that a coated carbon layer with a tubular shape was formed. For simplicity, only some of the most common CMMs are summarized and introduced below.

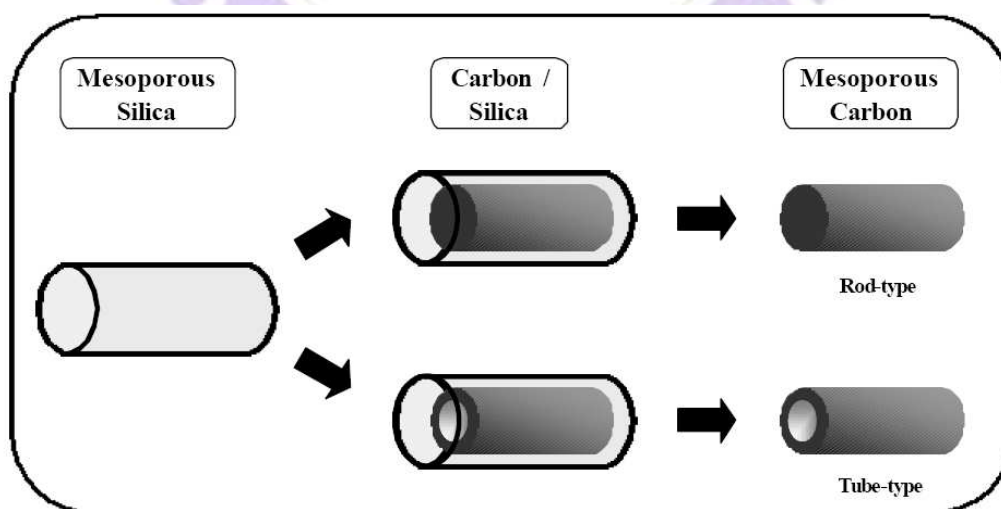


Fig. 2- 9 Schematic representation of the templated synthesis using mesoporous silicas as the hard templates. [Ryoo-2001-677]

(a) CMK-1^[Joo-2001-153]

The CMK-1 carbon can be prepared by impregnating carbon source in mesoporous silica MCM-48 template. The carbonization of sucrose results in the formation of rod-type carbon inside the silica channels. Because of the bicontinuous nature of the MCM-48 structure, the carbon networks formed in the two different kinds of channel systems are not interconnected and the space group, cubic Ia3d, is retained as long as silica frameworks are not removed. However, after removing the silica template, the two carbon networks seem to put together. The joining of the two carbon networks is attributed to the change of structural symmetry from cubic Ia3d to cubic I4132. The new ordered mesoporous structure is indicated by the XRD pattern and transmission electron microscopic (TEM) image shown in Fig. 2- 10.

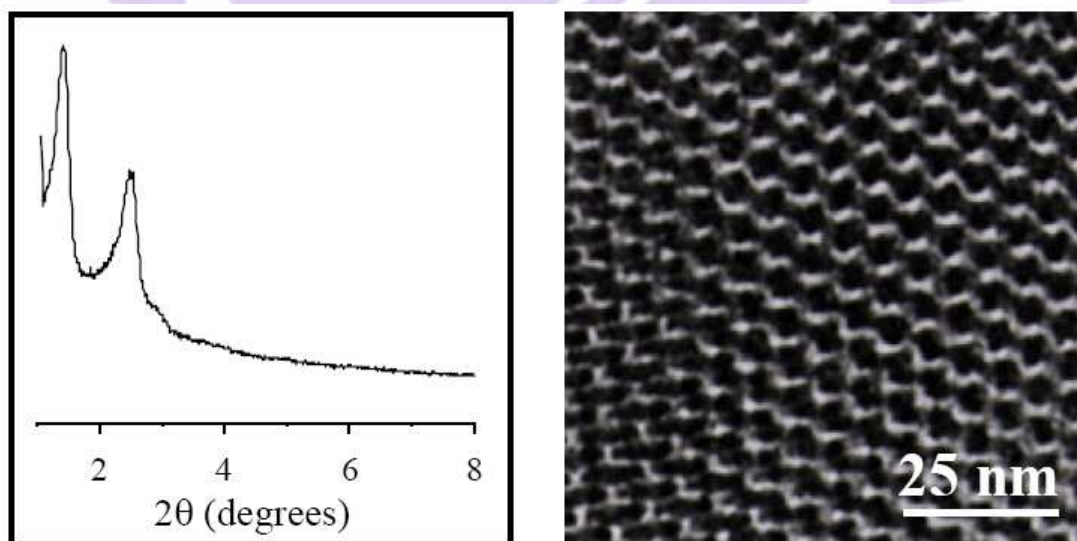


Fig. 2- 10 2-10 XRD pattern and TEM image of CMK-1 carbon after the complete removal of template.^[Joo-2001-153]

(b) CMK-3,^[Jun-2000-10712]**CMK-5**^[Darmstadt-2003-3300]

CMK-3 and CMK-5 carbons are negative replicas of the SBA-15 mesoporous silica template. The structures of CMK-3 (Fig. 2- 11) and CMK-5 (Fig. 2- 12) carbons

are composed of hexagonal arrangement of 1-D carbon rods and tubes structure, respectively. Because of the 3-D channel structure, the structure of the SBA-15 silica can be converted to the negative carbon replica exhibiting the same kind of structural symmetry.

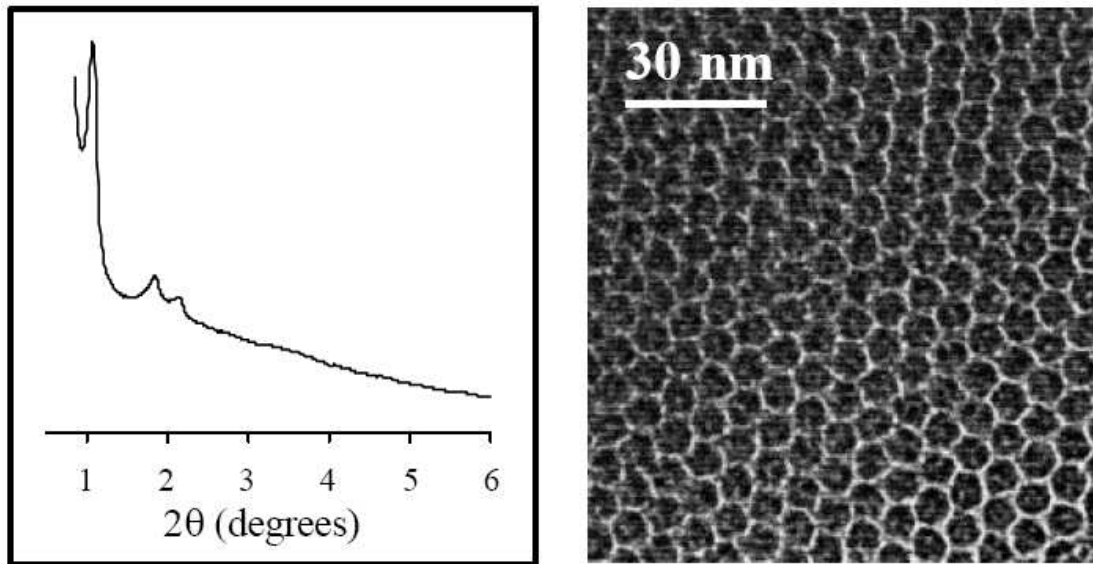


Fig. 2- 11 XRD pattern and TEM image of the CMK-3 carbon obtained after removal of the silica template. [Jun-2000-10712]

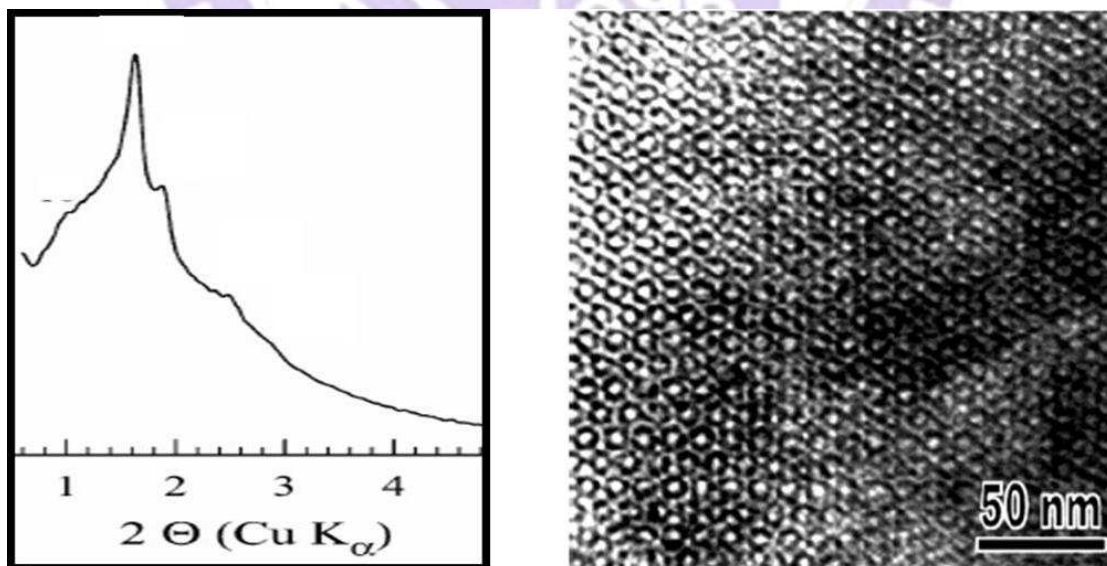


Fig. 2- 12 XRD pattern and TEM image of the CMK-5 carbon obtained after removal of the silica template. [Darmstadt-2003-3300]

2.2.2 Applications in fuel cells

Direct methanol fuel cells (DMFCs) are considered as prospective energy devices, whose R&D invoke a wide variety of different areas, such as fabrication of electrocatalysts and proton exchange membranes (PEM) as well as the corresponding membrane electrode assembly (MEA), cell stacks and system module design, etc. Among them, the enhancement of catalyst activity represents one of the most important issues. Therefore, carbon mesoporous materials such as CMK- n ($n = 1, 3, 5$) have drawn considerable attentions, owing to their unique physicochemical properties, such as high specific surface area ($> 1000 \text{ m}^2/\text{g}$), good electrical conductivity, acceptable chemical stability, and low cost^[Chang-2007-3078]

The concept of using CMMs as electrocatalyst support is illustrated in Fig. 2-13. Among various CMM materials, CMK-3 have attracted the most attentions in recent years. Pt metal/alloy precursors, such as H_2PtCl_6 , RuCl_3 , may be impregnated into CMK-3 structure followed by reduction processes, as illustrated in Fig. 2-14. Furthermore, catalyst implantation technologies are also making steady progress. A one step synthesis route was proposed by Liu et al. to prepare supported noble metal catalysts with good metal/alloy dispersion than the traditional post-impregnation method. Fig. 2-15 shows the schematic drawing of the one-step synthesis route, by which catalyst precursor are impregnated simultaneously with the carbon source (see Fig. 2-16b), as such, superior catalyst stability and catalytic activity were observed surpassing that prepared by the post-impregnation (see Fig. 2-16a)^{[Lin-2008-867;}

Liu-2006-3435]

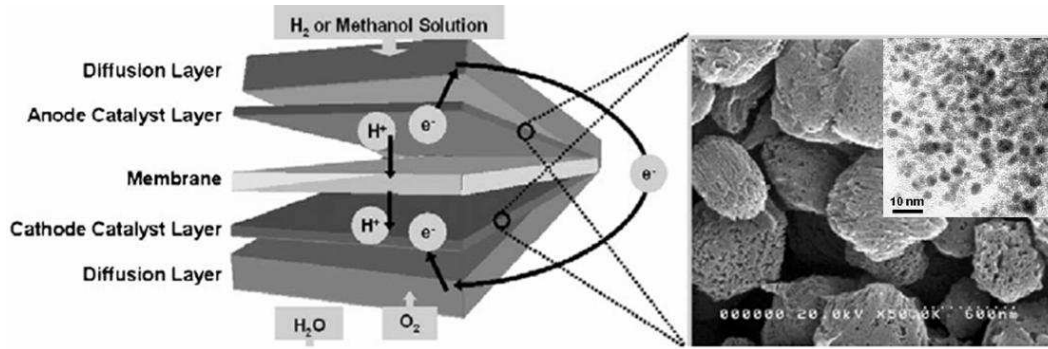


Fig. 2- 13 Schematic representation of a MEA structure for a fuel cell. CMM (shown in SEM image) supported catalysts (shown in TEM image) are embedded within the catalyst layer in a MEA. [Chang-2007-3078]



Fig. 2- 14 Synthesis of CMM Supported with PtRu Nanocatalysts. [Lin-2008-867]

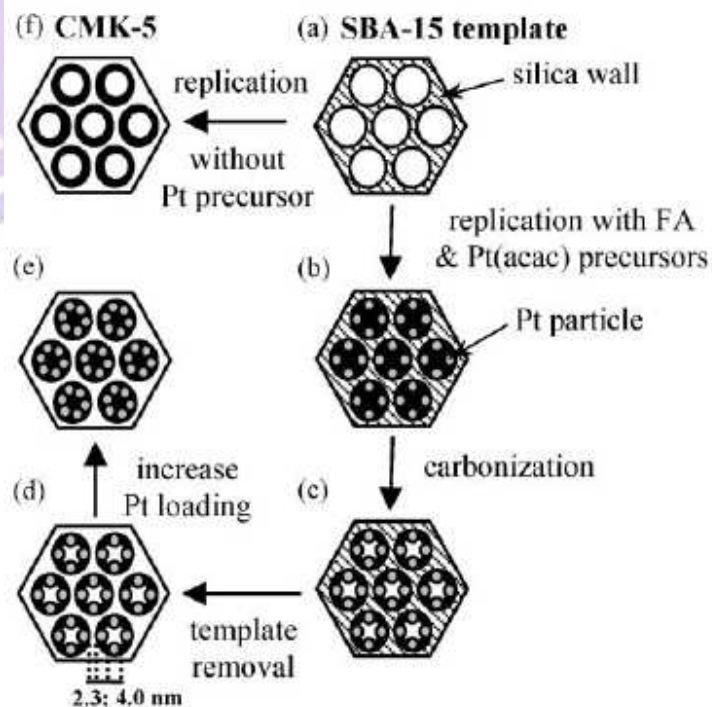


Fig. 2- 15 Schematic drawings of synthesis routes for (a) to (e) Pt-CMMs compared to that of (a) to (f) CMK-5. [Liu-2006a-3435]

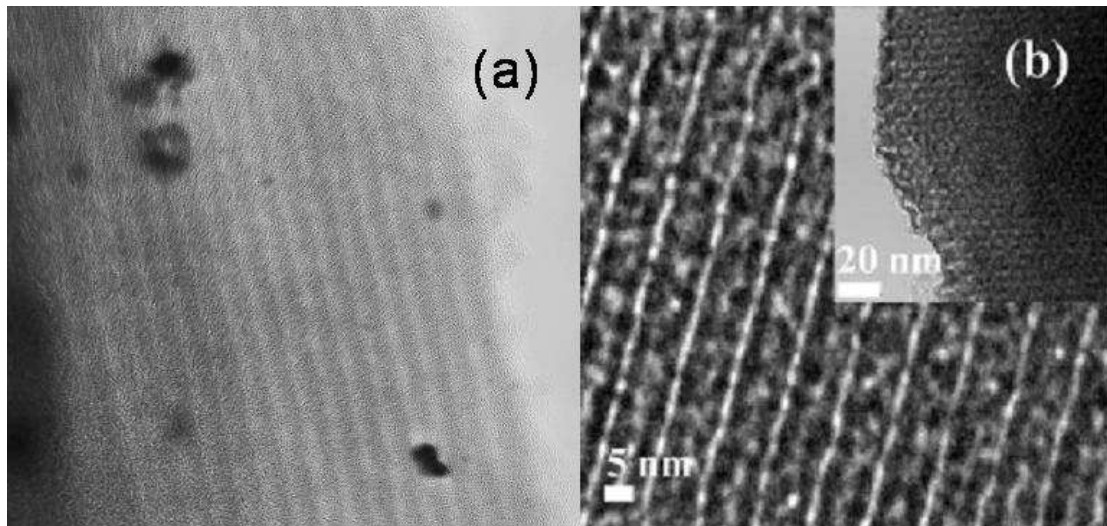
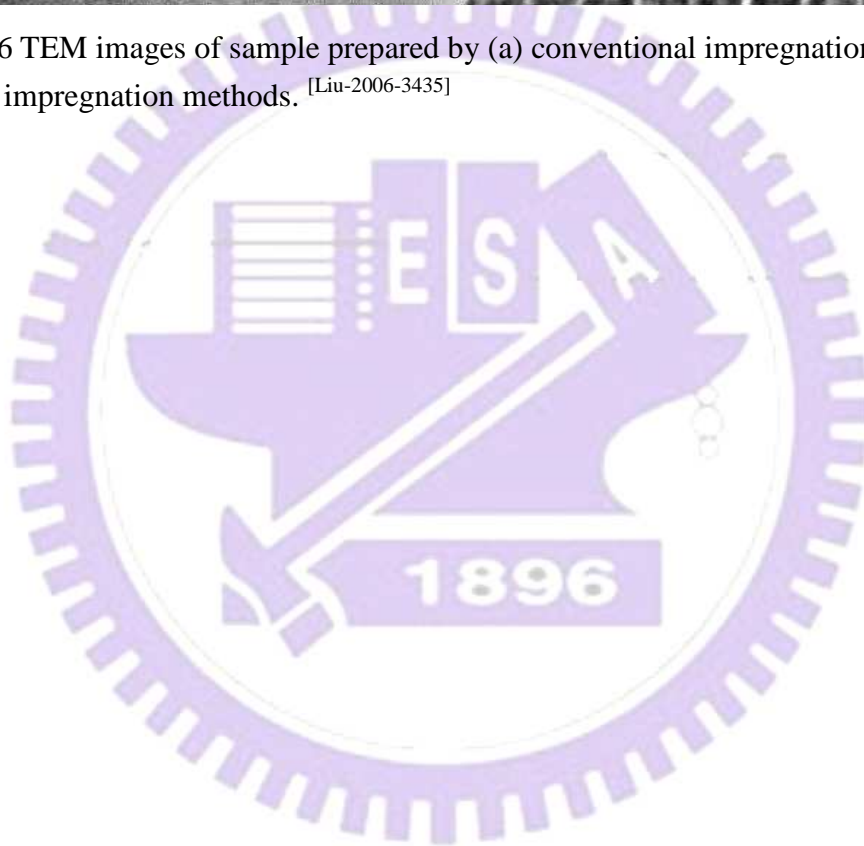


Fig. 2- 16 TEM images of sample prepared by (a) conventional impregnation, and (b) one-step impregnation methods. [Liu-2006-3435]



2.3 Carbon nanotubes (CNTs)

2.3.1. Structure, property, and classification

CNTs, which were formed from graphite sheets and first discovered in early twentieth century, are one of the most exciting new materials in the field of nanoscience and nanotechnology. CNTs may be classified based on either their structures, morphology, chirality, or number of layers ^{[Saito-2004-p35], [Pillai-2007-3011]}.

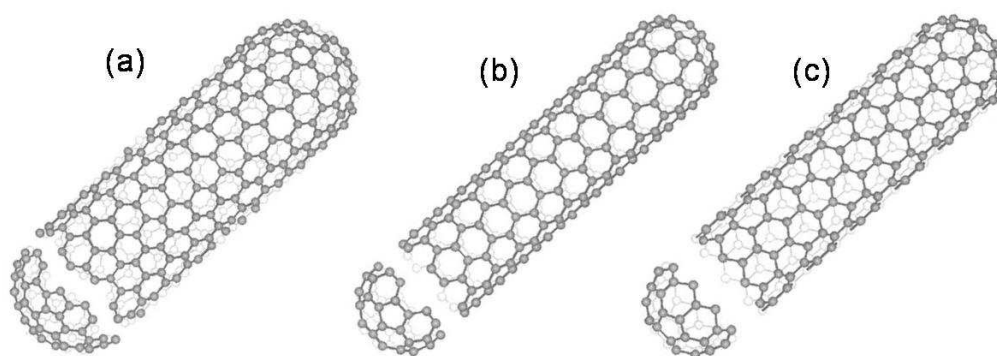


Fig. 2- 17 Schematics drawings of (a) Chiral-type, (b) Armchair, and (c) Zigzag CNTs. ^[Lau-2002-263]

Theoretically, a single-walled carbon nanotube (SWCNT) can be described as a layer of hexagonal graphene sheet rolled into a seamless cylinder, whilst a multi-walled carbon nanotube (MWCNT) is formed with multiple graphene layers. ^[Saito-2004-p35] This leads to different types of structural arrangements, which are typically classified as non-chiral and chiral structural types, depending on their rolling direction ^[Saito-2004-p35] For non-chiral structure of SWCNTs, the honey comb lattices of the nanotube are parallel to the tube axis, which can further be classified as armchair (Fig. 2- 17b) and zigzag (Fig. 2- 17c) arrangements. ^[Saito-1992-2204] For the armchair structure, two C-C bonds on opposite sides of each hexagonal lattice are

perpendicular to nanotube axis, whereas for the zig-zag structure, the bonds are parallel to nanotube axis. Unlike non-chiral structures, the C-C bonds in chiral structures (Fig. 2- 17a) are with an angle to the nanotube axis.

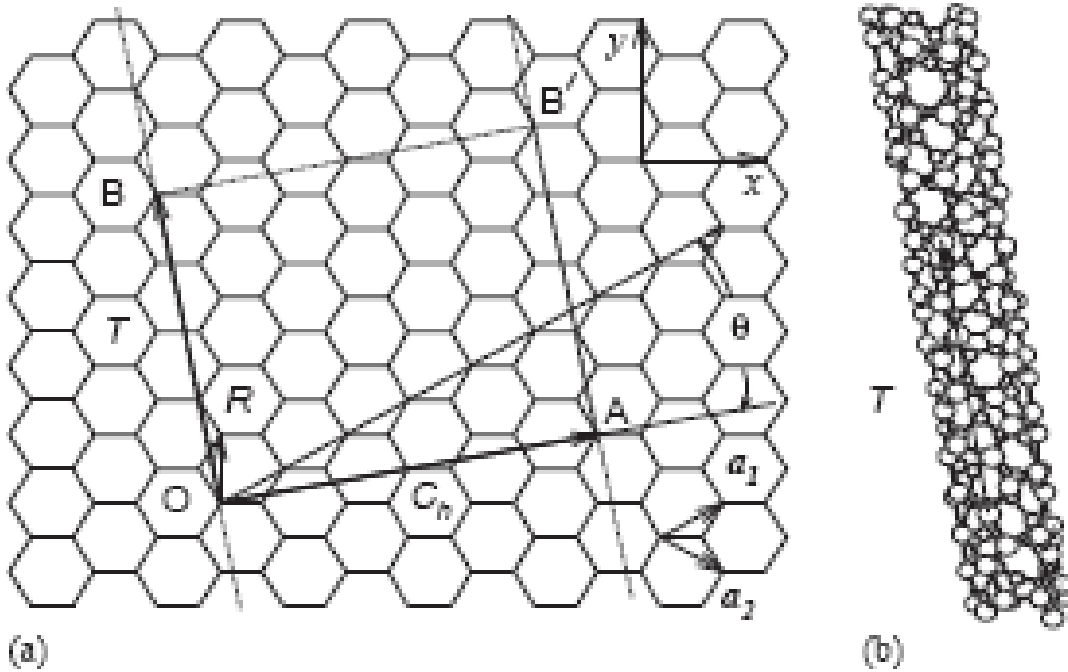


Fig. 2- 18 (a) The unrolled honeycomb lattice of a nanotube and (b) (4, 2) SWCNT, showing the translation vector T . [Dresselhaus-2005-p47]

As shown in Fig. 2- 18, when sites O and A, and B and B' are connected, respectively, a portion of a graphene sheet can thus be rolled seamlessly to form a SWCNT. Meanwhile, vectors OA and OB are defined as the chiral vector, C_h , and the translational vector T of the nanotube, respectively. [Saito-2004-p35] This rectangle portion, OAB'B, is then defined as a unit cell of the nanotube. Generally, a SWCNT is mathematically specified by a chiral vector, C_h , (Fig. 2- 18a), given by the following equation: [Dresselhaus-2005-47; Saito-2004-p35]

$$C_h = na_1 + ma_2 \equiv (n,m) \quad (\text{eq. 2-1})$$

where a_1 and a_2 are unit vectors of the two-dimensional (2D) hexagonal lattice and n and m are integers. Meanwhile, chiral vector is often described by a pair of indices (n, m) , for example, with a chiral vector $C_h = (n, m) = (4, 2)$, the nanotube in Fig. 2- 18 is described as a $(4, 2)$ SWCNT.

The structure of carbon nanotubes provides them with inherently unique electrical, physical, and chemical properties. Mechanically, owing to the presence of C-C bonds, CNTs normally exhibit a Young's modulus of 0.8~5.0 TPa and a tensile strength of 10~150 GPa. They are among the strongest and stiffest fibers known to date. Thermally, CNTs have a high thermal stability both under vacuum and air and an excellent thermal conductivity as high as ca. 3500 W/(m·K). In terms of the electrical properties, CNTs can either be metallic or semiconducting, depending on their tube diameter and chirality. Nanotubes with $n-m = 0$ are metallic while all the others are semiconducting.

Various kinds of CNTs have been developed over the past few decades, as such, many different approaches exist in terms of classification of CNTs. Normally, CNTs may be classified based on either their type(s) of walls (Single-/double-/Multi-) , [Bethune-1993-605; Iijima-1993-603; Wei-2003-753] chirality (zigzag/chiral/armchair), [Ge-1994-2284; Saito-1992-2204] tube morphology (bamboo-like/hollow, or helix/straight), [Bernaerts-1995-605] cap morphology (close/open), [Pan-1999-299] or growth mode (tip-/base-growth), [Abdi-2006; Bower-2000-2767; Chen-2004-1949; Chen-2000-2469; Choi-2002-3847; Choi-2001-2095; Dupuis-2005-929; Fan-1999-512; Gulino-2005-89; Hart-2006-1397; Hsu-2002-225; Kuo-2003-799; Lee-1999-461; Lee-2001-245; Lee-2000-3397; Lee-2004-1232; Lin-2003-1851; Melechko-2002-527; Murakami-2000-1776; Ren-1998-1105; Yap-2006-1622; Zhao-2006-159] etc.

2.3.2. Synthesis methods

(a) Arc-discharge method

CNTs were first synthesized by arc-discharge method, as reported by Iijima and co-workers in 1991.^[Iijima-1991-56] Fig. 2- 19 shows^[Saito-1995-979] the schematic drawing of the arc-discharge system, in which two graphite rods are used respectively as anode and cathode electrodes. During the CNT production process, arcing occurs when DC voltage is applied between these two electrodes. By incorporating a desirable amount of metallic catalysts, such as Fe, Co, Ni, and Y, SWCNTs are normally formed at the anode,^[Bethune-1993-605] while MWNTs can be fabricated by using pure graphite at both electrodes.

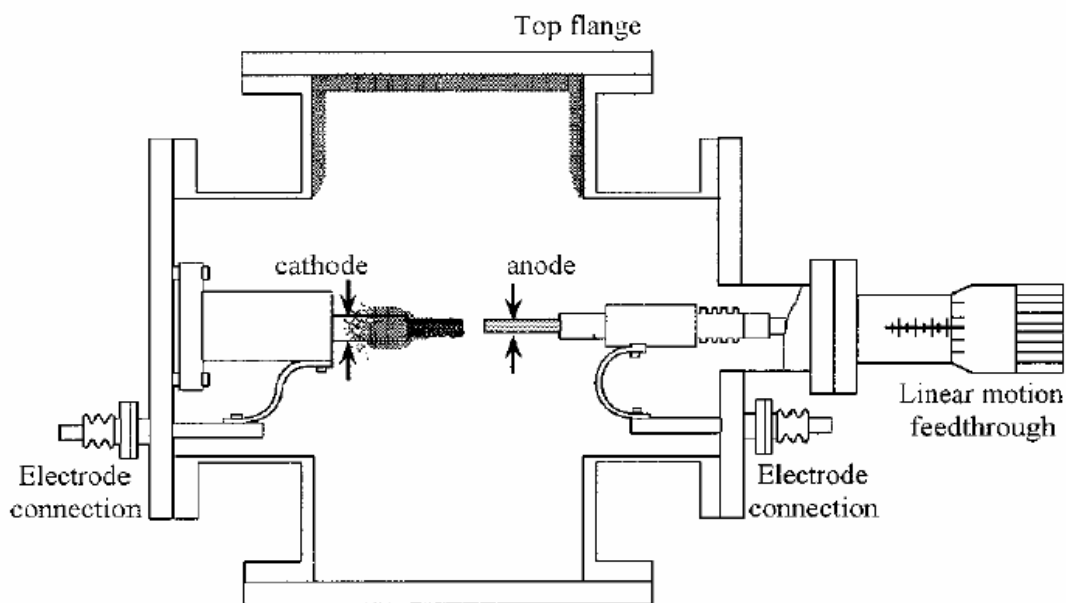


Fig. 2- 19 Schematic of arc-discharge system.^[Saito-1996-3062]

The discharge system is normally operated at a voltage ranging from 20 to 40 V and a current from 40 to 100 Ampere under either He or Ar gas pressure of ca. 10~500

Torr. Carbon clusters emerging from the anodic graphite rod via electron bombardment may be deposited on the cathode surface. These carbon products may include amorphous carbon, fullerenes, carbon cluster, carbon nanotubes, and other carbon structures. Therefore, post treatment is often required to purify the nanostructures for practical applications. In addition, the drawback of this method is its low yield in CNTs.

(b) Laser ablation

Laser ablation was first reported by Guo and co-worker in 1995,^[Guo-1995-49] as illustrate in Fig. 2- 20. An incident laser beam is applied to vaporize a graphite target under helium or argon gas atmosphere at a pressure of 500 Torr. The products are swept out by the flowing gas and eventually deposited on the water cooled collector. As such, it is also named as the laser vaporization method. Normally, the graphite target used in this scheme often contains a small amount of Co, Ni, Fe, or Y as catalyst, whose presence facilitates a more favorable condition for SWCNTs formation.

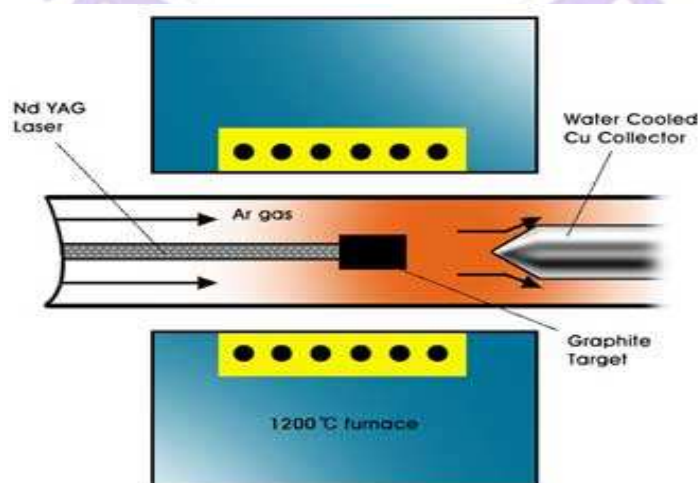


Fig. 2- 20 Schematic of the laser ablation system.^[Guo-1995-49]

(c) Chemical vapor deposition

Chemical vapor deposition (CVD) method has been known to be a mature technique in thin film processing. A variety of different films can be fabricated by CVD method, covering from metals, semiconductors to insulators. By using the CVD method, arrays of CNTs can be produced through decomposition of carbon-containing gaseous species (such as CH_4 , C_2H_2 , C_2H_4 , C_6H_6 , CO , etc.) on various substrates containing transition metal catalysts. During the CVD process, it is essential to introduce some forms of energy to decompose the precursor gases and to deposit the reaction product on the substrate surface. The energy introduced may be thermal, microwave, rf power, or other forms, thus, leading to different process names for the production of CNTs. For examples, microwave plasma enhanced CVD (MPE-CVD),^[Tsai-1999-3462] electron cyclotron resonance CVD (ECR-CVD),^[Kuo-2003-799] inductively coupled plasma CVD (ICP-CVD),^[Delzeit-2002-6027] RF plasma enhanced CVD (rf-PE-CVD),^[Kato-2004-2] DC plasma enhanced CVD (dc-PE-CVD),^[Hofmann-2007-602] thermal CVD,^[Lee-2000-3397] hot filament CVD (HF-CVD),^[Yang-2004-433] etc. In general, these CVD systems can be roughly classified as thermal and plasma CVD on the basis of their working principles. Typically, the former process includes a substrate preheating zone and CNTs are grown while the precursor gases are flowing through the catalyst/substrate (shown in Fig. 2- 21). Unlike thermal CVD, the heat source of plasma CVD mainly arising from the plasma, as illustrated by a dc-PE-CVD system in Fig. 2- 22.^[Melechko-2005-041301] Compared with arc-discharge and laser ablation methods, CVD enhanced by plasma is more economical (lower reaction temperature) and the reaction process can also be controlled more easily. Moreover, it is superior compared to other methods in terms of the purity, yield, and controlled alignment of

the CNT products. Recent advancements in plasma enhanced CVD have been focusing on the development and fabrication of vertically aligned CNTs.

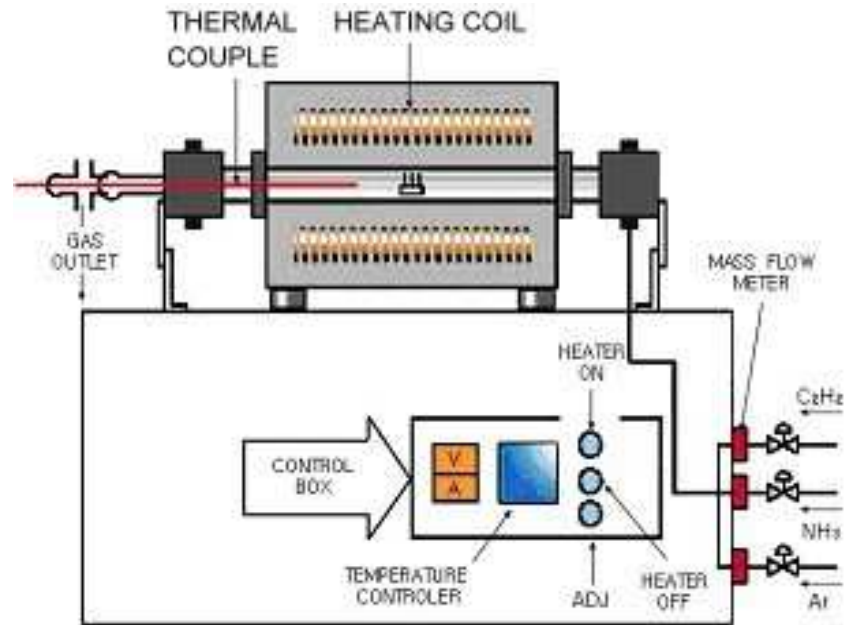


Fig. 2- 21 Schematic illustration of the thermal CVD system. [Lee -2001-245]

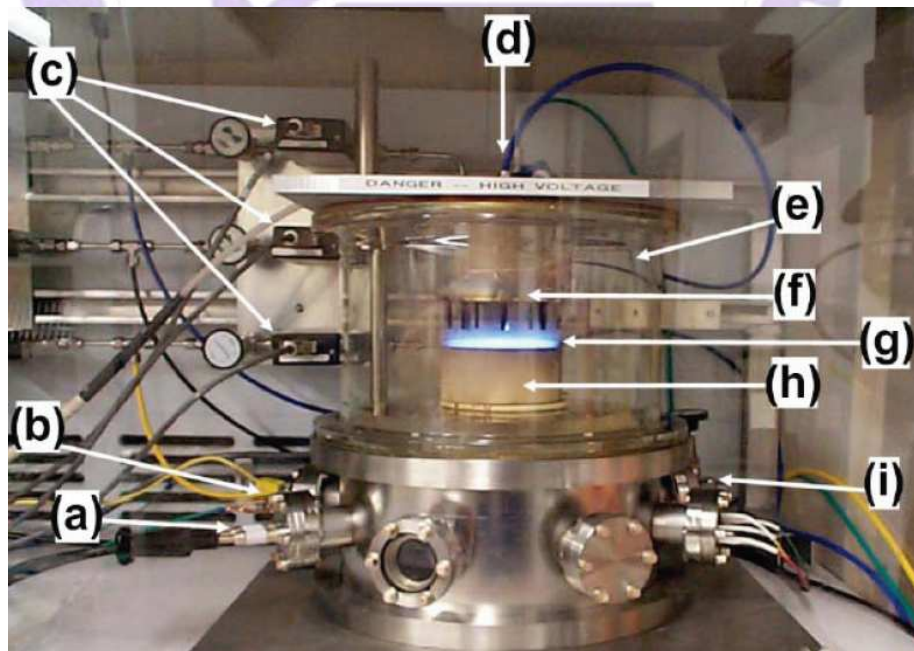


Fig. 2- 22 A dc-PE-CVD reactor for the fabrications of CNTs and nanofibers. [Chen-2005-p12]

2.3.3. Tip- and base-growth mechanisms

It is generally accepted that CNTs growth can be classified by the position of catalyst. It is called tip-growth when the catalyst is located on top of the CNT. In contrast, base-growth CNTs always have a catalyst between substrate and the bottom of CNTs. Since the position of the catalyst may affect the properties and applications of CNTs, many factors have been investigated and reported as summarized below:

(a) Catalyst particle size^[Gohier-2008-1331]

It was proposed that CNTs growth mechanism can switch from tip- to base-growth with decreasing catalyst particle size.^[Gohier-2008-1331] Based on the viewpoint of kinetic, it is considered that carbon patches have sufficient time to diffuse from the top surfaces of larger catalyst particles before the formation of a complete carbon cap. As shown in Fig. 2- 23 (steps 1 and 2), during the early stage of the CNT nucleation, carbon patches formed on the surfaces of a large catalyst particle may quickly diffuse to the catalyst/substrate interface and become more stable. The diffusion leaves the top of the catalyst exposed and makes available for further carbon absorption. Then, the liquid state catalysts were elongated after the nucleation,^[Kukovitsky-2000-65] shown as step 3 in Fig. 2- 23. Finally, the catalyst particles would be lift-off from the substrate (shown in Fig. 2- 23 step 4). Once the connection with the substrate is broken, tip-growth is the only available growth mechanism.

In the case of catalyst with smaller particle sizes, it is assumed that metal particles would be more active. Based on such an assumption, the metal catalyst should have stronger interactions with the carbon patches. Hence, after the carbon precursor was decomposed, a complete graphene cap would be formed and eventually

isolates the carbon source from the catalyst particle, as shown in Fig. 2- 24 (steps 2 and 3). Thus, the only possible diffusion path of carbon species is near the interface between the catalyst and the substrate. As such, carbons would be incorporated with the edges of the graphene cap and then be lift-away from the catalyst particle, as illustrated by step 4 in Fig. 2- 24.

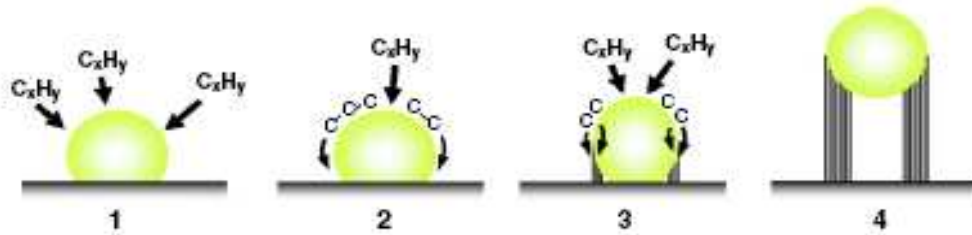


Fig. 2- 23 MWCNT growth scenario from large catalyst particles (typically $\gg 5$ nm). [Gohier-2008-1331]

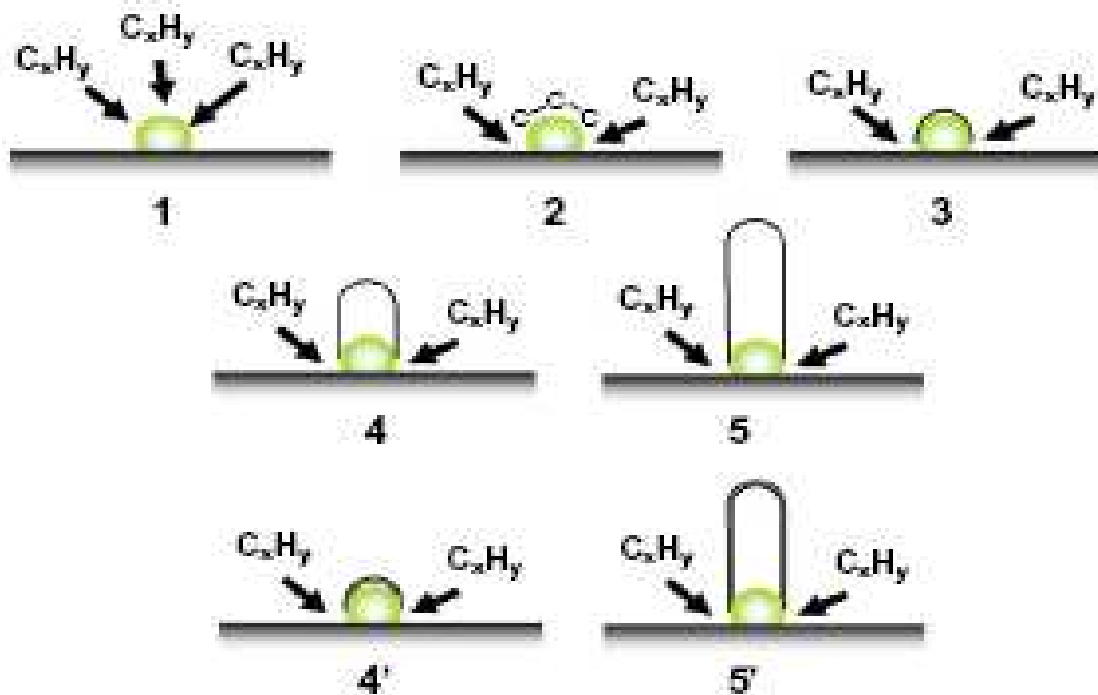


Fig. 2- 24 SWCNT and FWCNT growth scenario from small catalyst particles (typically < 5 nm). [Gohier-2008-1331]

(b) Gas flow ratio ^[Melechko-2002-527]

Since the nano structure and fabrication process of CNTs are rather similar to carbon nanofibers (CNFs), thus, factors affecting the growth mode of CNFs should also be applied to CNTs growth. For CNFs, the critical gas flow ratio (R_c) has shown to be the important factor affecting their growth mode. Fig. 2- 25 schematically illustrates the relationship between gas flow ratio ($R_g = C_2H_2/NH_3$) and growth mode of CNFs. Firstly, carbon precursor was decomposed and diffuses into the catalyst particle through both the catalyst-gas and catalyst-substrate interfaces, as shown in Fig. 2- 25a. Secondly, the nucleation of CNFs may then take place either at the catalyst-gas (Fig. 2- 25b) or at the catalyst-substrate (Fig. 2- 25d) interfaces, depending on whether the R_g is greater or smaller than the critical value. In the case of $R_g > R_c$, the adsorption rate of carbon atoms at the nanoparticle-gas interface should be higher than the desorption rate. Hence, the catalyst nanoparticle would be covered with a thin layer of carbon, except at the edge of catalyst-substrate interface. As such, carbon atoms would prefer to migrate into the catalyst near the substrate and precipitate at the top of catalyst, leading to the base-growth CNFs (Fig. 2- 25b & Fig. 2- 25c). In contrast, tip-growth CNFs should follow the pathway with $R_g < R_c$ (Fig. 2- 25a to Fig. 2- 25e).

(c) Adhesion force between catalyst and substrate ^[Bower-2000-2767]

Adhesion force between the catalyst and the substrate is another important factor affecting the CNTs growth mode. Its importance was first illustrated by the presence of cobalt silicide formed between a cobalt catalyst and a silicon substrate. Fig. 2- 26 displays the schematic drawing of the four-step growth model proposed by Bower., ^[Bower-2000-2767] It illustrates how the adhesion force between the catalyst and the

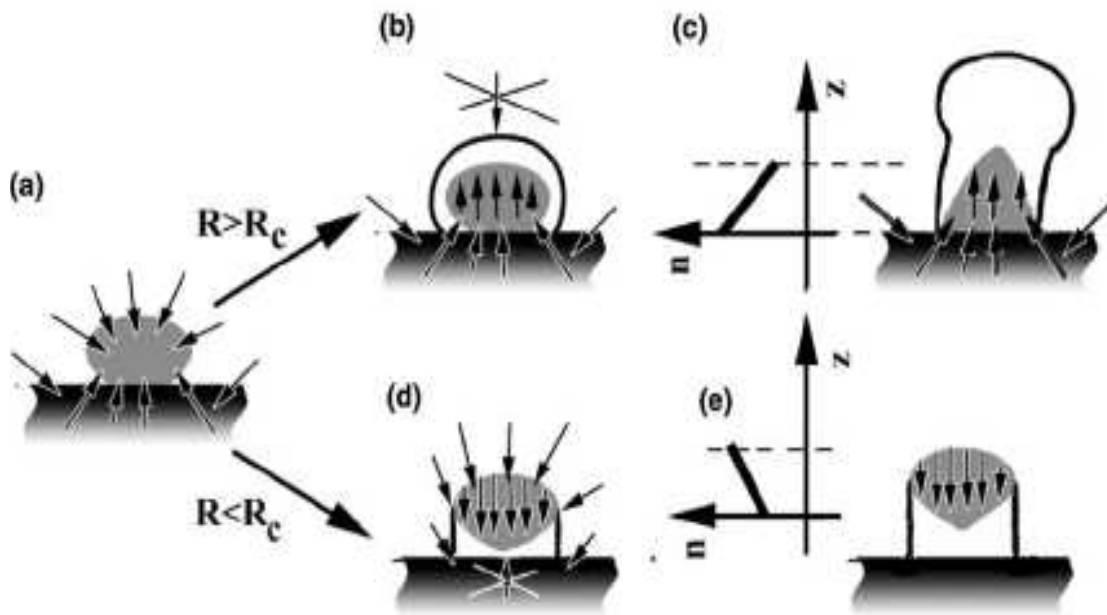


Fig. 2- 25 Three-phase model for the CNF growth mechanism. [Melechko-2002-527]

substrate affect the CNTs growth mode. Step 1 represents the deposition of the Co catalyst onto the Si substrate. In step 2, the Co film tends to transform into an isolated island in the presence of preheating treatment. Upon lifting the heating temperature to 1098 K, cobalt silicides, which are served as anchors or adhesion promoters during CNTs growth, will be formed between the catalyst and the substrate. Subsequently, in Step 3, CNTs would nucleate and grow by the base-growth mode. Finally, the cobalt island may transform into a conical shape and confined at the bottom ends of the CNTs. The growth of the carbon nanotubes may proceed till the conical cobalt particle is completely enclosed, as illustrated in step 4.

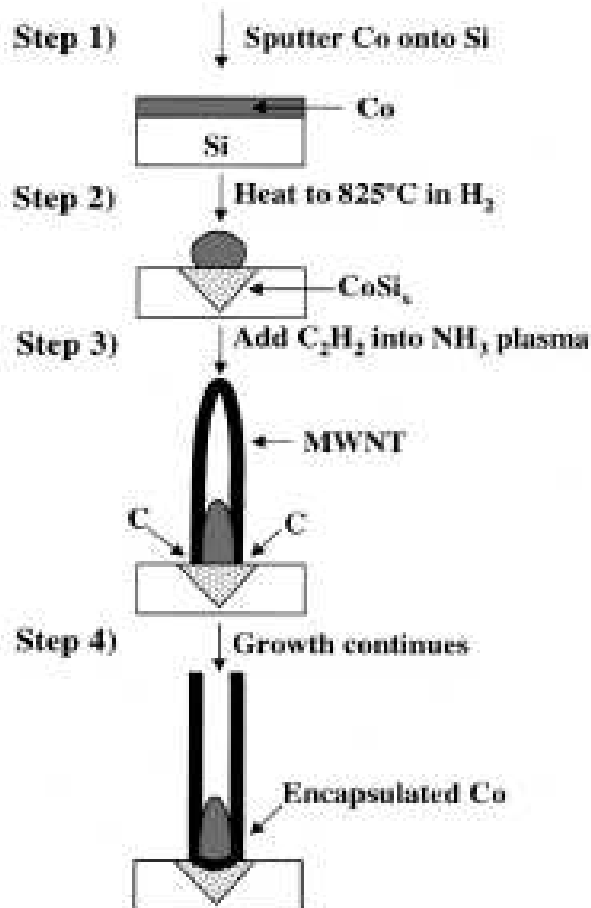


Fig. 2- 26 Schematics of the four-step growth model for CNTs growth. [Bower-2000-2767]

2.3.4. Other growth mechanisms

There are many other growth mechanisms of CNTs have been proposed. Herein, only a few well-accepted models are described:

(a) Vapor-liquid-solid model^[Kukovitsky-2000-65]

In this vapor-liquid-solid (VLS) model, metal in liquid state accepts carbon source in vapor state until the system becomes supersaturated. Consequently, the liquid metal acts as a catalyst to convert carbon from the vapor phase to the crystalline phase, thus CNTs were readily grown by precipitation of dissolved carbon from the droplet.

(b) Solid-liquid-solid model^[Gorbunov-2002-113]

In this model, ^[Gorbunov-2002-113] molten metal catalyst nanoparticles were allowed to penetrate an amorphous carbon aggregate to dissolve and eventually precipitate carbon atoms, which will arrange themselves in a graphene sheet in such a way that its orientation parallel to the supersaturated metal-carbon melt is not energetically favorable. Any local defects presence in this graphene sheet will lead to the formation of a SWCNT nucleus. This is followed by the subsequent incorporation of precipitated carbons at the edges of the growing nanotube, which are anchored to the catalyst nanoparticle by overlapping its unsaturated sp^2 orbital with the metal orbital of the catalyst nanoparticles.

(c) Baker's model^[Baker-1972-51]

Based on the VLS model, a five stage model was proposed by Baker in 1972, latter known as the Baker's model, which represents the most cited and accepted mode for the growth mechanism of carbon filaments and CNTs, whose growth stages are illustrated in Fig. 2- 27. According to this model, carbons originated from the gaseous precursor tend to dissolve into the liquid catalyst particle and precipitate on its surface to grow CNTs after the particle is supersaturated with carbon atoms. It is generally accepted that decomposition and dissolution of C atoms is exothermic, and precipitation of C atoms and growth of the CNT is endothermic, so that the temperature difference would arises between the hot region (C atoms dissolve into catalyst) and the cold region (C atoms precipitate to grow CNT).

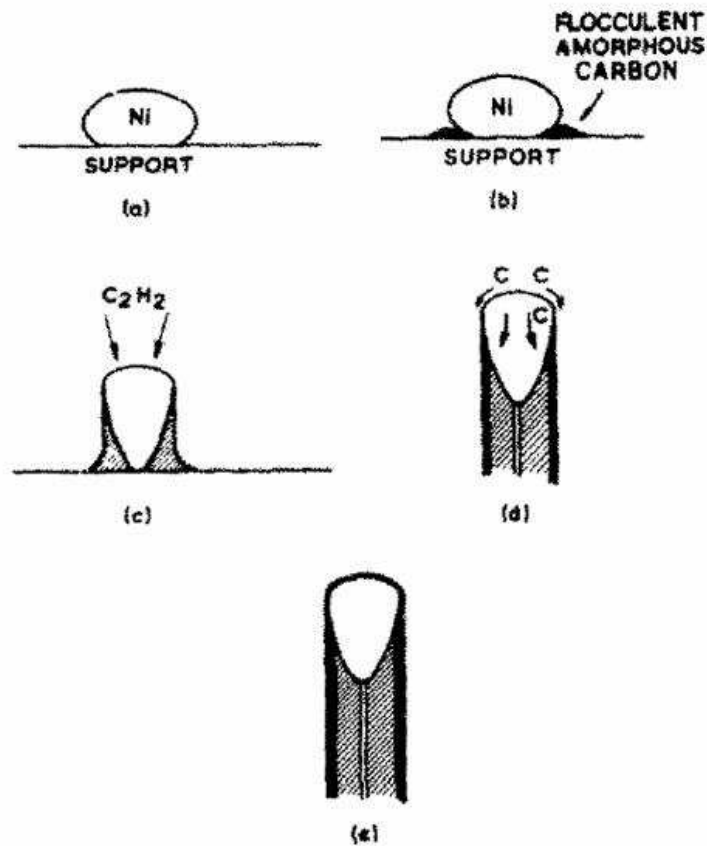


Fig. 2- 27 Various growth stages of carbon filaments based on the Baker's model. [Baker-1972-51]

(d) Mechanism of catalyst poisoning [Stadermann-2009-738]

Catalyst poisoning is one of the important issues related to CNTs growth. Nevertheless, more detailed mechanism was only made available until recently by Stadermann, [Stadermann-2009-738] who proposed to divide the growth mechanism of CNTs into several steps, as shown in Fig. 2- 28. Firstly, the carbon precursors (C_{gas}) were converted into an activated surface-bound form, C^* , which were can then diffuse through the catalyst particle and incorporate into a growing nanotube. Alternatively, C^* may also promote formation of amorphous carbon patches (C_{am}) on the catalyst particle surface. Secondly, the number density of C_{am} would increase with the growth time and finally cover the surface of the catalyst particle, hence, preventing the C^* to

decompose continuously on the catalyst, which served to supply the growth of CNTs. The aforesaid mechanism therefore provides a strong support to the irreversible growth cessation.

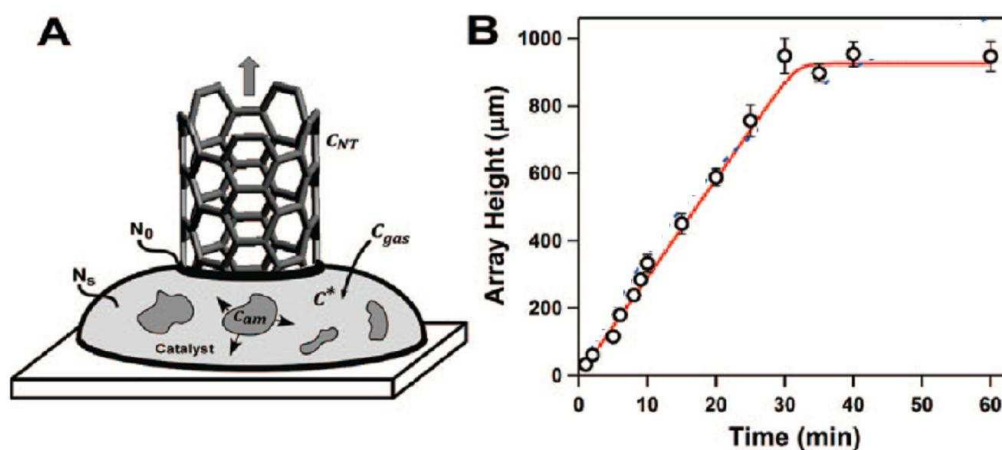


Fig. 2- 28 (a) Schematics of the poisoning/diffusion model of carbon nanotube growth termination, and (b) plot of the measured nanotube array height as a function of the growth time. [Stadermann-2009-738]

2.3.5. Applications in fuel cells

During the past decade, proton exchange membrane fuel cells (PEMFCs) and direct methanol fuel cells (DMFCs) have attracted lots of research attentions due to the world's energy crises and severe green house effect [Mu-2005-22212]. The supporting material for electrocatalyst is one of the key issues in fuel cells. Thus, CNTs become one of the most prominent candidates as the catalyst support materials due to their unique properties, such as good electrical conductivity and high surface area. [Raffaello-2005-233] Thus, considerable amounts of past research efforts have been devoted to the dispersion of Pt catalyst on CNTs. Fig. 2- 29a shows the TEM image of Pt dispersed on CNTs, and the corresponding distribution of the Pt particle size (ca. 17 nm) is shown in Fig. 2- 29b, revealing a uniform dispersion of Pt nanoparticles on CNT. In addition, further tests by cyclic voltammetry (C-V) (Fig. 2- 29c) also

confirmed that the Pt/CNT catalyst has a better performance than a common commercially available catalyst, E-TEK Pt/C.

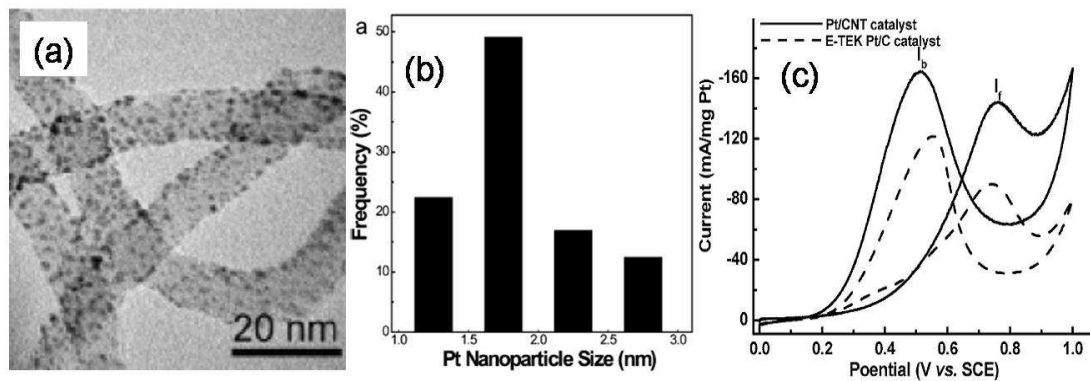


Fig. 2- 29 (a) TEM image of Pt/CNTs, (b) distribution of Pt particle size, and (c) C-V voltammograms of Pt/CNTs and a commercial sample, E-TEK Pt/C. [Mu-2005-22212]

2.4 Characterization of porous and nano carbon materials

The principles of typical analytical and spectroscopic techniques commonly used for characterization of porous and nano carbon materials are summarized below:

(a) Scanning electron microscopy (SEM)

Generally, a SEM apparatus consists of an electron gun, which serves to generate electron beams that, in turn, are accelerated under high voltage (0.4-40 keV). By deflecting the incident beams with the focusing coils, a two-dimensional image can be obtained by detecting the reflected secondary and backscattered electrons.

(b) Transmission electron microscopy (TEM)

Transmission electron microscopy (TEM) is by far the most important technique for studying microstructure of materials in great detail. Typically, an electron beam with accelerating voltage of 100-400 keV would illuminate a region of the specimen, which is immersed in the objective lens of the microscope. The transmitted and diffracted electrons are recombined by the objective lens to form a diffraction pattern in the back focal plane of that lens and a magnified image of the sample in its image plane. A number of intermediate lenses are used to project either the image or the diffraction pattern onto a fluorescent screen for observation. The screen is usually lifted and the image may be printed out on photographic film or stored for recording purposes.

(c) X-ray diffraction spectrometry (XRD)

XRD is a very important method for structural analyses of crystalline and

ordered nano-porous materials. Upon irradiating the substrate sample by a X-ray source, the radiation would interact with the electrons in the atoms, resulting in scattering. Depending on whether the atoms are organized in the same planes and the distances between the planes are the same, constructive and destructive interferences will occur, leading to diffraction peaks at characteristic angles. Typically, with a given excitation wavelength (λ ; typically for a Cu K_{α} X-ray source, $\lambda = 1.5418\text{\AA}$) and resultant diffraction angle (θ), the structural d-spacing (d) of the material can be calculated by the Bragg Equation.^[Cullity-1978-p84]

$$\lambda = 2d\sin\theta \dots \dots \dots \text{(Eq 2-2)}$$

(d) Raman spectroscopy^[Smith-2005-p2]

Raman spectroscopy is capable of providing information of molecular vibrations and hence is a common technique for sample identification and quantification. Normally, a monochromatic laser beam is used as the incident light source, upon irradiating on the substrate, photons may be absorbed, scattered, or not interacting with the sample. When the light is elastically scattered from an atom or molecule, the scattered photons have almost the same frequency with the incident photons. However, a small fraction of the light may be scattered during excitation, such scattered photons would have a frequency different from, and usually lower than, the frequency of the incident photons.^[Smith-2005-p2] As such, the energy difference between the monochromatic light and the Raman scattered light should be equal to the energy involved in changing the molecule's vibrational state.^[Smith-2005-p2] This energy difference is called the Raman shift.^[Smith-2005-p2] Typically several different Raman signals may often be observed; each being associated with different vibrational or rotational motions of molecules in the sample.

Typically, for the inspection of carbon nanostructures, two characteristic peaks are most likely to present in the Raman spectrum, namely the D and G bands. The *D* band, which normally locates at ca. 1300 cm^{-1} is associated with carbons with the sp^3 structures, such as functionalized and amorphous carbons, whereas the G band locates at ca. 1600 cm^{-1} is normally assigned to carbons with the sp^2 structure carbon, such as graphite.

(e) Thermogravimetric analysis (TGA)^[Lowell-2004-p13]

Thermogravimetric analysis (TGA) is a technique, which correlates the sample weight loss with temperature and is commonly employed in R&D of materials, for examples, in determining the absorbed moisture content, the level of inorganic and organic components, and decomposition points of explosives and solvent residues etc.

Typically, TGA experiment is carried out by raising the temperature gradually while monitoring the weight loss by a microbalance under controllable environment. Sample, which is loaded on a pan (typically made of platinum or ceramics), is placed in an electrical heating oven whose temperature may be measured accurately by a thermocouple.

(f) Nitrogen adsorption/desorption isotherm measurement

Nitrogen adsorption at 77.3 K is recommended by IUPAC for the determination of surface area and pore size distribution of porous materials. During the measurement, the sample is exposed in a controlled gas environment, and the volume (*V*) of the adsorbed and desorbed gas is measured against the relative pressure at constant temperature. A sorption isotherm is the plot of *V* versus P/P_0 , where *P* is the absolute pressure and P_0 is the saturation vapor pressure.

Since the shape of the sorption isotherm reflects the characteristics of the pore structure, physical sorption isotherms are classified into six types by the IUPAC, as shown in Fig. 2- 30. Type I isotherm is concave to the P/P_0 axis and reaches a limiting value while the relative pressure (P/P_0) is close to 1. The reversible Type I isotherm is typically observed for microporous solids with small external surfaces (e.g., activated carbons, microporous molecular sieves, zeolites and alumina). In other word, Type I isotherm features a high adsorption uptake at low relative pressures, the adsorption amount eventually reaches a plateau at high relative pressure, as limited by the accessible micropore volume. The reversible Type II curve is a typical sorption isotherm of non-porous or macroporous materials, representing the unrestricted monolayer-multilayer adsorption on their surfaces. Type III isotherms, which arise from weak adsorbate-solid and strong adsorbate-adsorbate interactions, are less common. The multi-layered adsorption in macroporous materials (pore size > 50nm) generally result in Type II or Type III adsorption isotherms, likewise for mesoporous materials with irregular pore systems. Type III adsorption isotherm commonly occurs during the adsorption of H_2O molecules in hydrophobic mesoporous materials.

The initial parts of the Type IV and Type V isotherms normally follow the same path as the Type II isotherm and hence may be attributed to monolayer-multilayer adsorptions. However, the most prominent characteristic of Type IV isotherms is the presence of the adsorption/desorption hysteresis loop. Due to metastable “gas” states or pore blockage, capillary condensation, and capillary evaporation in mesopores occur most often at different relative pressures, leading to the appearance of a hysteresis loop. A steep curve in the capillary condensation regime indicates a narrow pore-size distribution. The presence of Type IV isotherm may normally be considered as the signature of ordered mesoporous materials.

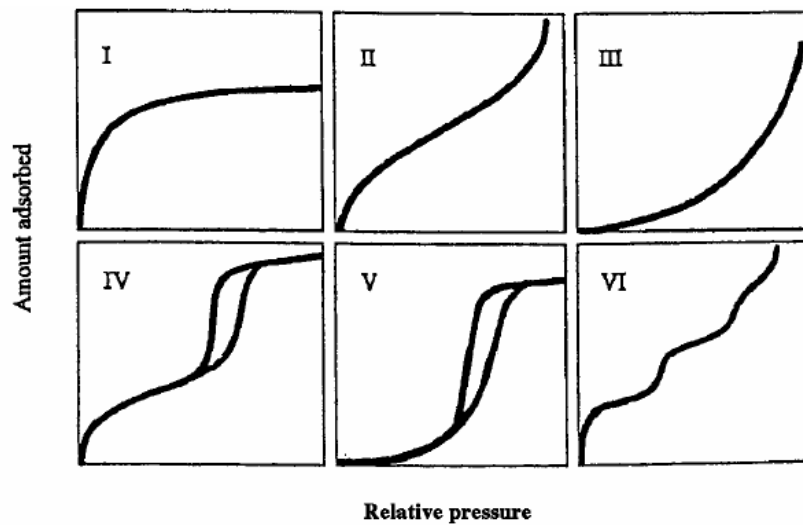


Fig. 2- 30 IUPAC classification of sorption isotherms.

For the classifications of hysteresis loops, it is well accepted a correlation between the shape of the hysteresis loop and the texture properties of the mesoporous adsorbent. Fig. 2- 31 shows the IUPAC classification of hysteresis loops. Where type H1 associate porous material consisting of well-defined cylindrical-like pore channels or agglomerates of compacts of approximately uniform spheres; type H2 hysteresis are usually disordered and with their pore size distribution net well defined; type H3 mesns non-rigid aggregates of plate-like particles which indicates a slit-shaped pores; and type H4, similar to type H3, associated with narrow slit pores, but including pores in microporous region. The dashed curves in the hysteresis loops reflect low pressure hysteresis, observable down to very low relative pressure, which may be associated with the change in the volume of the adsorbent, such as effect of non-rigid pore swelling or the irreversible uptake of moleculars in pores (pore of same width with the adsorptive molecule). In addition, chemisorption would also lead to an “open” hysteresis loops like this. On this situation, the interpretation of sorption isotherms showing low-pressure hysteresis is difficile and it is not possible to analysis the pore

size accurately.

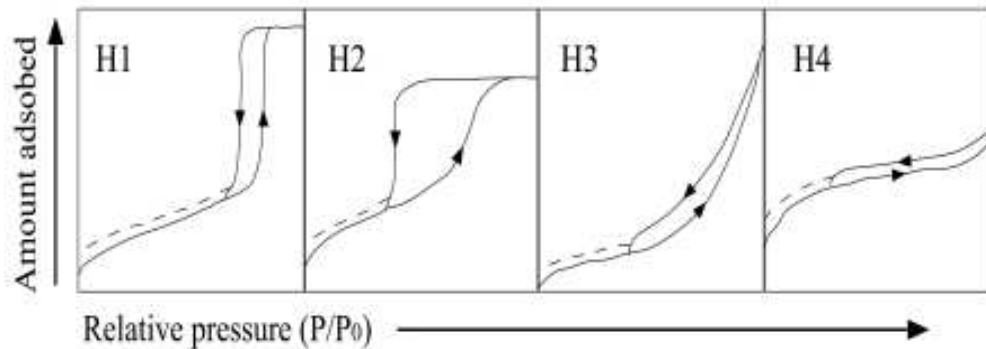


Fig. 2- 31 IUPAC classifications of hysteresis loops.

According to the isotherm, the porous pore size distribution can be achieved by Kelvin equation, where V is the molecular volume of the condensed liquid, γ is the surface tension of the liquid, P is the absolute pressure, P_0 is the saturation vapor pressure and r is the pore radius. The corresponding adsorption volume (V_{ad}) is measured by equation 2-5, where ΔP is the pressure increment while adsorption/desorption attend equilibrium station.

$$\ln(P/P_0) = -2\gamma V/rRT \dots\dots\dots(\text{Eq. 2-3})$$

$$V_{ad} = nRT/\Delta P \dots\dots\dots(\text{Eq. 2-4})$$

On the other hand, the microporous surface and pore volume can be achieved by t-plot method. Equation 2-6 shows the generalized form of t_p values (thickness of nitrogen sorpted at 77 K), by which equation, an adsorption isotherm can be drawn as a typical t-plot shown in Fig. 2-31. Typically, t-plots for non-microporous samples show an extrapolated straight passing through the origin, in which case, the slop is the area. In contrast, the t-plots of microporous samples will extrapolate to the adsorption

axis and show a positive intercept, which is equivalent to the micropore volume.

$$t_p = 6.0533 \left(\frac{1}{\ln(P_0/P)} \right)^{1/3} \dots\dots\dots(\text{Eq. 2-5})$$

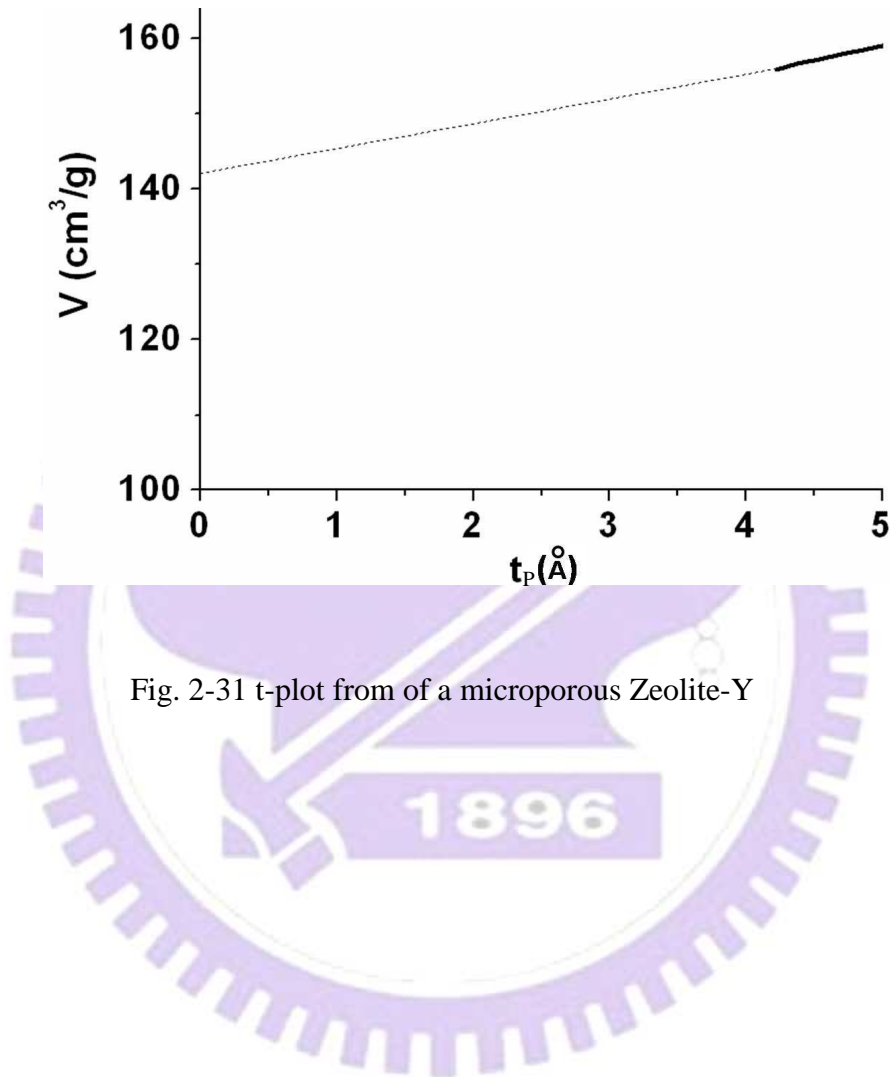


Fig. 2-31 t-plot from of a microporous Zeolite-Y

2.5 Electrode performance testing

(a) Cyclic voltammetry (C-V)

Cyclic voltammetry (C-V) is a technique most widely used for acquiring qualitative information about electrochemical reactions, for examples, on the thermodynamics of redox processes, the kinetics of heterogeneous electron-transfer reactions, and on coupled chemical reactions or adsorption processes. The most common potential wave form used during typical electrochemical experiments is the linear wave form, i.e., the potential is continuously changed as a linear function of time. Such variation of potential with time is known as the scan rate (v). During the C-V measurement, the direction of the potential is reversed at the end of the first scan, thus, leading to the typical isosceles triangle waveform. This has the advantage that the product of the electron transfer reaction occurred during the forward scan can be probed again during the reverse scan. In addition, C-V is also a powerful tool for the determination of formal redox potentials, detection of chemical reactions following the electrochemical reaction, and evaluation of electron transfer kinetics. The experiments were operated based on a three-electrode design: a platinum wire is served as the counter electrode and a saturated calomel electrode (SCE) was used as the reference electrode. The working electrode is a Pt wire attached with a 0.25 cm^2 thin Pt foil, which is used to contact with the testing sample.

(b) Chemisorption analysis

A pulse chemisorption analysis may be used to determine the active surface area, metal dispersion, and average particle size by applying suitable doses of reactant gas to the sample. Once all active sites have been completely reacted with the reactant gas,

the discretely injected gas volumes elute from the sample tube will remain uncharged. The amount of chemisorbed gas may therefore be inferred from the difference between the total amount of reactant gas injected into and the amount eluted from the sample. Consequently, the metal particle dispersion (PD), active surface (SA) area, and average particle size (APS) can be derived by the following equations:

$$PD = 100 \left(\frac{V_s \times SF}{SW \times 22414} \right) GMW \dots\dots\dots(Eq. 2-6)$$

$$SA_{Metallic} = \left(\frac{V_s}{SW \times 22414} \right) \times SF \times (6.023 \times 10^{23}) \times SA \dots\dots\dots(Eq. 2-7)$$

$$APS = \frac{6}{Den. \times (W_s / GMW) \times (6.023 \times 10^{23}) \times SA} \dots\dots\dots(Eq. 2-8)$$

where SF is the Stoichiometry factor, SW denotes sample weight (g), GMW stands for gram molecular weight (g/g-mole), $SA_{Metallic}$ represents the meta surface area (in m^2/g metal), APS is the active particle size, Den. is the calculated metal density (g/mL), and W_s represents the sample weight (in unit of g.) In addition, the parameters V_s and SA may be calculated from:

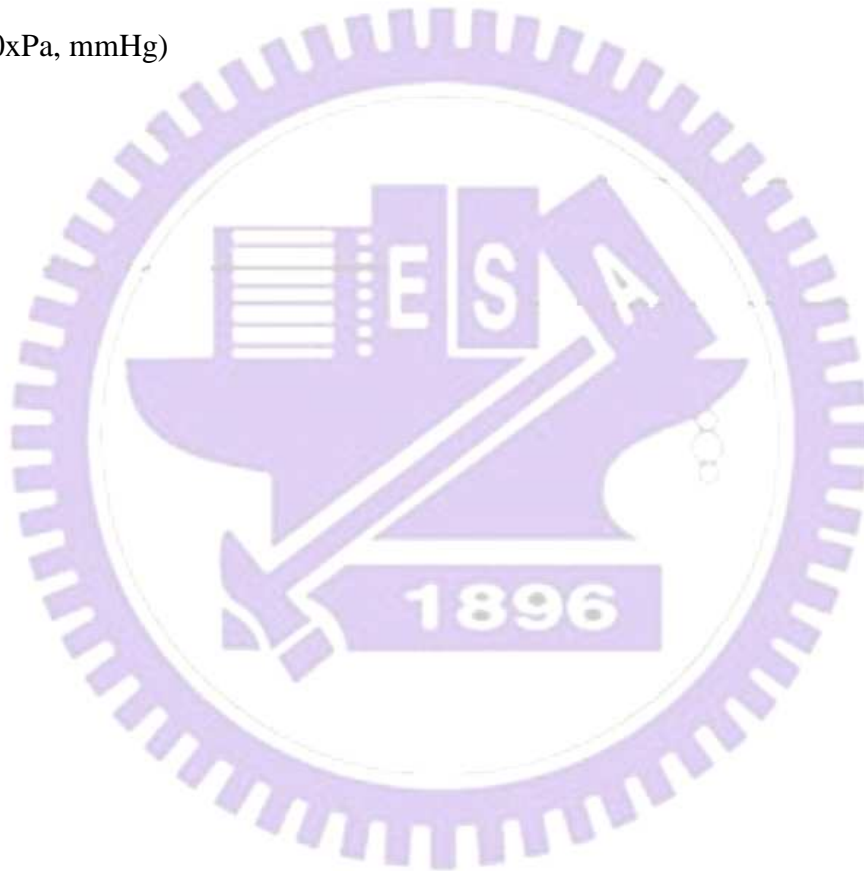
$$V_s = (I \times V_i) - V_{na} \dots\dots\dots(Eq. 2-9)$$

$$V_{STP} = \frac{V_a}{SW} \times \left(\frac{273.15K}{273.15K + T_a} \right) \times \left(\frac{P_a}{760mmHg} \right) \dots\dots\dots(Eq. 2-10)$$

$$V_m = V_{STP} \left(1 - \frac{P}{P_0} \right) \dots\dots\dots(Eq. 2-11)$$

$$SA = \frac{V_m}{22414} \times (6.023 \times 10^{23}) \times A_{N_2} \dots\dots\dots(Eq. 2-12)$$

where V_S is the volume adsorbed (mL at STP), SA is the specific surface area, I is the number of injections, V_i is the volume per injection (mL), V_{na} is the total volume not sorbed (ml), V_a is the sorption volume at ambient conditions (mL), V_{STP} is the sorption volume sorbed at STP (mL/g of sample), V_m is the volume of monolayer (mL), T_a represents ambient temperature (K), P is the absolute pressure of N_2 (estimated by $\%N_2/100 \times Pa$, mmHg), A_{N_2} is the surface area of the N_2 molecule ($m^2/molecule$, $16.210^{-20} m^2$), and P_0 is the Saturation pressure of N_2 (estimated by $\%N_2/100 \times Pa$, mmHg)



Chapter 3

Experimental details

3.1 Experimental flow chart

The results described in this dissertation were obtained from a series of different experiments, as illustrated in Fig. 3- 1. In brief, CMMs and CNTs are prepared by using porous substrates as templates in thermal CVD process without and with Fe catalyst, respectively. Moreover, the CMMs and CNTs are used as supports for metal (Pt) catalyst for DMFC anodes, the electrocatalysts are prepared by using H_2PtCl_6 as Pt precursor and reduced by a H_2 atmosphere. For the investigation of CNT growth mechanism, both thermal and plasma-enhanced CVD process are adopted to growth CNTs with cobalt catalyst on SBA-15 substrate and Si-wafer. The structure and properties of the nanostructured materials after each step were characterized by transmission electron microscopy (TEM), X-ray diffratometry (XRD), cyclic-voltammetry (C-V), chemisorption, thermogravimetric (TG), Raman, and/or N_2 adsorption/desorption analyses.

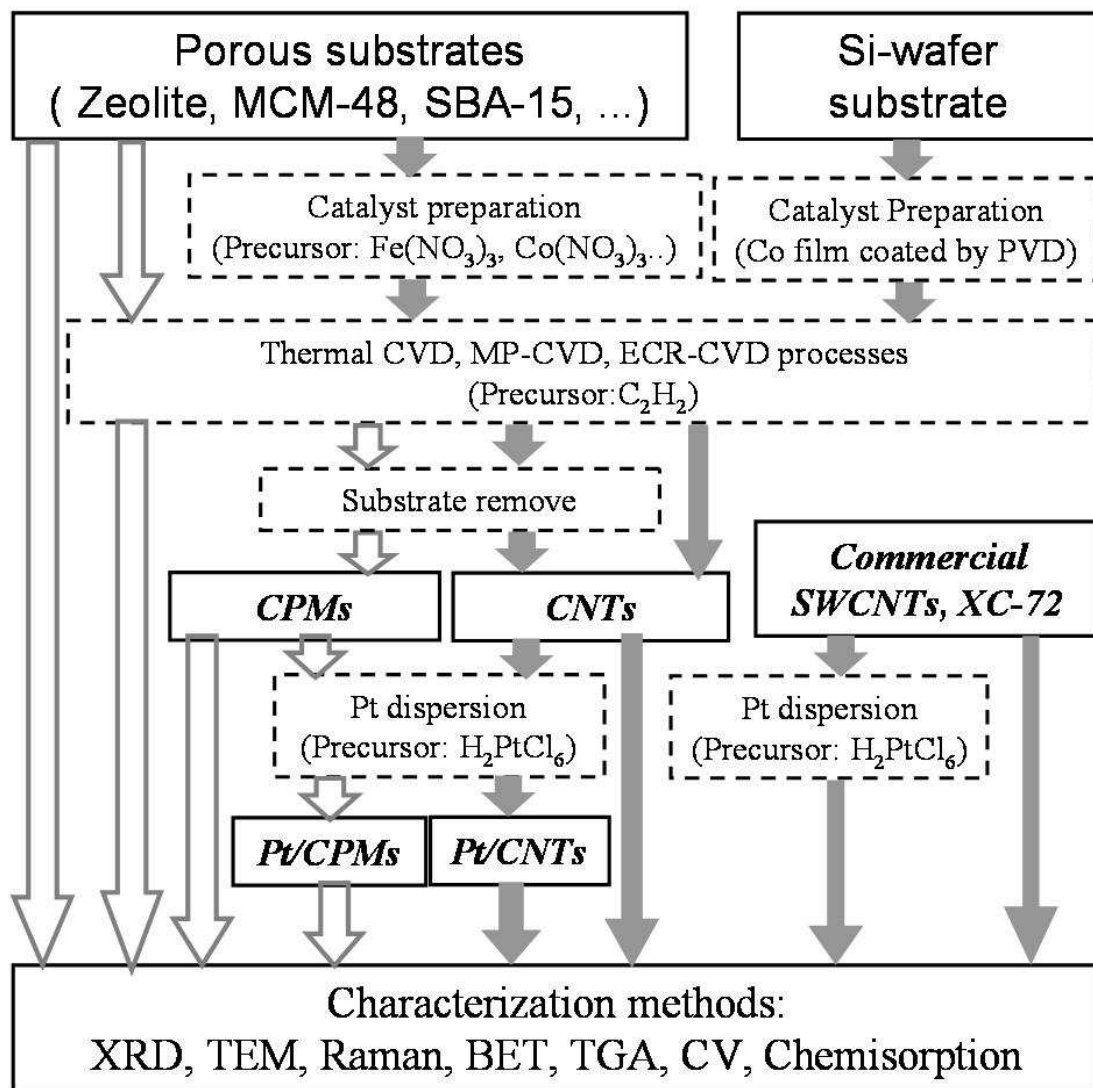


Fig. 3- 1 Flow chart of the experiments.

3.2 Row materials

All source gases and chemicals used in this dissertation are listed in Table 3- 1.

Table 3- 1 Chemicals and other row materials used.

Name	Formula	Supplier
Acetylene	C ₂ H ₂ (purity 99.9995%)	San Fu
Argon	Ar (purity 99.998%)	San Fu
Brij-30	C ₁₂ H ₂₅ (OCH ₂ CH ₂) ₄ OH)	Aldrich
Chloroplatinic Acid Hexahydrate	H ₂ PtCl ₆	Acros
Cobalt nitride	Co(NO ₃) ₃	Acros
Dichloromethane	CH ₂ Cl ₂	Acros
Hexadecyltrimethylammonium bromide (CTABr)	C ₁₆ H ₃₃ (CH ₃) ₃ NBr	Acros
Hydrochloric acid	HCl	Acros
Hydrofluoric acid	HF	Acros
Hydrogen	H ₂ (purity 99.9995%)	San Fu
Iron(III) Chloride	FeCl ₃	Acros
Iron nitride	Fe(NO ₃) ₃	Acros
P-type (100) silicon wafer	Si	
Sodium silicate solution	NaSiO ₃	Acros
Styrene	C ₈ H ₈	Aldrich
Sulfuric acid	H ₂ SO ₄	Acros
Tetraethyl orthosilicate (TEOS)	SiC ₈ H ₂₀ O ₄	Aldrich
Triblock copolymer (P ₁₂₃)	poly(ethylene oxide) ₂₀ - poly(propylene oxide) ₇₀ - poly(ethylene oxide) ₂₀	Acros
1,3,5-trimethylbenzene	C ₉ H ₁₂	Acros

* Regent grade chemicals

3.3 Features of CVD systems

The processing systems used for fabrication of various samples include thermal CVD, MP-CVD, ECR-CVD, and a laser deposition system. Their designs and working principles are summarized below:

(a) Thermal CVD

Fig. 3- 2 shows the schematic diagram of a home build thermal CVD system. In Fig. 3- 2 (a), a smaller quartz tube aligned coaxially with a larger quartz tube containing the specimens (porous substrates) at the bottom, so that the reactant gas mixture can flow through the specimen efficiently before exhausting from the top of the chamber. This represents a system without reactant gas preheating. On the other hand, Fig. 3- 2(b) illustrates a system with gas preheating: the reactant gas mixture was preheated before reaching the specimen, which is placed in a net of quartz wools to ensure better gas penetration. In contrast to the conventional thermal CVD systems, the main feature of this system is that the temperature difference between the precursor gas and the substrate can be manipulated.

(b) MP-CVD

A schematic diagram of microwave plasma (MP-) CVD system is shown in Fig. 3- 3. The system is comprised with six main components, namely the microwave generator, the wave-guides, the reaction chamber, the gas flow controller, the gas pressure controller, and the pumping system. In this particular set-up, a 1.3 kW microwave (2.45 GHz) generator from Tokyo electronic Corp. was used. The reaction chamber was made of a quartz tube (with inner and outer diameters of 47 and 50 mm,

respectively; China Quartz Corp.) in a microwave applicator made of aluminum alloy. The other components of the system include stainless steel specimen chamber and specimen holder, and a rotary pump (Hitachi Corp. Ltd). The upper electrode above the specimen holder facilitates the generation of DC bias on the specimen during deposition. A thermal couple embedded in the sample holder allows for monitoring the temperature of the substrate. The mass flow controller (MKS, model 247) is used to control the flow rates of source gases (Ar , H_2 , C_2H_2). The pressure of the sample chamber is monitored by a thermal couple vacuum gauge, and is regulated by an APC controller (MKS, model 263) through an absolute pressure gauge (MKS Baratron) and a throttling valve. The temperature of the specimens is dictated by the microwave power, pressure, and the distance to the plasma zone. There is no external heating system.

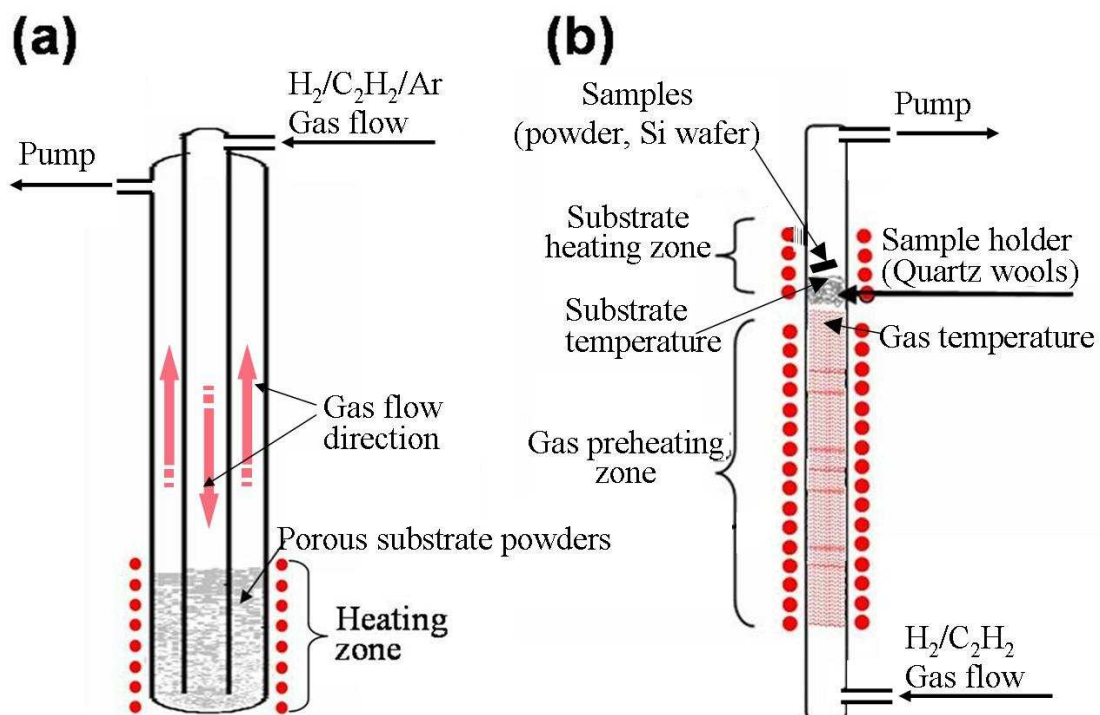


Fig. 3- 2 Schematic thermal CVD systems (a) without, (b) with gas preheating heater.

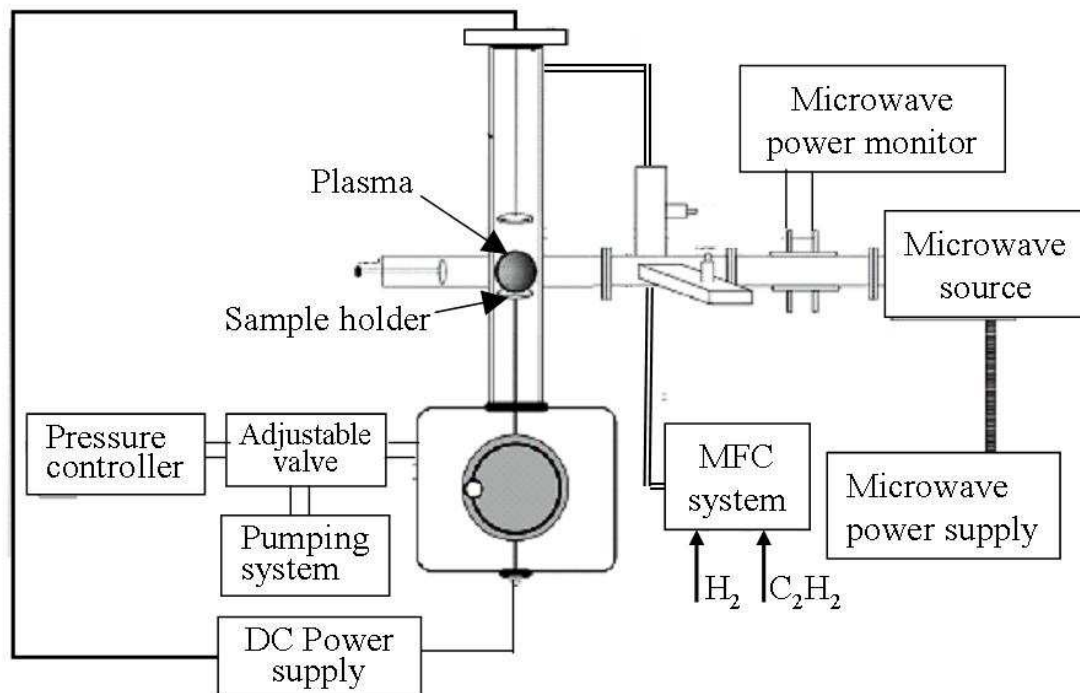


Fig. 3- 3 Schematic MP-CVD system.

(c) ECR –CVD

An illustrated example of the Electron Cyclotron Resonance Chemical Vapor Deposition (ECR-CVD) system is shown in Fig. 3- 4. The system consists of a microwave generator (2.45 GHz) capable of delivering a maximum power of 1200 W, three-spot circulator, tuner, wave guides, microwave applicator, reaction chamber, mass flow controller, electric coils, cooling copper coils, substrate heating stage, vacuum pump, and D.C. bias. The ECR-CVD system above has the advantages of high dissociation efficiency, low deposition temperature of CNTs, and a wider deposition area. Typically, such a system is characterized by the electric field (E) and the magnetic field (B) such that the electrons are accelerated by E to the direction perpendicular to B and orbiting in a plane also perpendicular to B with a cyclotron radius r_c . When the microwave angular frequency (ω) is identical to the angular frequency of the electron (v/r_c), the electrons will be in phase with the field at either

positive or negative E; a phenomenon known as electron cyclotron resonance (ECR), which takes place at $B = 875$ Gauss, corresponding to a frequency of 2.45 GHz for the activated media. The cyclotron radius (r_c) for the orbiting electrons (in B) can be expressed as: $r_c = m_e v / eB$, where v , e , m_e , and ω represents the electron velocity component perpendicular to B, the electron charge (coulombs), mass of electron, and the electron angular frequency, respectively.

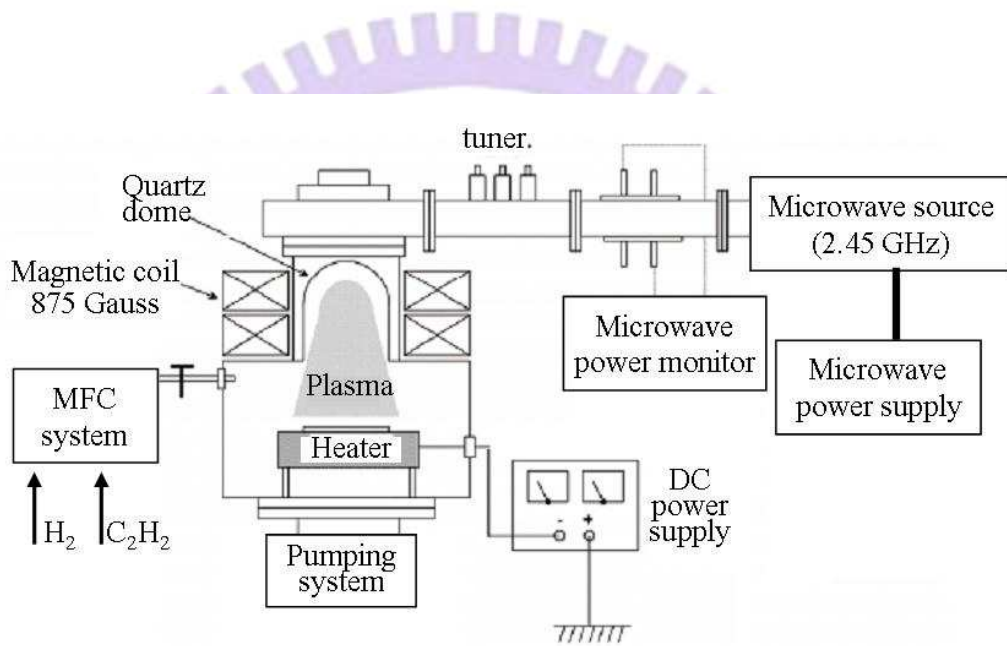


Fig. 3- 4 Schematic ECR-CVD system.

3.4 Preparation of porous silica

(a) MCM-41

The MCM-41 mesoporous silica was synthesized following the procedures reported earlier.^[Lin-1998-581] In brief, surfactant solution was first prepared by dissolving CTABr (7.7 g) in distilled water (85.0 mL). Sodium silicate solution (10.0g, NaSiO₃) was then added into the solution at 305 K under stirring. After stirring for about 30 min, 1.2 M of H₂SO₄ (8.0 g) was slowly added into the gel mixture. This step takes up to 30 min. The pH value of the final mixture was then adjusted to about 10 before the mixture was kept at 373 K for 48 h. The resultant solid products were recovered by filtration, washing with deionized water and drying in air at 373 K. Finally, the resultant products were calcined in air at 833 K for 6 hours to remove the surfactant (with a heating rate of 1.5 K/min).

(b) MCM-48

Highly stable MCM-48 mesoporous silica material was synthesized following the procedures reported earlier.^[Kim-1998-259] In brief, surfactant mixture solution was first prepared by dissolving both CTABr (7.6532 g) and Brij-30 (1.45 g) simultaneously in distilled water (60 mL). Then, sodium hydroxide (2.5 g) solution (in 5 mL water) was added to the surfactant solution and stirred for 0.5 h. The silica solution was then added to the above solution and the resulting mixture was shaken vigorously for 0.5 h and the resultant gel was kept at 373 K for crystallization. After 2 days, the mixture was cooled to room temperature (298 K) and pH of the solution was adjusted to 10 with acetic acid. Then, the mixture was kept for 373 K for another 2 days. The resulting product was filtered and washed with ethanol/water mixture and

dried in an oven at 373 K followed by calcined in air at 823 K for 6 h.

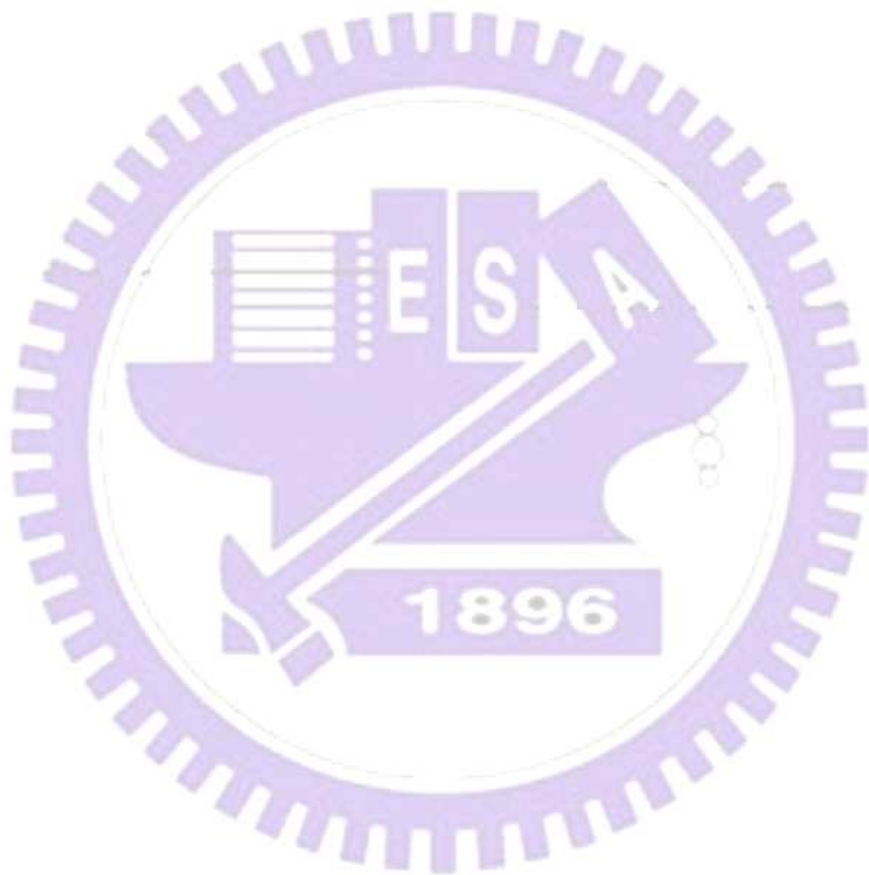
(c) SBA-15

The SBA-15 mesoporous silica was synthesized following the synthesis route reported by Zhao et al.^[Zhao-1998-548] Typically, tetraethyl orthosilicate (TEOS, Aldrich), which was used as the silica source, was added to an aqueous solution containing HCl and triblock copolymer (P₁₂₃ surfactant) at 313 K, with starting weight ratios of: 2.3 g TEOS / 1.0 g P₁₂₃ / 8.0 g HCl / 30.0 g H₂O. The mixture was stirred for about 2 hours before it was aged at 373 K for 2 days. The product was then filtered, washed with distillate water, dried at 373 K, and finally calcined in air at 833 K for 6 hours. On the other hand, an additional TMB (1,3,5-trimethylbenzene) is used to expand the pore size of SBA-15 during the preparation process.

(d) Photonic crystal

Photonic crystal (PC) macroporous silica was synthesized following the procedure reported by Holland et al.^[Holland-1999-795] Firstly, 1700 mL of DI water was heated to 343 K in a 3000 mL round-bottomed flask. After styrene (200 mL, Aldrich) was added, the solution was stirred with deaerated by nitrogen. Second, the aqueous solution of potassium persulfate (100 mL, 0.025 M, 343 K) was added into the above styrene solution to initiate the polymerization of the styrene, and keep stirring for 28 hours. Finally, the poly-styrene latex spheres were gathered by filtering and drying in air. This process was followed by silica replication process which millimeter-thick layers of latex spheres were deposited on filter paper in a Buchner funnel under vacuum and soaked with ethanol. Then, tetraethoxysilane (TESO) was added dropwise to cover the latex spheres completely during the filtration. After the composite product was dried in a vacuum evaporator, the latex spheres were removed

by calcination in air at 848 K for 7 hours. Finally, the photonic crystals with pore diameter ranging from 200 to 400 nm were obtained.



3.5 Preparation of carbon nanostructures

Various procedures have been adopted for the preparation of CNTs, including:

(a) Deposition of metal catalyst on porous supports

Three types of mesoporous silica, namely MCM-41, SBA-15, and pore expanded SBA-15 (denoted as PE-SBA-15) were synthesized by known recipes reported previously.^[Mou-2000-137; Zhao-1998-548] Iron (Fe) catalyst was loaded onto the mesoporous silicas *via* either co-precipitation or impregnation methods. For the former, 0.4 g of $\text{Fe}(\text{NO}_3)_3$ was stirring with 1.0 g of the target mesoporous silica material for 0.5 h in 20 mL of deionized water, followed by filtering, drying at 373 K, and a reduction treatment under H_2 atmosphere for 10 min before CNTs deposition. The Fe-containing mesoporous silicas obtained from the siliceous MCM-41 and SBA-15 are denoted as Fe(co)/MCM-41 and Fe(co)/SBA-15, respectively. In the case of (Fe) catalyst loading by impregnation method, proper amount of $\text{Fe}(\text{NO}_3)_3$ (estimated ca. half of pore volume of the corresponding support) was dissolved in 20 mL of deionized water, followed by adding 1.0 g of the target mesoporous silica. After being stirred for 0.5 h, the suspension was dried under vacuum. The obtained product was stirred in the presence of CH_2Cl_2 to facilitate migration of Fe precursors into the hydrophilic channels of the mesoporous silica^[Han-2000-2068] followed by removal of CH_2Cl_2 by evacuation. The above procedure was repeated once and the final product was subjected to reduction treatment, which was carried out by first slowly ramping (2 K/min) the temperature to 373 K under dried Ar, kept at the same temperature for 3 h, followed by reduction under H_2 environment before C_2H_2 was injected for CNTs

growth. The obtained Fe-containing mesoporous silicas derived from the siliceous MCM-41, SBA-15, and PE-SBA-15 are denoted as Fe(im)/MCM-41, Fe(im)/SBA-15, and Fe(im)/PE-SBA-15, respectively.

To incorporate Co catalyst onto the SBA-15 substrate, the mesoporous substrate was first added into 0.1M $\text{Co}(\text{NO}_3)_3(\text{aq})$ solution, and stirred till SBA-15 were completely suspending in the solution. The cobalt nitride coated SBA-15 were then collected by filtration and dried prior to further decomposing the catalyst into cobalt oxide (CoO_x) in an air furnace under 573 K. The Co oxides were finally reduced to Co in a hydrogen furnace at 1073 K and the supported catalyst so prepared is denoted as Co/SBA-15. Alternatively, a Co-coated (thickness ca. 10 nm) on Si wafer sample was prepared by sputtering method and is denoted as Co/Si (001). In addition, samples with bifunctional Pt-Fe metal catalyst loaded on MCM-48 mesoporous silica were prepared by using co-precipitation method described above by using $\text{H}_2\text{PtCl}_6 \cdot 6\text{H}_2\text{O}(\text{aq})$ and $\text{FeCl}_3(\text{aq})$ as the Pt and Fe precursors, respectively.

(b) Procedures involving thermal CVD

Carbon mesoporous materials (CPMs) and CNTs respectively synthesized using various mesoporous silicas templates and Fe- (or Co-) containing SBA-15 mesoporous silicas as substrates, were conducted by similar procedures summarized below: first, the template/substrate was placed into a quartz reactor, followed by heating the reactor and gas pre-heating zones to the target temperature (1073 or 1093 K) under vacuum. Then, a desirable amount of acetylene (which served as the carbon source), was introduced into the reactor together with mixture of H_2 and/or Ar gases. Then, the CPMs/CNTs products may be respectively collected by filtering and drying after removal of silica template/substrate by etching with 1 M HF solution of 50%

ethonal–50% H₂O. Similar procedures were adopted to prepare Pt-Fe containing hollow carbon capsule (HCC) and solid carbon capsule (SCC) by using either neat mesoporous silica or Pt-Fe loaded porous silicas as templates. Detailed preparation conditions for various CPMs and CNTs are depicted in Table 3- 2, and Table 3- 4.

Table 3- 2 Sample designations, processing conditions and diameters of CPMs and CNTs prepared by thermal CVD without gas preheating.

Sample design ^a	t ^b (min)	Substrate ^c Catalyst/Template	Gas flow ratio ^d (C ₂ H ₂ /H ₂ /Ar)	T _s ^e (K)	Diameter ^f (nm)
ZRC	40	-/Zeolite-Y	50/50/50	1073	< 1.3
CMT-1	40	-/MCM-48	50/50/50	1073	~ 2
CMT-2	60	-/SBA-15	50/50/0	1073	~ 3
HCC	40	-/MCM-48	50/50/0	1093	20 ~150
Pt-Fe/HCC	40	Pt-Fe/MCM-48	50/50/0	1093	20 ~150
Pt-Fe/SCC	40	Pt-Fe/MCM-48	50/50/0	1073	~. 2
PCC	120	-/PC	50/50/0	1073	~ 400
CNT-d3	20	Fe(im)/SBA-15	50/50/0	873	3
CNT-d5-10	20	Fe(co)/MCM-41	50/50/0	873	5 - 10
CNT-d8	20	Fe(im)/MCM-41	50/50/0	873	8
CNT-d10-30	20	Fe(co)/SBA-15	50/50/0	873	10 - 30
CNT-d17	20	Fe(im)/PE-SBA-15	50/50/0	873	17

^a Other processing condition: pressure 3 kPa ; specimen designation of CNT-d#1-#2 represents CNTs with diameter #1 or from #1 to #2.

^b Duration of processing time.

^c Template for producing CPMs or catalyst for synthesizing CNTs; where co in Fe(co)(template) and im in Fe(im)(template) represent Fe catalyst prepared by co-precipitation and by impregnation methods on a template substrate, respectively.

^d In unit of sccm / sccm / sccm.

^e Substrate temperature (*T_s*) during CPM or CNT deposition.

^f Pore diameter of porous carbon or tube diameter of CNTs.

Table 3- 3 Sample designations and their deposition conditions of CNTs by thermal CVD with gas preheating.

Sample desig. ^a	t ^b (min)	Catalyst / Substrate	Sub. Surface condition ^c	Temp. ^d T _G /T _S (K/K)	ΔT ^e	CNTs Growth Mode
A1-5	5					
A1-10	10					
A 1-15	15					
A 1-20	20	Co/SBA-15	R	300/1073	-	Base-growth
A 1-30	30					
A 1-40	40					
A 1-65	65					
A 1-90	90					
A 2-20	20	Co/Si (001)	S	300/1073	-	Base-growth
A 3-20	20	Co/SBA-15	R	1073/873	+	Tip-growth
A 4-20	20	Co/Si (001)	S	1073/873	+	Tip-growth
A 5-20	20	Co/SBA-15	R	923/923	~ 0	No CNTs
A 6-5	5					
A 6-10	10	Co/SBA-15	R	1073/1073	~ 0	No CNTs
A 6-15	15					
A 7-5	5					
A 7-10	10	- / SBA-15	R	300/1073	-	No CNTs
A 7-15	15					
A 8-5	5					
A 8-15	15	- / SBA-15	R	1073/1073	~ 0	No CNTs
A 8-25	25					

^a Other deposition conditions: H₂ / C₂H₂ = 50 / 50 (sccm / sccm); 3 kPa pressure

^b CNTs deposition time.

^c Conditions of the substrate surface, R = rough (porous) SiO₂ powders, and S = smooth polished Si wafer

^d T_G: the preheated temperature of the reactant gas; T_S: the substrate temperature during deposition.

^e ΔT = temperature of catalyst at the top minus at the bottom. Its sign represents the temperature increasing direction.

(c) Procedures involving plasma-enhanced CVD

The CNTs prepared by plasma-enhanced CVD may be divided into two categories, namely those by MP-CVD and ECR-CVD. For CNTs fabrication by plasma-enhanced CVD, a Co-coated (thickness ca. 10 nm) on Si wafer sample prepared by sputtering method, denoted as Co/Si (001), was used. The Co-coated substrate was first pretreated in H-plasma atmosphere to dissociate Co film into nanoparticles, followed by CNTs deposition with C₂H₂ and H₂ as reactant gases; detailed informations are depicted in Table 3- 4.

Table 3- 4 Sample designations and their deposition conditions by plasma-enhanced CVD.

Sample	Process ^a	W_{pre}/W_{gro} ^b (W/W)	V_{pre}/V_{gro} ^b (V/V)	T_{Si}/T_{Sf} ^b (K/K)	t ^c (min)	ΔT ^d	CNTs Growth Mode
B1	MP-CVD	800/800	100/120	740/773	5	+	Tip-growth
B2		1000/600	100/60	793/780	2	-	Base-growth
C1	ECR-CVD	250/270	100/120	773/803	5	+	Tip-growth
C2		300/240	120/100	1023/904	4	-	Base-growth

^a Types of plasma-enhanced CVD process applied; MP = microwave plasma CVD, ECR = electron cyclotron resonance CVD. The working pressure adopted during MP- and ECR-CVD is 1.3 kPa and 0.9 Pa, respectively.

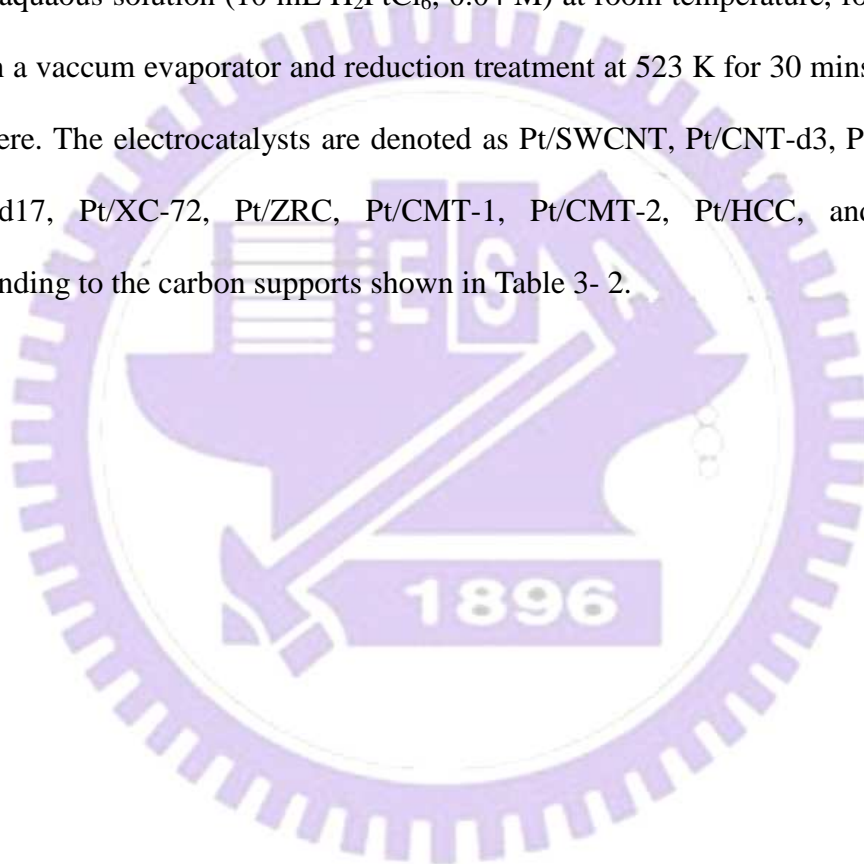
^b W_{pre} , and V_{pre} = microwave power, and bias voltage during the H-plasma pretreatment step ($H_2 = 50$ sccm), respectively. W_{dep} , V_{dep} , T_{Si} , and T_{Sf} = microwave power, bias voltage, initial and final substrate temperature of the deposition step (H_2/C_2H_2 flow ratio = 50/10 (sccm / sccm); pressure = 10 Torr), respectively.

^c CNTs deposition time in minute.

^d ΔT = temperature of catalyst at the top minus at the bottom, representing the direction of temperature increasing across a catalyst.

3.6 Preparation of carbon nanostructure-assisted DMFC electrocatalysts

To further explore their applications in fuel cell, the aforesaid carbon nanostructured materials, namely CPM and CNT materials were utilized as support for noble metal (Pt) catalyst. A hydrogen reduction process was adopted to disperse Pt on various carbon supports, typically, by first suspending ca. 0.2 g of the carbon in H_2PtCl_6 aqueous solution (10 mL H_2PtCl_6 , 0.04 M) at room temperature, followed by drying in a vacuum evaporator and reduction treatment at 523 K for 30 mins under H_2 atmosphere. The electrocatalysts are denoted as Pt/SWCNT, Pt/CNT-d3, Pt/CNT-d8, Pt/CNT-d17, Pt/XC-72, Pt/ZRC, Pt/CMT-1, Pt/CMT-2, Pt/HCC, and Pt/PCC corresponding to the carbon supports shown in Table 3- 2.



3.7 Structure and property characterization

The surface morphologies of each specimen were characterized by using a JEOL JSM-6700 field-emission SEM, and the microstructure of specimens were examined by TEM analysis. Typically, a Hitachi H-7100 (operated at 100 keV) and a JEOL JEM-2100 (200 keV) were adopted for the TEM and high-resolution TEM measurements. For TEM measurements, all specimens were dispersed by ultrasonication in acetone and dried on copper grid. In addition, the structuring ordering of the porous materials were examined by X-ray diffraction (XRD) patterns by using a PANalytical (X'Pert PRO) instrument using Cu K α radiation ($\lambda = 0.1541$ nm). Moreover, a Thermo K-alpha x-ray photoelectron spectroscopy (XPS) apparatus was adopted to characterize the nature of Pt metal of various samples. Thermogravimetric analyses (TGA) were also performed using a Netzsch TG-209 instrument under dried air atmosphere. The BET surface areas and pore size distributions of various porous materials, were evaluated by nitrogen adsorption/desorption measurements conducted at 77 K using a Quantachrome Autosorb-1 or Micromeritics ASAP 2010 analyzer after each sample was degassed at 200 °C under vacuum for at least 12 h. Two raman spectrometers respectively equipped with a Helium/Neon and an Ar laser at the wavelength of 632.8 and 514.5 nm (both were Jobin Yvon LabRam HR) were used for the aquisition of Raman spectra for various samples.

3.8 Electrode performance testings

(a) Characterization of electrochemical properties

The electrochemical properties of various supported carbon substrates as electrode materials (e.g., as anode in DMFC as well as cathode in thin film Li-battery) were evaluated by cyclic voltammetry (C-V) measurements conducted on a galvanostat/potentiostat (Autolab, PGSTAT30).

For application of DMFC at anode, the electrocatalytic activity measurements of sample with ca. 10 wt % Pt dispersed on either CMMs or a commercial XC-72 activated carbon were performed with a glassy carbon as the working electrode, Pt wire as the counter electrode, and Ag/KCl (3M) as a reference electrode at a scanning rate of 10 mV/s. The glossy carbon thin-film electrode was prepared by the following steps: first, ca. 10 mg of PtRu-loaded carbon sample was added into 5 mL of deionized water, followed by ultrasonic treatment for 0.5 h. Next, ca. 7.5 (or 20) μ L of the resultant suspension mixture was withdrawn and injected onto the glassy carbon electrode (diameter 3 or 5 mm), followed by drying in air at 333 K for 1 h. Finally, 7.5 (or 20) μ L of 1% Nafion (DuPont) solution was added as a binder under N₂ environment. Electrooxidation of MeOH was carried out with an electrolyte of 0.5 M H₂SO₄ and 1 M MeOH between -0.2 and 1.0 V at room temperature. Prior to each C-V measurement, the electrolytic solution was purged with high-purity N₂ (99.9%) for at least 0.5 h to remove the dissolved oxygen; subsequently, the experiment was conducted under purging N₂ condition.

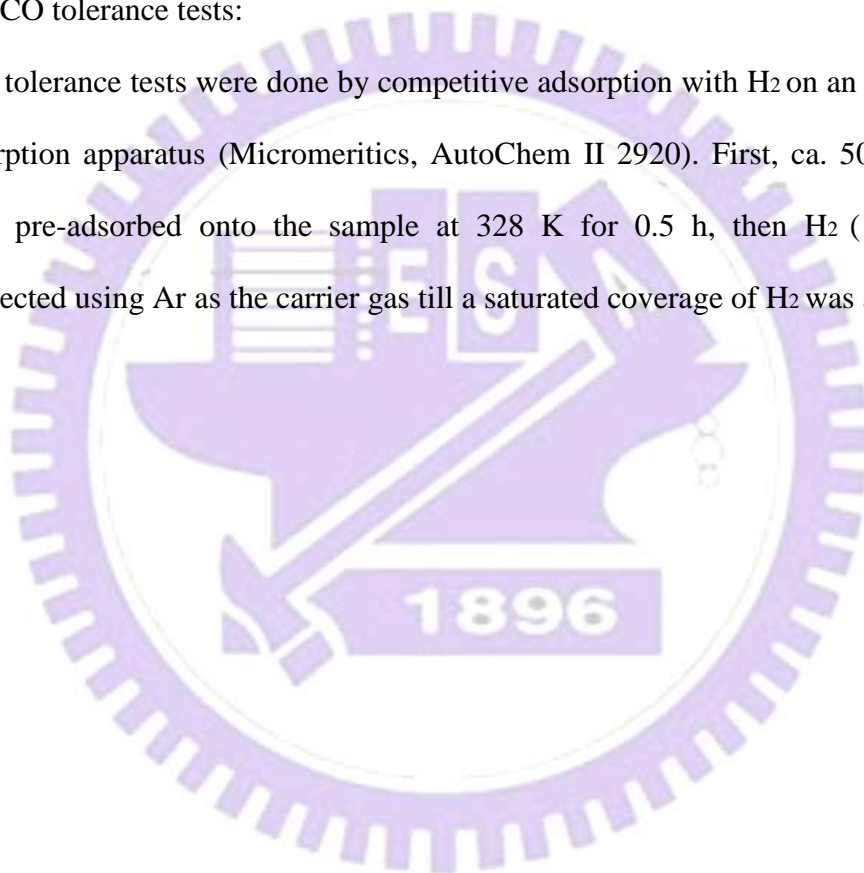
(b) Characterization of chemisorption properties

(i) Pt dispersion measurements:

The dispersions of platinum on various samples were measured by hydrogen chemisorption. For each run, ca. 0.02 g of Pt/carbon sample were pretreated by outgassing at 623 K for one hour, then, the first H₂ adsorption isotherm was measured after the sample was cooled to 305 K, followed by outgassing for one hour to obtain a second H₂ adsorption isotherm under the same conditions.

(ii) CO tolerance tests:

CO tolerance tests were done by competitive adsorption with H₂ on an automated chemisorption apparatus (Micromeritics, AutoChem II 2920). First, ca. 500 ppm of CO was pre-adsorbed onto the sample at 328 K for 0.5 h, then H₂ (10%) was pulse-injected using Ar as the carrier gas till a saturated coverage of H₂ was achieved.



Chapter 4

Process, structures and properties of CPMs and their applications in DMFC anodes

4.1 Effect of processing parameters on structures and properties of various carbon porous nanostructures

4.1.1 Conditions of fabrication porous carbon with tubular branches

As described in Section 3.5(a) and summarized in Table 3- 2, mesoporous carbons with tubular morphologies were synthesized by using the template-assisted CVD method. Among them, two novel carbon materials, namely CMT-1 and CMT-2 (Carbon Materials from Taiwan) were fabricated using MCM-48 and SBA-15 mesoporous silicas as templates, respectively. Fig. 4- 1 displays the XRD patterns of synthesized MCM-48, CMK-1, and CMT-1 materials, all of which show well-ordered mesoporous structures, as revealed by the characteristic diffraction peaks at small 2θ angles. That the novel CMT-1 material exhibited $[110]$ and $[211]$ peaks at the respective 2θ angles of ca. 1.4° and 2.5° , whereas the corresponding diffraction peaks for the CMK-1 sample were found at ca. 1.6° and 2.8° , indicates that these two mesoporous carbon materials may have rather similar structures. The XRD pattern of the CMK-1 is in good agreement with existing literatures.^[Joo-2001-153; Kaneda-2002-1256; Ohkubo-2002-6523; Ryoo-1999-7743]

Likewise, the XRD profile of the MCM-48 silica exhibited a main $[211]$ diffraction peak at $2\theta \sim 2.3^\circ$, also consistent with earlier

reports.^[Beck-1992-10834; Kim-1998-259; Kruk-1999-2568] Moreover, the N₂ adsorption/desorption isotherms obtained from MCM-48, CMK-1, and CMT-1 (Fig. 4- 2) all exhibited a typical type-IV isotherm with a broad hysteresis loop, which are typical characteristics of capillary condensation in mesoporous channels.^[Matos-2003-821-829; Ravikovitch-2002-1550; Sing-1985-603] Further analyses based on the desorption curves of the isotherms using the BJH method^[Barrett-1951-373] provide additional information on the pore size distributions (PSDs) (Fig. 4- 3), BET surface areas, and pore volumes of various samples, as depicted in Table 4- 1. Additional t-plot analyses illustrated in Section 2.4(g) further confirmed that these materials do not possess any microporosity with pore size < 1 nm. As can be seen from Table 4- 1, these porous carbons replicated from MCM-48 possess high BET surface areas over 1000 m²/g. However, unlike CMK-1 carbon, which revealed only one type of mesopore with average pore size of ca. 3.6 nm, the novel CMT-1 carbon appeared to possess two types of pores with diameters of ca. 1.5 and 3.3 nm.

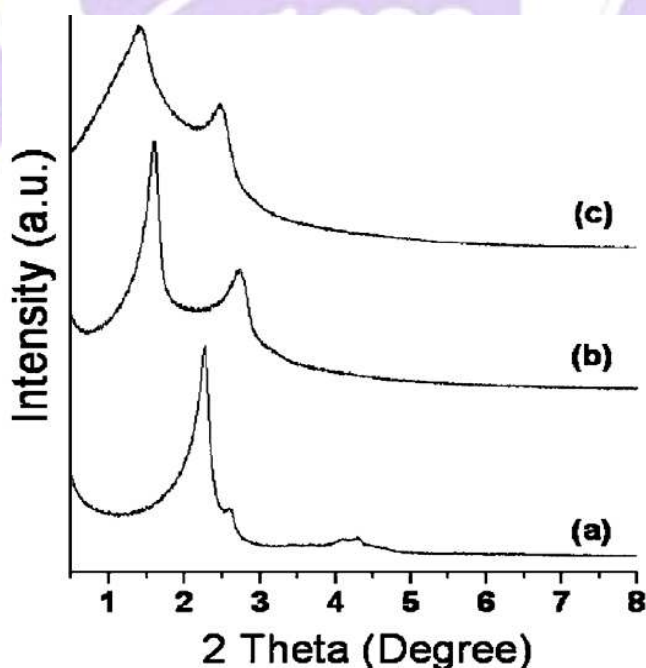


Fig. 4- 1 XRD patterns of (a) MCM-48, (b) CMK-1, and (c) CMT-1 mesoporous materials.

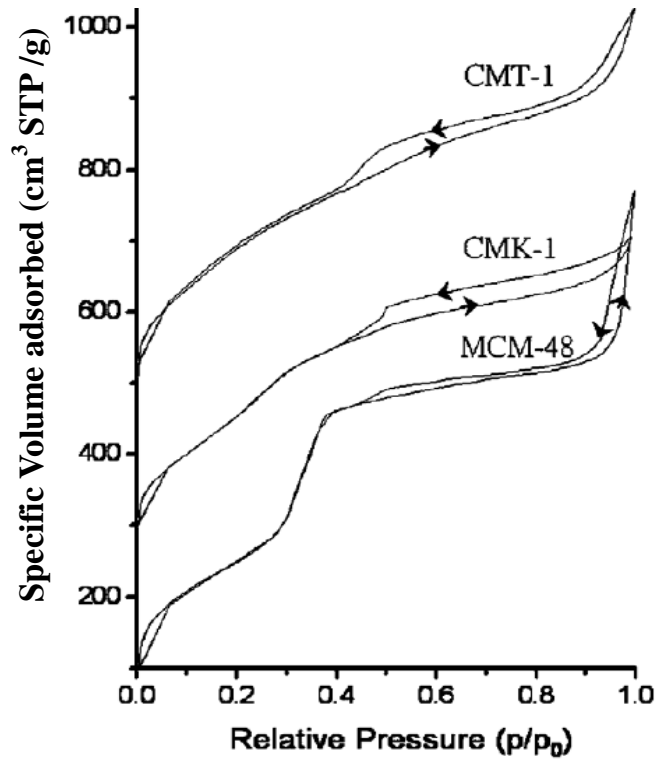


Fig. 4- 2 N₂ adsorption/desorption isotherms (77 K) of mesoporous MCM-48 silica, CMK-1, and CMT-1 mesoporous materials, where the isotherms for the CMK-1 and CMT-1 carbons are shifted vertically by 200 and 400 cm³ STP/g, respectively.

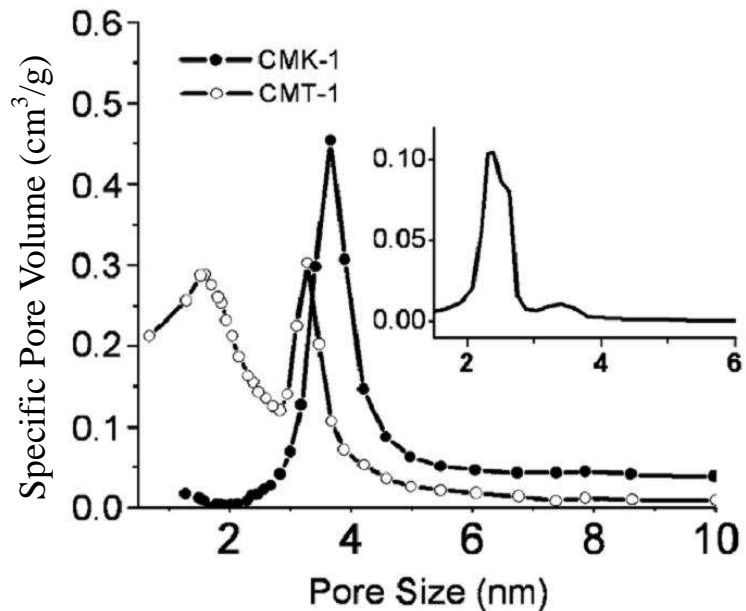


Fig. 4- 3 BJH pore size distribution of CMT-1, CMK-1, and MCM-48 (inset) mesoporous materials.

Table 4- 1 Textural properties of various mesoporous materials.

Porous material		D_{BJH}^a (nm)	S_{BET}^b (m ² /g)	V_p^c (cm ³ /g)
desig. ^d	component			
MCM-48	SiO ₂	2.4	923	0.68
CMK-1	Carbon	3.6	1238	0.75
CMT-1	Carbon	1.5; 3.3	1076	0.63

^a D_{BJH} : average pore diameter derived by BJH method

^b S_{BET} : specific surface area derived by BET analysis

^c V_p : specific pore volume

^d CMK-1 and CMT-1 are replicated from MCM-48 template

Additional investigations by Raman spectroscopy reveal that both CMK-1 and CMT-1 materials exhibit well-structured D-band and G-band near 1340 and 1600 cm⁻¹, respectively (Fig. 4- 4), indicating that these porous carbons possess typical graphite structures analogous to carbon nanotubes (CNTs).^[Kim-2003-4375] More specifically, the G-band can be attributed to graphitic structure and the D-band is normally ascribed due to structural defects or sp³ graphites requisite by the 3-D tubular structure.^[Prasetyo-1999-1909]

The TEM images of MCM-48 and CMT-1 in Fig. 4- 5 confirm that these mesoporous materials are indeed well-ordered, in consistent with the XRD results. Furthermore, the close-up TEM image (Fig. 4- 5c) near the edge of the CMT-1 sample particle (typically ca. 400–500 nm in size) clearly shows tubular carbons with average outer diameter of ca. 2.5 nm, which is also in excellent agreement with the N₂ adsorption/desorption data.

Based on the BJH pore size distribution in Fig. 4- 3 and Table 4- 1, the averaged pore size of the MCM-48 silica template is ca. 2.4 nm, corresponding to a maximum

outer diameter available for formation of the tubular CMT-1 carbon (Fig. 4- 5c). Thus, as illustrated in Fig. 4- 6, the two types of pores near 1.5 and 3.3 nm observed for the CMT-1 carbon can be respectively correlated to the inner diameter of the tubular CMT-1 and the wall thickness of the MCM-48 template. The latter represents the space between pore channels of MCM-48 and hence should be roughly equal to the pore size of CMK-1 (3.6 nm; see Table 4- 1), which is a direct replica of MCM-48. Taking the well-known inter-layer distance of graphite sheets of ca. 0.336 nm,^[Ogden-2002-69] a simple calculation therefore leads to an estimated average thickness of the CMT-1 carbon tubules corresponding to about 1.3 graphite sheet layers, in good agreement with the TEM analysis.

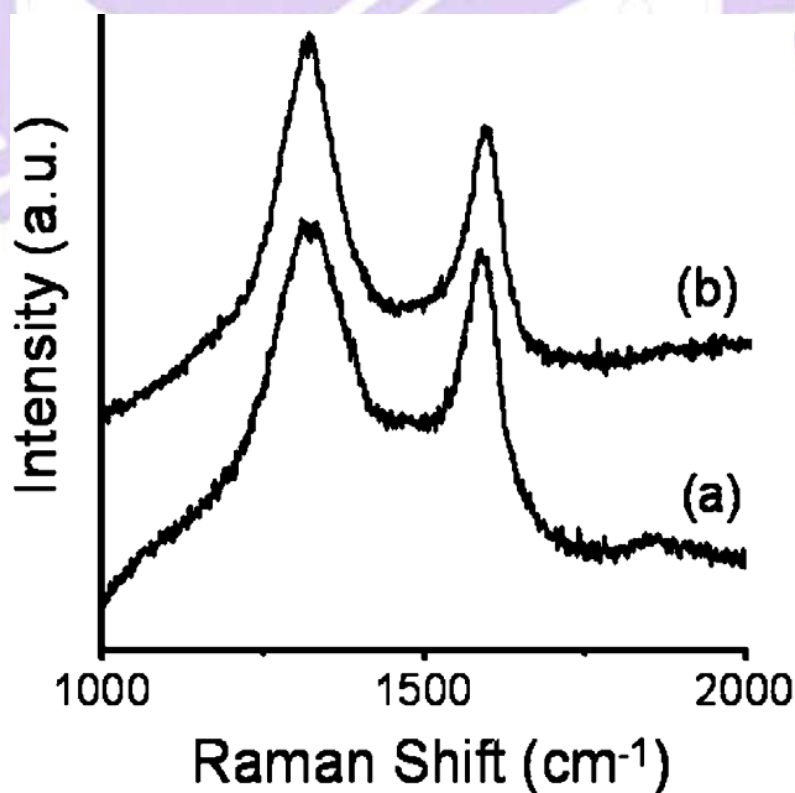


Fig. 4- 4 Raman spectra of (a) CMK-1 and (b) CMT-1 mesoporous carbons.

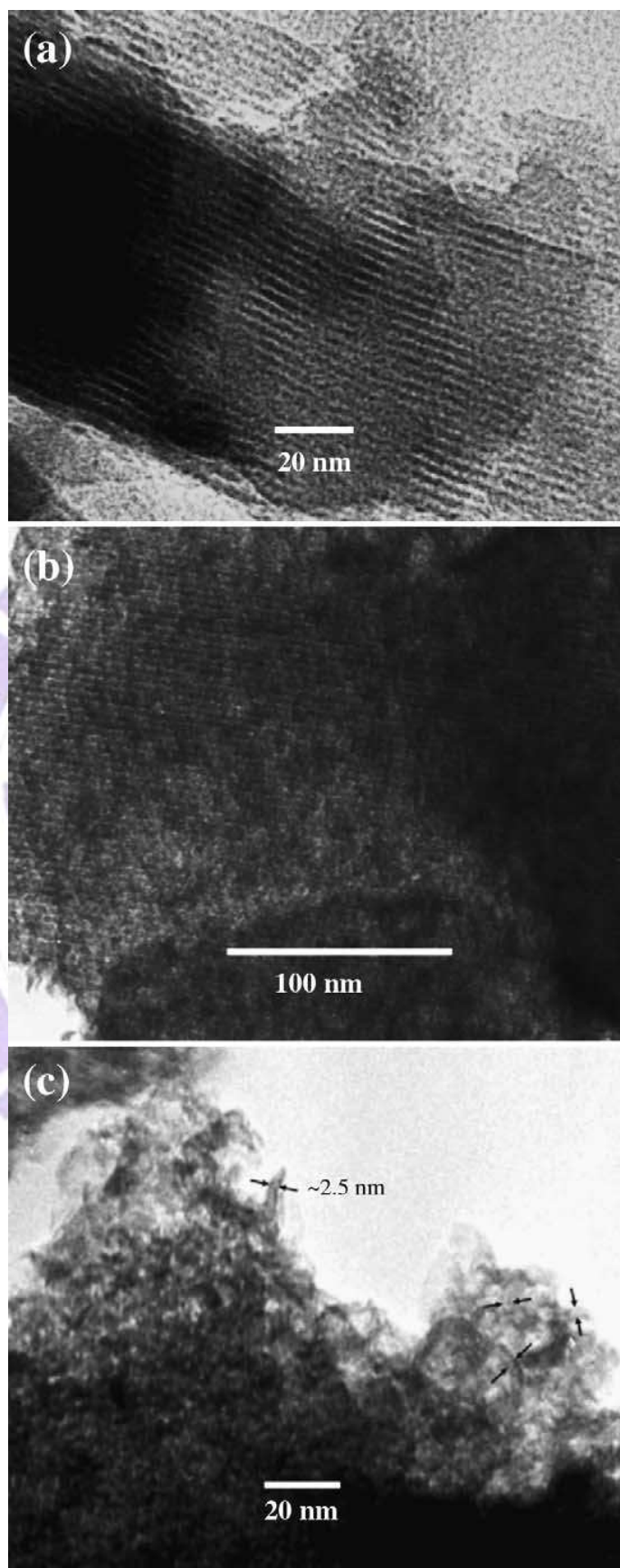


Fig. 4- 5 TEM images of a powder from (a) MCM-48 template and (b) CMT-1 mesoporous materials, respectively. The (c) is higher magnification image of (b).

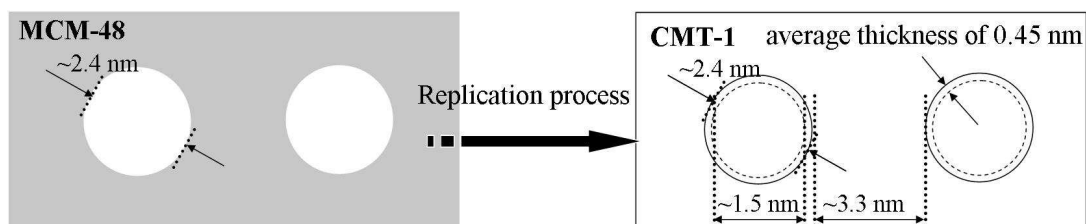


Fig. 4- 6 Schematic pore size and wall thickness of MCM-48 and CMT-1 mesoporous materials.

4.1.2 Effect of deposition temperature on morphology of porous carbons

It is found that deposition temperature is crucial to the pore structure of the carbon replicated by using MCM-48 as hard template. Compared with the CMT-1, which was replicated from MCM-48 under 1073 K (see Section 4.1), a hollowed carbon capsule (HCC) was obtained under as the deposition temperature was raised to 1093 K (Table 3- 2 and Fig. 4- 7 b). The effect of temperature on structure variations of the CMMs can be envisaged as followed: during the CVD process at elevated temperature (> 1073 K), the mesostructure of the MCM-48 silica could be collapsed to form structure with cavities greater than 20 nm in dimension, as shown in Fig. 4- 7a, which reveals the presence of coral-like mesostructured silica-carbon composite obtained in the absence of metal loading. Upon removal of the silica template by HF treatment, it is evident that HCC materials with cavities typically with sizes exceeding 20 nm were observed, as shown in Fig. 4- 7b. Such HCC materials may be advantageous as supports for metal (Pt, Ru) catalysts especially for applications as electrodecatalysts in DMFC.^[Hosomi-2000-269]

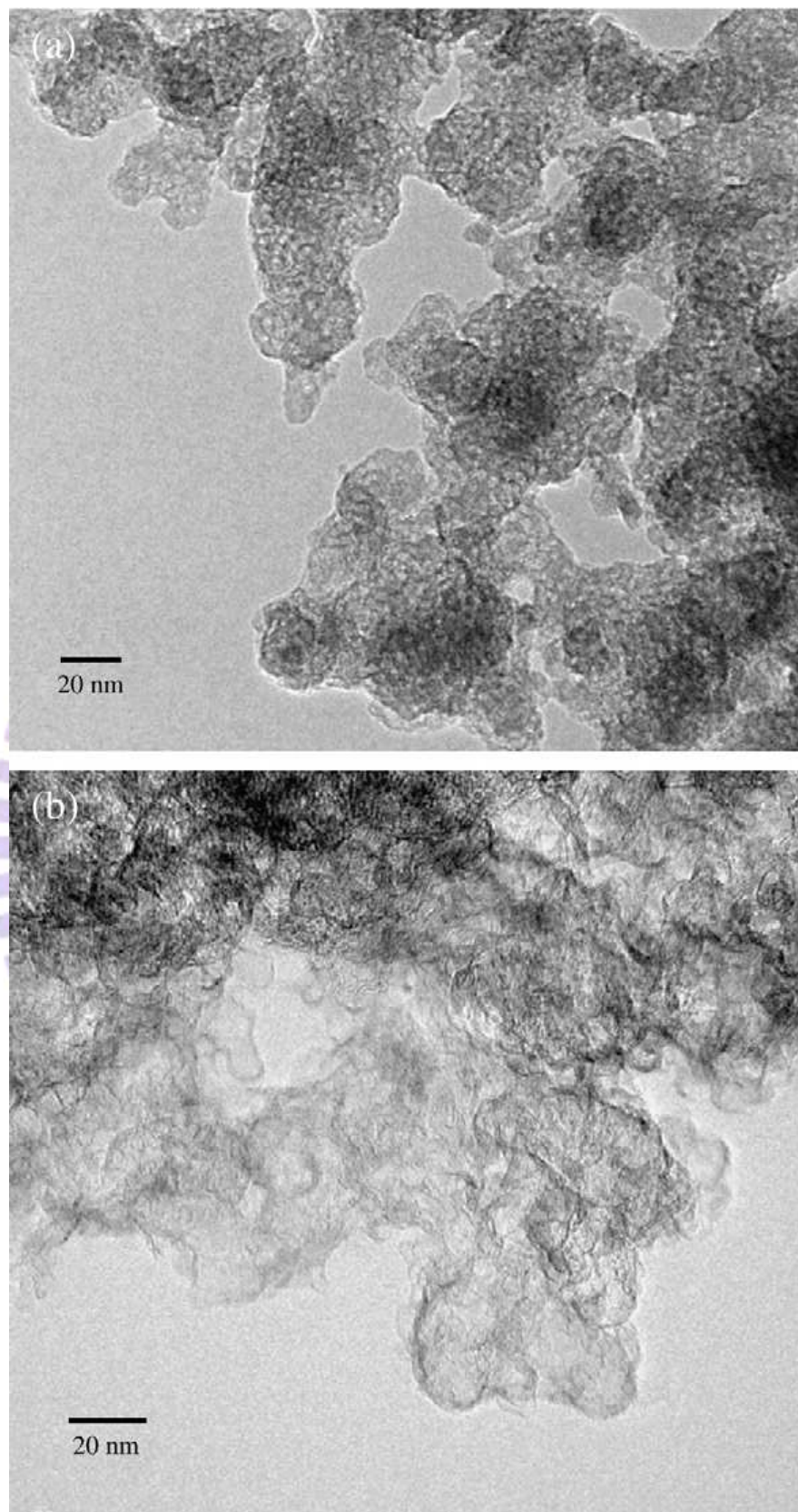


Fig. 4- 7 TEM images of (a) collapsed MCM-48 obtained after thermal CVD process at 1093 K, and (b) HCC mesoporous carbon.

4.1.3 Structure and properties of carbon porous materials

As described in Section 4.1, various CPMs with different pore sizes were prepared by the thermal CVD process using various templates. As a result, a diversified carbon materials with micro- (ZRC), meso- (CMT-1), and macroporosities (PCC) may be fabricated with different preparation conditions using zeolites, MCM-48, SBA-15, pore-expanded MCM-48, and photonic crystal; as summarized in Table 3- 2.

Fig. 4- 8 and Fig. 4- 9 display the TEM images of Zeolite-Y and its corresponding carbon replica (ZRC). The inset of Fig. 4- 8 indicates an ideal zeolite-Y structure with pore size of ca. 0.7 nm (see Section 2.1). That the ZRC material (Fig. 4- 8a) possess the same morphology with Zeolite-Y (Fig. 4- 9) indicates that the CVD process so utilized (see Section 4.1) has an excellent replication capability even for microporous systems. As such, ZRC with pore size as small as 0.7 nm may be readily synthesized; as revealed by the HRTEM image in Fig. 4- 9a. These observation also suggest that the CVD process so adopted represents a facile and speedy (typically within an hour or so) synthesis method for replicating CPMs from various porous silica templates. However, unlike Zeolite-Y, which revealed a well ordered structure (inset, Fig. 4- 9) the structure of the ZRC material so replicated appeared to lack long-range ordering (Fig. 4- 9b). This may be seen by the XRD patterns shown in Fig. 4- 10a and Fig. 4- 10 for the Zeolite-Y and ZRC, respectively. The broad peak observed for the latter indicates that ZRC material indeed lack of structural ordering after the removal of the zeolite template by HF treatment. This finding is therefore coincides with the aforesaid TEM results.

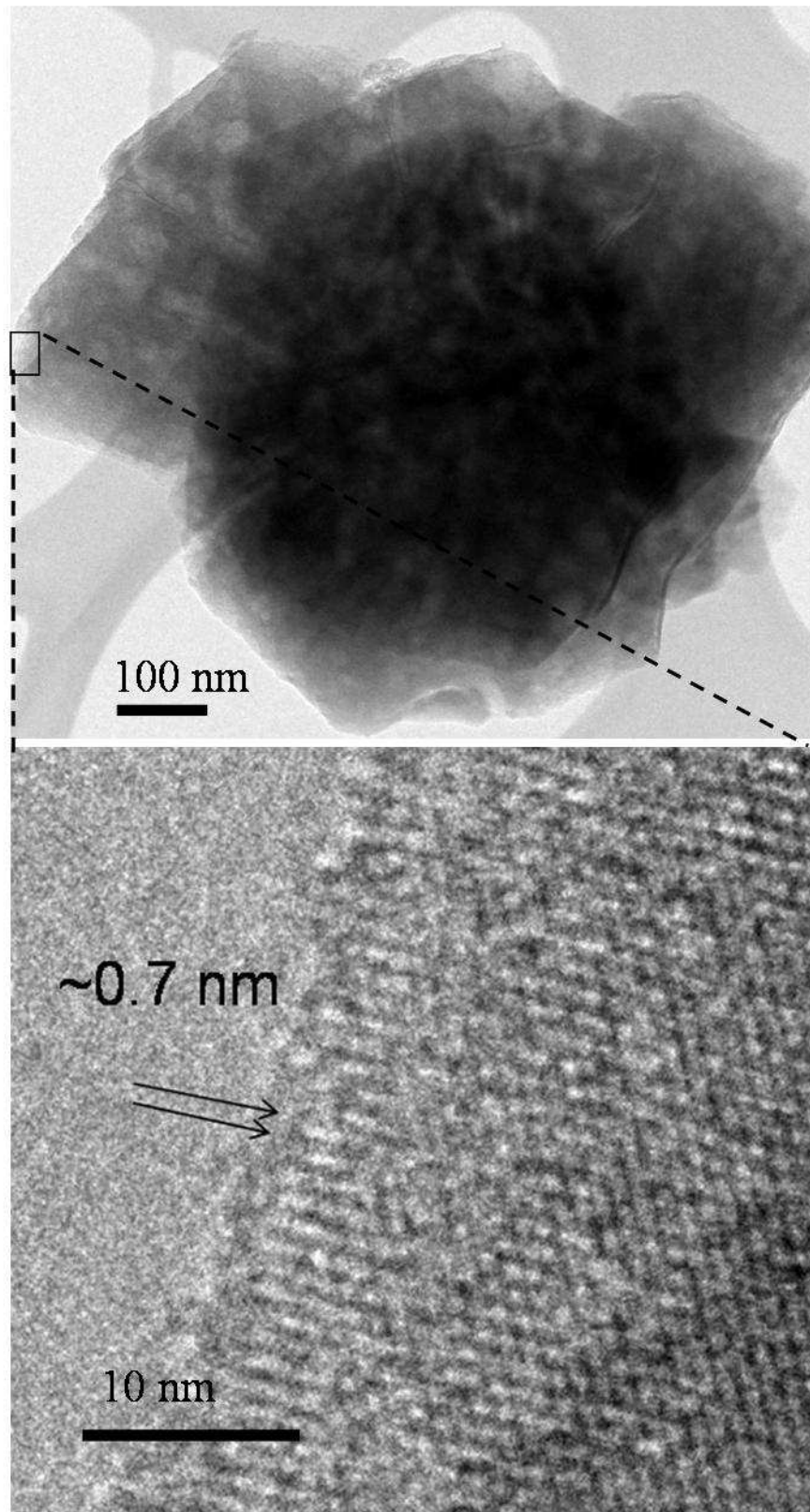


Fig. 4- 8 TEM image with an inset at higher magnification for Zeolite-Y.

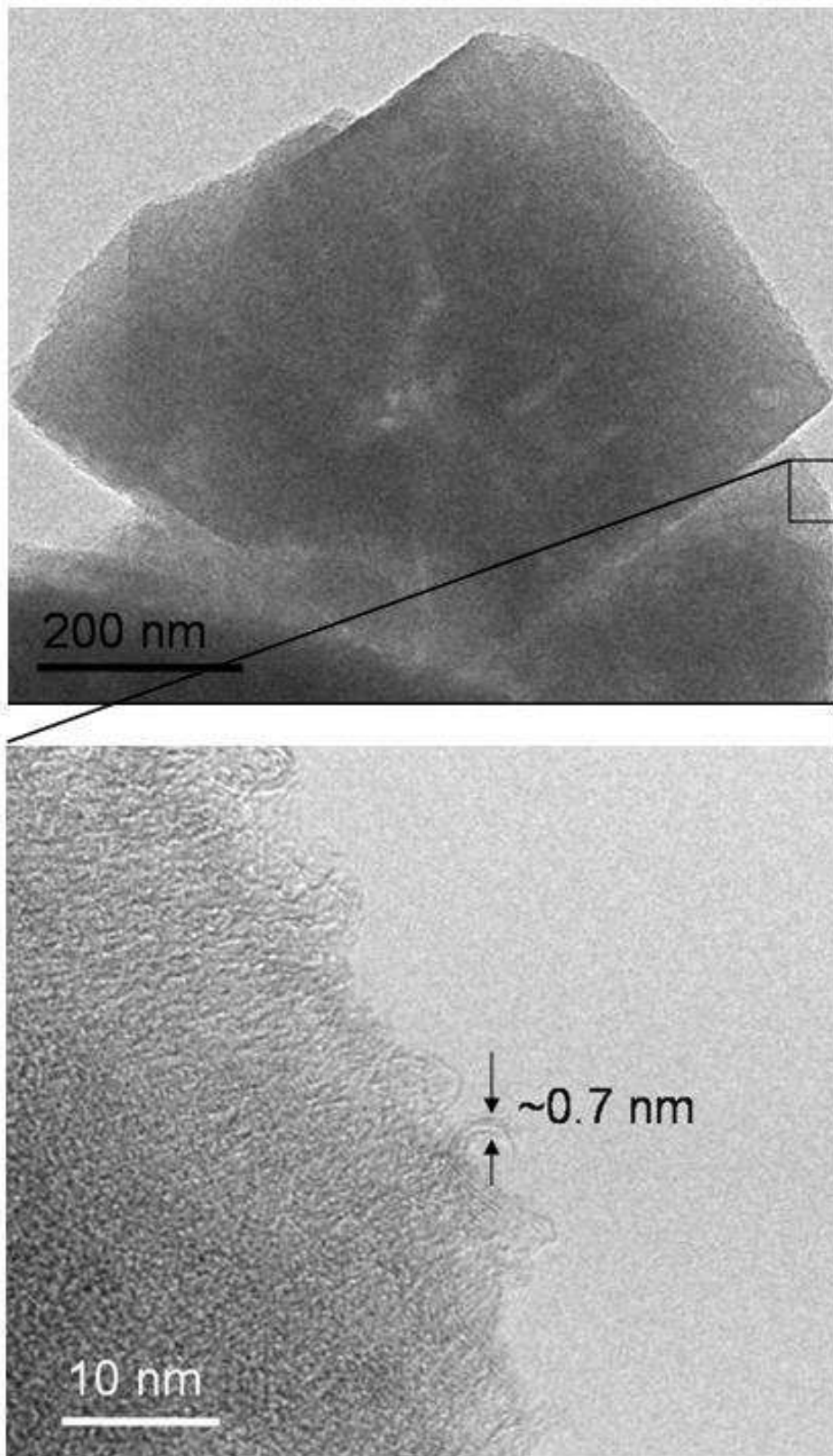


Fig. 4- 9 TEM and the corresponding HRTEM images of the ZRC microporous carbon.

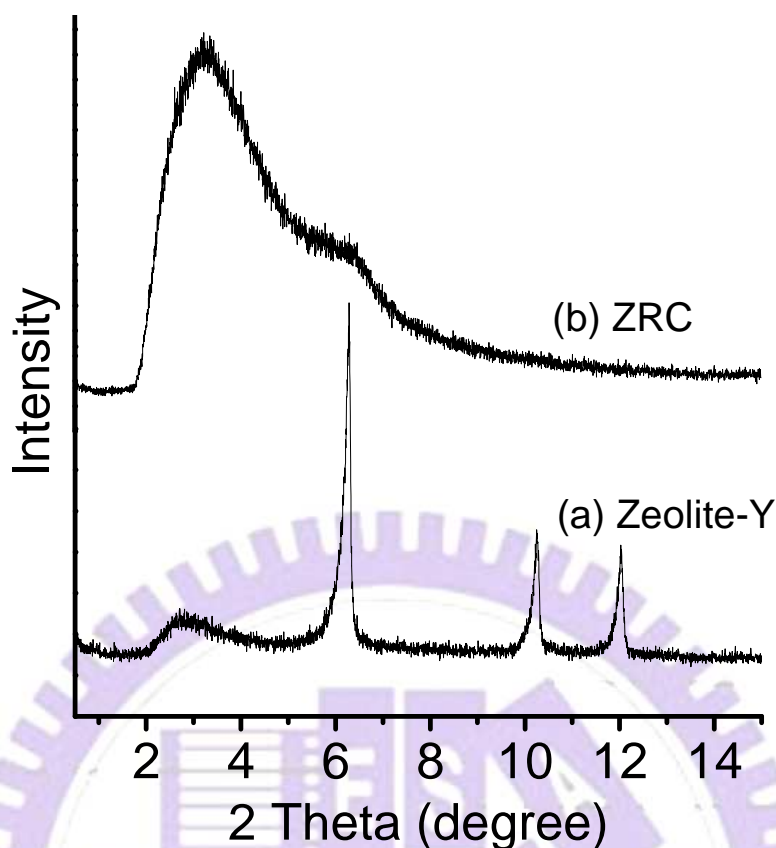


Fig. 4- 10 XRD patterns of (a) Zeolite-Y, and (b) ZRC microporous materials.

The N_2 adsorption/desorption isotherm curves obtained from the ZRC material shows a type-I isotherm (Fig. 4- 11a) at lower relative pressure (P/P_0) indicate a microporous structure; in line with the TEM analysis. Fig. 4- 12 and Fig. 4- 16 shows the pore size distributions of various CPMs; as estimated by the BJH method. As shown in Fig. 4- 12a, an average pore space of ca. 1.3 nm can be inferred between the tubular carbon in ZRC, which is almost coincide with the sodalite building unit of zeolite-Y (ca. 1.2 nm).^[Nagy-1998-192] Thus, it is indicative that ZRC possesses a replicated structure of Zeolite-Y and is constructed by tubular carbon with diameter of ca. 0.7 nm.

On the other hand, CMT-2 replicated from SBA-15 has a comparable structure ordering and tubular structure with that of CMK-5 (Fig. 4- 12) with tubular diameter

of ca. 8 nm and average pore size ca. 3 nm (see Fig. 4- 13 and Fig. 4- 14b). Fig. 4- 14 shows the respective XRD patterns of SBA-15 template and CMT-2. The XRD pattern of CMT-2 in Fig. 4- 14b exhibited well-resolved diffraction peaks, indicating the existence of long-range structure ordering with 2-D hexagonal symmetry similar to that of the tubular CMK-5 carbon material.^[Joo-2001-169] Similar to CMT-1, CMT-2 exhibit a type-IV isotherm with a broad hysteresis loop (Fig. 4- 11c), characteristic of capillary condensation in mesochannels.^[Matos-2003-821-829; Ravikovitch-2002-1550; Sing-1985-603] On the other hand, mesoporous HCC described in Section 4.3 also exhibits a type-IV isotherm (Fig. 4- 11d) but with type-H3 hysteresis loop, suggesting that HCC is a non-rigid aggregates of plate-like particles given rise to slit-shaped pores,^[Lowell-2004-] which is in agreement with the TEM results (Fig. 4- 7b).

For the fabrication of macroporous carbon, photonic crystal with pore size ca. 400 nm (denoted as PC; see Fig. 4- 15a), obtained by using latex sphere templating method,^[Holland-1999-795] was utilized as template. After the replication process, the resultant carbon with pore size of ca. 400 nm (Fig. 4- 15b) was denoted as PCC. It should be noted that both of the N₂ adsorption/desorption curves obtained from the commercial XC-72 (Fig. 4- 11f) and PCC (Fig. 4- 11e) exhibit the same type-III isotherm characteristics, which is typical for non-porous structure.^[Lowell-2004-p12] Unlike the HCC material, the BJH pore size distributions (PSDs) of XC-72 and PCC failed to represent the truth surface condition, as shown in Fig. 4- 15. This can be ascribed due to the extensive inter-particle pore surfaces and pore size exceeding the valid range. As such, the pore surface area of PCC mainly arose from the external surfaces. The distribution of surface area for various microporous, mesoporous, and macroporous CPMs are listed in Table 4- 2.

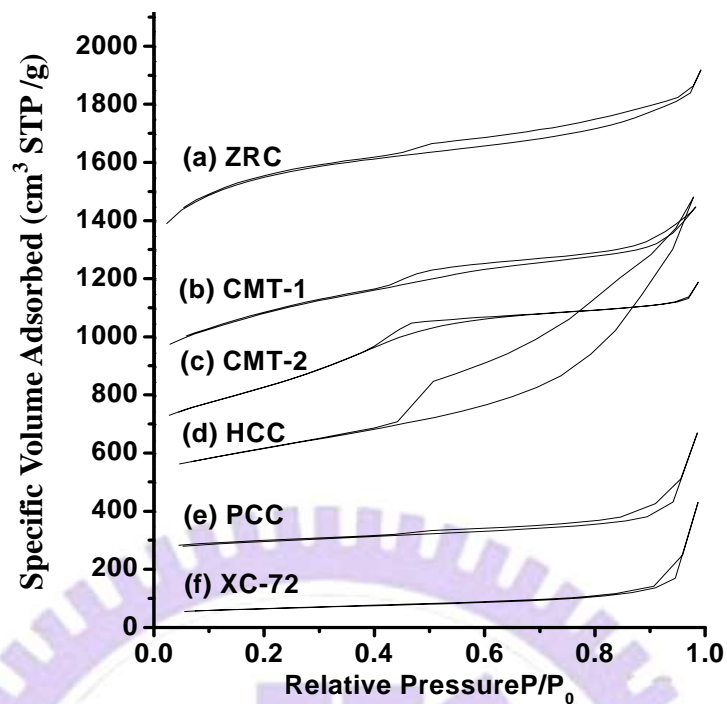


Fig. 4- 11 N₂ adsorption/desorption isotherms (77K) of (a) ZRC, (b) CMT-1, (c) CMT-2, (d) HCC, (e) PCC, and (f) XC-72, where (a) to (e) are shifted vertically by 1000, 800, 600, 400, and 200 cm³ STP/g, respectively.

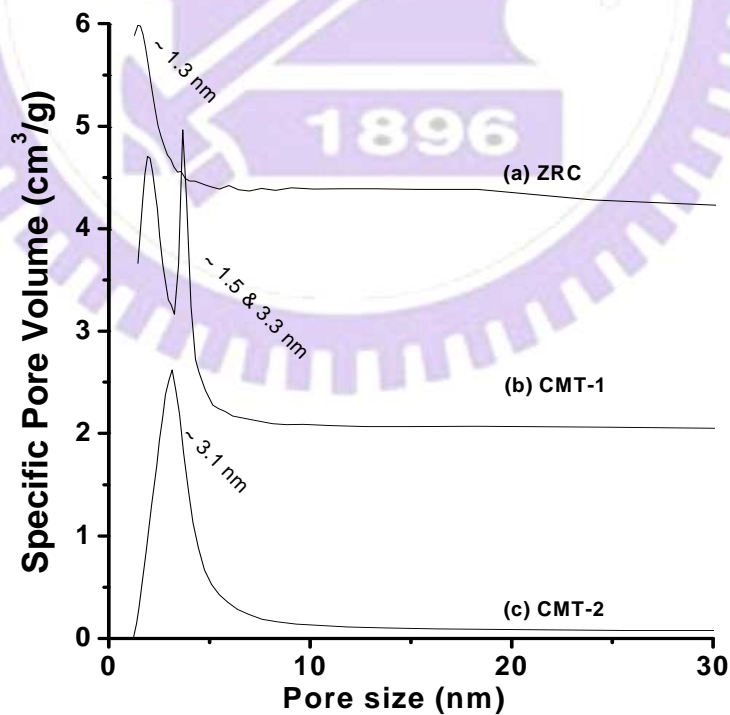


Fig. 4- 12 BJH pore size distributions of (a) ZRC, (b) CMT-1, and (c) CMT-2 porous carbon, where (a) and (b) are shifted vertically by 4 and 2 cm³ STP/g, respectively.

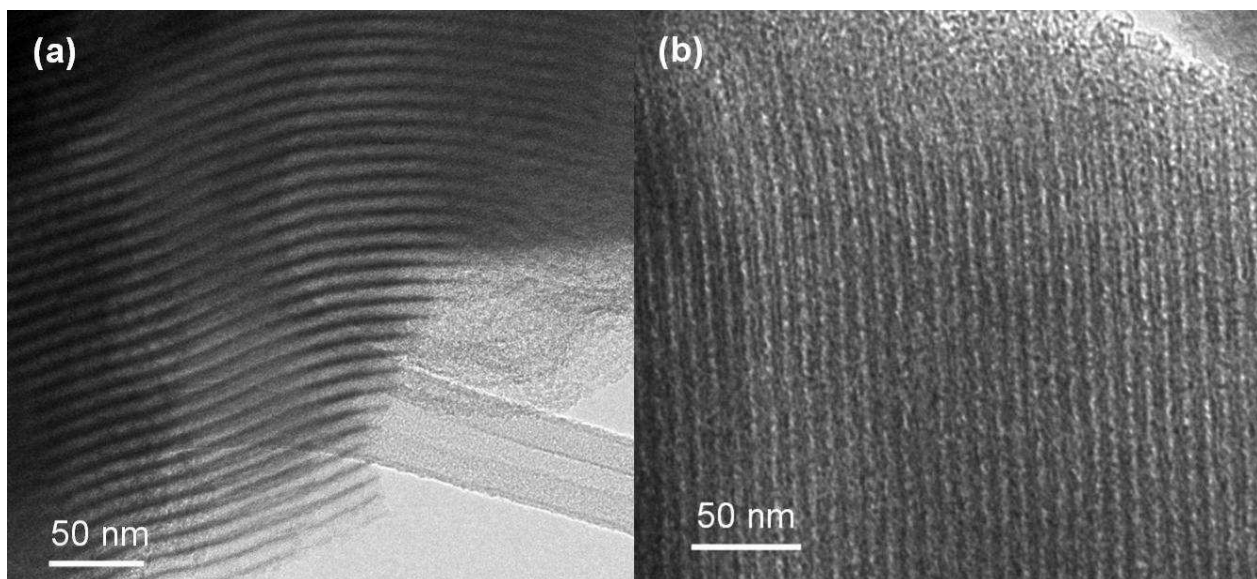


Fig. 4- 13 TEM images of (a) SBA-15, and (b) CMT-2 mesoporous materials.

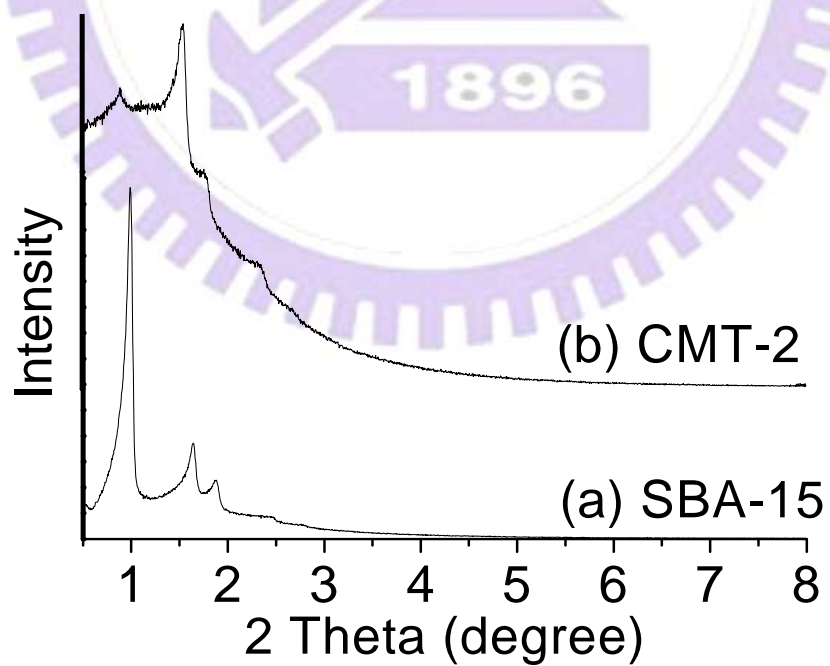


Fig. 4- 14 XRD patterns of (a) SBA-15, and (b) CMT-2 mesoporous materials.

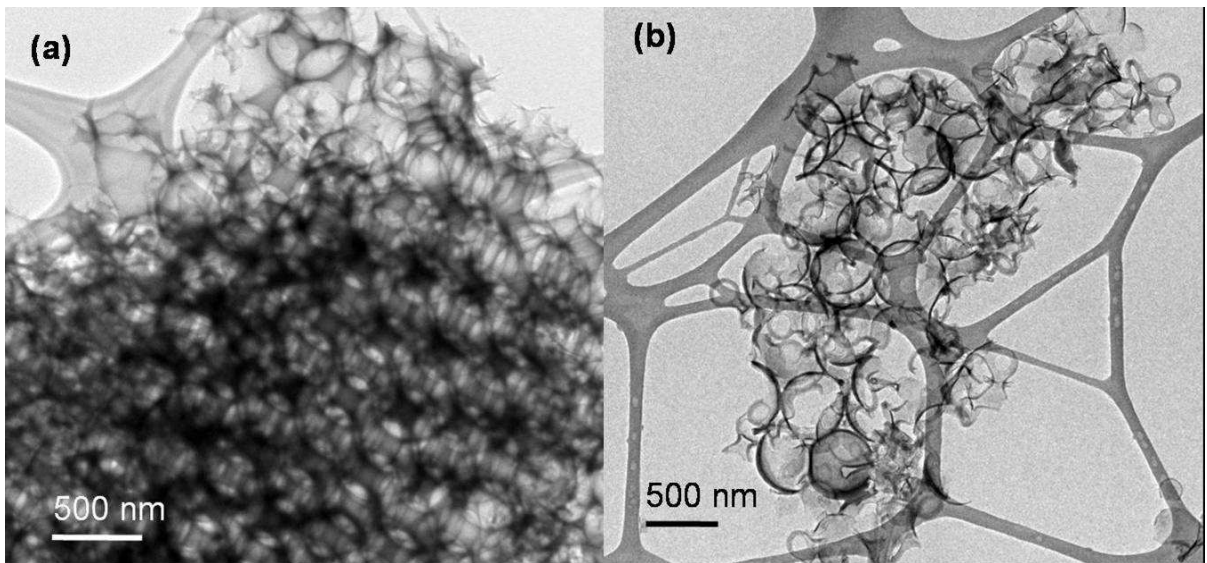


Fig. 4- 15 TEM images of (a) PC, and (b) PCC macroporous materials.

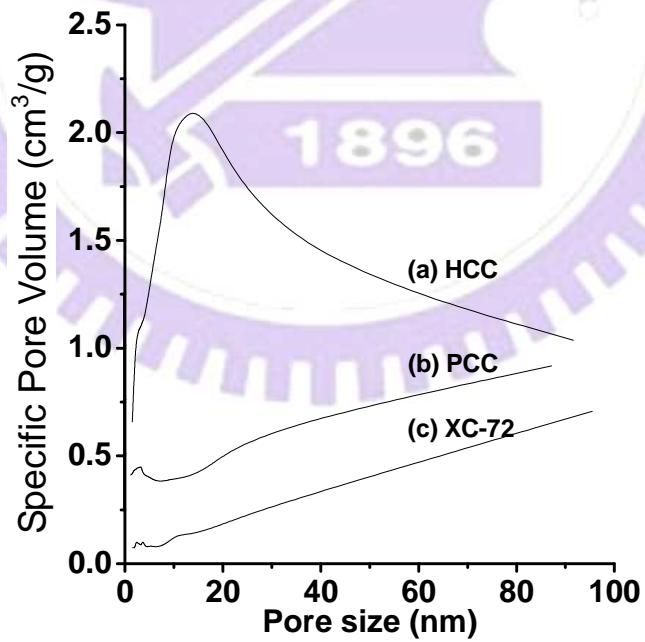


Fig. 4- 16 BJH pore size distributions of (a) XC-72, (b) PCC, and (c) HCC, where (a) and (b) are shifted vertically by 0.5 and 0.25 cm³/g, respectively.

Table 4- 2 List of specific surface area distribution for various CPM samples.

Sample design.	Specific Surface Area (m ² /g) ^a		
	Micropore	Mesopore	Macropore
ZRC	1235	647 ^b	
CMT-1	← 1229 ^c →		n
CMT-2	n	1194	n
HCC	n	← 783 ^d →	
PCC	n	n	337
XC-72	n	n	218

^a n: surface area in these pore ranges are either negligible or uncountable by the BJH method.

^b Value estimated by subtracting the microporous surface area (determined by t-plot analysis) from the total BET surface area.

^c CMT-1 possesses two types of pore systems, which spans over the micro- and mesoporous ranges.

^d Total surface area was adopted; the external surface area should be close to the inner surface area of the HCC, however, their BET surface areas can not be determined in this pore range.

4.2 Electrocatalyst performance of DMFC anode with Pt-Fe dispersed capsule-like porous carbon

As described in Sections 3.5(a), the HCC supported Pt-Fe catalyst was fabricated by first incorporating Pt-Fe onto the mesoporous MCM-48 silica, proceeded by carbon coating using the CVD process at 1093 K. The TEM images of the resultant product before and after removal of the silica template are shown in Fig. 4- 17a and Fig. 4- 17b, respectively. It can be clearly seen that the synthesis of the HCC supported Pt-Fe catalyst is accompanied by the growth of CNTs owing to the presence of Fe catalyst during the carbonization process. Moreover, the TEM image prior to the removal of silica template (Fig. 4- 17a) clearly show that the Pt-Fe particles were well isolated between the interfaces of the silica template and the carbon film, leading to a uniform dispersion of Pt-Fe alloy particles in the internal surfaces of the HCC after the removal of the silica template (Fig. 4- 17b). Further examinations of the Pt-Fe/HCC supported catalyst by HRTEM (Fig. 4- 18a and Fig. 4- 18b) revealing that well dispersed Pt-Fe alloy nanoparticles with size ranging between 2 to 10 nm were embedded in the walls of the HCC material, which exhibit a highly graphitic structure.

As described in Section 4.1, the CMT-1 material^[Guo-1995-10694] was further obtained by replication method under the similar CVD process but at a slightly lower temperature (1073 K) than that of the aforementioned Pt-Fe/HCC supported catalyst. It is anticipated that if the experiment were carried out with pre-loaded Pt-Fe precursors on MCM-48, followed by CVD process at 1073 K, a Pt-Fe based catalyst supported on CMT-1 would have obtained. However, to our surprise, the resultant

material did not possess the anticipated CMT-1 structure, rather, it exhibited CNTs co-existing with solid carbon capsule (SCC) material embedded with Pt-Fe nanoparticles, as shown in the TEM images (Fig. 4- 19a) and corresponding HRTEM image (Fig. 4- 19b). However, unlike Pt-Fe/HCC, the size of the Pt-Fe particles in Pt-Fe/SCC were found to be more uniform, typically in the range of 2–5 nm. In this context, the reason that a ordered mesostructured cannot be form may be due to the high Pt-Fe loading, which may led to distortion of the carbon framework structure, as proposed in our earlier study on fabrication of PtRu supported on carbon mesoporous materials (CMMs)^[Liu-2006-3435]

The aforementioned results are consistent with analyses by XRD. Fig. 4- 20 displays the small-angle diffraction patterns of the mesoporous MCM-48 silica template (Fig. 4- 20a), the CMT-1 carbon mesoporous material directly replicated from MCM-48 by CVD process at 1073 K in the absence of metal catalyst (Fig. 4- 20b), the Pt- Fe/SCC supported catalyst fabricated by pre-doping Pt-Fe on MCM-48 followed by CVD process at 1073 K (Fig. 4- 20c), the parent MCM-48 silica after thermal treatment at 1093 K (Fig. 4- 20d), and the Pt-Fe/HCC supported catalyst fabricated at 1093 K (Fig. 4- 20e). It is clear that by performing the CVD process at a lower temperature (1073 K) in the presence of Pt-Fe catalyst, the resultant Pt-Fe/SCC supported material (Fig. 4- 20c) did not possess the anticipated CMT-1 mesostructure (Fig. 4- 20b). In addition, for the Pt-Fe/HCC material prepared at 1093 K (Fig. 4- 20e), partial collapse of the MCM-48 structure were observed, which is good agreement with the TEM results obtained for HCC.

Fig. 4- 21 shows the cyclic voltammograms obtained from Pt-Fe/HCC (with 30 wt.% Pt and 7.5 wt.% Fe), Pt-Fe/SCC (with 30 wt.% Pt and 7.5 wt.% Fe), and a commercial Johnson–Matthey (Pt–Ru/AC; 30 wt.% Pt, 15 wt.% Ru on XC-72

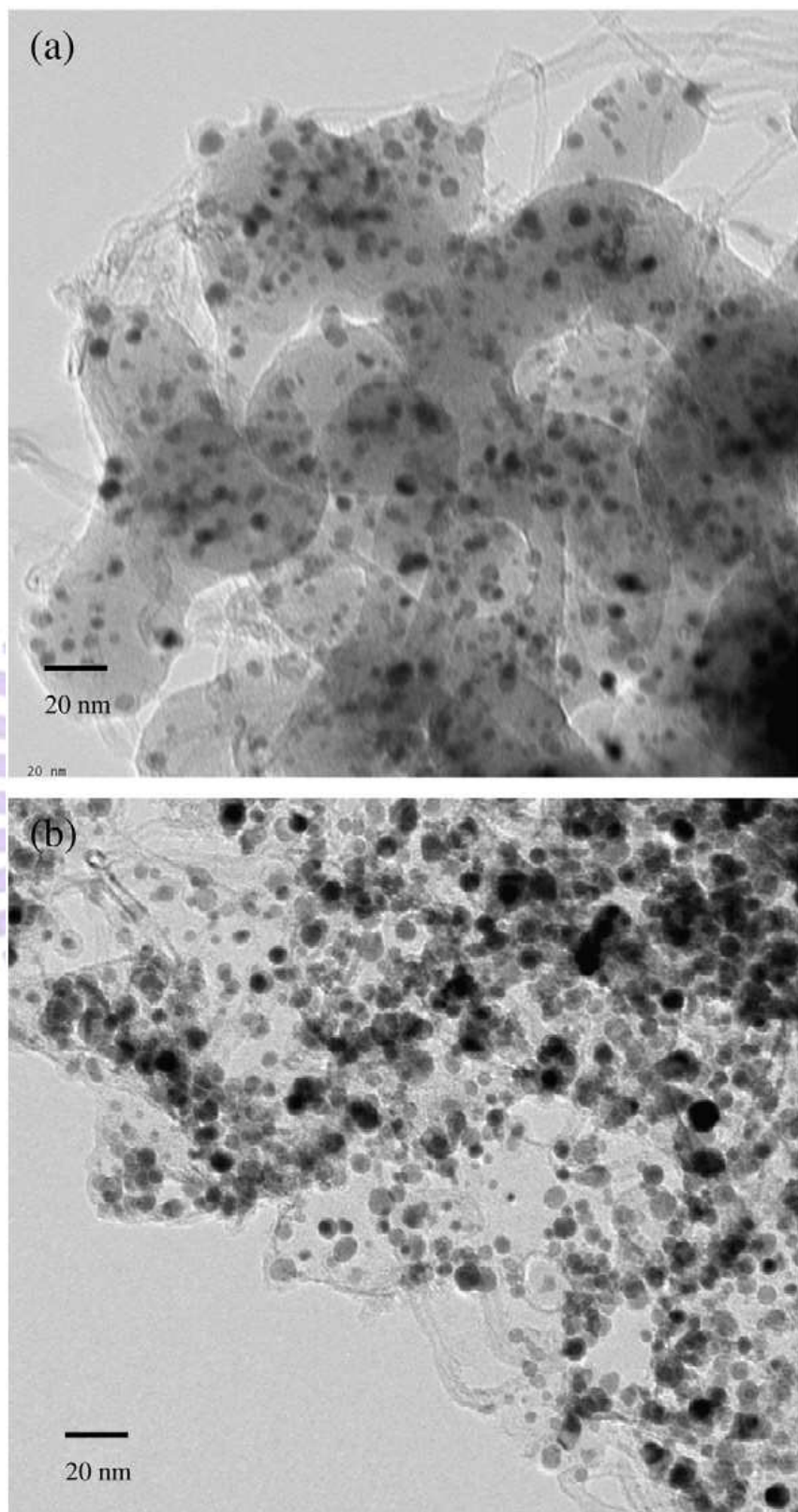


Fig. 4- 17 TEM images of Sample Pt-Fe/HCC (a) with and (b) without silica template.

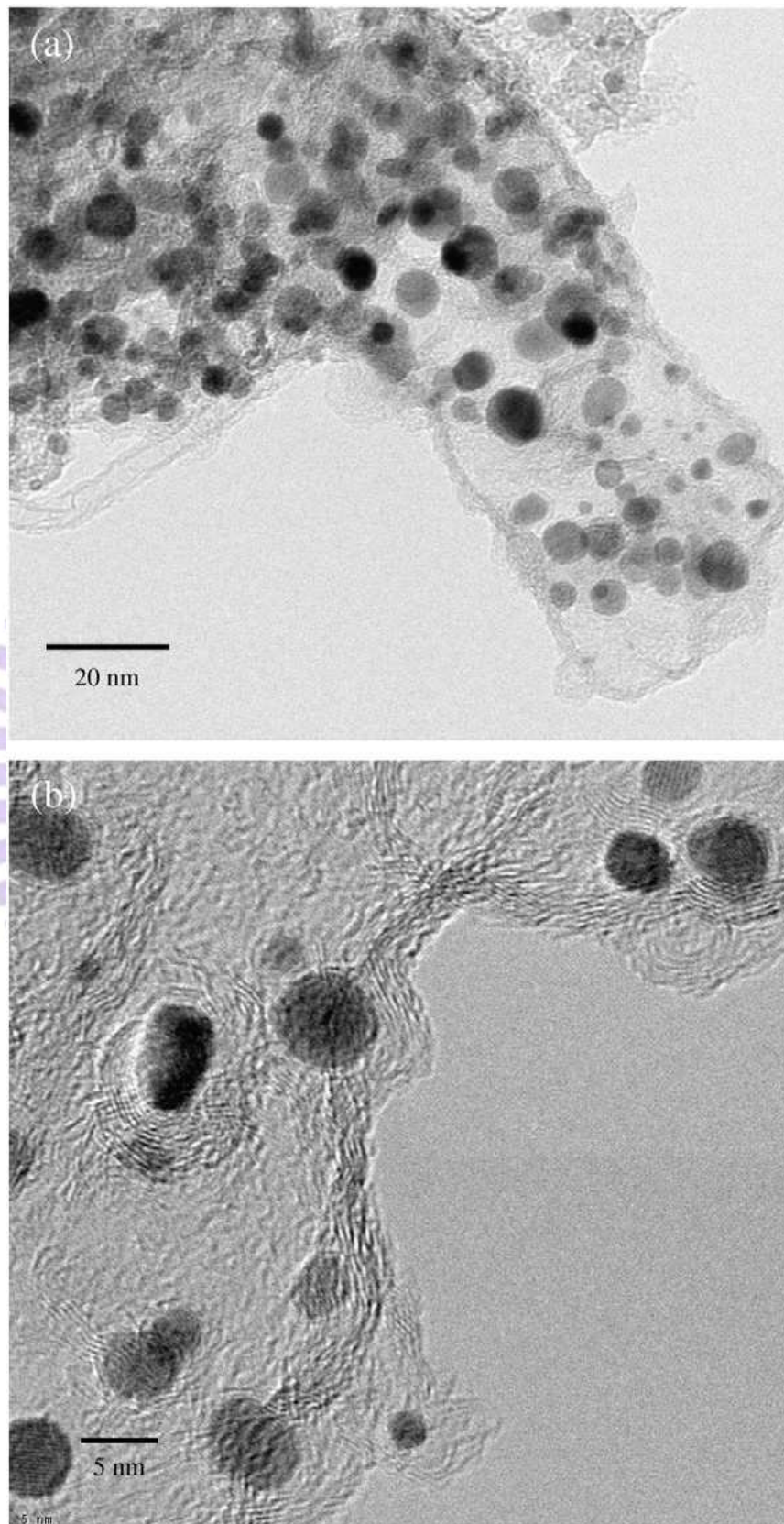


Fig. 4- 18 (a) TEM and (b) HRTEM images of Sample Pt-Fe/HCC.

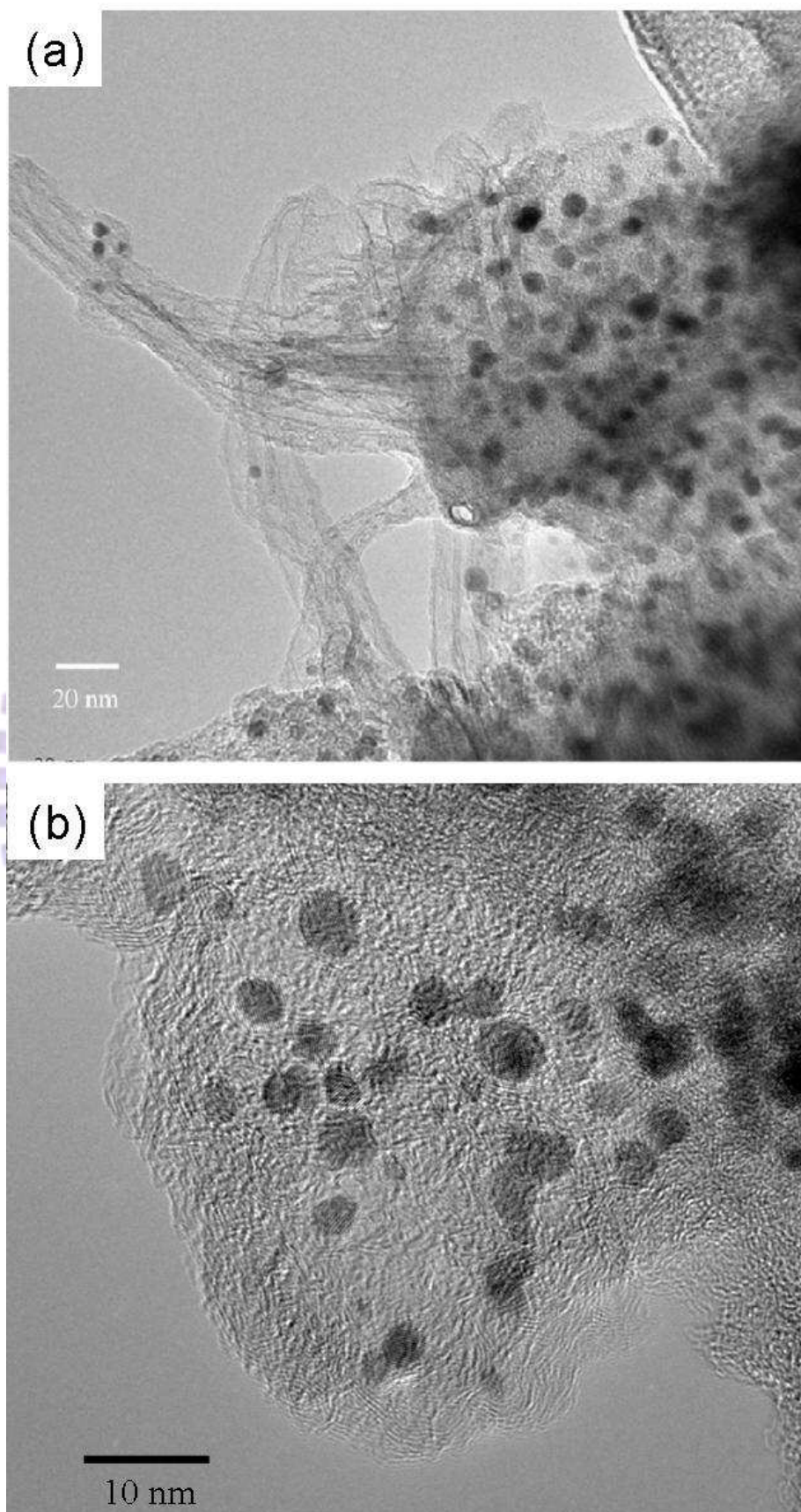


Fig. 4- 19 (a) TEM and (b) HRTEM images of Sample Pt-Fe/SCC.

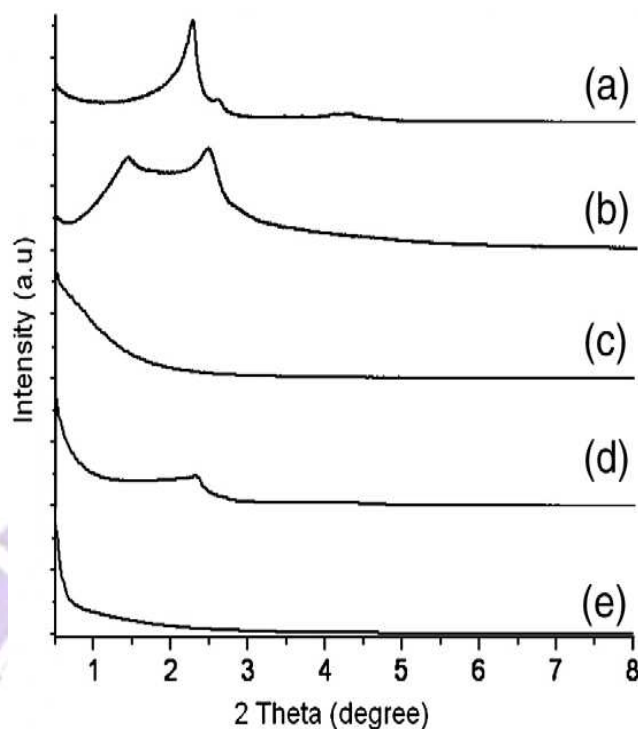


Fig. 4- 20 Small-angle XRD patterns of Samples (a) MCM-48 template treated at 1073 K, (b) CMT-1, (c) Pt-Fe/SCC, (d) MCM-48 treated at 1093 K, and (e) Pt-Fe/HCC.

activated carbon) catalysts. Although the averaged particle size for the Pt-Fe/HCC electrocatalyst is larger than the JM (Pt-Ru/AC), nonetheless, the mass activity for the former (0.0028 A) is slightly higher than that of the latter (0.0026 A). This may be ascribed to: (i) the improved electrical conductivity of the co-existing CNTs and the excellent graphitic structure of the HCC, (ii) the well-dispersed Pt-Fe catalyst, (iii) the introduction of secondary Fe metal that tends to enhance the utilization of Pt,^[Ryoo-2001-677] and (iv) superior mass transport properties of the HCC support with typical cavity size exceeding 20 nm. On the other hand, that the Pt-Fe/SCC catalyst exhibited the lowest mass activity may be attributed to the structure of the SCC support, leading to an overall decrease in the surface area of the Pt-Fe catalyst.

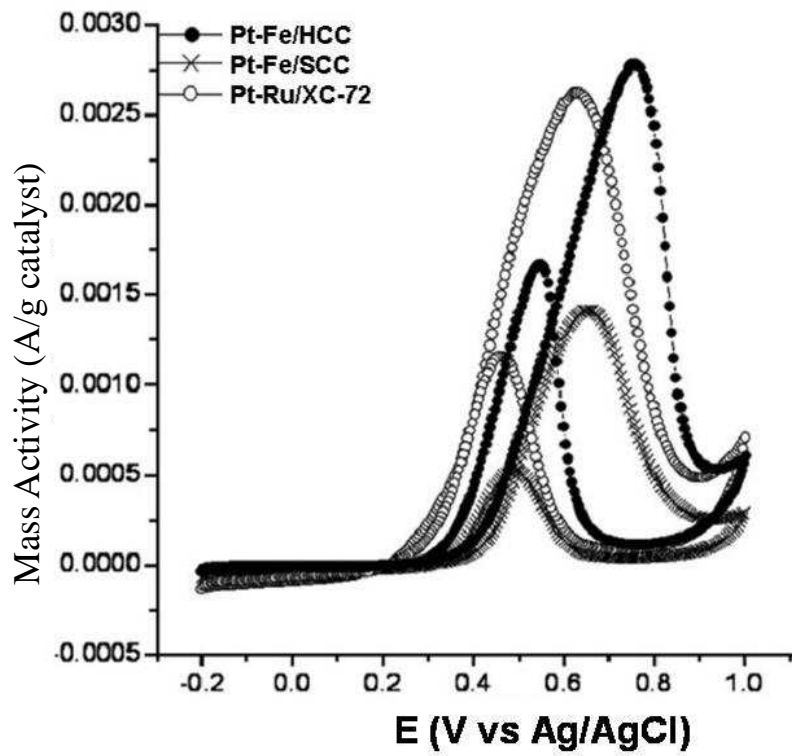
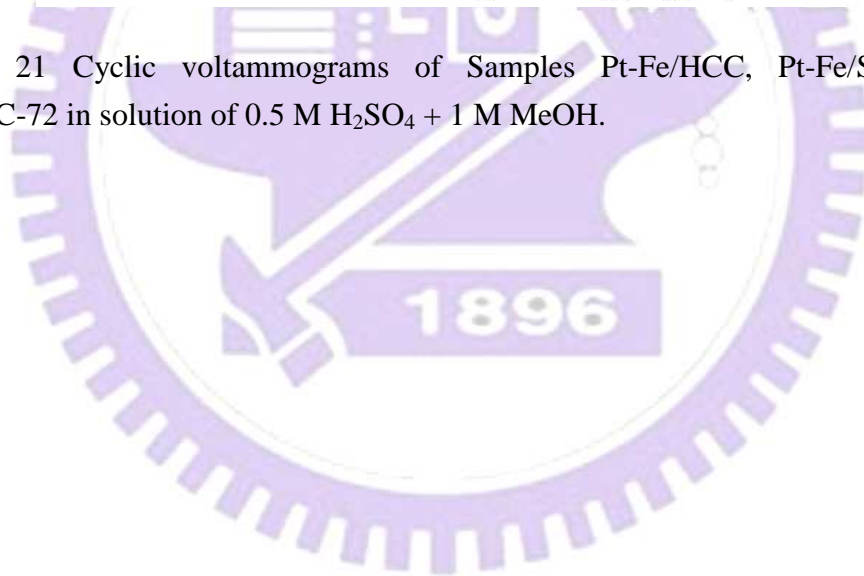


Fig. 4- 21 Cyclic voltammograms of Samples Pt-Fe/HCC, Pt-Fe/SCC, and Pt-Ru/XC-72 in solution of 0.5 M H_2SO_4 + 1 M MeOH.



4.3 Effect of carbon pore size on Pt dispersion in DMFC anodes and their electrocatalytic performance

The aforesaid CPMs with varied pore characteristics (Table 4- 2) were further applied as supports for Pt, the physical and electrochemical properties of the Pt/CPM supported catalyst were examined and compared with that of a commercial catalyst, namely Pt/XC-72, as depicted in Table 4- 3. A more detailed discussion on the process involved in incorporating the Pt catalyst (loading ca. 10 wt%) on various carbon supports and their subsequent reduction treatments can be found in Section 3.6. Note that since the ratio of the G- and D-band intensities (I_G/I_D) obtained from the Raman spectrum is commonly used to represent the relative concentration of sp^2 and sp^3 structures and hence may be served as an index for graphitization degree of the sample. Accordingly, the fact that similar I_G/I_D ratios were observed for the CPMs and XC-72 indicates that these types of carbon materials have roughly the same degree of graphitization and hence electronic properties (See Table 4- 3).

The TEM images of various Pt/CPMs supported catalysts are depicted in Fig. 4- 22. Among them, the Pt/ZRC sample appears to have the highest Pt dispersion, as shown in Fig. 4- 23a. The above observation may be attributed to the fact that, unlike other CPMs, the ZRC carbon support possesses only microporosities. As such, it is hypothesized that the porosity of the carbon support may play a role while dispersing the Pt metal catalyst, particularly for Pt nanoparticles less than 1 nm in size. For comparison, the percentages of the small Pt particle (size < 1 nm) presented in various CPMs are depicted in Fig. 4- 23b, which follow the order: Pt/ZRC (38%) > Pt/CMT-2 (30%) ~ Pt/CMT-1 (27%) > Pt/HCC (15%) > Pt/PCC (8%) ~ Pt/XC-72 (6%).

Table 4- 3 Sample designations and physicochemical properties of Samples Pt/CPM and Pt/XC-72.

Sample design.	Pt ^a (wt %)	C ^b (S/cm)	I _G /I _D ^c	I _f ^d (mA)	I _r ^d (mA)	I _f /I _r ^d	D ^e (%)	D _p ^f (nm)	S _M ^g (m ² gPt ⁻¹)	CO-t ^h (%)
Pt/ZRC	12.5	1.61	0.85	122	25	4.88	45.4	2.49	112.1	48.83
Pt/CMT1	12.8	1.14	0.68	136	60	2.26	22.4	5.05	55.4	27.93
Pt/CMT2	11.6	1.1	0.77	140	97	1.44	19.8	5.71	48.9	18.14
Pt/HCC	9.3	2.07	0.74	282	194	1.45	20.5	5.51	50.7	10.60
Pt/PCC	9.5	2.38	0.73	655	628	1.04	56.8	1.99	140.42	7.78
Pt/XC72	12.5	1.79	0.70	353	349	1.01	32.6	3.47	80.6	1.74

^a Pt loading measured by TGA analysis.

^b Electrical conductivity.

^c Relative intensities observed for the G- and D-bands obtained from Raman spectrum; the Pt/CPMs do always enkindled under laser irradiation during Raman examination.

^d Ratio of maximum current densities obtained from the forward (I_f) and reversed scan (I_r) during C-V analysis.

^e Pt dispersion measured by H₂ chemisorption (at 305 K).

^f Pt particle size derived from H₂ chemisorption measurements.

^g Metallic surface area of Pt particles derived from H₂ chemisorption.

^h CO-tolerance estimated by competitive adsorption of H₂ after preadsorbing ca. 500 ppm of CO.

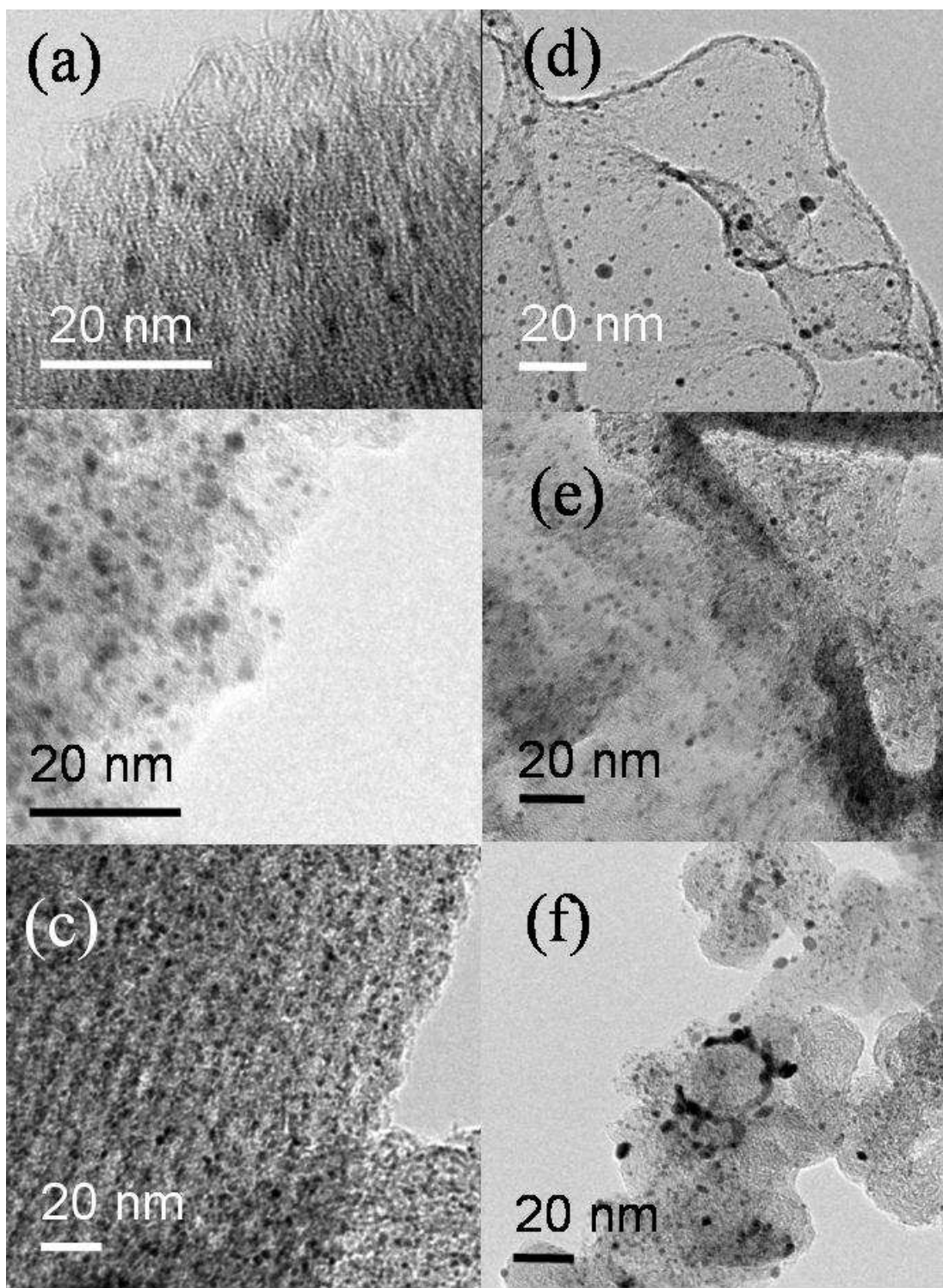


Fig. 4- 22 TEM images of Samples (a) Pt/ZRC, (b) Pt/CMT-1, (c) Pt/CMT-2, (d) Pt/HCC, (e) Pt/PCC, and (f) Pt/XC-72, respectively.

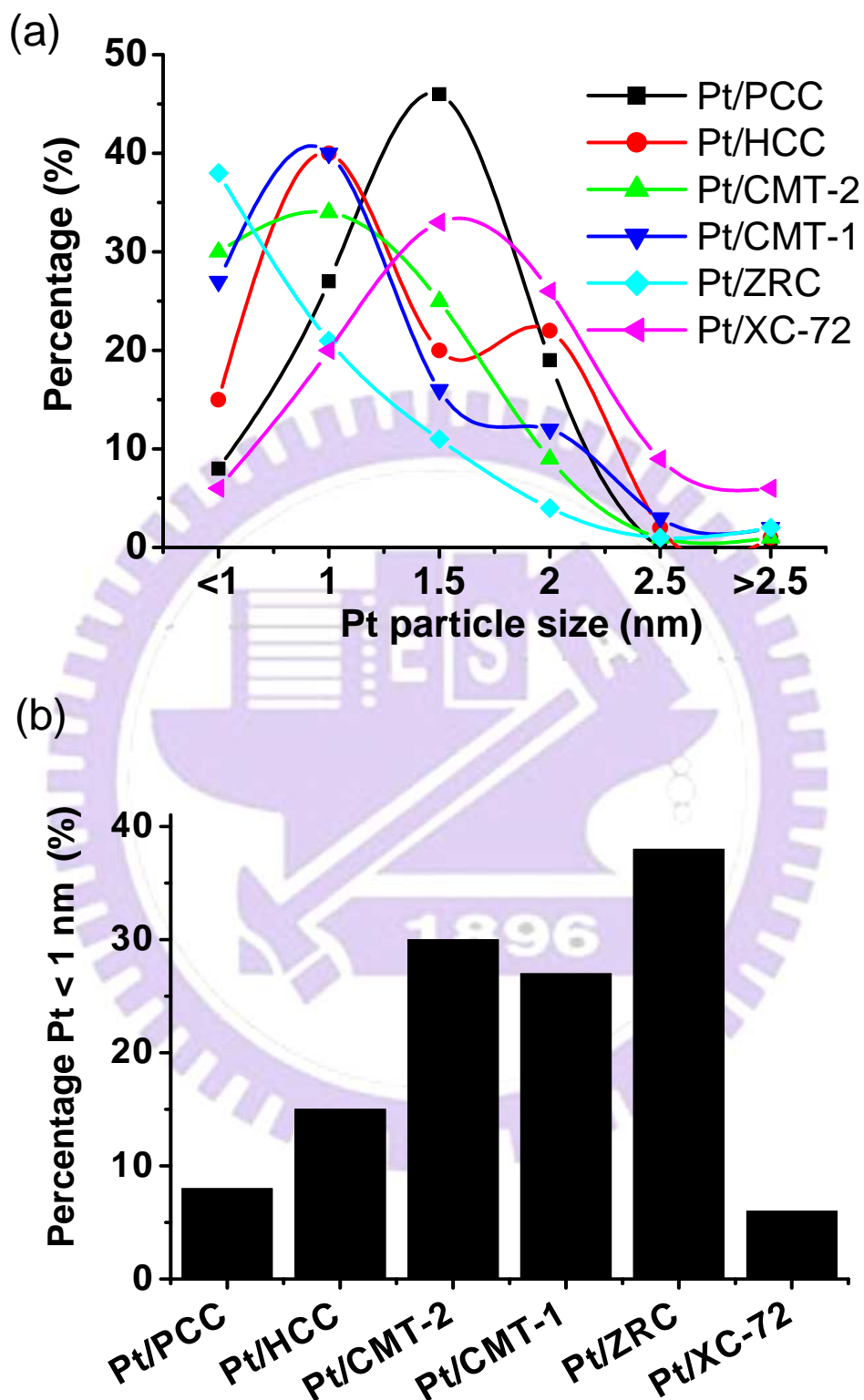


Fig. 4- 23 (a) Curve of Pt particle size distribution in various Pt/CPM Samples, and (b) the corresponding histogram of the distributions of Pt particle size < 1 nm.

Furthermore, the electrocatalytic performances of Pt/XC-72 and various Pt/CPMs supported catalysts during methanol oxidation reaction (MOR) were examined by cyclic voltammograms (C-V) measurements under 1.0 M CH₃OH and 0.5 M H₂SO₄ at room temperature; the results are depicted in Fig. 4- 24. Since the mass activity of the anodic peak occurred at ca. 0.6 V during the forward scan (I_f) is associated with the catalytic activity during methanol oxidation, whereas the reversed anodic peak (at ca. 0.4–0.5 V) mass activity (I_r) is mainly related to the extent of deactivation by the deposition of carbonaceous species on the surfaces of the catalyst.^[Lei-2009-5985; Liu-2008-1622] Thus, for purpose of comparison, only selected regions under operating potential region of 0.1-0.65 V (for forward scans) and 0.7-0.45 V (for reverse scans) are shown in Fig. 4- 25a and Fig. 4- 25b, respectively. For convenience, electrocatalytic properties of various Pt/CPMs, including their electronic conductivities (C), current densities (I_f & I_r), I_f/I_r and I_G/I_D ratios, tolerances for CO poisoning (CO-t), and the dispersions (D), particle sizes (D_p), and metallic surface areas (S_M) of the Pt metal particles are depicted in Table 4- 3 together with the Pt/XC-72 commercial catalyst.

Since Pt/ZRC is more abundant with small Pt nanoparticles (size < 1 nm; see Fig. 4- 23b), the sample is anticipated to have a superior electrocatalytic performance as anodic catalyst than the other Pt/CPMs. However, as shown in Fig. 4- 24 and Fig. 4- 25a, Pt/ZRC appeared to have a lower forward peak current (I_f) than the others (Table 4- 3). It is noted that the degree of graphitization (i.e., the I_G/I_D value) and conductivities (C) appeared to be irrelevant to the value of I_f , rather, the latter tends to increase with increasing pore size of the carbon supports (Table 4- 2 and Table 4- 3). For example, an I_f value of ca. 160 mA/mg Pt was observed for the Pt/ZRC, Pt/CMT-1, and Pt/CMT-2 catalysts; which are only one-half of what observed for the

Pt/XC-72 catalyst (I_f ca. 353 mA/mg Pt). The above result may be attributed to the possibility that the Pt nanoparticles immersed in the porous CPMs may not be fully exposed to the methanol solution during C-V measurements. In other words, diffusion of methanol may be partially hindered in the micropores/mesopores of the CPMs during the C-V tests, implying that internal surface areas within microporous/mesoporous CPM supports have nearly no effect on the overall electrocatalytic performances of the Pt/CPM electrocatalysts.

On the other hand, the Pt/PCC catalyst appeared to have the largest forward anodic peak current (I_f) among various Pt/CPMs, even though its carbon support (PCC) possesses only ca. one-third of the surface area compared to CMT-1 and CMT-2 (Table 4- 2). The aforementioned results may be associated with the fact that the surface area observed was predominantly from the external surfaces of the PCC. Similar observation was observed for the Pt/HCC catalyst. The same argument prevails for the observed increase in I_f value by ca. 1.8 folds in the Pt/PCC than the Pt/XC-72 catalysts.

Considering the effect of pore size on catalytic performances of the Pt/CPM catalysts, the relative ratio of I_f/I_r may be served as an index to evaluate the tolerance for CO poisoning (CO-t), as listed in Table 4- 3. It is intriguing that even though the Pt/ZRC catalyst exhibited a lower forward peak current (I_f) than the other Pt/CPMs, a superior value of I_f/I_r ratio was observed compared to Pt/XC-72 and other Pt/CPMs. Moreover, the I_f/I_r ratio observed for Pt/CPMs (Table 4- 3) is found to increase with decreasing pore size of CPMs (Table 4- 2) and with increasing percentage of small Pt nanoparticle with size less than 1 nm (Fig. 4- 23b).

To further justify the above findings, additional pulsed H_2 chemisorption studies

were conducted in the presence of the pre-adsorbed CO (ca. 500 ppm), which represents a competitive adsorption of CO with H₂, as shown in Fig. 4- 26. Accordingly, the corresponding dispersions (D), particle sizes (D_p), and metallic surface areas (S_M) of the Pt metal are depicted in Table 4- 3. For examples, a S_M value of ca. 112 m²/g Pt was observed for the Pt/ZRC sample, among them, ca. 47% of the metal surfaces remain active after the catalyst was intentionally poisoned by pre-adsorbing 500 ppm of CO. Whereas in the case of Pt/XC-72, nearly all metal Pt surfaces were inactivated by pre-adsorbed CO. The same trend for activity may be inferred by comparing the I_f/I_r and CO-t values of Pt/CPMs vs. Pt/XC-72 supported catalysts listed in Table 4- 3.

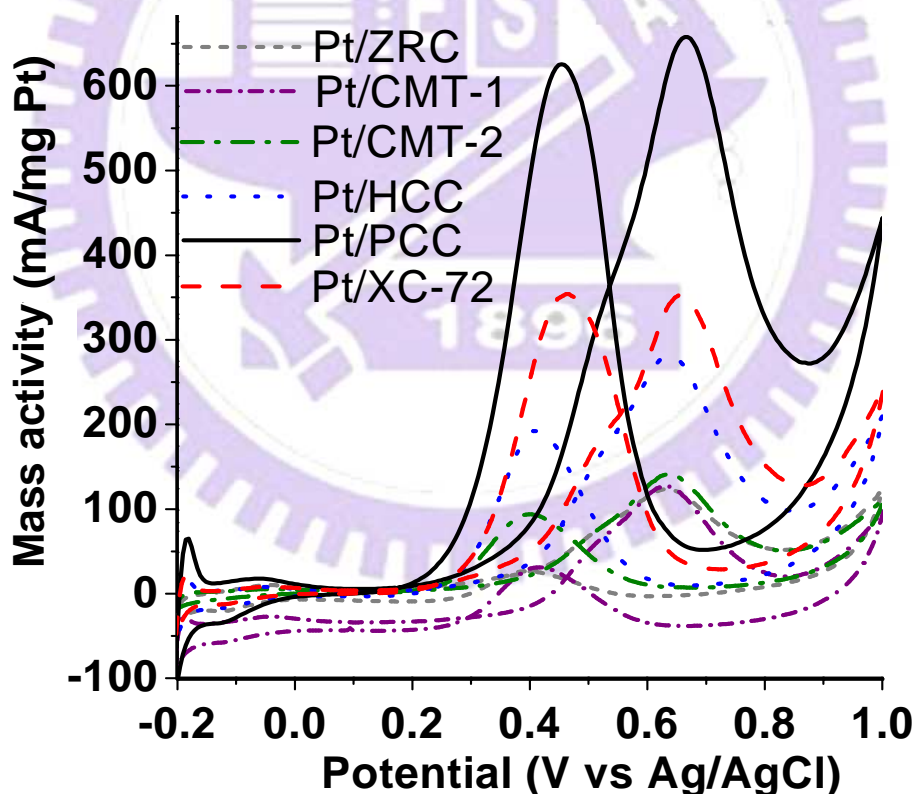


Fig. 4- 24 Cyclic voltammograms of various Samples of Pt/CPMs and Pt/XC-72 electrocatalysts in solution of 0.5 M H₂SO₄ + 1 M MeOH.

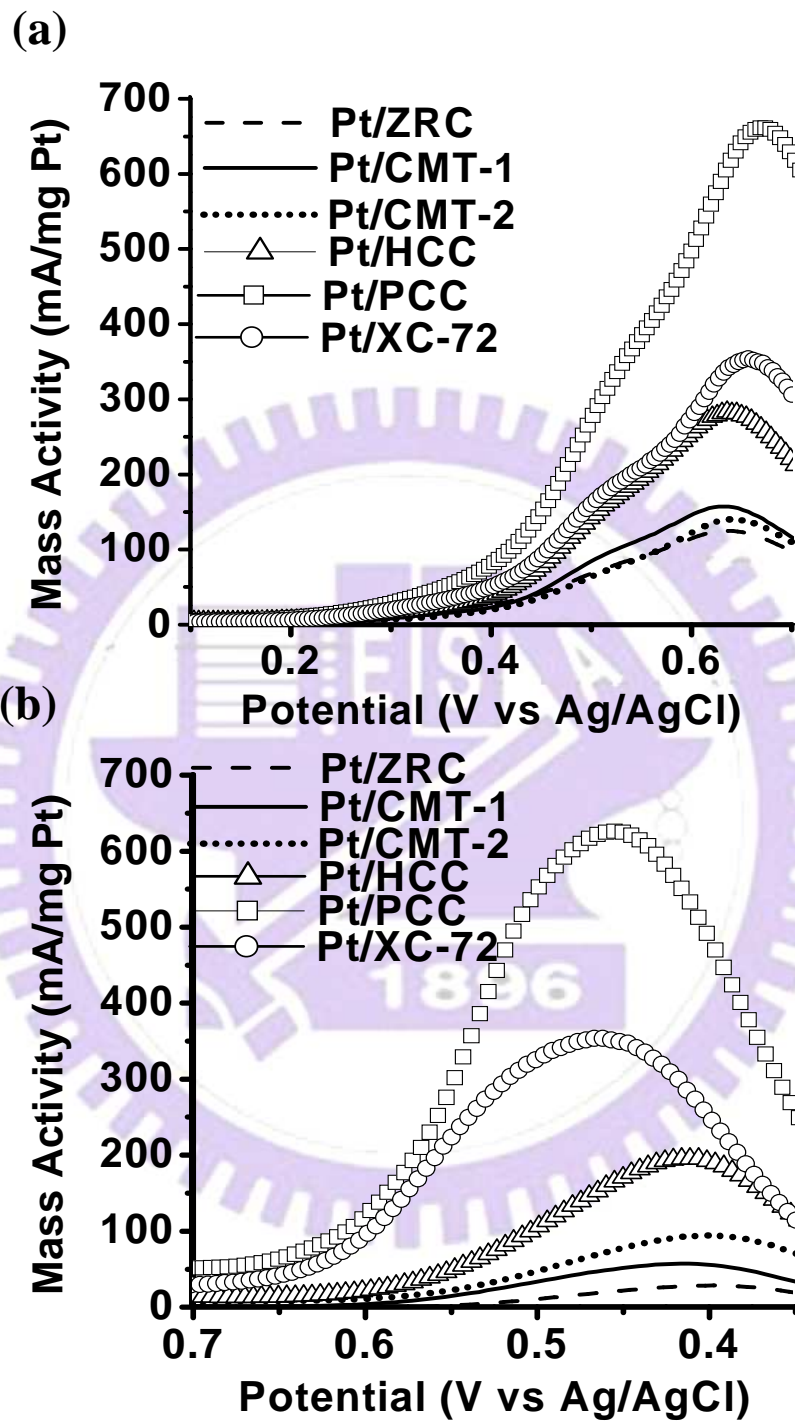


Fig. 4- 25 (a) forward, and (b) reverse C-Vs scans of various Samples of Pt/CPM and Pt/XC-72.

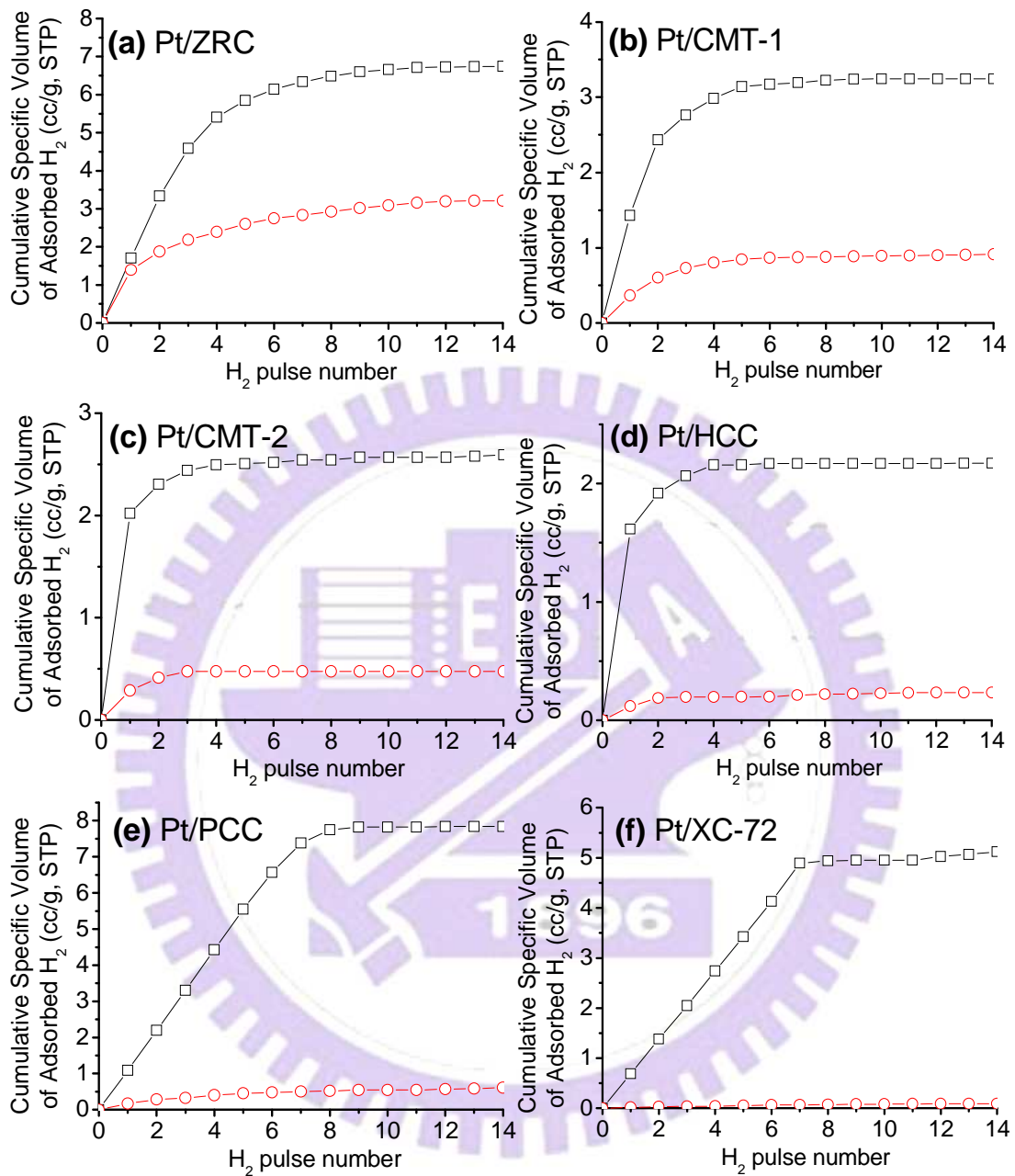


Fig. 4- 26 Pulsed H₂ chemisorption profiles without (square symbol) and with (circular symbol) pre-adsorption of 500 ppm CO for Samples, (a) Pt/ZRC, (b) Pt/CMT-1, (c) Pt/CMT-2, (d) Pt/HCC, (e) Pt/PCC, and (f) Pt/XC-72, respectively.

Chapter 5

Process, structures and properties of CNTs and their applications in DMFC anodes

5.1 Effect of Fe catalyst treatment procedures on CNTs diameter

Mesoporous silicas (MCM-41 and SBA-15) were used as supports for the Fe catalyst for fabrication of CNTs using the CVD method. The XRD patterns of the parent MCM-41 and SBA-15 mesoporous silicas as well as their corresponding Fe-incorporated counterparts prepared by either co-precipitation or impregnation methods are shown in Fig. 5- 1. Both siliceous SBA-15 and MCM-41 showed three well-resolved diffraction peaks that may be indexed as (100), (110), and (200) reflections associated with the well-ordered hexagonal arrays of mesopores.^[Beck-1992-10834; Zhao-1998-548; Zhao-1998-6024] The method applied in loading Fe onto the mesoporous silica appears to have significant effects on the mesostructure of the Fe-containing mesoporous silicas. Clearly, the Fe(co)/MCM-41 and Fe(co)/SBA-15 samples prepared *via* the co-precipitation method tend to retain the ordered structures of their parent silica supports, although substantial decreases in intensities of the diffraction peaks were evident. On the other hand, Fe-containing mesoporous silicas prepared by the impregnation method, i.e., Fe(im)/MCM-41 and Fe(im)/SBA-15, exhibited a main d_{100} diffraction peak with nearly diminishing higher order (d_{110} and d_{200}) peaks. Thus, unlike Fe(co)/MCM-41 and Fe(co)/SBA-15,

incorporation of Fe catalyst by impregnation method tends to lose the integrity of long-range structural ordering of their parent mesoporous silicas, as observed for XRD patterns in Fig. 5- 1. The same conclusion may be drawn from the TEM results in Fig. 5- 2. It is worth pointing out that a parallel alignment of pore channels should be observed when the electron beam was introduced perpendicular to the channel axis (Fig. 5- 2a and Fig. 5- 2d), whereas hexagonal packing of cylindrical mesopores prevail when the electron beam was introduced along the channel axis (see insets in Fig. 5- 2a and Fig. 5- 2d). It is clear that the Fe(co)/MCM-41 and Fe(co)/SBA-15 samples (Fig. 5- 2b and Fig. 5- 2e) retained the hexagonal pore systems of their respective parent silicas. However, it is also evident that the co-precipitation process invoked led to a heterogeneous dispersion of Fe particles on the external surfaces of the mesoporous silica supports.

On the other hand, while the TEM images of Fe(im)/MCM-41 and Fe(im)/SBA-15 seemingly showed well ordered hexagonal pore systems, incorporation of Fe onto porous templates by impregnation method led to partial formation of Fe nanorods within the pore channels (Fig. 5- 2c and Fig. 5- 2f). In this context, the diameter of the Fe nanorods should be constrained by the pore aperture of the mesoporous silica supports, thus leading to substantial reductions in their scattering contrasts,^[Mercier-1997-500; Lim-1999-3285; Jana-2007-2492] as observed in Fig. 5- 2. Moreover, in the case of treatment by impregnation method, notable changes in the wall thickness (W_d) of the samples before and after Fe loading were observed. Thus, the notable decrease in the intensity of the main d_{100} diffraction peak and the disappearance of the higher order peaks observed for Fe(im)/MCM-41 and Fe(im)/SBA-15 in Fig. 5- 1 may be ascribed due to the presence of Fe nanorods in the mesochannels of the silica supports rather than degradation of their mesostructures.

Nitrogen adsorption/desorption isotherms obtained from various samples are shown in Fig. 5- 3 together with their corresponding PSDs. The structure features of various samples were also depicted in Table 5- 1. Comparing with their parent silica materials, Fe-containing mesoporous silica typically showed smaller pore volumes and broader pore size distributions (PSDs) regardless of the method adopted in incorporating the Fe catalyst. While the Fe(co)/MCM-41 and Fe(co)/SBA-15 samples showed similar pore sizes (D_{BJH}) compared to their respective silica supports, slight decreases in pore volumes (V_p) and BET surface areas (S_{BET}) were observed after loading the Fe catalyst (Table 5- 1). On the other hand, notable decreases in D_{BJH} , V_p , and S_{BET} were observed for the Fe(im)/MCM-41 and Fe(im)/SBA-15 compared to their respective siliceous counterparts before loading the Fe catalyst (Table 5- 1). These observations are in line with the aforesaid XRD and TEM results, that is, incorporation of the Fe catalyst by impregnation method led to formation of Fe nanorods within the pore channels of the parent mesoporous silicas, whereas samples prepared using the co-precipitation method resulted in a inhomogeneous dispersion of Fe nanoparticles (typically, ca. 20 nm in size) on the external surfaces of mesoporous silicas.

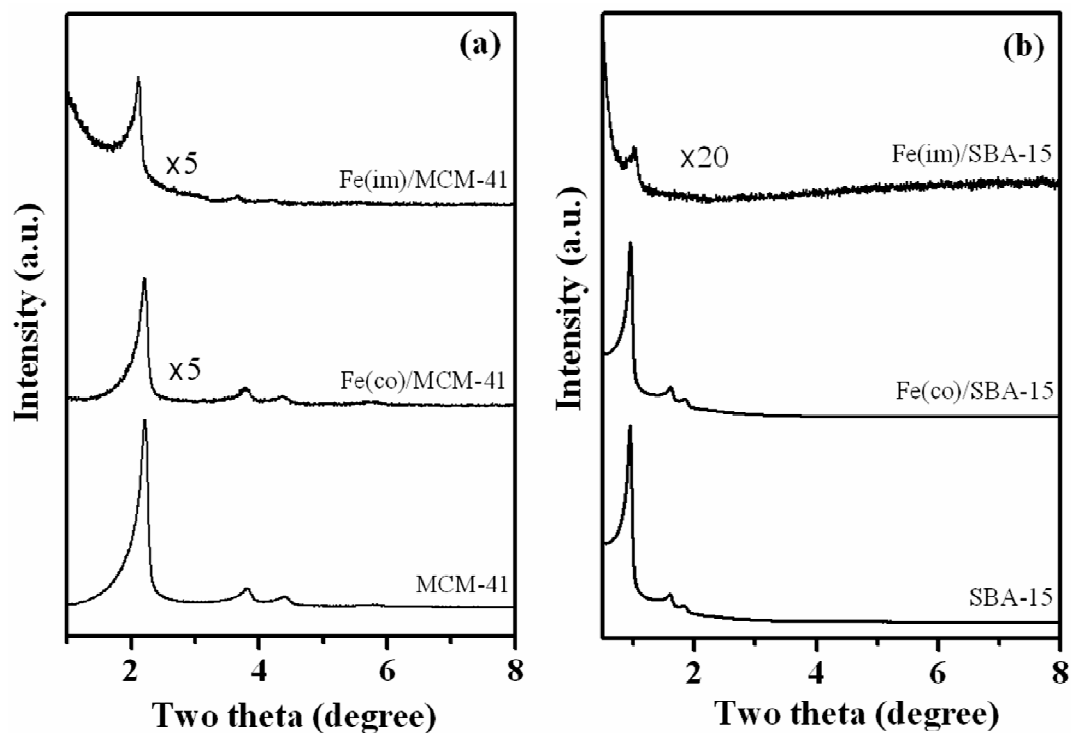


Fig. 5- 1 Small-angle XRD patterns with and without Fe in Templates of (a) MCM-41 and (b) SBA-15, respectively.

Table 5- 1 Structure features of various porous silica substrates with and without Fe in the pores.

Sample design.	d_{100}^a (nm)	D_{BJH}^b (nm)	S_{BET}^c (m ² /g)	V_p^d (cm ³ /g)	W_d^e (nm)
MCM-41	4.0	2.9	1153	0.97	1.7
Fe(co)/MCM-41	4.0	2.8	949	0.79	1.8
Fe(im)/MCM-41	4.2	2.6	540	0.50	2.2
SBA-15	9.4	9.1	823	1.30	1.7
Fe(co)/SBA-15	9.4	9.2	739	1.27	1.6
Fe(im)/SBA-15	8.7	8.6	498	0.64	1.4
PE-SBA-15	---	18.0	709	1.64	---
Fe(im)/PE-SBA-15	---	17.5	464	0.63	---

^a d_{100} : interplane spacing of (100) plane

^b D_{BJH} : pore diameter derived by BJH method

^c S_{BET} : BET specific surface area

^d V_p : specific pore volume

^e W_d : wall thickness, $W_d = 2d_{100}/\sqrt{3} - D_{BJH}$.

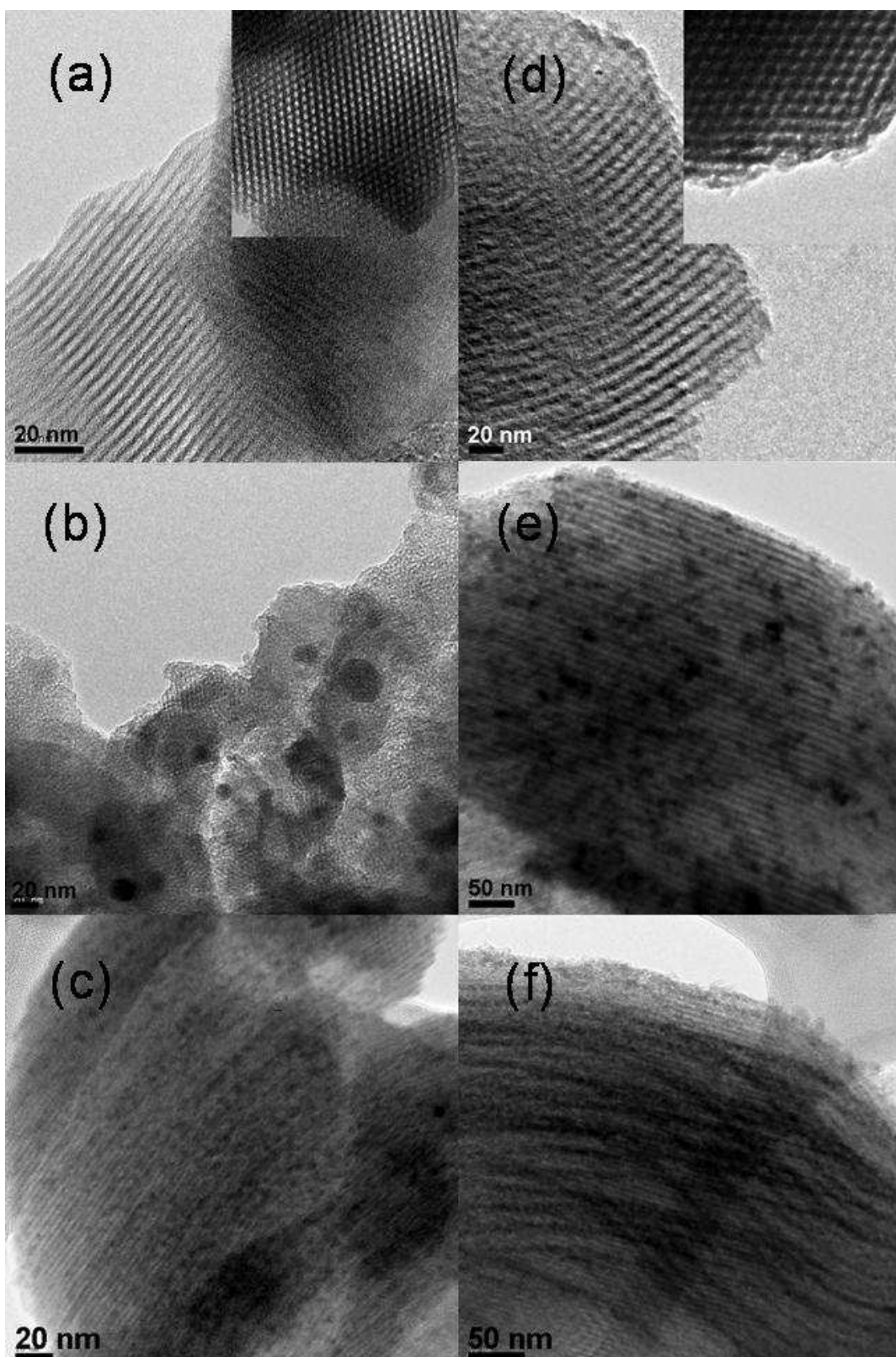


Fig. 5- 2 TEM images of Templates of (a) MCM-41 and (d) SBA-15 with inset showing different viewing directions and Samples of (b) Fe(co)/MCM-41, (c) Fe(im)/MCM-41, (e) Fe(co)/SBA-15, and (f) Fe(im)/SBA-15, respectively.

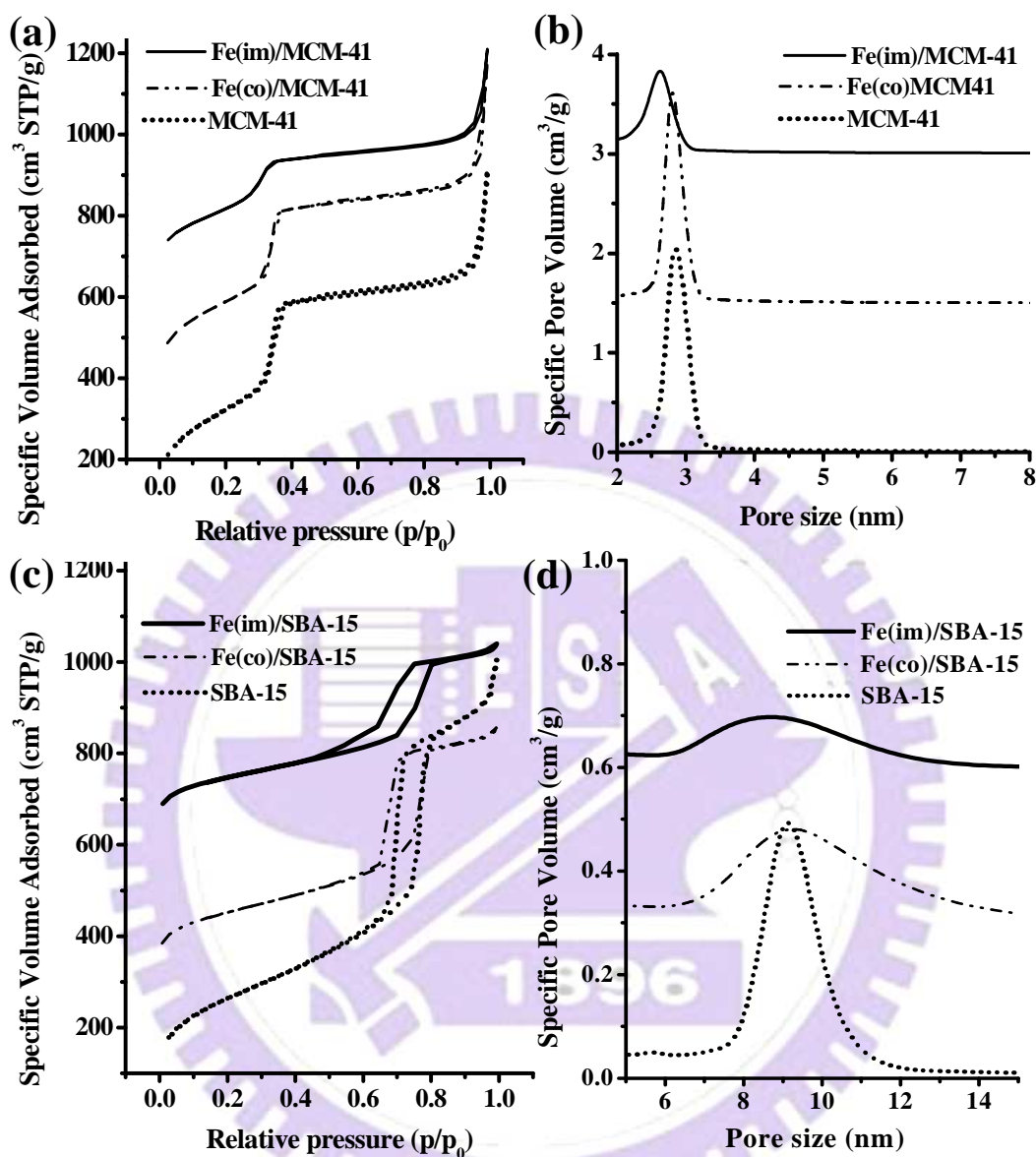


Fig. 5- 3 Nitrogen adsorption/desorption isotherms of Template with and without Fe catalyst of (a) MCM-41 and (c) SBA-15, and (b, d) their corresponding pore size distribution curves, where the isotherms of Substrates Fe(co)/MCM-41, Fe(im)/MCM-41, Fe(co)/SBA-15, and Fe(im)/SBA-15 were shifted vertically by 300, 600, 300, and 600, respectively, whereas the corresponding pore size distribution curves were shifted vertically by 1.5, 3.0, 0.3, and 0.6, respectively.

Typical TEM micrographs of CNTs synthesized by CVD process using various Fe-containing mesoporous silicas as catalysts are depicted in Fig. 5- 4. In the cases of using the Fe(co)/MCM-41 (Fig. 5- 4a) and Fe(co)/SBA-15 (Fig. 5- 4c) supported catalysts, the obtained CNTs typically possessed an average diameter greater than 5 and 10 nm, respectively, which were apparently greater than the pore sizes of their corresponding catalyst templates (see Table 5- 1). These observations are in parallel to the existing literature reports. ^[Somanathan-2008-5643; Wang-2005-151; Yang-2005-303] In contrast, the CNTs synthesized using the Fe(im)/MCM-41 and Fe(im)/SBA-15 catalysts were found to exhibit a uniform diameter of ca. 3 and 8 nm, respectively, in close resemblance with the average pore sizes of the corresponding parent mesoporous silicas (2.9 and 9.1 nm, respectively; see Table 5- 1). The above results indicate that Fe-containing mesoporous silicas so designed and prepared can be employed not only as catalysts to fabricate CNTs but also as templates to manipulate the diameters of the synthesized CNTs. To further verify these points, an additional PE-SBA-15 sample with expanded pore size of 18 nm (Table 5- 1 and Fig. 5- 5a) was synthesized. After incorporating the Fe catalyst by impregnation method, the resultant Fe(im)/PE-SBA-15 sample was employed as catalyst (and template) to produce CNTs. As shown in Fig. 5- 5b, the CNTs so fabricated also possessed a rather uniform diameter (ca. 17 nm) comparable to the pore size of the Fe(im)/PE-SBA-15 catalyst. It is noteworthy that the CNTs produced by CVD process using the Fe-containing mesoporous silicas reported herein also exhibited superior high yields in terms of atom efficiency. For examples, a CNT yield as high as 0.3 g was obtained in a CVD duration of 20 min by using ca. 1.0 g of Fe(im)/SBA-15 as catalyst/template. Likewise, a respective CNT yield of 0.1 and 0.4 g/20 min were attained when Fe(im)/MCM-41 and Fe(im)/PE-SBA-15 were employed.

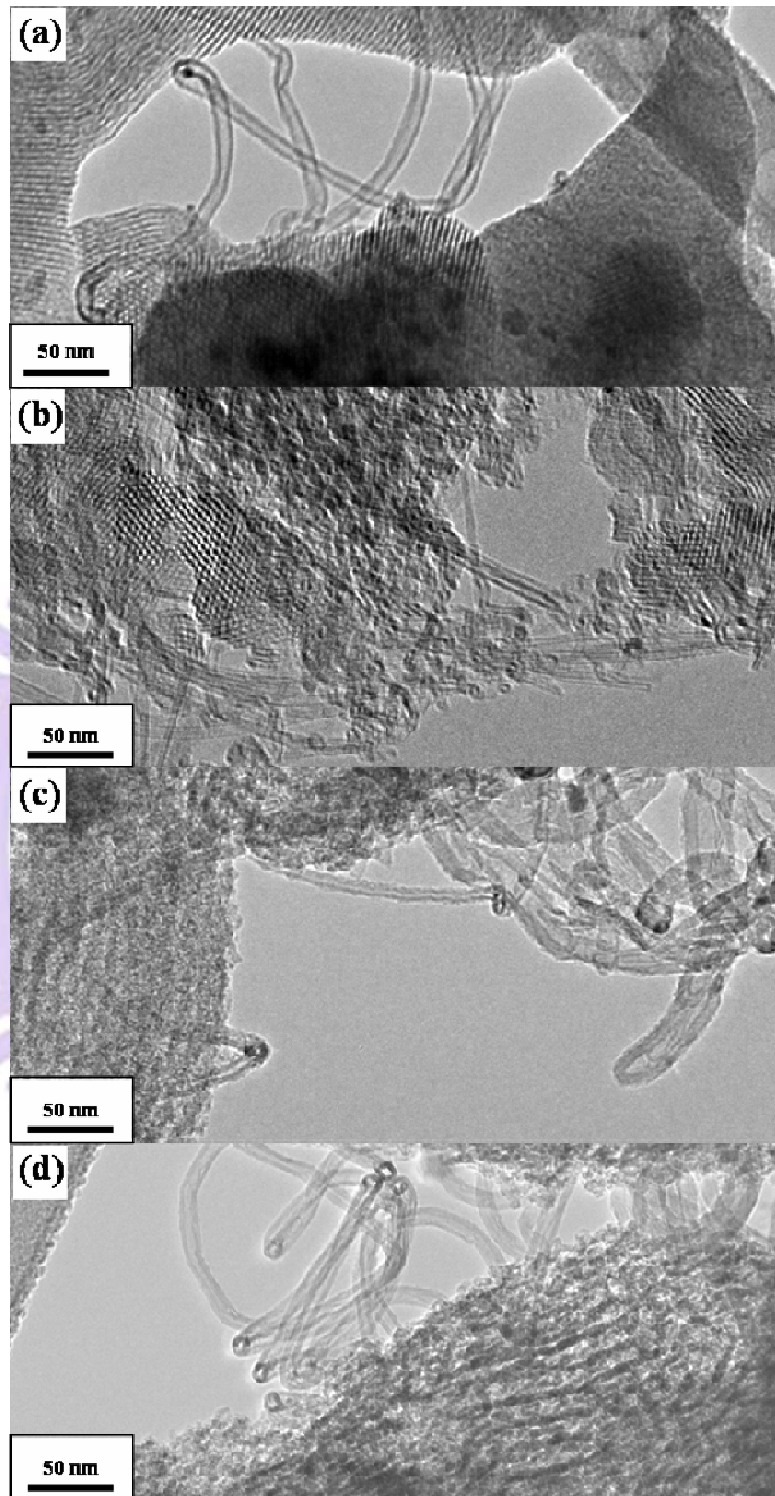


Fig. 5- 4 TEM images of Samples in Table 3-2 of CNTs deposited on Substrates of (a) Fe(co)/MCM-41, (b) Fe(im)/MCM-41, (c) Fe(co)/SBA-15, and (d) Fe(im)/SBA-15, respectively.

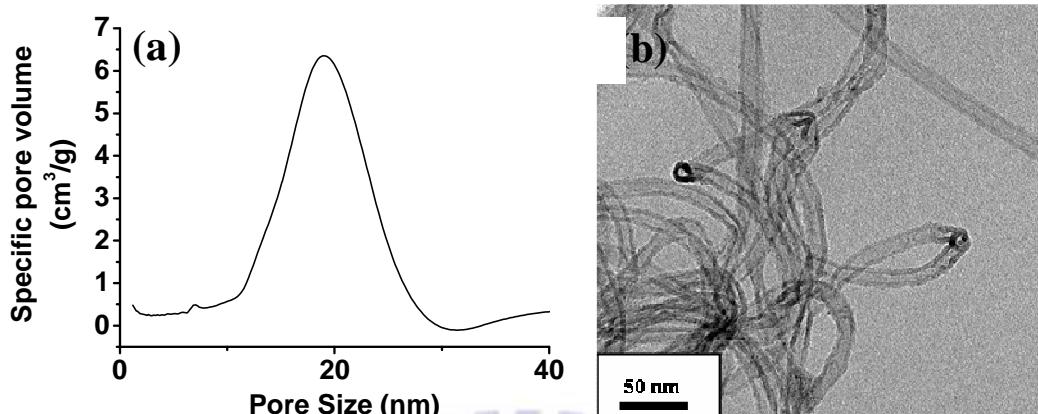
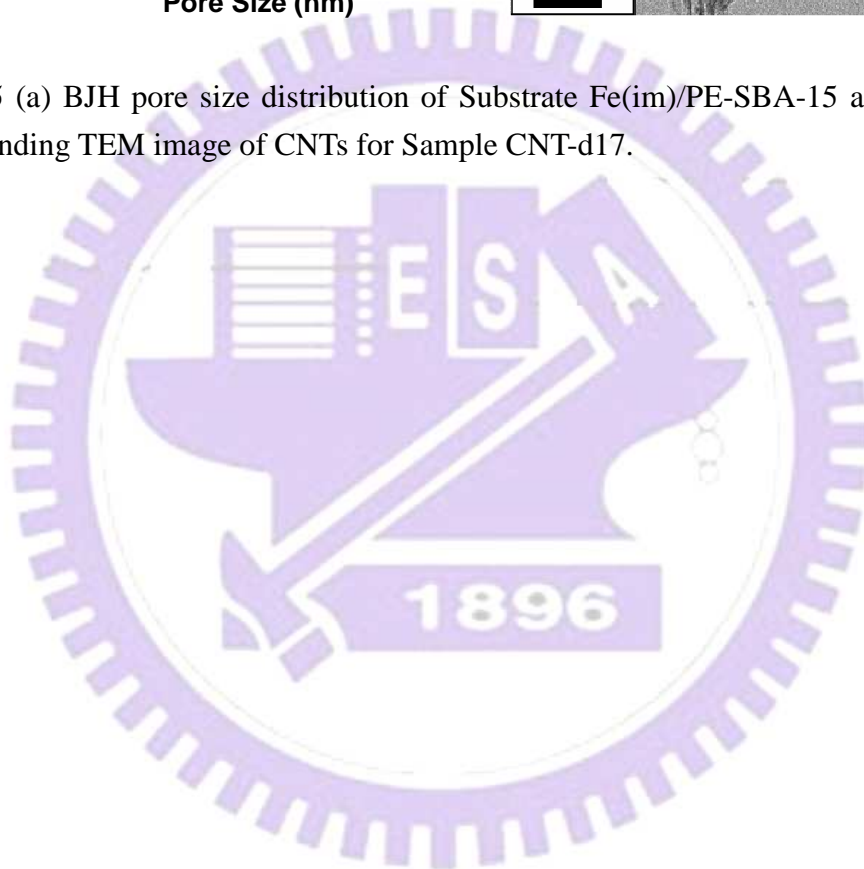


Fig. 5- 5 (a) BJH pore size distribution of Substrate Fe(im)/PE-SBA-15 and (b) the corresponding TEM image of CNTs for Sample CNT-d17.



5.2 Effects of tube diameter on performance of CNT-assisted DMFC anodes

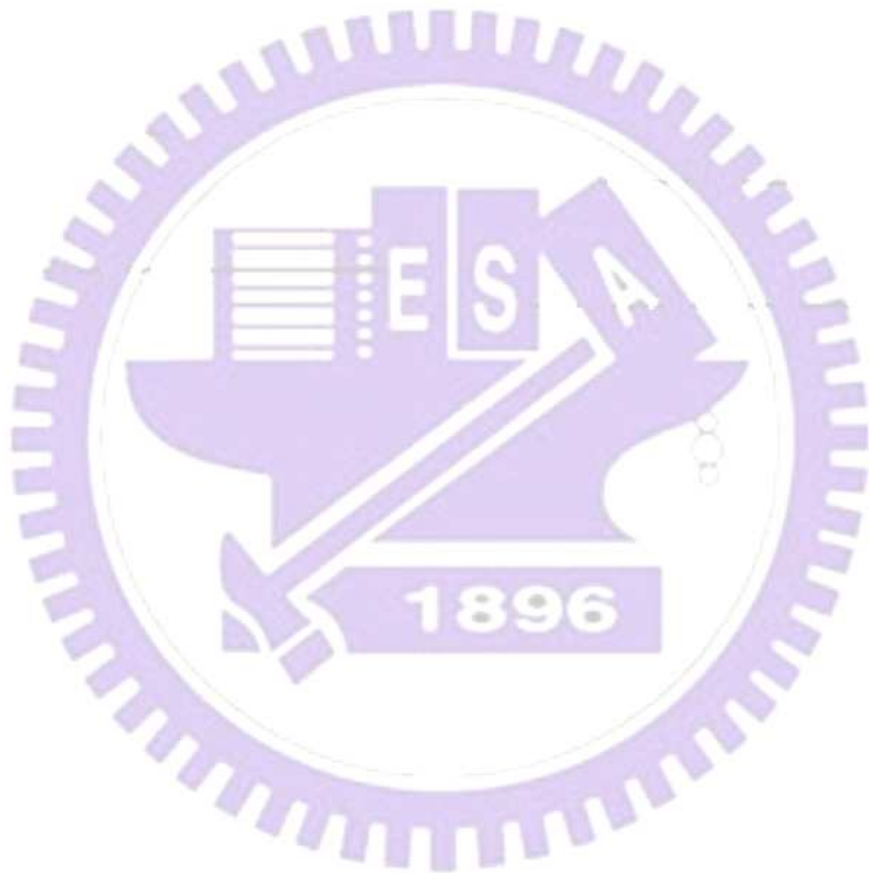
The multi-wall CNTs synthesized by using the Fe(im)/MCM-41, Fe(im)/SBA-15, and Fe(im)/PE-SBA-15 catalyst possess an average diameter of ca. 3, 8, and 17 nm, respectively. These CNTs with uniform diameters were subsequently used as supports for Pt catalyst, the resultant supported Pt/C catalyst samples are denoted as Pt/CNT-d3, Pt/CNT-d8, and Pt/CNT-d17, respectively. Fig. 5- 6 displays their corresponding TEM images and Pt particle size distributions together with two commercial samples, namely Pt/SWCNT and Pt/XC-72. Their corresponding Fe and Pt metal contents are depicted in Table 5- 2. As can be observed in Fig. 5- 6, majority of the Pt/C samples with CNTs as supports show Pt particle size predominately in the range of 1-2 nm. However, unlike the Pt/CNT-d8 and Pt/CNT-d17 samples, which showed uniform Pt dispersions (Fig. 5- 6b and Fig. 5- 6c) typically with Pt particle size ≤ 2 nm, the Pt/CNT-d3 sample appeared to have lower Pt dispersion similar to that of the Pt/SWCNT and Pt/XC-72 samples. Pt particles exceeding 10 nm can be identified in the latter three samples, as shown in Fig. 5- 6a, Fig. 5- 6d, and Fig. 5- 6e. A closer examination of the TEM profile for the Pt/CNT-d3, and Pt/SWCNT sample revealed that the CNTs tend to bundle together, leading to an inhomogeneous dispersion of Pt nanoparticles (see inset in Fig. 5- 6a & d), and Pt particles embedded in the bundles (Fig. 5- 6a & d). Thus, it is indicative that, in terms of Pt dispersion and whether it is exposed in methanol, CNT supports with larger diameters (preferably exceeding 8 nm) are loath to bundling and hence are more preferable as supports for the metal catalyst. In addition, it is noted that CNT supports with a larger diameters tend to favor a more homogeneous dispersions of Pt nanoparticles, as can be inferred

from the particle size distributions shown in Fig. 5- 6b and Fig. 5- 6c for Pt/CNT-d8 and Pt/CNT-d17, respectively.

The electrocatalytic performances of various Pt/C catalysts during MOR are shown in Fig. 5- 7. All Pt/C samples displayed cyclic voltammograms associated with forward (I_f) and reverse (I_r) peak current densities (shown in Fig. 5- 7), which represent catalytic activity and resistance toward catalyst deactivation (by coking) over the catalyst during MOR, respectively.^[Tiwari-2008-6516; Liu-2004-8234] Regarding to the MOR activity, Fig. 5- 7a indicates that it increase with the increment of the tube diameter (from SWCNT to CNT-d17). These results is in accordance with our prediction (in last paragraph) from TEM analysis, which indicates that a smaller tube size give rise to a greater amount of tube bundling, more probability for Pt particles to be embedded within the bundles (shown in Fig. 5- 6) and hence poorer MOR activity. In addition, the above discussion is also in agreement with the discussion in Section 4.3 that Pt particles embedded in micro- and meso-pore possess lower activity due to the limitation of methanol transfer in porous networks.

Regarding to the CO-tolerance, the Pt/CNT-d3, Pt/CNT-d8, Pt/CNT-d17, Pt/SWCNT and Pt/XC-72 (Table 5- 2) samples exhibited I_f/I_r ratios only slight different from each other, indicating that the effects of CNT diameter (0.4 - 17 nm) on CO-tolerance are not significant. Since Pt-particles smaller than 1 nm exhibit greater CO-tolerance (as indicated in Section 4.3), TEM results Fig. 5- 6 suggest that the probabilities of small Pt-particles (< 1 nm) do not significant vary with CNT diameters, and hence the CO-tolerance which is in accordance with the similar I_f/I_r ratios. On the other hand, there are various amount of residual Fe catalyst in CNT supports (CNT-d3, CNT-d8, CNT-d17, and SWCNTs), different ratio of Fe in these Pt/CNT samples (Table 5- 2). However, it is well accepted that residual Fe catalyst

form CNT growth are always encapsulated in the end of CNTs. Therefore, it is reasonable that Fe particles are isolated by CNTs from alloying with Pt catalyst, and hence the CO-tolerance does not affected by the cointaining of Fe catalyst.



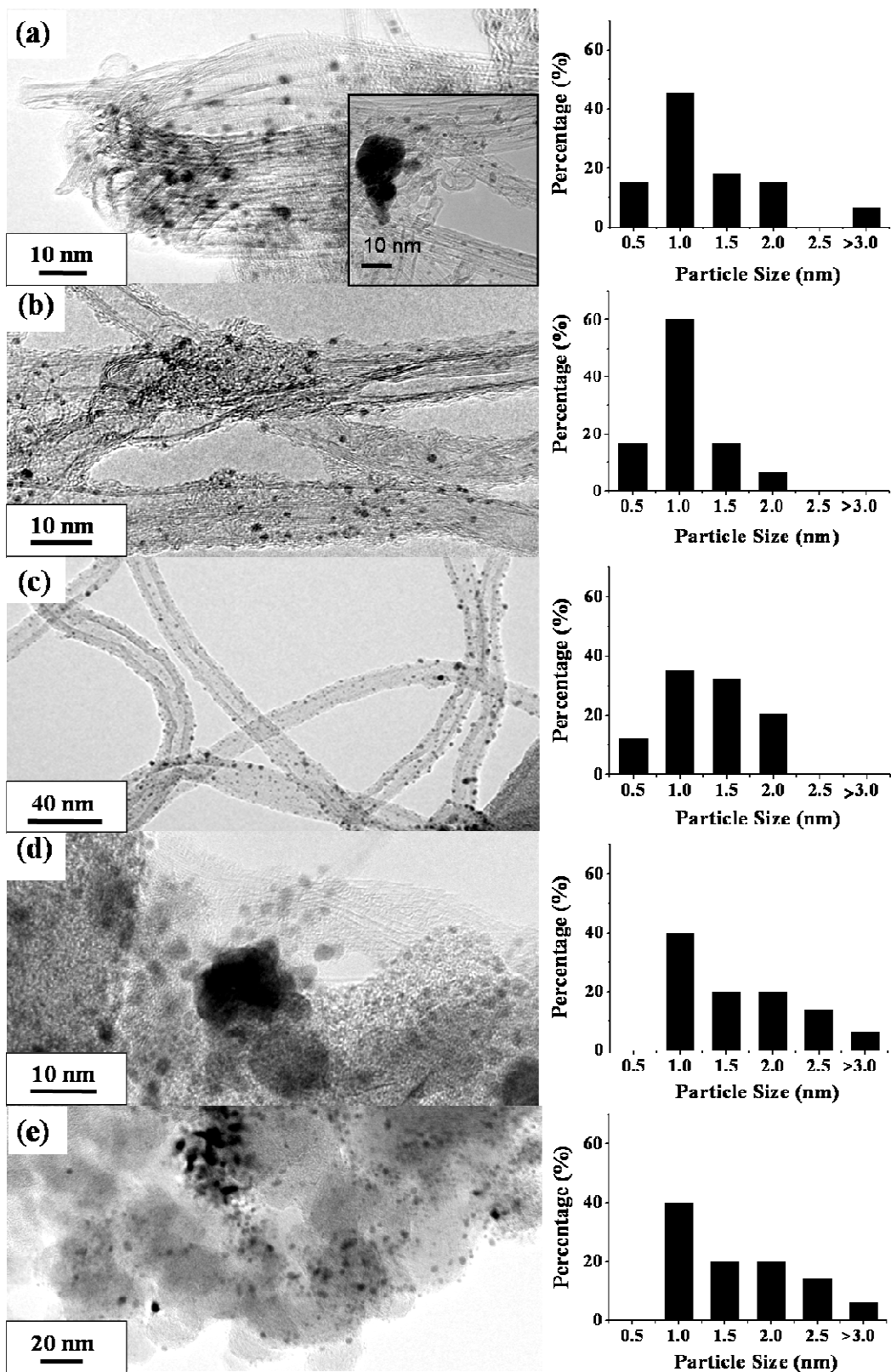


Fig. 5- 6 (Left) TEM images and (Right) the corresponding Pt particle size distribution of Samples, (a) Pt/CNT-d3, (b) Pt/CNT-d8, (c) Pt/CNT-d17, (d) Pt/SWCNT, and (e) Pt/XC-72, respectively.

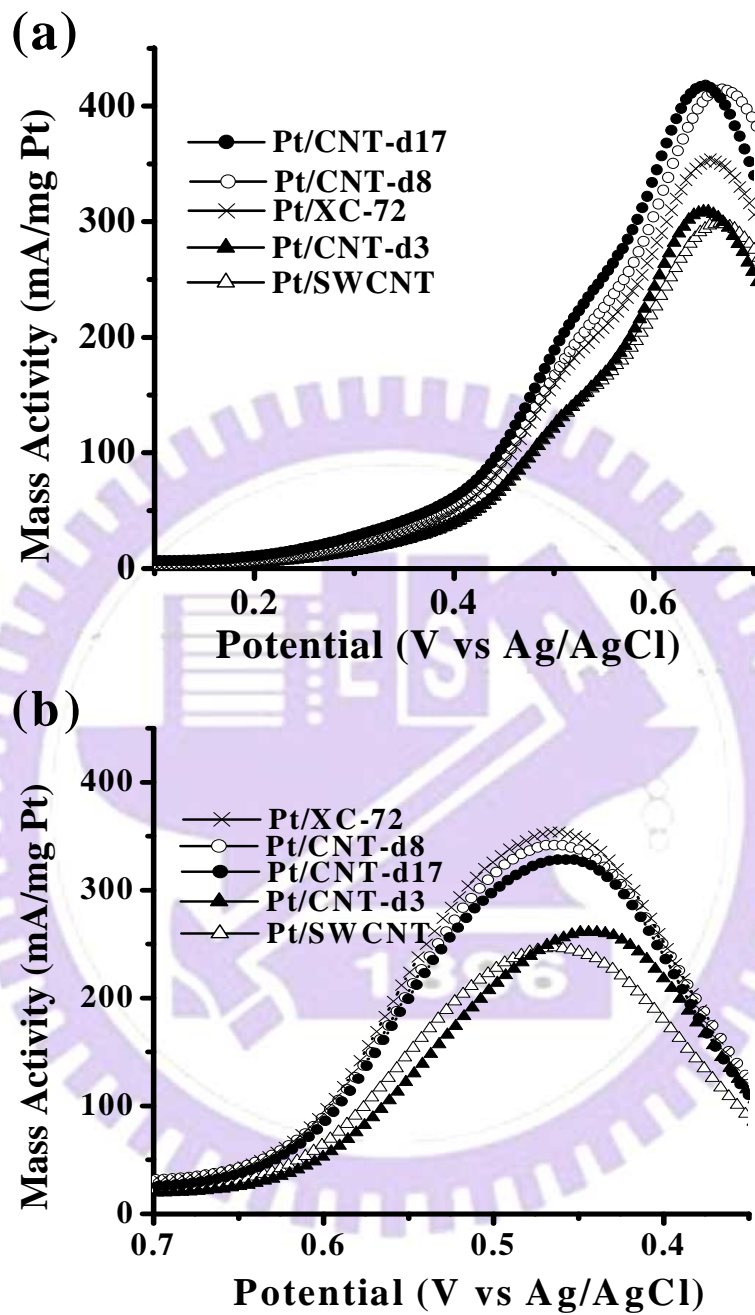


Fig. 5- 7 (a) forward and (b) reverse C-V scans of various Samples Pt/CNT and Pt/XC-72.

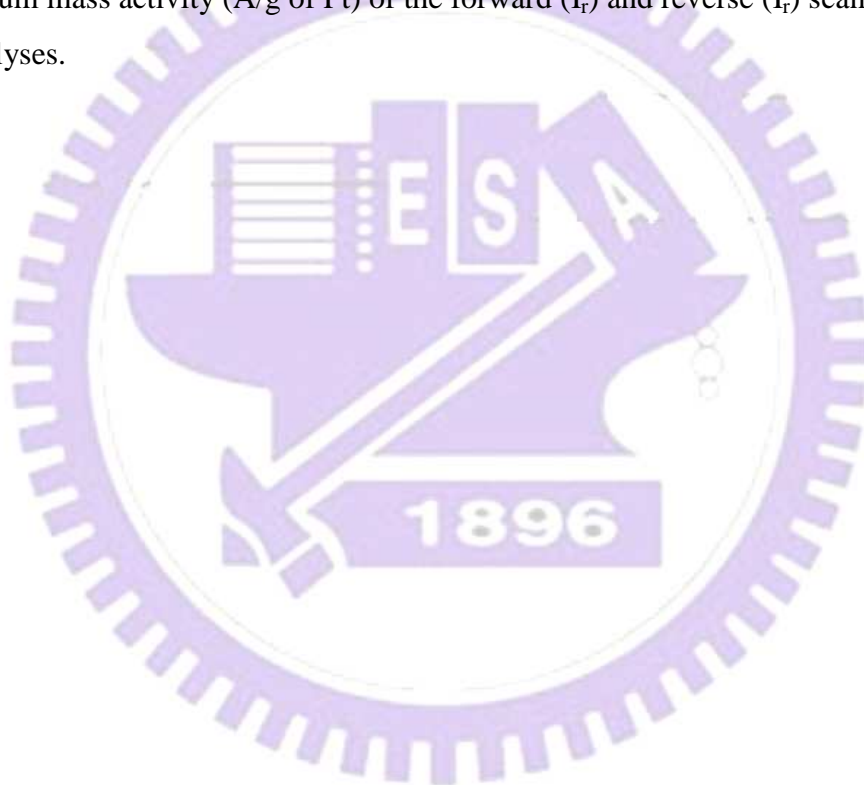
Table 5- 2 Sample designations, and their physicochemical properties of Pt- and/or Fe-incorporated samples with the Samples in Table 3 as the substrates.

Sample design.	Metal contents ^a		I_G/I_D ^b	I_f ^c (A/g of Pt)	I_r ^c (A/g of Pt)	I_f/I_r
	Fe	Pt				
Pt/CNT-d3	2.6	12.9	0.80	354	294	1.20
Pt/CNT-d8	4.8	9.3	0.80	392	321	1.22
Pt/CNT-d17	5.2	10.5	0.77	414	316	1.31
Pt/SWCNT	4.5	12.9	0.74	310	262	1.18
Pt/XC-72	---	12.5	0.72	353	349	1.01

^a wt % of Pt and Fe in electrocatalyst samples measured by TGA analysis.

^b I_G/I_D represents Raman intensity ratio of G-band and D-band.

^c Maximum mass activity (A/g of Pt) of the forward (I_f) and reverse (I_r) scans during C-V analyses.



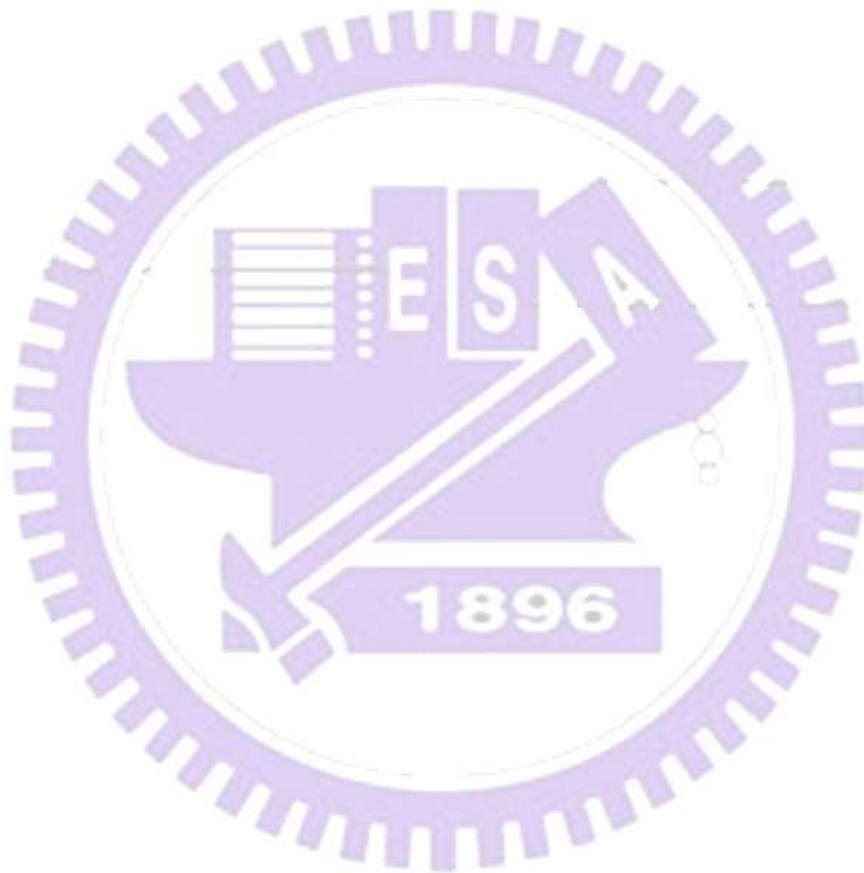
5.3 Comparison of CPMs- and CNT-assisted DMFC

anodes

Fig. 4- 25 and Fig. 5- 7 show the C-V examinations of CPMs- and CNT-assisted anode catalysts. Regarding to the I_f value which is the index of MOR activity, the results indicate that they are in the order of Pt/PCC (628) > Pt/HCC (194) > Pt/CMT-2 (97) > Pt/CMT-1 (60) > Pt/ZRC (25) and Pt/CNT-d17 (414) > Pt/CNT-d8 (392) > Pt/CNT-d3 (354) > Pt/SWCNT (310). These results indicate that the MOR activities are increasing with the increasing of pore size and tube diameter on CPM and CNT supports, respectively, both can be attributed to the limitation of methanol transfer in carbon nanostructures. Here, Pt dispersed macroporous carbon (i.e. Pt/PCC) possesses greatest MOR activity among Pt/CPMs (pore size ca. 400 nm) and Pt/CNTs (diameter ca. 17 nm), due to the effect of methanol transfer limitation would be dropped by its extremely huge pore size (400 nm).

Regarding to the I_f/I_r ratio which is the index of CO-tolerance, Fig. 4- 25 and Fig. 5- 7 indicates that CPM-assisted anode catalysts (1.04-4.88) are normally greater than CNT-assisted one (around 1.2). The decreasing of CPM pore diameter can increase the probability of Pt particle smaller than 1 nm (Fig. 4- 23), and hence increasing the CO-tolerance, i.e. Pt/ZRC (4.88) > Pt/CMT-1 (2.26) > Pt/CMT-2 (1.44) \approx Pt/HCC (1.45) \approx Pt/PCC (1.04). However, the effect is not obviously on CNT-diameters for CNT-assisted anode catalysts (as shown in Fig. 5- 6), i.e. Pt/SWCNT (1.18) \approx Pt/CNT-d3 (1.20) \approx Pt/CNT-d8 (1.22) \approx Pt/CNT-d17 (1.31). In short, Pt dispersed microporous carbon (i.e. Pt/ZRC) exhibits smallest pore diameter (\sim 1 nm) which can increasing the probability of Pt particle smaller than 1 nm, and then possesses greatest CO-tolerance among Pt/CPMs and Pt/CNTs.

Therefore, it can be summarised that greater MOR activity with greater CO-tolerance can only be achieved by dispersing Pt ($< 1 \text{ nm}$) on macroporous carbon supports. Such that, methods to disperse Pt particle well ($< 1 \text{ nm}$) on macroporous carbon would be important in the future investigations.



Chapter 6

Effects of temperature difference across catalyst particle on CNTs growth mode

6.1. Inherent differences between thermal CVD and plasma-enhanced CVD processes

Majority of CNTs deposited by plasma-enhanced and thermal CVD methods are normally categorized by the tip-growth^[Abdi-2006-1219; Chen-2004-1949; Chen-2000-2469; Hart-2006-1397; Hsu-2002-225; Kuo-2003-799; Lin-2003-1851; Murakami-2000-1776; Ren-1998-1105; Yap-2006-1622] and base-growth^[Choi-2002-3847; Choi-2001-2095; Fan-1999-512; Gulino-2005-89; Lee-1999-461; Lee-2001-245; Lee-2000-3397; Zhao-2006-159] modes, respectively. Regarding to the growth modes of CNTs, adhesion force between the catalyst and substrate was proposed to be the controlling factor.^[Bower-2000-2767; Dupuis-2005-929] Nevertheless, such adhesion force mechanism was found to be inadequate in interpreting some of the CNTs growth modes in different growth systems. One of the possible factors, the direction of temperature increasing across the catalyst, may be overlooked.

For CNT growth by thermal CVD process, substrates temperature (T_s) is often maintained at a fixed temperature while introducing the reaction gases into the reaction chamber without preheating. As a result, the temperature at the top of the catalyst (T_{ct}), which is in contact with the injecting gases, is generally lower than that at the bottom of the catalyst (T_{cb}) that is in contact with the substrate, as illustrated in Fig. 6- 1. In contrast, in the case of plasma-enhanced CVD, the reaction gases are

normally ionized by microwave to reach a plasma state, whose temperature (T_p) is often higher than the substrate temperature (T_s). In other words, the temperature at the top of the catalyst particles close to the plasma zone is higher than that at the bottom of the substrate. As such, the direction of the temperature increasing across the catalyst particles should be pointing downward and upward for the thermal and plasma-enhanced CVD, respectively. This explains why the CNT growth modes are generally different, as mentioned above. By defining ΔT as the temperature difference between the top and down of the catalyst, as shown in Fig. 6- 1 and Eq. (5A-1), then ΔT is generally < 0 and > 0 for CNTs deposited by thermal and plasma-enhanced CVD, respectively. In other word, ΔT is an index for determining the direction of temperature increasing across the catalyst particles. In order to examine effect of ΔT on CNTs growth mode, experiments have been designed and carried out such that the temperature across the catalyst may be controlled so that $\Delta T < 0$, ~ 0 , or > 0 .

$$\Delta T = T_{Ct} - T_{Cb} \text{ or } T_p - T_s \quad (5A-1)$$

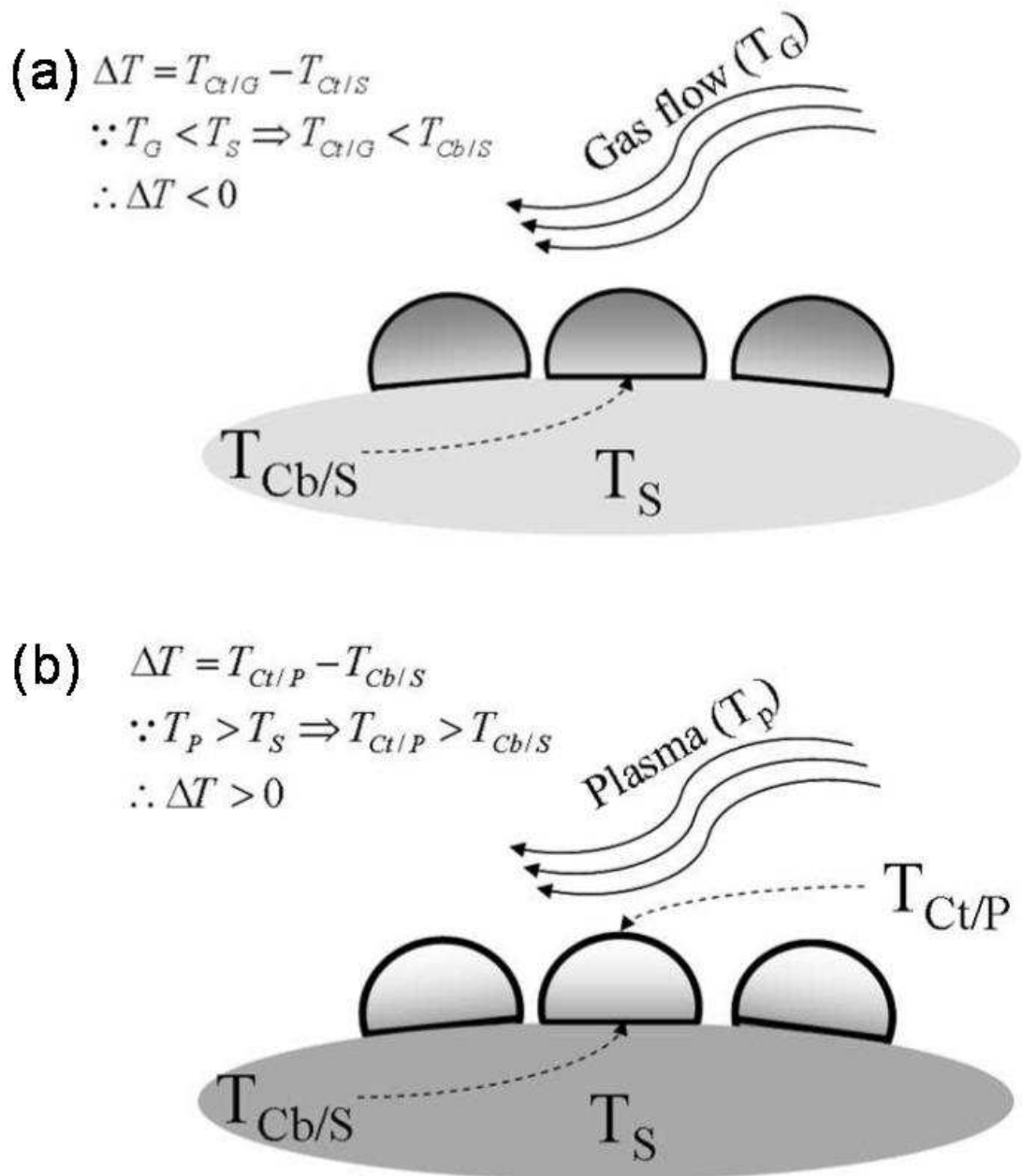


Fig. 6- 1 Schematics of temperature profiles across a catalyst particle for different deposition systems: (a) thermal and (b) plasma-enhanced CVD systems.

6.2. Effect of substrate and deposition conditions on CNTs growth by thermal CVD

The bright field and the corresponding dark field TEM images of the as-deposited CNTs on nanoporous Co/SBA-15 substrate prepared by thermal CVD method without the reaction gases pre-heating treatment (i.e., Sample A1-20; see Table 3- 3) are shown in Fig. 6- 2a and b. For comparison, the TEM image of CNTs prepared by similar conditions but deposited on Co/Si(100) wafer (i.e., Sample A2-20; Table 3- 3) is shown in Fig. 6- 3. These images suggest that base-growth CNTs are formed by thermal CVD method, regardless of whether they are deposited on nanoporous silica (rough surface) or silicon wafer (smooth surface) substrates. These observations are in line with the existing literatures for fabrication of CNTs by thermal CVD method. [Choi-2002-3847; Choi-2001-2095; Fan-1999-512; Gulino-2005-89; Lee-1999-461;

Lee-2001-245; Lee -2000-3397; Zhao-2006-159] As mentioned earlier, it has been proposed that the adhesion force between the metal catalyst and the substrate is one of the controlling factors that may affect the CNTs growth mode.^[Bower-2000-2767] However, our results above clearly contradict with this proposal, since the adhesion force for Co/SBA-15 is anticipated to be considerably greater than that of Co/Si(100) simply because a larger contacting area or mechanical locking effect should be present in the former case. Thus, the adhesion force between the metal catalyst and substrate should not be the dominant effect responsible for the CNTs growth mode. Rather, the temperature increasing across the catalyst should be the predominant factor controlling the CNTs growth mode. In this context, the observed base-growth CNTs should be provoked by

$\Delta T = T_G - T_S < 0$ (gas temperature < substrate temperature), typical for thermal CVD processes.

To further confirm the effect of ΔT on CNTs growth, two additional experiments were performed to deposit CNTs by the similar CVD method but with $\Delta T = T_G - T_S > 0$. This was accomplished by depositing the CNTs in the presence of gas pre-heating (Fig. 3- 2b), such that the temperature at the top of the supported catalyst was set to be higher than at the bottom (i.e., $T_G > T_S$). The resultant CNTs fabricated using Co/SBA-15 and Co/Si(100) were designated as Samples A3-20 and A4-20 Table 3- 3, respectively. In these two cases, the reaction gases were preheated to a temperature (1073 K) higher than the substrate (873 K) before entering the reaction chamber. As can be seen from the TEM images in Fig. 6- 4 and Fig. 6- 5, tip-growth CNTs were observed in this case ($\Delta T > 0$) instead of base-growth CNTs (which were prepared with ($\Delta T < 0$)).

In addition, three more experiments were conducted to obtain Samples A6-5, A6-10, and A6-15 (see Table 3- 3), which were done by depositing the sample specimen on Co/SBA-15 by thermal CVD method under the condition of $\Delta T \sim 0$ (i.e., $T_G \approx T_S$). As exemplified by the TEM images of Sample A6-5 in Fig. 6- 6, no obvious yield of CNTs were presence on the external surfaces of the Co/SBA-15 supported catalyst, rather, only onion-like graphitic carbon layers (Fig. 6- 6) were observed. Since Sample A6-5 were obtained after a deposition time of 5 minutes, it is indicative that the catalyst particles were deactivated rapidly as soon as they were wrapped with outer layers of carbons, leading to nearly null yield in CNTs.

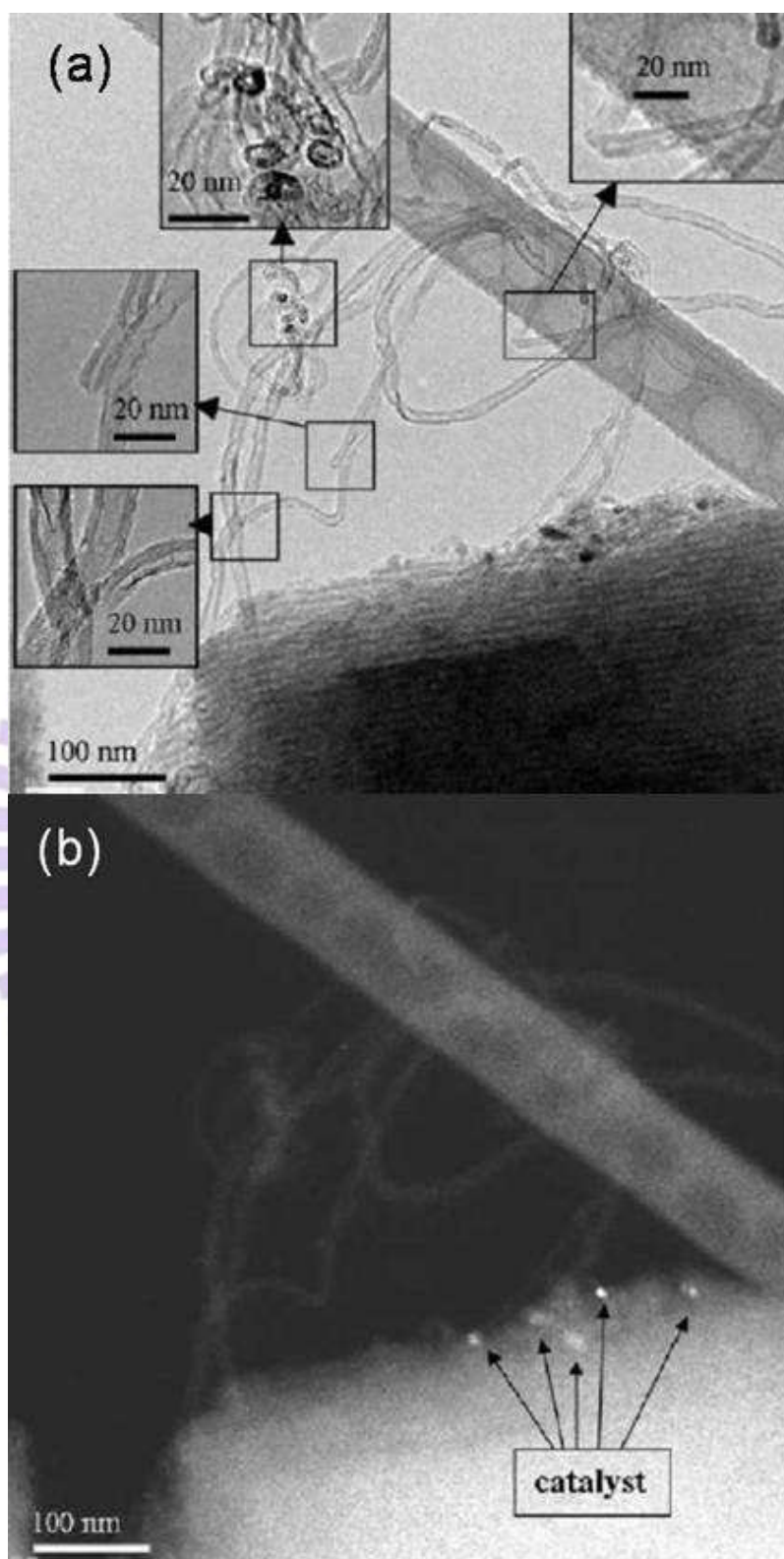


Fig. 6- 2 TEM images of the as-deposited CNTs on SBA-15 substrate by thermal CVD without gas preheating, with insets showing local images at higher magnifications: (a) bright field and (b) the corresponding dark field images, respectively (Sample A1-20).

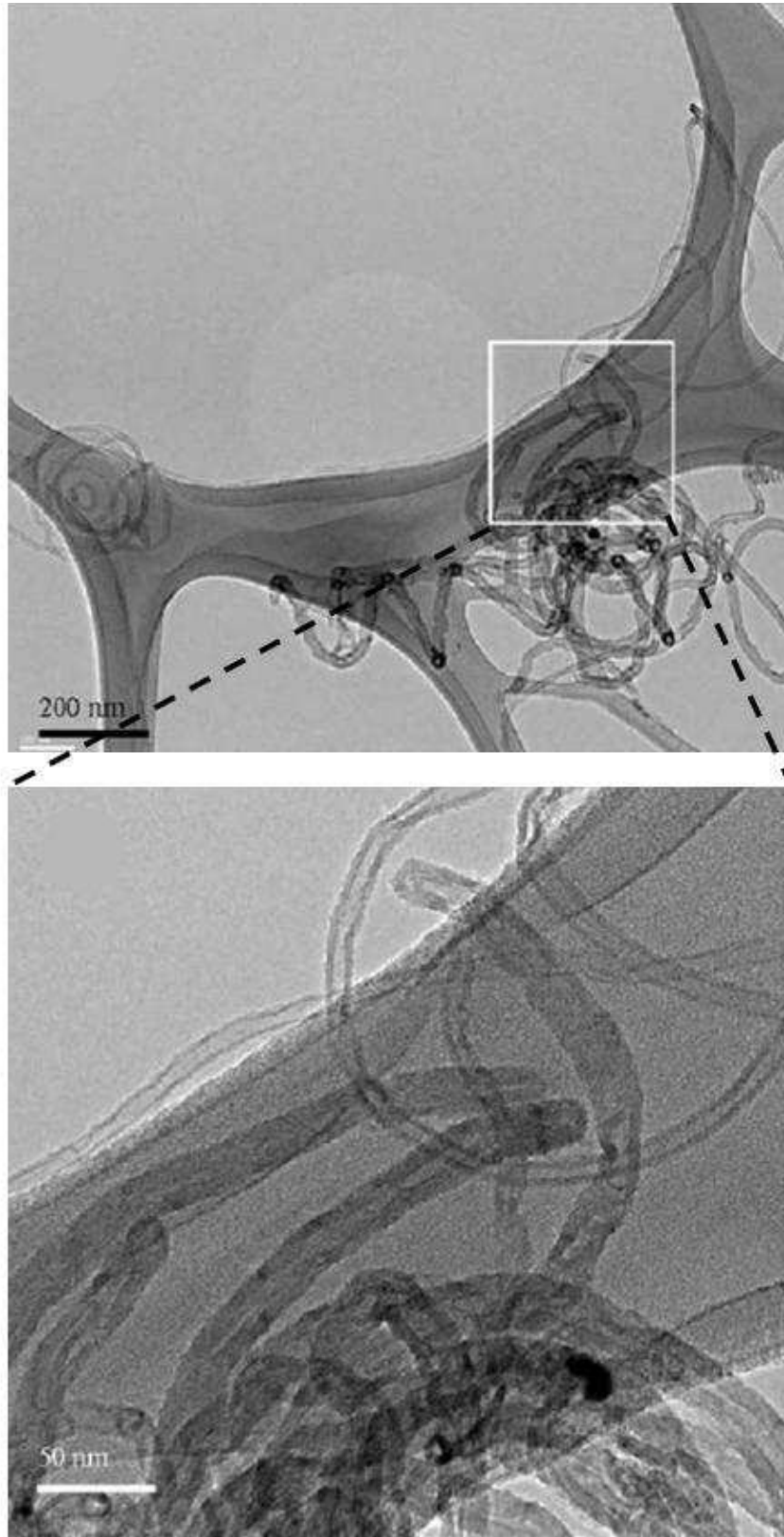


Fig. 6- 3 TEM image of the as-deposited CNTs on Si substrate by thermal CVD without gas preheating, with inset at higher magnification (Sample A2-20).

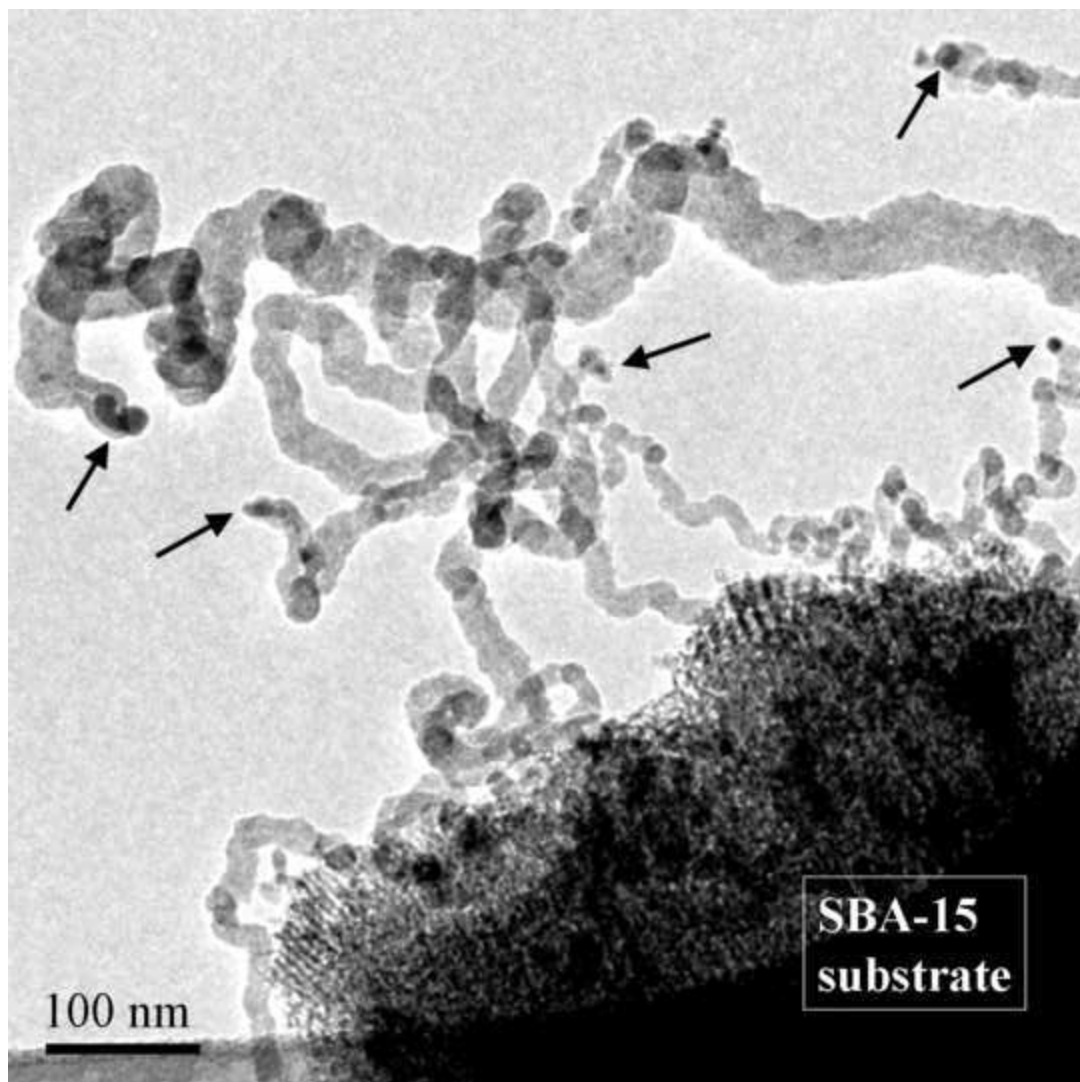


Fig. 6- 4 TEM images of the as-deposited CNTs on SBA-15 substrate by thermal CVD with gas preheating ($T_G > T_S$).

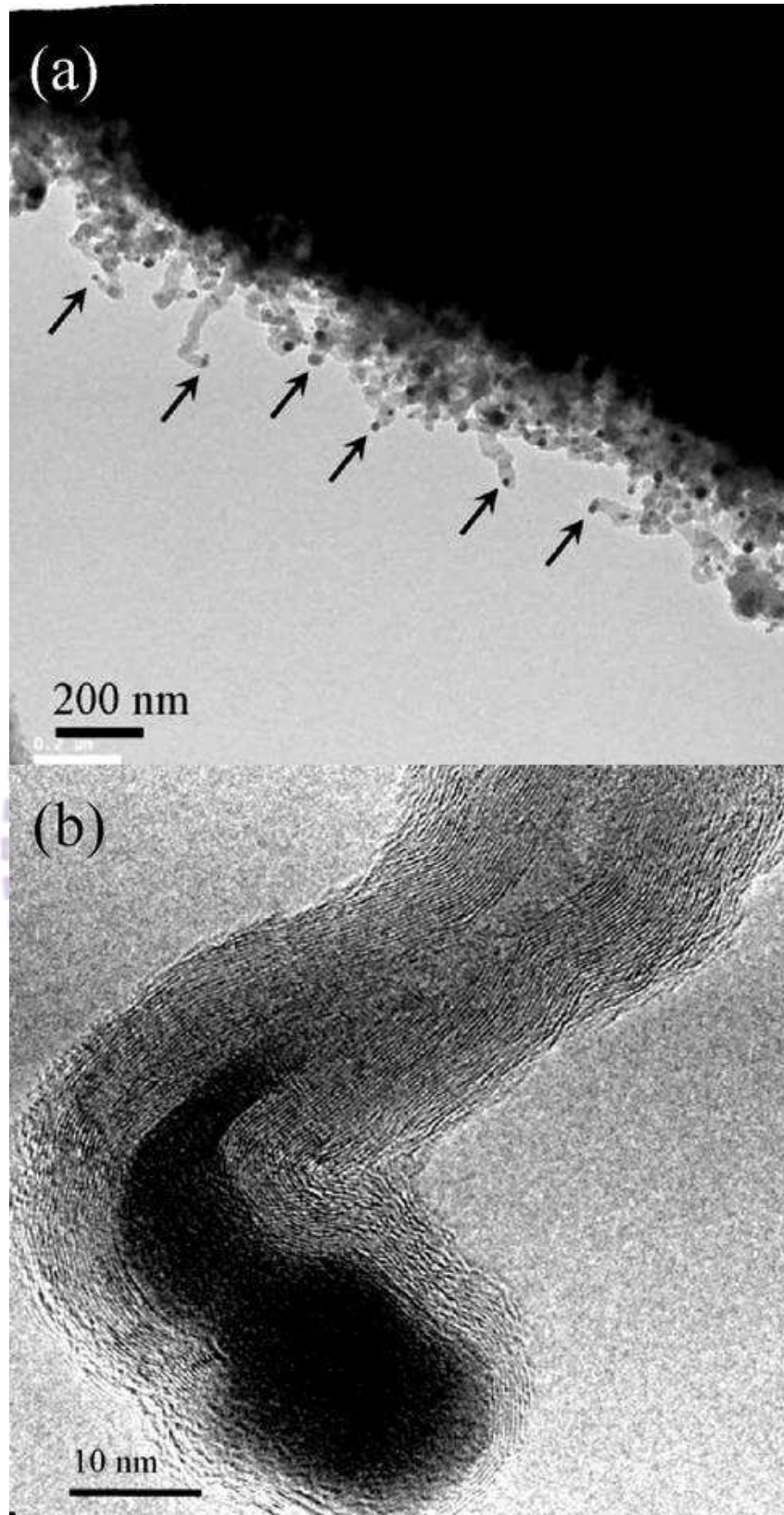


Fig. 6- 5 (a) TEM image of the as-deposited CNTs on Si substrate by thermal CVD with gas preheating ($T_G > T_S$), (b) the corresponding image at higher magnification (Sample A4-20).

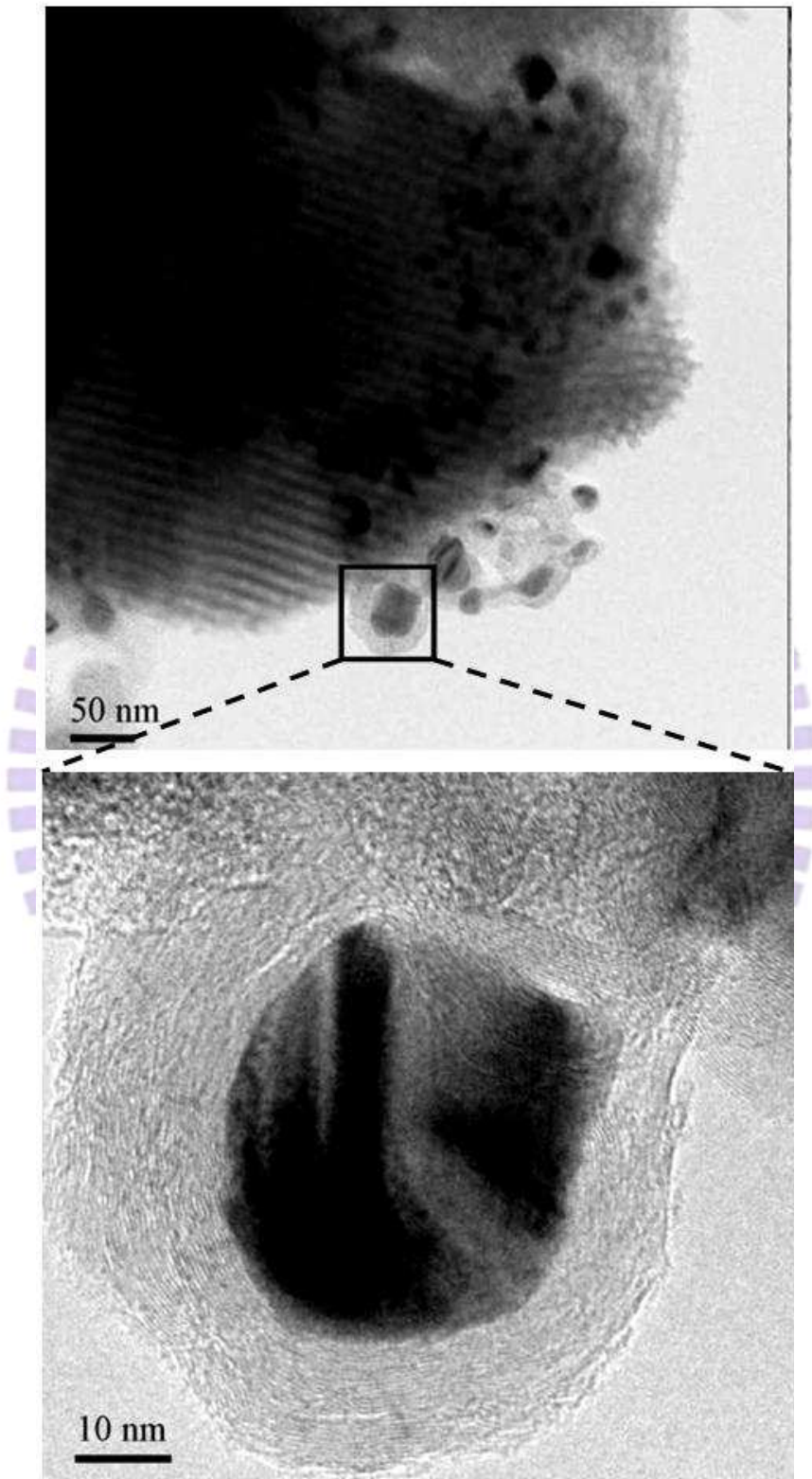


Fig. 6- 6 TEM image of the as-deposited CNTs on Si substrate by thermal CVD with gas preheating, with inset at higher magnification ($T_G = T_S$) (Sample A6-5).

Further verification were also conducted by comparing the production rates of different samples prepared with $\Delta T < 0$ and $\Delta T \sim 0$. The weights of the sample specimens so prepared were analyzed by TGA under a heating rate of $5^\circ\text{C}/\text{min}$ and an air flow rate of 15 sccm. Accordingly, the carbon yield, as defined in Eq. (5A-2) below, can be derived to represent the total carbon content (including CNTs, if present) produced after the CVD process.

$$\text{yield}(\text{wt}\%) = \frac{W_c}{100 - W_w} \times 100 \quad (5A-2)$$

where W_w is the weight loss during the first stage occurring at ca. 373 K (Fig. 6- 7), which may be attributed to H_2O absorbed in the hydrophilic Co/SBA-15 substrate; W_c is the weight loss during the second stage, which should be mainly due to oxidation of carbon with oxygen. As may be seen from Fig. 6- 7, the residual weight at the final stage should be mainly contributed by the Co/SBA-15 supported catalyst (or SBA-15 alone in case of substrate without a catalyst). As a result, variations in total carbon yield vs. deposition time for four different thermal CVD processes are shown in Fig. 6- 8. For comparison, the carbon yields obtained from SBA-15 substrates with and without the Co catalyst under the conditions of $\Delta T < 0$ (A1- and A7-series samples; Table 3- 3) and $\Delta T \sim 0$ (A6- and A8-series samples) are presented in Fig. 6- 8. For carbons deposited on Co/SBA-15 under $\Delta T < 0$ (i.e., the A1-series sample; $T_S = 1073$ K; $T_G = 300$ K; Table 4), which is typical in most thermal CVD processes, a rapid increase in carbon yield during initial deposition and eventually level off at extended deposition time (Fig. 6- 8). The curve can be roughly divided into two contributions whose slopes should be associated with the growth rates of different carbon species. For matter of convenience, we attribute the slope obtained during initial deposition

period (< 20 min) to the CNTs growth rate, whereas the slope at extended deposition time (> 20 min) may be assigned due to non-CNTs carbon species, respectively. Note that during the initial deposition of about 20 min, the deposited carbons are predominantly CNTs, as illustrated in Fig. 6- 2. However, a slower growth rate (ca. 0.33 wt%/min) was observed for other carbon species. It is noteworthy that the slope of this latter curve is nearly parallel to the slope of the A7-series samples obtained by using neat SBA-15 substrate (in absence of the Co catalyst), which represent growth rate of carbon species that lack characteristics of CNTs. In other words, in the case of A1-series sample, the Co/SBA-15 supported catalyst, which facilitates the CNTs growth, tends to be deactivated upon extended deposition (> 20 min). [Chen-2004-1949; Duesberg-2004-354; Futuba-2005-056104; Jeong-2002-11; Kanzow-1998-525; Lee-2004-1450; Pal-2008-1; Stadermann-2009-738]

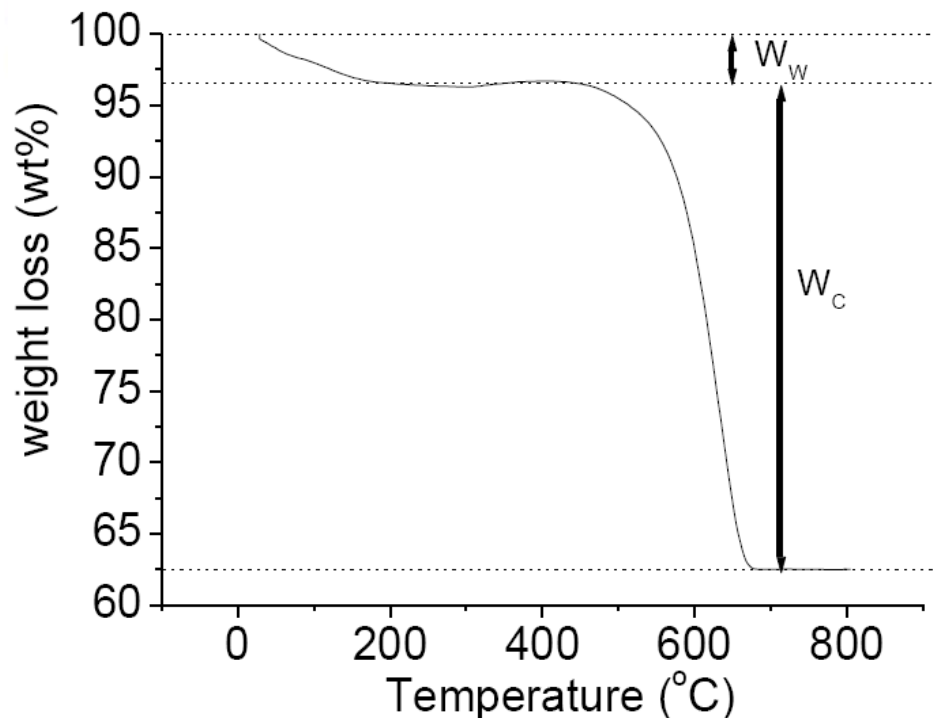


Fig. 6- 7 TGA curve of the as-deposited CNTs on SBA-15 substrate by thermal CVD without gas preheating (Sample A1-20).

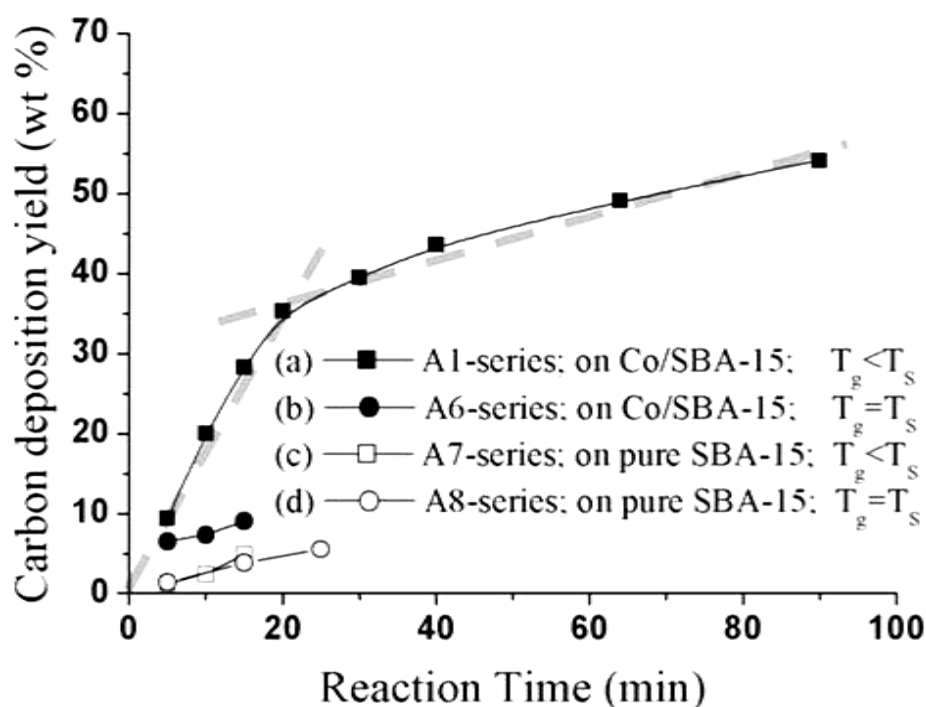


Fig. 6- 8 Carbon yield (wt %) versus reaction time curves of the as-deposited CNTs deposited by thermal CVD for A1, A6, A7, and A8 series Samples.

On the other hand, for A6- and A8-series samples, which were both prepared under thermal CVD condition of $\Delta T \sim 0$, obtained by deposition on SBA-15 with and without the Co catalyst, respectively, their carbon growth rates were not only nearly identical but also parallel to that observed for the A7-series samples ($\Delta T < 0$; on neat SBA-15). On the basis of the onion-like carbons observed for the A6-5 samples in Fig. 6- 6, it is indicative that the A6-, A7-, and A8-series samples, which were prepared either under $\Delta T \sim 0$ condition on Co/SBA-15 supported catalyst or on neat SBA-15 in the absence of the Co catalyst, should exhibit non-CNT carbon species with similar characteristics, most likely onion-like carbons similar to that shown in Fig. 6- 6. Thus, it is conclusive that temperature difference (ΔT) across the catalyst/substrate should represent one of the key factors controlling the CNTs growth by thermal CVD method.

6.3. Effect of deposition conditions on CNT growth by plasma-enhanced CVD

Regarding the effect of temperature difference (ΔT) on the growth mode of CNTs deposited by plasma-enhanced CVD, MP-CVD and/or ECR-CVD were normally adopted to grow CNTs under $\Delta T > 0$ and/or $\Delta T < 0$ conditions. In the case of plasma-enhanced CVD, manipulation of ΔT may be achieved by varying the substrate temperature during the growth process of CNTs, as illustrated in Fig. 6- 9. During the pretreatment stage, the temperature of the substrate rapidly increases from room temperature to a temperature T_{Si} , which may be defined as the initial temperature of the substrate during the CNT growth process. Subsequently the substrate may either be subjected to heating or cooling, which could be manipulated by adjusting the microwave power and the bias Table 3- 4 at the substrate. Consequently, such an increase or decrease in the final substrate temperature (T_{Sf}) leading to a temperature difference, i.e., $\Delta T > 0$ or $\Delta T < 0$ across the catalyst nanoparticles, respectively. Fig. 6- 10a and Fig. 6- 10b display the TEM images of CNTs deposited by MP-CVD under condition of $\Delta T > 0$ and $\Delta T < 0$, respectively. It indicative that the temperature difference, ΔT , across the catalyst nanoparticles indeed play an important role in the growth mode of CNTs, as can be identified by the tip- and base-growth modes observed in Fig. 6- 10a ($\Delta T > 0$) and Fig. 6- 10b ($\Delta T < 0$), respectively. The same conclusions can also be drawm for CNTs deposited by ECR-CVD, as shown in Fig. 6- 11a and Fig. 6- 11b, which show TEM images of CNTs prepared under the condition of $\Delta T > 0$ and $\Delta T < 0$, respectively.

Thus, it is conclusive that the direction of temperature increasing (ΔT) indeed plays a crucial role in dictating the growth mode of CNTs regardless of the deposition methods (viz., thermal-, MP-, or ECR-CVD) applied, as proposed in Fig. 6- 12.

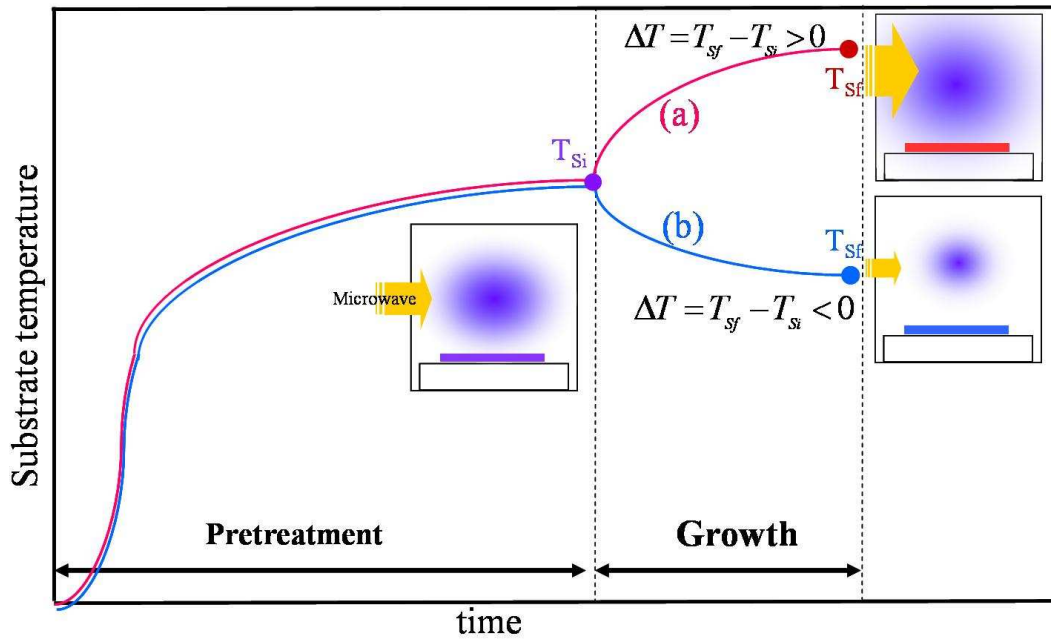


Fig. 6- 9 Schematic diagram showing substrate temperature variations during growth stage for (a) temperature-rising and (b) temperature-declining processes.

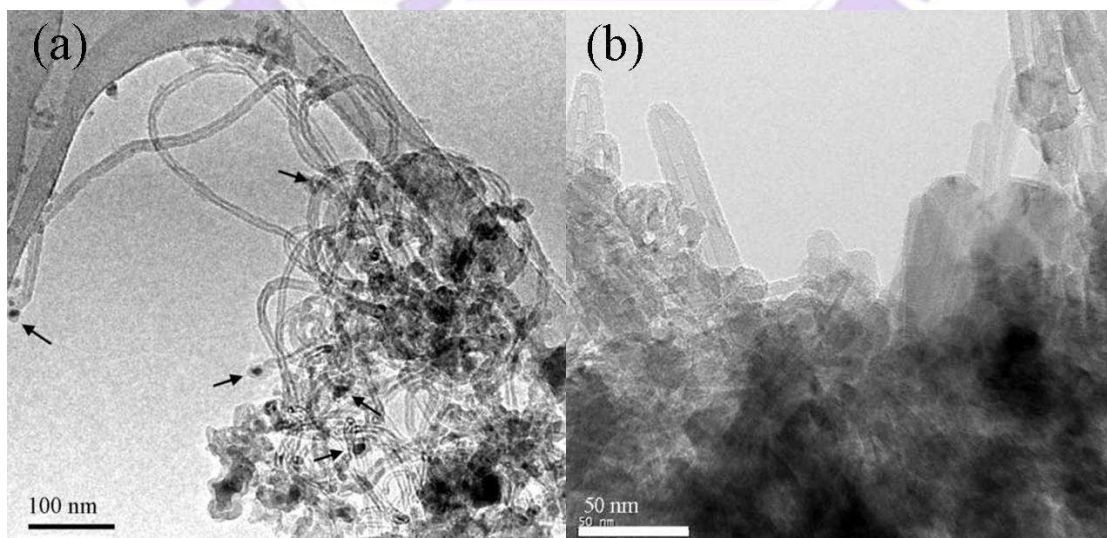


Fig. 6- 10 TEM images of the as-deposited CNTs on Si substrate by MP-CVD with schemes of (a) B1 and (b) B2 Samples in Table 3-4, respectively.

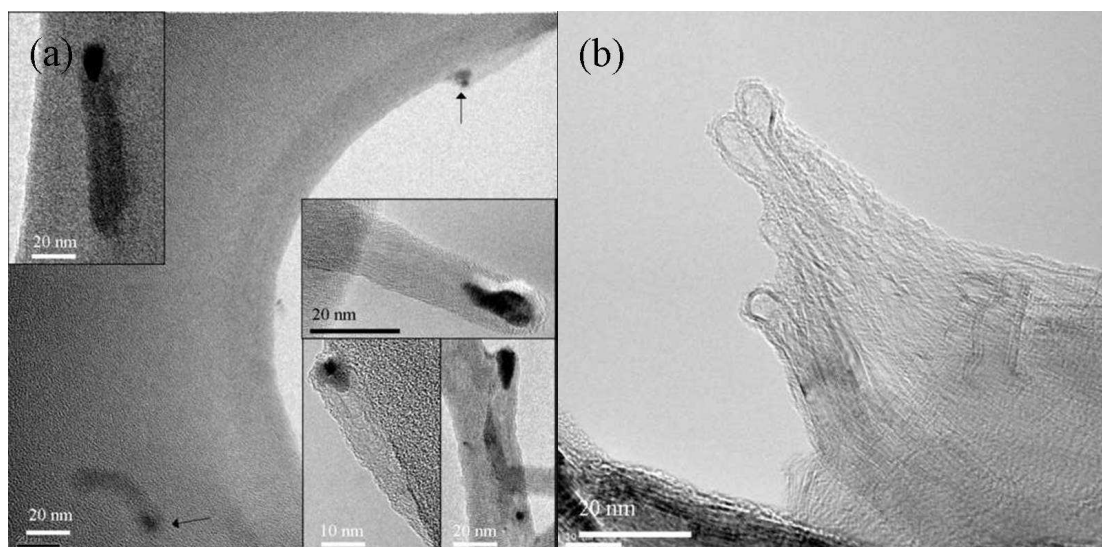


Fig. 6- 11 TEM images of the as-deposited CNTs on Si substrate by ECR-CVD with schemes of (a) C1 and (b) C2 Samples in Table 3-4, respectively, where the insets are showing images at different locations.

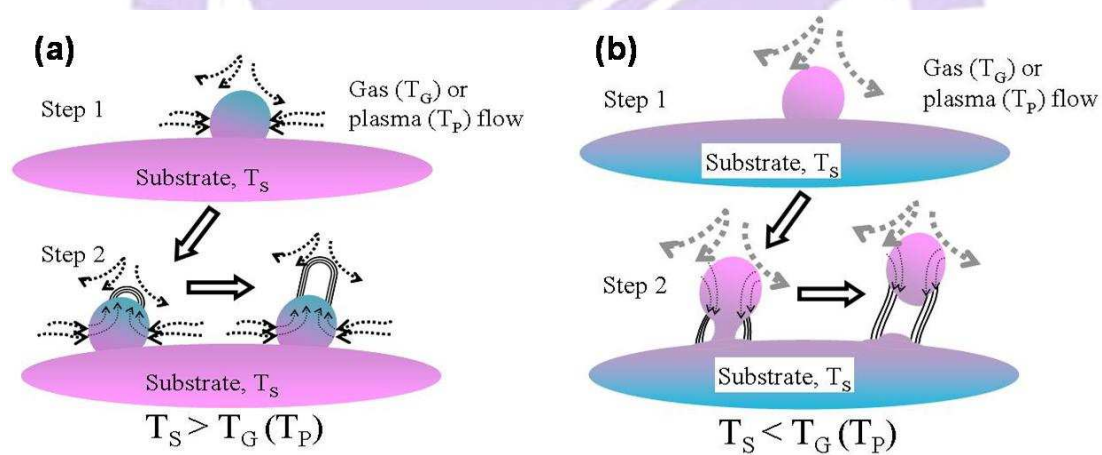


Fig. 6- 12 My proposed CNTs growth models, (a) base-growth and (b) tip-growth mechanisms.

6.4. My proposed CNTs growth mechanism based on temperature difference

The detailed effects of ΔT on CNTs growth mode may further be realized by the growth mechanisms proposed in Fig. 6- 12. In brief, the CNT growth process may be roughly divided into two steps. In the case of $\Delta T = T_G - T_S < 0$, Fig. 6- 12a illustrates the concept of the base-growth model, which commonly occurred during traditional thermal-CVD system or specially designed plasma-enhanced CVD systems. In step 1, the precursors are decomposed and/or reacted with the substrate to produce carbon species. Subsequently, they are then dissolved by the catalyst nanoparticles till reaching the solubility limit, which is dictated by the substrate temperature. In step 2, due to cooling effect of the precursor flow, the temperature at the top surfaces of the catalyst nanoparticles is relatively lower than that at the bottom surfaces. As such, carbon super saturation near the top surfaces of the catalyst should be relatively higher than that near the bottom surfaces. Consequently, precipitation of carbon prefers to take places at the top of catalyst, resulting the base-growth CNTs. Note that precipitation of carbon at the top of catalysts should also leads to local cooling effect (due to the endothermic nature of the reaction) and hence may further enhance the ΔT effect.^[Baker-1972-51; Kanzow-1998-525] On the contrary, Fig. 6- 12b illustrates the condition of $\Delta T = T_G - T_S > 0$, in this case, the gas or plasma is at a higher temperature than the substrate. Therefore, carbon in the catalyst is anticipated to precipitate at the cooler (bottom) side of the catalyst. As a result, the carbons tend to push the catalyst nanoparticles upward, resulting the tip-growth CNTs.

Chapter 7

Conclusions

In this study, CPMs with tailored pore sizes and CNTs with dictated diameters were successfully prepared by silica-template-assisted CVD method, and adopted as supporting materials on DMFC anodes. Studies to explore effects of key parameters on growth mode of CNTs on various substrates in both thermal and plasma-enhanced CVD processes were conducted. From the experimental results, the following conclusions can be drawn.

- (a) CPMs with uniform pore sizes ranging from 1 to 400 nm and MWCNTs with tube diameters ranging from 3 to 17 nm could be rapidly and successfully fabricated by CVD processes via guiding of silica or zeolite templates. The results also show that SBA-15, PCC, and Zeolite-Y templates can be used to produce CPMs with porous structures, and MCM-48 template to produce branched structures. The I_G/I_D ratios of CPMs and MWCNTs after silica removal are about 0.7 - 0.8, independent of pore or tube sizes. The values are about the same as commercial SWCNTs and XC-72 activated carbon material.
- (b) The anode made of CPMs dispersed with Pt-particles can be adopted to obtain the MOR activity going up to 655 A/g of Pt, but CO-tolerance going down to 1.0 for CPMs pore size of 400 nm. In other words, a compromise in MOR activity and CO-tolerance is required in real applications by adopting suitable pore size of CPMs. The pore size dependence of CPMs on MOR activity is related to channel limitation of methanol transfer by smaller pores. The results also show that

CO-tolerance is correlated with surface condition variation due to nano effect, when a significant amount of Pt-particles with sizes less than 1 nm is met.

(c) The anode made of CNTs dispersed with Pt-particles and Fe catalyst particles can be adopted to obtain MOR activity up to 414 A/g of Pt by using CNTs of 17 nm in diameter. The CO-tolerance in this case is around 1.2 – 1.3, independent of tube size. It indicates that the performance is better than the commercial carbon materials, where the MOR activity and CO-tolerance by using commercial SWCNTs and XC-72 activated carbon material are 310 A/g of Pt, 1.2 and 353 A/g of Pt, 1.0, respectively.

(d) The grow modes of tip- and base-growth mechanisms of CNTs by CVD processes are found that ΔT plays a crucial role, where ΔT is defined as local temperature difference between the top (close to gas atmosphere) and bottom (in contact with the substrate) sides of a catalyst particle. ΔT is basically an index of the temperature increasing direction across the catalyst particle. Through reaction gas preheating or without gas preheating in thermal CVD, or variation of temperature heating sequence in plasma CVD, ΔT can be successfully manipulated to become > 0 , ~ 0 or < 0 to vary the growth modes of CNTs to become tip-, onion-like or base-growth modes, respectively. Sign of ΔT , i.e. the direction of temperature increasing across a catalyst particle, is essentially to direct carbon diffusion direction to precipitate at the cooler side of the catalyst.

Chapter 8

Future outlooks

This dissertation not only exposes the potentials of CPMs and CNTs on enhancing the performance of DMFC anode, but also explores the factor dominating the CNT growth mode. However, there are some subject should be further studied.

1. Although it is indicated that Pt nanoparticle smaller than 1 nm exhibit superior CO-tolerance capacities, the detailed mechanism is not understood. Further NMR experiments might be able to explore this mechanism, which is scientific importance and technological significance for the future applications of DMFC anode.
2. Even though MOR activity of Pt/CPMs can be increased by increasing CPM pore size, it also accompanied with decreasing of CO-tolerance. On the other hand, it is found that Pt particle $< 1\text{nm}$ exhibit superior CO-tolerance. Therefore, further study on how to well disperse Pt particles on macroporous carbon should be able to get two advantages together in onematerials.

References

A

1. Abdi, Y., J. Koohsorkhi, J. Derakhshandeh, S. Mohajezadeh, H. Hoseinzadegan, M. D. Robertson, J. C. Bennet, X. Wu and H. Radamson, *Mater. Sci. Eng. C* 26 (2006) 1219 "PECVD-grown carbon nanotubes on silicon substrates with a nickel-seeded tip-growth structure".

B

1. Baerlocher, C., W. M. Meler and D. H. Olson, *Atlas of Zeolite framework types*, p140 (International zeolite association, 2001).
2. Baker, R. T. K., M. A. Barber, P. S. Harris, F. S. Feates and R. J. Waite, *J. Catal.* 26 (1) (1972) 51, "Nucleation and growth of carbon deposits from the nickel catalyzed decomposition of acetylene".
3. Barrett, E. P., L. G. Joyner and P. P. Halenda, *J. Am. Chem. Soc.* 73 (1) (1951) 373, "The determination of pore volume and area distribution in porous substances. 1. computations from nitrogen isotherms".
4. Beck, J. S., J. C. Vartuli, W. J. Roth, M. E. Leonowicz, C. T. Kresge, K. D. Schmitt, C. T. W. Chu, D. H. Olson, E. W. Sheppard, S. B. Mccullen, J. B. Higgins and J. L. Schlenker, *J. Am. Chem. Soc.* 114 (27) (1992) 10834, "A new family of mesoporous molecular-sieves prepared with liquid-crystal templates".
5. Bernaerts, D., X. B. Zhang, X. F. Zhang, S. Amelinckx, G. V. Tendeloo, J. V. Landuyt, V. Ivanov and J. B. Nagy, *Philos. Mag. A* 71 (1995) 605, "Electron microscopy study of coiled carbon tubules".
6. Bethune, D. S., C. H. Kiang, M. S. Devries, G. Gorman, R. Savoy, J. Vazquez and R. Beyers, *Nature* 363 (1993) 605, "Cobalt- Catalysed growth of carbon nanotubes with single-atomic-layer wall".
7. Bower, C., O. Zhou, W. Zhu, D. J. Werder and S. Jin, *Appl. Phys. Lett.* 77 (2000) 2767, "Nucleation and growth of carbon nanotubes by microwave plasma chemical vapor deposition".

C

1. Calleja, G., R. Van Grieken, R. García, J. A. Melero and J. Iglesias, *J. Mol. Catal. A: Chem.* **182-183** (2002) 215, "Preparation of titanium molecular species supported on mesostructured silica by different grafting methods".
2. Campbell, M., D. N. Sharp, M. T. Harrison, R. G. Denning and A. J. Turberfield, *Nature* **404** (2000) 53, "Fabrication of photonic crystals for the visible spectrum by holographic lithography".
3. Chang, H., S. H. Joo and C. Pak, *J. Mater. Chem.* **17** (2007) 3078, "Synthesis and characterization of mesoporous carbon for fuel cell applications".
4. Chen, P. L., J. K. Chang, C. K. Kuo and F. M. Pan, *Diamond Relat. Mater.* **13** (2004) 1949, "Anodic aluminum oxide template assisted growth of vertically aligned carbon nanotube arrays by ECR-CVD".
5. Chen, P. L., Anodic aluminum oxide template assisted growth and electron field emission of carbon nanotubes and titanium oxide nanodots, p12 (Ph. D. Dissertation, NCTU, 2005).
6. Chen, Y., D. T. Shaw and L. Guo, *Appl. Phys. Lett.* **76** (2000) 2469, "Field emission of different oriented carbon nanotubes".
7. Choi, G. S., Y. S. Cho, S. Y. Hong, J. B. Park, K. H. Son and D. J. Kim, *J. Appl. Phys.* **91** (2002) 3847, "Carbon nanotubes synthesized by Ni-assisted atmospheric pressure thermal chemical vapor deposition".
8. Choi, H. C., M. Shim, S. Bangsaruntip, and H. Dai, *J. Am. Chem. Soc.*, **124** (31) (2002) 9058, "Spontaneous Reduction of Metal Ions on the Sidewalls of Carbon Nanotubes"
9. Choi, K. S., Y. S. Cho, S. Y. Hong, J. B. Park and D. J. Kim, *J. Eur. Ceram. Soc.* **21** (2001) 2095, "Effects of ammonia on the alignment of carbon nanotubes in metal-assisted thermal chemical vapor deposition".
10. Cullity, B. D., *Elements of X-ray diffraction*, p84 (Addison-Wesley, 1978).

D

1. Darmstadt, H., C. Roy, S. Kaliaguine, T. W. Kim and R. Ryoo, *Chem. Mater.* **15** (2003) 3300, "Surface and pore structures of CMK-5 ordered mesoporous carbons by adsorption and surface spectroscopy".
2. Delzeit, L., I. Mcaninch, B. A. Cruden, D. Hash, B. Chen, J. Han and M. Meyyappan, *J. Appl. Phys.* **91** (9) (2002) 6027, "Growth of multiwall carbon

nanotubes in an inductively coupled plasma reactor".

3. Dresselhaus, M. S., G. Dresselhaus, R. Saito and A. Jorio, *Phys. Rep.* **409** (2005) 47, "Raman spectroscopy of carbon nanotubes".
4. Duesberg, G. S., A. P. Graham, F. Kreupl, M. Liebau, R. Seidel, E. Unger and W. Hoenlein, *Diamond Relat. Mater.* **13** (2004) 354, "Ways towards the scaleable integration of carbon nanotubes into silicon based technology".
5. Dupuis, A. C., *Prog. Mater. Sci.* **50** (2005) 929, "The catalyst in the CCVD of carbon nanotubes - a review".

E

1. Eswaramoorthi, I., and L. P. Hwang, *Diamond Relat. Mater.*, **6** (2007) 1571, "Anodic titanium oxide: A new template for the synthesis of larger diameter multi-walled carbon nanotubes"

F

1. Fan, S., M. G. Chapline, N. R. Franklin, T. W. Tomblor, A. M. Cassell and H. Dai, *Science* **283** (1999) 512, "Self-oriented regular arrays of carbon nanotubes and their field emission properties".
2. Futuba, D. N., K. Hata, T. Yamada, K. Mizuno, M. Yumura and S. Iijima, *Phys. Rev. Lett.* **95** (2005) 056104, "Kinetics of water-assisted single-walled carbon nanotube synthesis revealed by a time-evolution analysis".

G

1. Gao, F., Q. Lu, X. Liu, Y. Yan and D. Zhao, *Nano Lett.* **1** (2001) 743, "Controlled synthesis of semiconductor PbS nanocrystals and nanowires inside mesoporous silica SBA-15 phase".
2. Gao, F., Q. Lu and D. Zhao, *Chem. Phys. Lett.* **360** (5-6) (2002) 585, "In situ adsorption method for synthesis of binary semiconductor CdS nanocrystals inside mesoporous SBA-15".
3. Ge, M. and K. Sattler, *Appl. Phys. Lett.* **65** (18) (1994) 2284, "Scanning tunneling microscopy of single-shell nanotubes of carbon".
4. Gohier, A., C. P. Ewels, T. M. Minea and M. A. Djouadi, *Carbon* **2008** (2008)

1331, "Carbon nanotube growth mechanism switches from tip- to base-growth with decreasing catalyst particle size".

5. Gorbunov, A., O. Jost, W. Pompe and A. Graff, *Carbon* **40** (1) (2002) 113, "Solid-liquid-solid growth mechanism of single-wall carbon nanotubes".
6. Gulino, G., R. Vieira, J. Amadou, P. Nguyen, M. J. Ledoux, S. Galvagno, G. Centi and C. Pham-Huu, *Appl. Cata. A: General* **279** (2005) 89, "C₂H₆ as an active carbon source for a large scale synthesis of carbon nanotubes by chemical vapour deposition".
7. Guo, T., P. Nikolaev, A. G. Rinzler, D. Tomanek, D. T. Colbert and R. E. Smalley, *J. Phys. Chem.* **99** (27) (1995) 10694, "Self-assembly of tubular fullerenes".
8. Guo, T., P. Nikolaev, A. Thess, D. T. Colbert and R. E. Smalley, *Chem. Phys. Lett.* **243** (1995) 49, "Catalytic growth of single-walled nanotubes by laser vaporization".

H

1. Han, Y. J., G. D. Stucky and A. Butler, *J. Am. Chem. Soc.* **121** (1999) 9897, "Mesoporous silicate sequestration and release of proteins".
2. Han, Y. J., J. M. Kim and G. D. Stucky, *Chem. Mater.* **12** (2000) 2068, "Preparation of noble metal nanowires using hexagonal mesoporous silica SBA-15".
3. Hart, A. J., B. O. Boskovic, A. T. H. Chuang, V. B. Golovko, J. Robertson, B. F. G. Johnson and A. H. Slocum, *Nanotechnology* **17** (2006) 1397, "Uniform and selective CVD growth of carbon nanotubes and nanofibres on arbitrarily microstructured silicon surfaces".
4. Hoa, N. D., N. V. Quy, Y. Cho, and D. Kim, *Sens. Actuators B*, **127** (2007) 447, "An ammonia gas sensor based on non-catalytically synthesized carbon nanotubes on an anodic aluminum oxide template".
5. Hofmann, S., R. Sharma, C. Ducati, G. Du, C. Mattevi, C. Cepek, M. Cantoro, S. Pisana, A. Parvez, F. Cervantes-Sodi, A. C. Ferrari, R. Dunin-Borkowski, S. Lizzit, L. Petaccia, A. Goldoni and J. Robertson, *Nano Lett.* **7** (2007) 602, "In situ observations of catalyst dynamics during surface-bound carbon nanotube nucleation".
6. Holland, B. T., C. F. Blanford and A. Stein, *Science* **281** (1998) 538, "Synthesis of macroporous minerals with highly ordered three-dimensional arrays of spheroidal voids".

- Holland, B. T., C. F. Blanford, T. Do and A. Stein, *Chem. Mater.* **11** (1999) 795, "Synthesis of highly ordered, three-dimensional, macroporous structures of amorphous or crystalline inorganic oxides, phosphates, and hybrid composites".
- Hosomi, T., T. Maki and T. Kobayashi, *Thin Solid Films* **368** (2) (2000) 269, "Enhanced diamond film growth by Xe-added microwave plasma CVD".
- Hsu, C. M., C. H. Lin, H. L. Chang and C. T. Kuo, *Thin solid films* **420** (2002) 225, "Growth of the large area horizontally-aligned carbon nanotubes by ECR-CVD".
- Hsu, C. M., H. J. Lai and C. T. Kuo, *J. Vac. Sci. Technol. A* **22** (2004) 1461, "Growth behavior and interfacial reaction between carbon nanotubes and Si substrate".
- Huang, M. H., A. Choudrey and P. Yang, *Chem. Commun.* (2000) 1063, "Ag nanowire formation within mesoporous silica".

I

- Iijima, S., *Nature* **354** (1991) 56, "Helical microtubules of graphic carbon".
- Iijima, S. and T. Ichihashi, *Nature* **363** (1993) 603, "Single-shell carbon nanotubes of 1-nm diameter".
- Im, W. S., Y. S. Cho, G. S. Choi, F. C. Yu, and D. J. Kim, *Diamond Relat. Mater.*, **13** (2004) 1214, "Stepped carbon nanotubes synthesized in anodic aluminum oxide templates"

J

- Jana, S., B. Dutta, R. Bera and S. Koner, *Langmuir* **23** (2007) 2492, "Anchoring of copper complex in MCM-41 matrix: A highly efficient catalyst for epoxidation of olefins by tert-BuOOH".
- James, G., C. Shen, R. G. Herman and K. Klier, *J. Phys. Chem. B* **106** (2002) 9975, "Sulfonic acid-functionalized mesoporous silica: synthesis, characterization, and catalytic reaction of alcohol coupling to ethers".
- Jeong, H. J., Y. M. Shin, S. Y. Jeong, Y. C. Choi, Y. S. Park, S. C. Lim, G. S. Park, I. T. Han, J. M. Kim and Y. H. Lee, *Chem. Vap. Deposition* **8** (2002) 11, "Anomalies in the growth temperature and time dependence of carbon nanotube growth".

4. Jeong, S. H., H. Y. Hwang, S. K. Hwang, and K. H. Lee, *Carbon*, **42** (2004) 2073, "Carbon nanotubes based on anodic aluminum oxide nano-template"
5. Joo, S. H., C. Pak, D. J. You, S.-A. Lee, H. I. Lee, J. M. Kim, H. Chang, and D. Seung, *Electrochimica Acta*, **52** (4) (2006) 1618, "Ordered mesoporous carbons (OMC) as supports of electrocatalysts for direct methanol fuel cells (DMFC): Effect of carbon precursors of OMC on DMFC performances"
6. Joo, S. H., S. J. Choi, I. Oh, J. Kwak, Z. Liu, O. Terasaki and R. Ryoo, *Nature* **412** (6843) (2001) 169, "Ordered nanoporous arrays of carbon supporting high dispersions of platinum nanoparticles".
7. Joo, S. H., S. Jun and R. Ryoo, *Micropor. Mesopor. Mat.* **44** (2001) 153, "Synthesis of ordered mesoporous carbon molecular sieves CMK-1".
8. Jun, S., S. H. Joo, R. Ryoo, M. Kruk, M. Jaroniec, Z. Liu, T. Ohsuna and O. Terasaki, *J. Am. Chem. Soc.* **122** (43) (2000) 10712, "Synthesis of new, nanoporous carbon with hexagonally ordered mesostructure".

K

1. Kaneda, M., T. Tsubakiyama, A. Carlsson, Y. Sakamoto, T. Ohsuna, O. Terasaki, S. H. Joo and R. Ryoo, *J. Phys. Chem. B* **106** (6) (2002) 1256, "Structural study of mesoporous MCM-48 and carbon networks synthesized in the spaces of MCM-48 by electron crystallography".
2. Kanzow, H., A. Schmalz and A. Ding, *Chem. Phys. Lett.* **295** (1998) 525, "Laser-assisted production of multi-walled carbon nanotubes from acetylene".
3. Kato, T., G. H. Jeong, T. Hirata and R. Hatakeyama, *Thin Solid Films* **457** (1) (2004) 2, "Structure control of carbon nanotubes using radio-frequency plasma enhanced chemical vapor deposition".
4. Kim, J. M., S. K. Kim and R. Ryoo, *Chem. Commun.* (2) (1998) 259, "Synthesis of MCM-48 single crystals".
5. Kim, T. W., I. S. Park and R. Ryoo, *Angew. Chem. Int. Edit.* **42** (36) (2003) 4375, "A synthetic route to ordered mesoporous carbon materials with graphitic pore walls".
6. Kresge, C. T., M. E. Leonowicz, W. J. Roth, J. C. Vartuli and J. S. Beck, *Nature* **359** (1992) 710, "Ordered mesoporous molecular sieves synthesized by a liquid-crystal template mechanism".
7. Kruk, M., M. Jaroniec, R. Ryoo and J. M. Kim, *Chem. Mater.* **11** (9) (1999) 2568, "Characterization of high-quality MCM-48 and SBA-1 mesoporous

silicas".

8. Kukovitsky, E. F., S. G. L'vov and N. A. Sainov, *Chem. Phys. Lett.* **317** (2000) 65, "VLS-growth of carbon nanotubes from the vapor".
9. Kuo, C. H., A. Bai, C. H. Huang, Y. Y. Li, C. C. Hu, and C. C. Chen, *Carbon*, **43** (2005) 2760, "Diameter control of multiwalled carbon nanotubes using experimental strategies"
10. Kuo, C. T., C. H. Lin and A. Y. Lo, *Diamond Relat. Mater.* **12** (3-7) (2003) 799, "Feasibility studies of magnetic particle-embedded carbon nanotubes for perpendicular recording media".
11. Kyotani, T., L. F. Tsai, and A. Tomita, *Chem. Mater.*, **8** (1996) 2109, "Preparation of ultrafine carbon tubes in nanochannels of an anodic aluminum oxide film"

L

1. Lau, A. K. T. and D. Hui, *Comp. Pt. B* **33** (4) (2002) 263, "The revolutionary creation of new advanced materials-carbon nanotube composites".
2. Lee, C. J., D. W. Kim, T. J. Lee, Y. C. Choi, Y. S. Park, Y. H. Lee, W. B. Choi, N. S. Lee, G. S. Park and J. M. Kim, *Chem. Phys. Lett.* **312** (1999) 461, "Synthesis of aligned carbon nanotubes using thermal chemical vapor deposition".
3. Lee, C. J. and J. Park, *Appl. Phys. Lett.* **77** (21) (2000) 3397, "Growth model of bamboo-shaped carbon nanotubes by thermal chemical vapor deposition".
4. Lee, C. J., S. C. Lyu, Y. R. Cho, J. H. Lee and K. I. Cho, *Chem. Phys. Lett.* **341** (3-4) (2001) 245, "Diameter-controlled growth of carbon nanotubes using thermal chemical vapor deposition".
5. Lee, K. Y., S. I. Honda, M. Katayama, T. Miyake, K. Himuro, K. Oura, J. G. Lee, H. Mori and T. Hirao, *J. Vac. Sci. Technol. B* **23** (4) (2004) 1450, "Vertically aligned growth of carbon nanotubes with long length and high density".
6. Lee, W. Y., T. X. Liao, Z. Y. Juang and C. H. Tsai, *Diamond Relat. Mater.* **13** (2004) 1232, "Patterned aligned growth of carbon nanotubes on porous structure templates using chemical vapor deposition methods".
7. Lei, Z. B., M. Y. Zhao, L. Q. Dang, L. Z. An, M. Lu, A. Y. Lo, N. Y. Yu and S. B. Liu, *J. Mater. Chem.* **19** (33) (2009) 5985, "Structural evolution and electrocatalytic application of nitrogen-doped carbon shells synthesized by pyrolysis of near-monodisperse polyaniline nanospheres".

8. Li, W., C. Liang, W. Zhou, J. Qiu, Z. Zhou, G. Sun, and Q. Xin, *J. Phys. Chem. B*, **107** (26) (2003) 6292, "Preparation and Characterization of Multiwalled Carbon Nanotube-Supported Platinum for Cathode Catalysts of Direct Methanol Fuel Cells".
9. Li, W. Z., D. Z. Wang, S. X. Yang, J. G. Wen, and Z. F. Ren, *Chem. Phys. Lett.*, **335** (2001) 141, "Controlled growth of carbon nanotubes on graphite foil by chemical vapor deposition".
10. Lim, M. H., and A. Stein, *Chem. Mater.* **11** (1999) 3285, "Comparative studies of grafting and direct syntheses of inorganic-organic hybrid mesoporous materials".
11. Lin, C. C., P. Y. Lo, C. H. Lin and C. T. Kuo, *Diamond Relat. Mater.* **14** (2005) 778, "Structure and property features of the catalyst-assisted carbon nanostructures on Si wafer by catalyst ion implantation and ECR-CVD".
12. Lin, C. H., H. L. Chang, C. M. Hsu, A. Y. Lo and C. T. Kuo, *Diam. Relat. Mater.* **12** (10-11) (2003) 1851, "The role of nitrogen in carbon nanotube formation".
13. Liu, A. M., K. Hidajat, S. Kawi and D. Y. Zhao, *Chem. Commun.* (2000) 1145, "A new class of hybrid mesoporous materials with functionalized organic monolayers for selective adsorption of heavy metal ions".
14. Lin, H. P., S. Cheng and C. Y. Mou, *Chem. Mater.* **10** (1998) 581, "Mesoporous molecular sieves MCM-41 with a hollow tubular morphology".
15. Lin, M. L., C. C. Huang, M. Y. Lo and C. Y. Mou, *J. Phys. Chem. C* **112** (2008) 867, "Well-ordered mesoporous carbon thin film with perpendicular channels: application to direct methanol fuel cell".
16. Liu, Z., X.Y. Ling, X. Su and J.Y. Lee, *J. Phys. Chem. B* **108** (2004) 8234, "Carbon-supported Pt and PtRu nanoparticles as catalysts for a direct methanol fuel cell".
17. Liu, S. H., R. F. Lu, S. J. Huang, A. Y. Lo, S. H. Chien and S. B. Liu, *Chem. Commun.* (32) (2006) 3435, "Controlled synthesis of highly dispersed platinum nanoparticles in ordered mesoporous carbon".
18. Liu, S. H., W. Y. Yu, C. H. Chen, A. Y. Lo, B. J. Hwang, S. H. Chien and S. B. Liu, *Chem. Mater.* **20** (4) (2008) 1622, "Fabrication and characterization of well-dispersed and highly stable PtRu nanoparticles on carbon mesoporous material for applications in direct methanol fuel cell".
19. Lowell, S., J. E. Shields, M. A. Thomas and M. Thommes, *Characterization of porous solids and powders: surface area, pore size and density*, p3 p12 (Kluwer Academic Publishers, 2004).

20. Lu, G. Q. and X. S. Zhao, Nanoporous materials: science and engineering, p6 (Imperial College Press, 2004).

M

1. Matos, J. R., M. Kruk, L. P. Mercuri, M. Jaroniec, L. Zhao, T. Kamiyama, O. Terasaki, T. J. Pinnavaia and Y. Liu, *J. Am. Chem. Soc.* **125** (3) (2003) 821, "Ordered mesoporous silica with large cage-like pores: Structural identification and pore connectivity design by controlling the synthesis temperature and time".
2. Melechko, A. V., V. I. Merkulov, D. H. Lowndes, M. A. Guillorn and M. L. Simpson, *Chem. Phys. Lett.* **356** (2002) 527, "Transition between 'base' and 'tip' carbon nanofiber growth modes".
3. Melechko, A. V., V. I. Merkulov, T. E. Mcknight, M. A. Guillorn, K. L. Klein, D. H. Lowndes and M. L. Simpson, *J. Appl. Phys.* **97** (4) (2005) 041301, "Vertically aligned carbon nanofibers and related structures: Controlled synthesis and directed assembly".
4. Mercier, L., and T. J. Pinnavaia, *Adv. Mater.* **9** (1997) 500, "Access in mesoporous materials: advantages of a uniform pore structure in the design of a heavy metal Ion adsorbent for environmental remediation".
5. Mihi, A., H. Míguez, I. Rodríguez, S. Rubio and F. Meseguer, *Phys. Rev. B* **71** (2005) 125, "Surface resonant modes in colloidal photonic crystals".
6. Mou, C. Y. and H. P. Lin, *Pure Appl. Chem.* **72** (2000) 137, "Control of morphology in synthesizing mesoporous silica".
7. Mu, Y., H. Liang, J. Hu, L. Jiang and L. Wan, *J. Phys. Chem. B* **109** (2005) 22212, "Controllable Pt nanoparticle deposition on carbon nanotubes as an anode catalyst for direct methanol fuel cells".
8. Murakami, H., M. Hirakawa, C. Tanaka and H. Yamakawa, *Appl. Phys. Lett.* **76** (2000) 1776, "Field emission from well-aligned, patterned, carbon nanotube emitters".

N

1. Nagy, J. B., P. Bodart, I. Hannus and I. Kiricsi, DecaGen Ltd. (1998) 192, "Synthesis, characterization and use of zeolite microporous materials".

O

1. Ogden, J. M., Phys. Today **55** (4) (2002) 69, "Hydrogen: The fuel of the future?".
2. Ohkubo, T., J. Miyawaki, K. Kaneko, R. Ryoo and N. A. Seaton, J. Phys. Chem. B **106** (25) (2002) 6523, "Adsorption properties of templated mesoporous carbon (CMK-1) for nitrogen and supercritical methane - Experiment and GCMC simulation".

P

1. Pal, S. K., S. Talapatra, S. Kar, L. Ci, R. Vajtai, T. Borca-Tasciuc, L. S. Schadler and P. M. Ajayan, Nanotechnology **19** (2008) 1, "Time and temperature dependence of multi-walled carbon nanotube growth on Inconel 600".
2. Pan, Z. W., S. S. Xie, B. H. Chang, L. F. Sun, W. Y. Zhou and G. Wang, Chem. Phys. Lett. **97** (1999) 299, "Direct growth of aligned open carbon nanotubes by chemical vapor deposition".
3. Pillai, S. K., S. S. Ray and M. Moodley, J. Nanosci. Nanotechnol. **7** (2007) 3011, "Purification of single-walled carbon nanotubes".
4. Prasetyo, I. and D. D. Do, Carbon **37** (12) (1999) 1909, "Pore structure alteration of porous carbon by catalytic coke deposition".

R

1. Raffaele, R. P., B. J. Landi, J. D. Harris, S. G. Bailey and A. F. Hepp, Mater. Sci. Eng., B **116** (3) (2005) 233, "Carbon nanotubes for power applications".
2. Ravikovitch, P. I. and A. V. Neimark, Langmuir **18** (5) (2002) 1550, "Density functional theory of adsorption in spherical cavities and pore size characterization of templated nanoporous silicas with cubic and three-dimensional hexagonal structures".
3. Ren, X. M., P. Zelenay, S. Thomas, J. Davey and S. Gottesfeld, J. Power Sources **86** (2000) 111, "Recent advances in direct methanol fuel cells at Los Alamos National Laboratory".
4. Ren, Z. F., Z. P. Huang, J. W. Xu, J. H. Wang, P. Bush, M. P. Siegal and P. N.

- Provencio, *Science* **282** (1998) 1105, "Synthesis of large arrays of well-aligned carbon nanotubes on glass".
5. Rouquerol, J., D. Avnir, C. W. Fairbridge, D. H. Everett, J. H. Haynes, N. Pernicone, J. D. F. Ramsay, K. S. W. Sing and K. K. Unger, *Pure Appl. Chem.* **66** (1994) 1739, "Recommendations for the characterization of porous solids".
 6. Ryoo, R., S. H. Joo and S. Jun, *J. Phys. Chem. B* **103** (37) (1999) 7743, "Synthesis of highly ordered carbon molecular sieves via template-mediated structural transformation".
 7. Ryoo, R., S. H. Joo, M. Kruk and M. Jaroniec, *Adv. Mater.* **13** (9) (2001) 677, "Ordered mesoporous carbons".

S

1. Saito, R., M. Fujita, G. Dresselhaus and M. S. Dresselhaus, *Appl. Phys. Lett.* **60** (1992) 2204, "Electronic-structure of chiral graphene tubules".
2. Saito, R., G. Dresselhaus and M. S. Dresselhaus, *Physical properties of carbon nanotubes*, p35 (Imperial College Press, 2004).
3. Saito, Y., K. Nishikubo, K. Kawabata and T. Matsumoto, *J. Appl. Phys.* **80** (1996) 3062, "Carbon nanocapsules and single-layered nanotubes produced with platinum-group metals (Ru, Rh, Pd, Os, Ir, Pt) by arc discharge".
4. Satio, Y., *Carbon* **33** (1995) 979, "Nanoparticles and filled nanocapsules".
5. Schumacher, K., P. I. Ravikovitch, A. D. Chesne, A. V. Neimark and K. K. Unger, *Langmuir* **16** (2000) 4648, "Characterization of MCM-48 Materials".
6. Segura, R. A., W. Ibáñez, R. Aoto, S. Hevia, P. Häberle and N. J., *Nanotechnol.* **6** (2006) 1945, "Growth morphology and spectroscopy of multiwall carbon nanotubes synthesized by pyrolysis of iron phthalocyanine".
7. Selvam, P., S. K. Bhatia and C. G. Sonwane, *Ind. Eng. Chem. Res.* **40** (2001) 3237, "Recent advances in processing and characterization of periodic mesoporous MCM-41 silicate molecular sieves".
8. Shao, Y., J. Liu, Y. Wang and Y. Lin, *J. Mater. Chem.* **19** (2009) 46, "Novel catalyst support materials for PEM fuel cells: current status and future prospects".
9. Sing, K. S. W., D. H. Everett, R. a. W. Haul, L. Moscou, R. A. Pierotti, J. Rouquerol and T. Siemieniowska, *Pure Appl. Chem.* **57** (4) (1985) 603, "Reporting physisorption data for gas solid systems with special reference to

the determination of surface-area and porosity (recommendations 1984)".

10. Smith, E. and G. Dent, Modern raman spectroscopy- A practical approach, p2 (John Willey & Sons Ltd, 2005).
11. Somanathan, T., and A. Pandurangan, Appl. Surf. Sci. **254** (2008) 5643, "Catalytic activity of Fe, Co and Fe-Co-MCM-41 for the growth of carbon nanotubes by chemical vapour deposition method".
12. Song, I. K., W. J. Yu, Y. S. Cho, G. S. Choi and D. Kim, Nanotechnol. **15** (2004) S590, "The determining factors for the growth mode of carbon nanotubes in the chemical vapour deposition process".
13. Stadermann, M., S. P. Sherlock, J. B. In, F. Fornasiero, H. G. Park, A. B. Artyukhin, Y. Wang, J. J. De Yoreo, C. P. Grigoropoulos, O. Bakajin, A. A. Chernov and A. Noy, Nano lett. **9** (2009) 738, "Mechanism and kinetics of growth termination in controlled chemical vapor deposition growth of multiwall carbon nanotube arrays".

T

1. Tiwari, J.N., F.M. Pan, R.N. Tiwari and S.K. Nandi, Chem. Commun. (2008) 6516, "Facile synthesis of continuous Pt island networks and their electrochemical properties for methanol electrooxidation".
2. Tsai, S. H., C. W. Chao, C. L. Lee and H. C. Shih, Appl. Phys. Lett. **74** (23) (1999) 3462, "Bias-enhanced nucleation and growth of the aligned carbon nanotubes with open ends under microwave plasma synthesis".

V

1. Vartuli, J. C., W. J. Roth, J. S. Beck, S. B. Mccullen and C. T. Kresge, Molec. Siev. **1** (1998) 97, "The synthesis and properties of M41S and related mesoporous materials".

W

1. Wang, N., Z. K. Tang, G. D. Li, and J. S. Chen, *Science*, **408** (2000) 50, "Materials science: Single-walled 4 Å carbon nanotube arrays".
2. Wang, X.Q., M. Wang, H.X. Jin, Z.H. Li and P.M. He, Appl. Surf. Sci. **243**

- (2005) 151, "Preparation of carbon nanotubes at the surface of Fe/SBA-15 mesoporous molecular sieve".
3. Wei, J., B. Jiang, X. Zhang, H. Zhu and D. Wu, *Chem. Phys. Lett.* **376** (2003) 753, "Raman study on double-walled carbon nanotubes".
 4. Wei, Y. Y., G. Eres, V. I. Merkulov, and D. H. Lowndes, *Appl. Phys. Lett.*, **78** (2001) 1394, "Effect of catalyst film thickness on carbon nanotube growth by selective area chemical vapor deposition".

X

1. Xu, J., Z. Luan, H. He, W. Zhou and L. Kevan, *Chem. Mater.* **10** (1998) 3690, "A Reliable Synthesis of Cubic Mesoporous MCM-48 Molecular Sieve".
2. Xu, J., K. Hua, G. Sun, C. Wang, X. Lv and Y. Wang, *Electrochem. Commun.* **8** (2006) 982, "Electrooxidation of methanol on carbon nanotubes supported Pt-Fe alloy electrode".

Y

1. Yang, Q., C. Xiao, W. Chen and A. Hirose, *Diamond Relat. Mater.* **13** (3) (2004) 433, "Selective growth of diamond and carbon nanostructures by hot filament chemical vapor deposition".
2. Yang, Y., J. D. York, J. Xu, S. Lim, Y. Chen and G. L. Haller, *Micropor. Mesopor. Mater.* **86** (2005) 303, "Statistical design of C10-Co-MCM-41 catalytic template for synthesizing smaller-diameter single-wall carbon nanotubes".
3. Yao, B. D., and N. Wang, *J. Phys. Chem. B*, **105** (2001) 11395, "Carbon nanotube arrays prepared by MWCVD".
4. Yap, H. Y., B. Ramaker, A. V. Sumant and R. W. Carpick, *Diamond Relat. Mater.* **15** (2006) 1622, "Growth of mechanically fixed and isolated vertically aligned carbon nanotubes and nanofibers by DC plasma-enhanced hot filament chemical vapor deposition".

Z

1. Zhao, D., Q. Huo, J. Feng, B.F. Chmelka and G.D. Stucky, *J. Am. Chem. Soc.* **120** (1998) 6024, "Nonionic triblock and star diblock copolymer and oligomeric surfactant syntheses of highly ordered, hydrothermally stable, mesoporous silica structures".
2. Zhao, D., J. Feng, Q. Huo, N. Melosh, G. H. Fredrickson, B. F. Chmelka and G. D. Stucky, *Science* **279** (1998) 548, "Triblock copolymer syntheses of mesoporous silica with periodic 50 to 300 angstrom pores".
3. Zhao, J., F. Gao, Y. Fu, W. Jin, P. Yang and D. Zhao, *Chem. Commun.* (2002) 752, "Biomolecule separation using large pore mesoporous SBA-15 as a substrate in high performance liquid chromatography".
4. Zhao, N., C. He, Z. Jiang, J. Li and Y. Li, *Mater. Lett.* **60** (2006) 159, "Fabrication and growth mechanism of carbon nanotubes by catalytic chemical vapor deposition".



Vita

姓名：駱安亞 (An-Ya Lo)

出生年月日：民國 64 年 11 月 25 日

聯絡電話：0918037048

通訊住址：台北縣三峽鎮學成路 276 號 16 樓之 6

電子郵件信箱：lo_an-ya@hotmail.com

學歷：

博士：國立交通大學材料科學與工程學系 民國 93 年 9 月 ~ 民國 99 年 7 月

碩士：國立交通大學材料科學與工程學系 民國 89 年 9 月 ~ 民國 91 年 6 月

大學：私立逢甲大學材料科學與工程學系 民國 85 年 9 月 ~ 民國 89 年 6 月

經歷：

1. 中央研究院 原子與分子科學研究所 民國 92 年 1 月 ~ 民國 97 年 2 月
研究助理

期刊論文(與本論文相關&已發表者)：

1. **A.Y. Lo**, S.B. Liu, C.T. Kuo, “Effect of temperature gradient direction in the catalyst nanoparticle on CNTs growth mode”, *Nanoscale Res. Lett.*, (accepted at 17 May 2010; published online at 26 June 2010).
2. **A.Y. Lo**, S.H. Liu, S.J. Huang, C.T. Kuo, S.B. Liu, “Hollowed carbon capsule based Pt - Fe/carbon electrocatalysts prepared by chemical vapor infiltration method”, *Diamond Relat. Mater.* 17 (2008) 1541 - 1544.
3. **A.Y. Lo**, S.J. Huang, W.H. Chen, Y.R. Peng, C.T. Kuo, S.B. Liu, “Template-assisted synthesis of mesoporous tubular carbon nanostructure by chemical vapor infiltration method”, *Thin Solid Films* 498 (2006) 193 - 197.

期刊論文(與本論文相關&投稿中)：

4. **A.Y. Lo**, N. Yu, S.J. Huang, S.H. Liu, C.T. Kuo, S.B. Liu, “Fabrication route and DMFC anode performance of diameter controlled CNTs”, *Diamond Relat. Mater.*, submitted (2010).
5. **A.Y. Lo**, N. Yu, S.H. Liu, C.T. Kuo, S.B. Liu “Effect of pore size of the carbon porous supports on catalytic performance of DMFC at anode”, (preparing)

其它期刊論文(與本論文無關)：

6. **A.Y. Lo**, C.S. Sun, W.S. Tseng, C.T. Kuo, “Process and properties of the carbon nanotube assisted LiCoO₂ thin-film battery electrode by pulsed laser deposition”, *J.*

- Vac. Sci. Technol. B 27 (6) (2009) 3067-3072.
7. **A.Y. Lo**, S.H. Liu, S.J. Huang, H.K. Shen, C.T. Kuo, S.B. Liu, “Synthesis of uniform carbon nanotubes by chemical vapor infiltration method using SBA-15 mesoporous silica as template”, *Stud. Surf. Sci. Catal.*, 165 (2007) 409-412.
 8. Y. Ding, **A.Y. Lo**, S.J. Huang, P.H. Wu, C. Liu, R. Tan, D. Yin, Z. Fu, D. Yin, C.T. Hung, Z. Lei, N. Yu, S.B. Liu, “Epoxidation of olefins over gold nanoparticles supported on periodic mesoporous organosilicas: Effects of pore architecture and surface modification method of the supports” *Microporous Mesoporous Mater.* (submitted)
 9. Z.B. Lei, Y. Cao, L. Dang, **A.Y. Lo**, N.Y. Yu, S.B. Liu, “Adsorption of lysozyme on spherical mesoporous carbons (SMCs) replicated from colloidal silica arrays by chemical vapor deposition”, *J. Colloid Interface Sci.*, Vol. 339 (2009) 439–445.
 10. Z.B. Lei, S.Y. Bai, L. Dang, H.A. Xia, Q. Xu, Y. Cao, L.H. An, M. Zhao, **A.Y. Lo**, S.B. Liu, “Fe₂O₃/SBA-15 catalyst synthesized by chemical vapor infiltration for Friedel–Crafts alkylation reaction”, *Microporous Mesoporous Mater.*, Vol. 123 (2009) 306-313.
 11. S.H. Liu, W.Y. Yu, C.H. Chen, **A.Y. Lo**, B.J. Huang, S.H. Chien, S.B. Liu, “Fabrication and characterization of well-dispersed and highly stable PtRu nanoparticles on carbon mesoporous material for applications in direct methanol fuel cell”, *Chem. Mater.*, Vol. 20 (2008) 1622-1628.
 12. W.S. Tseng, C.Y. Tseng, P.K. Chuang, **A.Y. Lo**, C.T. Kuo, “A High Efficiency Surface Modification Process for Multiwalled Carbon Nanotubes by Electron Cyclotron Resonance Plasma”, *J. Phys. Chem. C*, Vol. 112, (2008) 18431-18436.
 13. S.H. Liu, R.F. Lu, S.J. Huang, **A.Y. Lo**, W.H. Chen, W.Y. Yu, S.H. Chien, S.B. Liu, “Fabrication of highly dispersed Pt nanoparticles in tubular carbon mesoporous materials for hydrogen energy applications”, *Stud. Surf. Sci. Catal.*, Vol. 165 (2007) 853-856.
 14. S.H. Liu, R.F. Lu, S.J. Huang, **A.Y. Lo**, S.H. Chien and S.B. Liu, “Controlled synthesis of highly dispersed platinum nanoparticles in ordered mesoporous carbons”, *Chem. Commun.*, (2006) 3435–3437.
 15. W.H. Chen, H.H. Ko, A. Sakthivel, S.J. Huang, S.H. Liu, **A.Y. Lo**, and S.B. Liu, “A solid-state NMR, FT-IR, and TPD study on acid properties of sulfated and metal-promoted zirconia: influence of promoter and sulfation treatment”, *Catal. Today*, Vol. 116 (2006) 111-120.
 16. A. Sakthivel, W.H. Chen, S.H. Liu, S.J. Huang, **A.Y. Lo**, Y.H. Hsu, S.D. Lin, and S.B. Liu, “Acidity and catalytic behaviors of ordered mesoporous aluminosilicate materials containing zeolite building units”, *Catal. Lett.*, Vol. 108, (2006) 173-178.

17. W.H. Chen, S.J. Huang, H.H. Ko, **A.Y. Lo**, H.K. Lee, L.L. Wu, C.F. Cheng, and S.B. Liu, "Acidity and Sorption Properties of Nano-Sized Mesoporous Aluminosilicate Materials", *Stud. Surf. Sci. Catal.*, Vol. 156 (2005) 657-662.
18. C.T. Kuo, C.H. Lin, **A.Y. Lo**, "Feasibility studies of magnetic particle-embedded carbon nanotubes for perpendicular recording media", *Diamond Relat. Mater.*, Vol. 12 (2003) 799-805
19. C.H. Lin, H.L. Chang, C.M. Hsu, **A.Y. Lo**, C.T. Kuo, "The role of nitrogen in carbon nanotube formation", *Diamond Relat. Mater.*, Vol. 12 (2003) 1851-1857.

國際研討會論文：

1. **A.Y. Lo**, N. Yu, S.H. Liu, C.T. Kuo, S.B. Liu "Effect of pore size of the carbon porous supports on catalytic performance of DMFC at anode", International Green Energy Conference, Waterloo, Ontario, Canada, June 1-3 2010 (Oral)
2. **A.Y. Lo**, N. Yu, S.J. Huang, C.T. Kuo, and S.B. Liu, "Fabrication of CNTs with controlled diameters and their applications as electrocatalyst supports for DMFC" 4th International Conference on New Diamond and Nano Carbons, Suzhou, China, May 16-20, 2010
3. **A.Y. Lo**, S.B. Liu, C.T. Kuo, "Effect of temperature gradient on CNTs growth", 2009 International thin films conference, Taipei, Taiwan, Dec. 14-16, 2009 (Oral)
4. **A.Y. Lo**, S.H. Liu, S.J. Huang, C.T. Kuo, S.B. Liu, "Hollowed carbon capsule based Pt-Fe/carbon electrocatalysts prepared by chemical vapor infiltration method", 18th European conference on diamond, diamond-like materials, carbon nanotubes, and nitrides, Berlin, Germany, Sept. 9-14 2007
5. **A.Y. Lo**, P.H. Wu, S.H. Liu, S.J. Huang, H.K. Shen, C.T. Kuo, S.B. Liu, "Novel Process to Fabricate Carbon Nanotubes Powders with Controllable Size by Using Mesoporous Silica as Catalyst Template", International Conference on Superhard Coatings, Ein-Gedi, Israel, Feb. 27- Mar. 1 2006
6. **A.Y. Lo**, S.J. Huang, W.H. Chen, S.H. Liu, Y.R. Peng, C.T. Kuo, S.B. Liu, "Syntheses of Tubular Carbon Mesoporous Materials and Carbon Nanotubes by Chemical Vapor Infiltration Method", The 23rd Taiwan Symposium on Catalysis and Reaction Engineering, Kaoshiung, Taiwan, June 23-24 2005
7. **A.Y. Lo**, W.H. Chen, S.J. Huang, and S.B. Liu, "Synthesis nano-sized tubule carbon with cubic structure by chemical vapor infiltration method", The 3rd Asian Conference on Chemical Vapor Deposition, Taipei, Taiwan, Nov. 12-14 2004